FRAMEWORK MATERIALS FOR SOLAR ENERGY UTILIZATION

Cheng Wang

A dissertation submitted to the faculty of the University of North Carolina at Chapel Hill in partial fulfillment of the requirements for the degree of Doctor of Philosophy in the Department of Chemistry (Inorganic).

Chapel Hill
2013

Approved by:

Wenbin Lin

Cynthia Schauer

Thomas Meyer

Malcolm Forbes

David Nicewicz

ABSTRACT

CHENG WANG: Framework Materials For Solar Energy Utilization
(Under the direction of Wenbin Lin)

The ever-increasing global demand for energy has stimulated a new wave of research activities on generating clean and renewable energy using sunlight. Following the molecular approach adopted by green plants, scientists have developed various molecular systems that are capable of converting photons to high energy redox equivalents, as well as molecular catalysts for both water oxidation and proton/CO_2 reduction. There are however not efficient ways of assembling these functional molecular components into hierarchical organizations to convert sunlight energy into chemical energy.

Metal-organic frameworks (MOFs) are a class of crystalline materials that are constructed from well-defined molecular building blocks and metal-cluster connecting nodes. Similarly, crosslinked polymers (CPs) are built from well-designed organic precursors and represent a new class of robust materials. These framework materials provide a potential platform to organize different molecular components to achieve artificial photosynthesis. In this thesis, I will report our efforts on assembling MOFs and CPs for light harvesting, water oxidation, and photocatalytic proton and CO_2 reduction. These materials not only provide a unique opportunity to integrate different functional molecular components hierarchically for energy conversion or organic transformation, but also allow the elucidation of molecular mechanisms for related reactions.

Acknowledgements

I wish to thank many people for making this thesis possible. First, I want to thank my advisor, Professor Wenbin Lin, for giving me the opportunity to work on several interesting projects. I feel truly fortunate to have his constant encouragement to become a strong, confident and independent chemist.

I deeply appreciate help and supports from my current and previous lab mates: in no particular order—Della Rocca, J.; deKrafft, K.; Kent, Caleb.; Falkowski, J.; Huxford, R.; Liu, D.; Duggan, E.; Wanderley, M.; Zhang, T.; Kramer, S.; Barret, S.; Poon, C.; Lu, K.; Abney, C.; Lin, Z; Ma, L; Xie, Z.; Zheng, M.; Song, F.; Vivero Esocoto, J.; Wang, J.-L.; Liu, Y.; Carboni, M.; He, C.; Sawano, T.; Wen, L.; Peng, Y.; Wierschen, A.; Hess, A.; It is enjoyable experience working and discussing with them. It is a treasure of my life.

I also thank all the faculty and staff members in University of North Carolina at Chapel Hill for their teaching and help for me to learn new knowledge and experimental skills.

TABLE OF CONTENTS

LIST OF TABLES

LIST OF FIGURES

Figure

LIST OF SCHEMES

Scheme

LIST OF ABBREVIATIONS

MOF	Metal-organic framework
SBU	Secondary building unit
DMF	Dimethylformamide
DMA	Dimethylamine
TFA	Trifluoroacetic acid
PXRD	Powder X-ray diffraction
TGA	Thermogravi-metricanalysis
ICP-MS	Inductively coupled plasma mass spectrometry
ESI	Electrospray ionization
NMR	Nuclear magnetic resonance
UV-Vis	Ultraviolet-visible spectroscopy
NIR	Near Infrared
GC	Gas Chromatography
CIF	Crystallographic information file
MLCT	Metal-to-ligand charge transfer

Chapter 1

Framework Materials for Solar Energy Utilization: An Introduction

The development of our modern civilization relies on sufficient energy supplies. As our fossil fuel supply dwindles, new energy resources must be developed to sustain the global society. In addition to their limited supply, rapid consumption of fossil fuels also caused ecological problems like emission of green-house gases. The search of a green, large-scale and sustainable energy supply is a top priority for the society now.

Solar energy is one of the few alternative energy sources that could be scaled up to meet our future needs.[1,2] The amount of solar energy that reaches our planet in one hour is more than enough to fuel the world for one year.[1,2] Solar energy can be converted into heat, electricity, or fuels. Considering the ease for storage and transportation, solar fuels and electricity are more desirable. Practical and cost-effective technologies for ultra-large scale solar electricity and solar fuel production do not currently exist, and require breakthroughs in basic science.

Whether converting solar energy to electricity or to chemical energy, three fundamental steps are needed[3]: first, antenna absorb sunlight and efficiently transport the excitations to charge separation centers; second, charge separation centers convert the excitation energy to electrochemical energy (redox equivalents); third, the generated electrons and holes are either used to carry out energy-gaining chemical reactions or transported to power lines to perform useful works. All the three steps can be studied separately, but to achieve solar energy harvesting and storage, a device including all the

components needs to be built. The efficiency of the overall system will not only depend on the individual parts, but also on how these parts are integrated.

Both the first photovoltaic and artificial photo-driven water splitting systems were achieved in solid state semiconductor systems.[4] However, more interest has been put into using small molecules to harvest sunlight energy in recent years.[3,5-9] In these strategies, the different functional parts can be constructed from different groups of small molecules, and the effectiveness of these subsystems can be optimized separately, taking advantage of structure tuning of small molecules. For example, many antenna systems have been constructed from porphyrins or other cyclic tetrapyrroles.[9] $Ru(bpy)_3^{2+}$ (bpy=2,2'-bipyridine) based chromophores have also been extensively studied to serve both as antenna and charge separation centers.[10-15] More molecular catalysts have been developed for a range of energy-storing reactions, such as water oxidation,[16-25] hydrogen production[1,2,5,6,9] and carbon dioxide reduction.[26-37] In addition, photocatalytic molecular systems capable of a range of organic transformations have also been developed, showing alternative mild, clean, and atom-efficient ways to perform otherwise energy-consuming reactions.[38-52]

With a goal to develop usable device, however, it is not enough to have some small molecules freely moving in the solution. Strategies to construct these different components in a sequential and integrated structure must be developed. One promising design of such a system is the photoelectrochemical cell (PEC).[1-3] In this "dye-sensitized solar cell" configuration, molecular excitation and excited-state formation are followed by electron transfer injection into the conduction band of a semiconductor, and molecular catalysts capable of water oxidation, or hydrogen production, or CO_2 reduction are

attached to the electrode through surface chemistry. Self-assembly of large molecules into nano- or micro- size entities have also been identified as an alternative way to organize an integrated sunlight harvesting system,[9] although it is less attractive than the PEC strategy to device engineers, due to the lack of controllability and transportability to existing technologies.

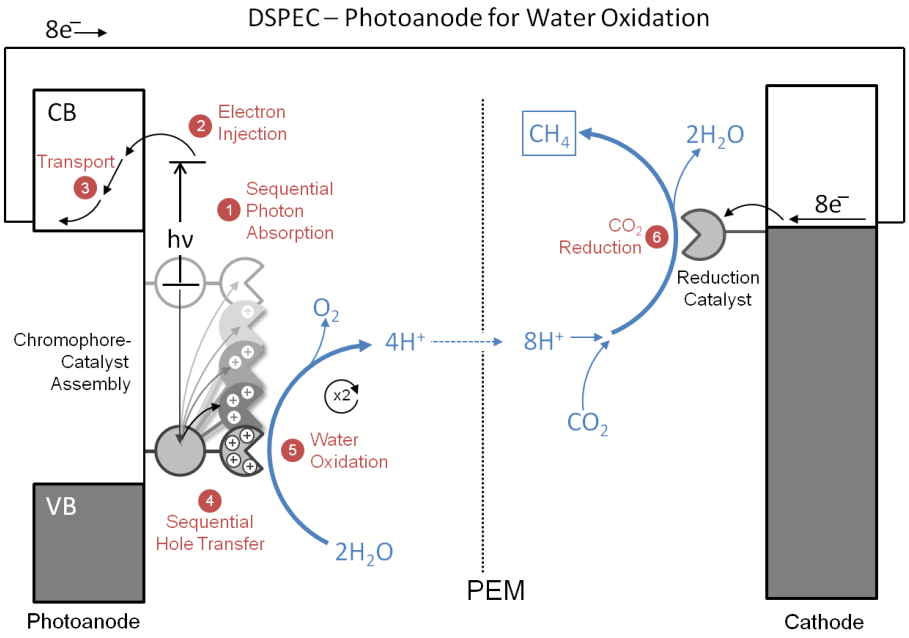

Figure 1. A dye-sensitized photoelectrochemical cell (DSPEC) for CO_2 reduction on the cathode and water oxidation on the anode. The CO_2 reduction can be replaced by proton reduction as well (Copyright: UNC EFRC)

We propose that framework materials can also serve as a platform to integrate different molecular components into a working system. As different types of molecules can be incorporated into one framework in an ordered and connected manner, a framework of molecular machines can facilitate the transfer of energy or excited electrons in the system. Framework materials can either be developed into separate entities capable of solar energy conversion or be integrated into the PEC blueprint. From

another perspective, it is also possible to use phosphor-incorporated framework solids as recyclable and reusable photocatalysts for fine chemical synthesis.

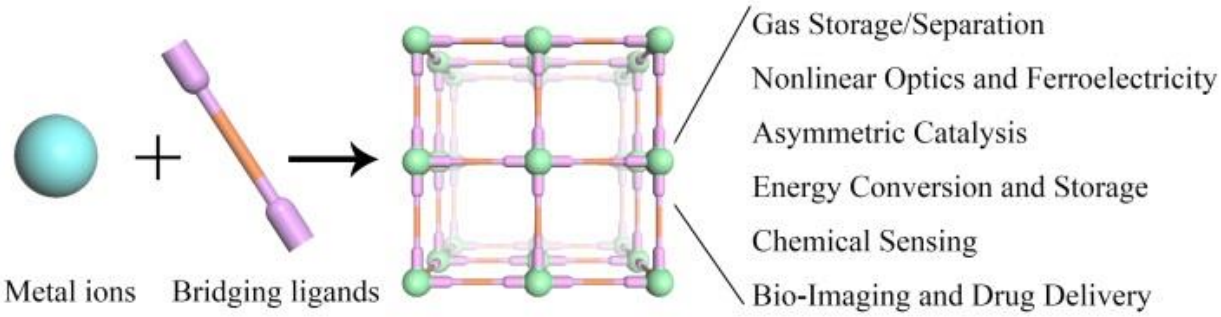

Figure 2. Synthesis of functional MOFs for various applications. (Art credited to Liu, D.)

Metal-organic frameworks (MOFs), also known as coordination polymers or coordination networks, are crystalline materials built from metal ions or metal clusters bridged by organic linkers to form one-, two-, or three-dimensional structures.[53-55] With Prussian blue[56-59] and metal phosphonates[60-64] as their prototypes, coordination polymers were well documented in the inorganic chemistry literature in the last century.[65-74] This field however remained relatively unexplored, primarily because of the difficulty typically encountered in growing large single crystals of coordination polymers that are suitable for X-ray diffraction studies and the lack of easy-to-use computer programs for visualizing complicated structures of most coordination polymers. Robson and co-workers revitalized the field of coordination polymers by reporting the synthesis, X-ray structural characterization, and early topological analysis of coordination polymers built from Cu(I), Zn(II), Cd(II) metal connecting points and cyano- or nitrile-bridging ligands in a series of seminal papers in 1989 and early 1990's.[75-79] Shortly after Robson's papers,

a number of research groups, including those of Fujita, Yaghi, Zaworotko, Kitagawa, Moore/Lee, and Férey, reported the synthesis and characterization of a large number of coordination polymers/MOFs built from many different metal connecting points and bridging ligands.[80-90]

Based on the early topological studies by Robson and coworkers, Yaghi, O'Keeffe, and co-workers carried out systematic synthesis and topological analysis of porous MOFs, demonstrated the zeolitic properties of MOFs, and popularized the concepts of secondary building units and reticular nature of many MOFs.[53,54,91,92] Permanent porosity of MOFs was demonstrated by Kitagawa et al. and Yaghi et al. using pyridine- and carboxylate-based bridging ligands in 1997 and 1998, respectively.[93,94] Yaghi and co-workers first realized the potential of using porous MOFs as storage materials for gaseous molecules of technological importance, such as methane, hydrogen, and carbon dioxide.[92] In parallel to the works done by Yaghi and O'Keeffe, the Lin group initiated a research program in 1997 to use MOFs as a platform to incorporate molecular functionalities into solid materials, with the central premise that MOFs are distinct from traditional inorganic materials because they could be synthesized from well-defined molecular building blocks by taking advantage of both the reliability of molecular synthesis and the hierarchical organization afforded by crystal engineering. The first series of isoreticular MOFs with noncentrosymmetric structures was rationally designed based on 3-D diamondoid networks and 2-D grid structures using systematically elongated pyridinecarboxylate ligands.[95-99] As a result of the intrinsic electronic and structural asymmetry of pyridinecarboxylate building blocks, these MOFs showed second-order nonlinear optical properties.

Since these early studies, the MOF field has witnessed explosive growth in the past decade. Many research groups around the world have contributed to various aspects of MOFs, exploring their applications in many fields such as gas storage/seperation,[92,100-105] nonlinear optics,[95-99] ferroelectricity,[106-109] conductivity/semiconductivity,[110-112] magnetism,[113] luminescence,[114-117] chemical sensing,[118-123] catalysis,[124-129] biomedical imaging,[130-134] drug delivery,[135-140] and solar energy harvesting.[141-145]

Light harvesting molecules like $Ru(bpy)_3^{2+}$ have been built into MOF systems, and excitation energy migration in these frameworks has been quantitatively studied by detecting energy transfer from a $Ru(bpy)_3^{2+}$ entity to a doped $Os(bpy)_3^{2+}$ entity.[141,142] Taking advantage of crystalline structures of MOFs, these studies can bring in new mechanistic insights into the solar energy research. It is thus reasonable to use MOFs as a platform to build multi-component light harvesting systems.

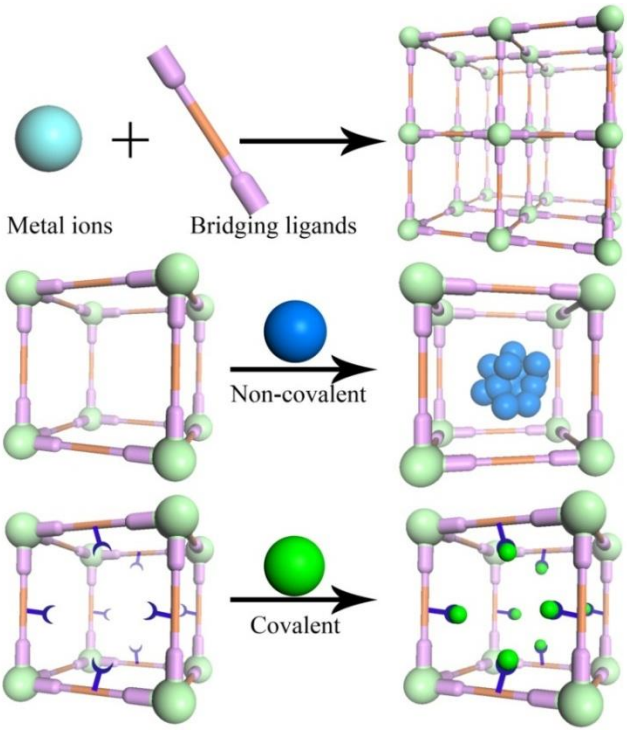

Figure 3. Metal-Organic Frameworks Functionalization. (Art credited to Liu, D.)

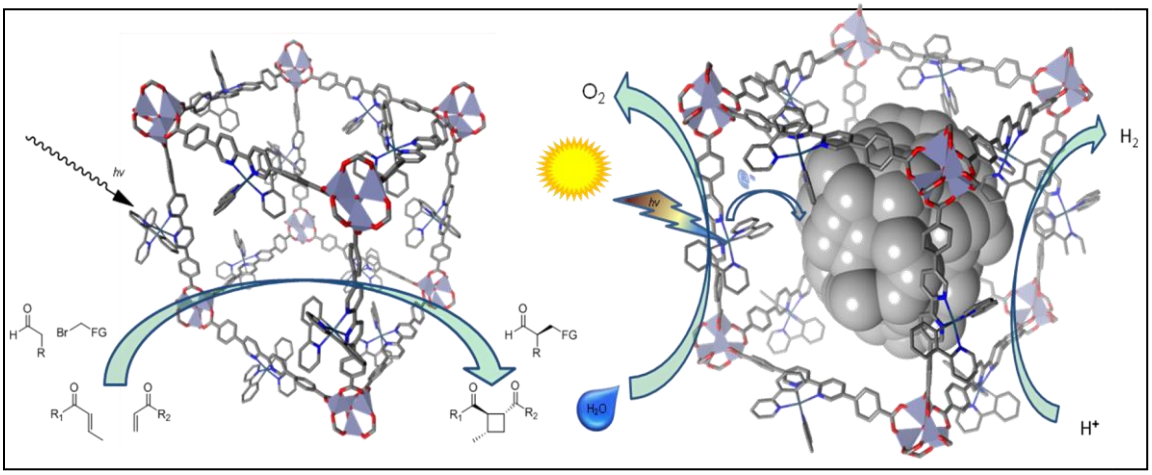

Figure 4. Metal-Organic Frameworks for Artificial Photosysnthesis (Art credited to Falkowski, J. M.)

Crosslinked polymers (CPs), including crystalline covalent-organic frameworks, can also be built from well-designed organic precursors and represent a new class of robust, nanoporous materials.[146-151] Like the MOF counterparts, CPs have shown great promise in gas storage and separation,[149,151] heterogeneous catalysis[152] and light harvesting.[147,148] Although CPs are not always crystalline materials as MOFs, they are advantageous over MOFs in many practical senses since they are in general more chemically and mechanically stable.

In this thesis, I will be describing my research in using metal-organic frameworks and crosslinked polymers as platforms to study energy-harvesting related reactions including water oxidation, photo-driven proton reduction, CO_2 reduction, and photocatalytic organic transformations.

References

(1) Gust, D.; Moore, T. A.; Moore, A. L. *Acc. Chem. Res.* **2009**, *42*, 1890.

(2) Hammarström, L.; Hammes-Schiffer, S. *Acc. Chem. Res.* **2009**, *42*, 1859.

(3) Concepcion, J. J.; Jurss, J. W.; Brennaman, M. K.; Hoertz, P. G.; Patrocinio, A. O. v. T.; Murakami Iha, N. Y.; Templeton, J. L.; Meyer, T. J. *Acc. Chem. Res.* **2009**, *42*, 1954.

(4) Fujishima, A.; Honda, K. *Nature* **1972**, *238*, 37.

(5) Dubois, M. R.; Dubois, D. L. *Acc. Chem. Res.* **2009**, *42*, 1974.

(6) Esswein, M. J.; Nocera, D. G. *Chem. Rev.* **2007**, *107*, 4022.

(7) Morris, A. J.; Meyer, G. J.; Fujita, E. *Acc. Chem. Res.* **2009**, *42*, 1983.

(8) Narayanam, J. M. R.; Stephenson, C. R. J. *Chem. Soc. Rev.* **2011**, *40*, 102.

(9) Wasielewski, M. R. *Acc. Chem. Res.* **2009**, *42*, 1910.

(10) Gafney, H. D.; Adamson, A. W. *J. Am. Chem. Soc.* **1972**, *94*, 8238.

(11) Bock, C. R.; Meyer, T. J.; Whitten, D. G. *J. Am. Chem. Soc.* **1974**, *96*, 4710.

(12) Calvert, J. M.; Caspar, J. V.; Binstead, R. A.; Westmoreland, T. D.; Meyer, T. J. *J. Am. Chem. Soc.* **1982**, *104*, 6620.

(13) Caspar, J. V.; Kober, E. M.; Sullivan, B. P.; Meyer, T. J. *J. Am. Chem. Soc.* **1982**, *104*, 630.

(14) Durham, B.; Caspar, J. V.; Nagle, J. K.; Meyer, T. J. *J. Am. Chem. Soc.* **1982**, *104*, 4803.

(15) Li, J.; Diers, J. R.; Seth, J.; Yang, S. I.; Bocian, D. F.; Holten, D.; Lindsey, J. S. *J. Org. Chem.* **1999**, *64*, 9090.

(16) Blakemore, J. D.; Schley, N. D.; Balcells, D.; Hull, J. F.; Olack, G. W.; Incarvito, C. D.; Eisenstein, O.; Brudvig, G. W.; Crabtree, R. H. *J. Am. Chem. Soc.* **2010**, *132*, 16017.

(17) Concepcion, J. J.; Jurss, J. W.; Templeton, J. L.; Meyer, T. J. *J. Am. Chem. Soc.* **2008**, *130*, 16462.

(18) Duan, L.; Fischer, A.; Xu, Y.; Sun, L. *J. Am. Chem. Soc.* **2009**, *131*, 10397.

(19) Ellis, W. C.; McDaniel, N. D.; Bernhard, S.; Collins, T. J. *J. Am. Chem. Soc.* **2010**, *132*, 10990.

(20) Geletii, Y. V.; Huang, Z.; Hou, Y.; Musaev, D. G.; Lian, T.; Hill, C. L. *J. Am. Chem. Soc.* **2009**, *131*, 7522.

(21) Hull, J. F.; Balcells, D.; Blakemore, J. D.; Incarvito, C. D.; Eisenstein, O.; Brudvig, G. W.; Crabtree, R. H. *J. Am. Chem. Soc.* **2009**, *131*, 8730.

(22) McDaniel, N. D.; Coughlin, F. J.; Tinker, L. L.; Bernhard, S. *J. Am. Chem. Soc.* **2008**, *130*, 210.

(23) Tseng, H. W.; Zong, R.; Muckerman, J. T.; Thummel, R. *Inorg. Chem.* **2008**, *47*, 11763.

(24) Yin, Q.; Tan, J. M.; Besson, C.; Geletii, Y. V.; Musaev, D. G.; Kuznetsov, A. E.; Luo, Z.; Hardcastle, K. I.; Hill, C. L. *Science* **2010**, *328*, 342.

(25) Zong, R.; Thummel, R. P. *J. Am. Chem. Soc.* **2005**, *127*, 12802.

(26) Behar, D.; Dhanasekaran, T.; Neta, P.; Hosten, C. M.; Ejeh, D.; Hambright, P.; Fujita, E. *J. Phys. Chem. A* **1998**, *102*, 2870.

(27) Doherty, M. D.; Grills, D. C.; Fujita, E. *Inorg. Chem.* **2009**, *48*, 1796.

(28) Grodkowski, J.; Behar, D.; Neta, P.; Hambright, P. *J. Phys. Chem. A* **1997**, *101*, 248.

(29) Grodkowski, J.; Dhanasekaran, T.; Neta, P.; Hambright, P.; Brunschwig, B. S.; Shinozaki, K.; Fujita, E. *J. Phys. Chem. A* **2000**, *104*, 11332.

(30) Grodkowski, J.; Neta, P. *J. Phys. Chem. A* **2000**, *104*, 1848.

(31) Grodkowski, J.; Neta, P.; Fujita, E.; Mahammed, A.; Simkhovich, L.; Gross, Z. *J. Phys. Chem. A* **2002**, *106*, 4772.

(32) Hawecker, J.; Lehn, J. M.; Ziessel, R. *J. Chem. Soc., Chem. Commun.* **1983**, 536.

(33) Hori, H.; Johnson, F. P. A.; Koike, K.; Ishitani, O.; Ibusuki, T. *J. Photochem. Photobiol., A* **1996**, *96*, 171.

(34) Hori, H.; Koike, K.; Suzuki, Y.; Ishizuka, M.; Tanaka, J.; Takeuchi, K.; Sasaki, Y. *J. Mol. Catal. A: Chem.* **2002**, *179*, 1.

(35) Jordan, P.; Fromme, P.; Witt, H. T.; Klukas, O.; Saenger, W.; Krausz, N. *Nature* **2001**, *411*, 909.

(36) Takeda, H.; Koike, K.; Inoue, H.; Ishitani, O. *J. Am. Chem. Soc.* **2008**, *130*, 2023.

(37) Tinnemans, A. H. A.; Koster, T. P. M.; Thewissen, D. H. M. W.; Mackor, A. *Recl.: J. R. Neth. Chem. Soc.* **1984**, *103*, 288.

(38) Andrews, R. S.; Becker, J. J.; Gagne, M. R. *Angew. Chem. Int. Ed. Engl.* **2010**, *49*, 7274.

(39) Chen, W.; Rein, F. N.; Rocha, R. C. *Angew. Chem. Int. Ed. Engl.* **2009**, *48*, 9672.

(40) Condie, A. G.; Gonzalez-Gomez, J. C.; Stephenson, C. R. *J. Am. Chem. Soc.* **2010**, *132*, 1464.

(41) Dai, C.; Narayanam, J. M.; Stephenson, C. R. *Nat. Chem.* **2011**, *3*, 140.

(42) Fukuzumi, S.; Kishi, T.; Kotani, H.; Lee, Y.-M.; Nam, W. *Nat. Chem.* **2011**, *3*, 38.

(43) Ischay, M. A.; Anzovino, M. E.; Du, J.; Yoon, T. P. *J. Am. Chem. Soc.* **2008**, *130*, 12886.

(44) Lang, X.; Ji, H.; Chen, C.; Ma, W.; Zhao, J. *Angew. Chem. Int. Ed. Engl.* **2011**.

(45) Narayanam, J. M.; Stephenson, C. R. *Chem. Soc. Rev.* **2011**, *40*, 102.

(46) Narayanam, J. M.; Tucker, J. W.; Stephenson, C. R. *J. Am. Chem. Soc.* **2009**, *131*, 8756.

(47) Neumann, M.; Fuldner, S.; Konig, B.; Zeitler, K. *Angew. Chem. Int. Ed. Engl.* **2011**, *50*, 951.

(48) Nicewicz, D. A.; MacMillan, D. W. *Science* **2008**, *322*, 77.

(49) Su, F.; Mathew, S. C.; Mohlmann, L.; Antonietti, M.; Wang, X.; Blechert, S. *Angew. Chem. Int. Ed. Engl.* **2011**, *50*, 657.

(50) Tucker, J. W.; Nguyen, J. D.; Narayanam, J. M.; Krabbe, S. W.; Stephenson, C. R. *Chem. Commun.* **2010**, *46*, 4985.

(51) Xie, Z.; Wang, C.; Dekrafft, K. E.; Lin, W. *J. Am. Chem. Soc.* **2011**, *133*, 2056.

(52) Zen, J. M.; Liou, S. L.; Kumar, A. S.; Hsia, M. S. *Angew. Chem. Int. Ed. Engl.* **2003**, *42*, 577.

(53) Yaghi, O. M.; O'Keeffe, M.; Kanatzidis, M. *J. Solid State Chem.* **2000**, *152*, 1.

(54) Eddaoudi, M.; Moler, D. B.; Li, H. L.; Chen, B. L.; Reineke, T. M.; O'Keeffe, M.; Yaghi, O. M. *Acc. Chem. Res.* **2001**, *34*, 319.

(55) Ferey, G. *Chem. Mater.* **2001**, *13*, 3084.

(56) Itaya, K.; Uchida, I.; Neff, V. D. *Acc. Chem. Res.* **1986**, *19*, 162.

(57) Entley, W. R.; Girolami, G. S. *Science* **1995**, *268*, 397.

(58) Ferlay, S.; Mallah, T.; Ouahes, R.; Veillet, P.; Verdaguer, M. *Nature* **1995**, *378*, 701.

(59) Sato, O.; Iyoda, T.; Fujishima, A.; Hashimoto, K. *Science* **1996**, *272*, 704.

(60) Clearfield, A.; Stynes, J. A. *J. Inorg. & Nucl. Chem.* **1964**, *26*, 117.

(61) Guang, C.; Hong, H. G.; Mallouk, T. E. *Acc. Chem. Res.* **1992**, *25*, 420.

(62) Clearfield, A. In *Progress in Inorganic Chemistry, Vol 47*; Karlin, K. D., Ed. 1998; Vol. 47, p 371.

(63) Rao, C. N. R.; Natarajan, S.; Choudhury, A.; Neeraj, S.; Ayi, A. A. *Acc. Chem. Res.* **2001**, *34*, 80.

(64) Yu, J. H.; Xu, R. R. *Acc. Chem. Res.* **2003**, *36*, 481.

(65) Kubo, M.; Kishita, M.; Kuroda, Y. *J. Polymer Sci.* **1960**, *48*, 467.

(66) Berg, E. W.; Alam, A. *Anal. Chimica Acta* **1962**, *27*, 454.

(67) Block, B. P.; Roth, E. S.; Schaumann, C. W.; Simkin, J.; Rose, S. H. *J. Am. Chem. Soc.* **1962**, *84*, 3200.

(68) Block, B. P.; Simkin, J.; Ocone, L. R. *J. Am. Chem. Soc.* **1962**, *84*, 1749.

(69) Glick, M. D.; Dahl, L. F. *Inorg. Chem.* **1966**, *5*, 289.

(70) Wrobleski, J. T.; Brown, D. B. *Inorg. Chem.* **1979**, *18*, 2738.

(71) Diel, B. N.; Inabe, T.; Jaggi, N. K.; Lyding, J. W.; Schneider, O.; Hanack, M.; Kannewurf, C. R.; Marks, T. J.; Schwartz, L. H. *J. Am. Chem. Soc.* **1984**, *106*, 3207.

(72) Fujii, Y.; Matsutani, K.; Kikuchi, K. *J. Chem. Soc.-Chem. Commun.* **1985**, 415.

(73) Eggers, S. H.; Kopf, J.; Fischer, R. D. *Organometallics* **1986**, *5*, 383.

(74) Collman, J. P.; McDevitt, J. T.; Leidner, C. R.; Yee, G. T.; Torrance, J. B.; Little, W. A. *J. Am. Chem. Soc.* **1987**, *109*, 4606.

(75) Hoskins, B. F.; Robson, R. *J. Am. Chem. Soc.* **1989**, *111*, 5962.

(76) Abrahams, B. F.; Hoskins, B. F.; Robson, R. *J. Chem. Soc.-Chem. Commun.* **1990**, 60.

(77) Gable, R. W.; Hoskins, B. F.; Robson, R. *J. Chem. Soc.-Chem. Commun.* **1990**, 1677.

(78) Gable, R. W.; Hoskins, B. F.; Robson, R. *J. Chem. Soc.-Chem. Commun.* **1990**, 762.

(79) Hoskins, B. F.; Robson, R. *J. Am. Chem. Soc.* **1990**, *112*, 1546.

(80) Yaghi, O. M.; Li, G. M.; Groy, T. L. *J. Solid State Chem.* **1995**, *117*, 256.

(81) Yaghi, O. M.; Li, G. M.; Li, H. L. *Nature* **1995**, *378*, 703.

(82) Yaghi, O. M.; Li, H. L. *J. Am. Chem. Soc.* **1995**, *117*, 10401.

(83) Fujita, M.; Kwon, Y. J.; Miyazawa, M.; Ogura, K. *J. Chem. Soc.-Chem. Commun.* **1994**, 1977.

(84) Fujita, M.; Kwon, Y. J.; Washizu, S.; Ogura, K. *J. Am. Chem. Soc.* **1994**, *116*, 1151.

(85) Copp, S. B.; Subramanian, S.; Zaworotko, M. J. *J. Chem. Soc.-Chem. Commun.* **1993**, 1078.

(86) Subramanian, S.; Zaworotko, M. J. *J. Chem. Soc.-Chem. Commun.* **1993**, 952.

(87) Cheetham, A. K.; Ferey, G.; Loiseau, T. *Angew. Chem. Int. Edit. Engl.* **1999**, *38*, 3268.

(88) Kitagawa, S.; Matsuyama, S.; Munakata, M.; Emori, T. *J. Chem. Soc.-Dalton Trans.* **1991**, 2869.

(89) Kitagawa, S.; Matsuyama, S.; Munakata, M.; Osawa, N.; Masuda, H. *J. Chem. Soc.-Dalton Trans.* **1991**, 1717.

(90) Kitagawa, S.; Munakata, M.; Tanimura, T. *Chem. Lett.* **1991**, 623.

(91) Kim, J.; Chen, B. L.; Reineke, T. M.; Li, H. L.; Eddaoudi, M.; Moler, D. B.; O'Keeffe, M.; Yaghi, O. M. *J. Am. Chem. Soc.* **2001**, *123*, 8239.

(92) Eddaoudi, M.; Kim, J.; Rosi, N.; Vodak, D.; Wachter, J.; O'Keeffe, M.; Yaghi, O. M. *Science* **2002**, *295*, 469.

(93) Kondo, M.; Yoshitomi, T.; Seki, K.; Matsuzaka, H.; Kitagawa, S. *Angew. Chem. Int. Edit. Engl.* **1997**, *36*, 1725.

(94) Li, H.; Eddaoudi, M.; O'Keeffe, M.; Yaghi, O. M. *Nature* **1999**, *402*, 276.

(95) Lin, W. B.; Evans, O. R.; Xiong, R. G.; Wang, Z. Y. *J. Am. Chem. Soc.* **1998**, *120*, 13272.

(96) Evans, O. R.; Xiong, R. G.; Wang, Z. Y.; Wong, G. K.; Lin, W. B. *Angew. Chem. Int. Edit. Engl.* **1999**, *38*, 536.

(97) Evans, O. R.; Lin, W. B. *Chem. Mater.* **2001**, *13*, 2705.

(98) Evans, O. R.; Lin, W. B. *Chem. Mater.* **2001**, *13*, 3009.

(99) Evans, O. R.; Lin, W. *Acc. Chem. Res.* **2002**, *35*, 511.

(100) Wang, Z.; Tanabe, K. K.; Cohen, S. M. *Chem.- Euro. J.*, **2010**, *16*, 212.

(101) Rowsell, J. L.; Yaghi, O. M. *Angew. Chem. Int. Edit. Engl.* **2005**, *44*, 4670.

(102) Zhao, D.; Yuan, D. Q.; Zhou, H. C. *Energy Environ. Sci.* **2008**, *1*, 222.

(103) Ma, L.; Jin, A.; Xie, Z.; Lin, W. *Angew. Chem. Int. Edit. Engl.* **2009**, *48*, 9905.

(104) Li, J. R.; Sculley, J.; Zhou, H. C. *Chem. Rev.* **2012**, *112*, 869.

(105) Sumida, K.; Rogow, D. L.; Mason, J. A.; McDonald, T. M.; Bloch, E. D.; Herm, Z. R.; Bae, T. H.; Long, J. R. *Chem. Rev.* **2012**, *112*, 724.

(106) Cui, H.; Wang, Z.; Takahashi, K.; Okano, Y.; Kobayashi, H.; Kobayashi, A. *J. Am. Chem. Soc.* **2006**, *128*, 15074.

(107) Tang, Y.-Z.; Huang, X.-F.; Song, Y.-M.; Hong Chan, P. W.; Xiong, R.-G. *Inorg. Chem.* **2006**, *45*, 4868.

(108) Ye, Q.; Song, Y.-M.; Wang, G.-X.; Chen, K.; Fu, D.-W.; Hong Chan, P. W.; Zhu, J.-S.; Huang, S. D.; Xiong, R.-G. *J. Am. Chem. Soc.* **2006**, *128*, 6554.

(109) Zhang, W.; Xiong, R.-G. *Chem. Rev.* **2011**, *112*, 1163.

(110) Kobayashi, Y.; Jacobs, B.; Allendorf, M. D.; Long, J. R. *Chem. Mater.* **2010**, *22*, 4120.

(111) Hendon, C. H.; Tiana, D.; Walsh, A. *Phys. Chem. Chem. Phys.* **2012**, *14*, 13120.

(112) Narayan, T. C.; Miyakai, T.; Seki, S.; Dincă, M. *J. Am. Chem. Soc.* **2012**, *134*, 12932.

(113) Kurmoo, M. *Chem. Soc. Rev.* **2009**, *38*, 1353.

(114) Ma, L.; Evans, O. R.; Foxman, B. M.; Lin, W. *Inorg. Chem.* **1999**, *38*, 5837.

(115) Rieter, W. J.; Taylor, K. M. L.; An, H.; Lin, W.; Lin, W. *J. Am. Chem. Soc.* **2006**, *128*, 9024.

(116) Allendorf, M. D.; Bauer, C. A.; Bhakta, R. K.; Houk, R. J. T. *Chem. Soc. Rev.* **2009**, *38*, 1330.

(117) Cui, Y. J.; Yue, Y. F.; Qian, G. D.; Chen, B. L. *Chem. Rev.* **2012**, *112*, 1126.

(118) Allendorf, M. D.; Houk, R. J.; Andruszkiewicz, L.; Talin, A. A.; Pikarsky, J.; Choudhury, A.; Gall, K. A.; Hesketh, P. J. *J. Am. Chem. Soc.* **2008**, *130*, 14404.

(119) Chen, B.; Wang, L.; Xiao, Y.; Fronczek, F. R.; Xue, M.; Cui, Y.; Qian, G. *Angew. Chem. Int. Edit. Engl.* **2009**, *48*, 500.

(120) Lan, A.; Li, K.; Wu, H.; Olson, D. H.; Emge, T. J.; Ki, W.; Hong, M.; Li, J. *Angew. Chem. Int. Edit. Engl.* **2009**, *48*, 2334.

(121) White, K. A.; Chengelis, D. A.; Gogick, K. A.; Stehman, J.; Rosi, N. L.; Petoud, S. *J. Am. Chem. Soc.* **2009**, *131*, 18069.

(122) Kreno, L. E.; Leong, K.; Farha, O. K.; Allendorf, M.; Van Duyne, R. P.; Hupp, J. T. *Chem. Rev.* **2011**, *112*, 1105.

(123) Wanderley, M. M.; Wang, C.; Wu, C.-D.; Lin, W. *J. Am. Chem. Soc.* **2012**, *134*, 9050.

(124) Hu, A.; Ngo, H. L.; Lin, W. *Angew. Chem. Int. Edit. Engl.* **2003**, *42*, 6000.

(125) Hu, A.; Ngo, H. L.; Lin, W. *J. Am. Chem. Soc.* **2003**, *125*, 11490.

(126) Wu, C. D.; Hu, A.; Zhang, L.; Lin, W. *J. Am. Chem. Soc.* **2005**, *127*, 8940.

(127) Ma, L.; Falkowski, J. M.; Abney, C.; Lin, W. *Nat. Chem.* **2010**, *2*, 838.

(128) Song, F.; Wang, C.; Falkowski, J. M.; Ma, L.; Lin, W. *J. Am. Chem. Soc.* **2010**, *132*, 15390.

(129) Zhang, T.; Song, F.; Lin, W. *Chem. Commun.* **2012**, *48*, 8766.

(130) Rieter, W. J.; Taylor, K. M. L.; An, H. Y.; Lin, W. L.; Lin, W. B. *J. Am. Chem. Soc.* **2006**, *128*, 9024.

(131) Taylor, K. M. L.; Rieter, W. J.; Lin, W. *J. Am. Chem. Soc.* **2008**, *130*, 14358.

(132) deKrafft, K. E.; Xie, Z.; Cao, G.; Tran, S.; Ma, L.; Zhou, O. Z.; Lin, W. *Angew. Chem. Int. Edit. Engl.* **2009**, *48*, 9901.

(133) Liu, D.; Huxford, R. C.; Lin, W. *Angew. Chem. Int. Edit. Engl.* **2011**, *50*, 3696.

(134) deKrafft, K. E.; Boyle, W. S.; Burk, L. M.; Zhou, O. Z.; Lin, W. *J. Mater. Chem.* **2012**, *22*, 18139.

(135) Rieter, W. J.; Pott, K. M.; Taylor, K. M.; Lin, W. *J. Am. Chem. Soc.* **2008**, *130*, 11584.

(136) Lin, W.; Rieter, W. J.; Taylor, K. M. *Angew. Chem. Int. Edit. Engl.* **2009**, *48*, 650.

(137) Taylor-Pashow, K. M. L.; Rocca, J. D.; Xie, Z.; Tran, S.; Lin, W. *J. Am. Chem. Soc.* **2009**, *131*, 14261.

(138) Horcajada, P.; Gref, R.; Baati, T.; Allan, P. K.; Maurin, G.; Couvreur, P.; Ferey, G.; Morris, R. E.; Serre, C. *Chem. Rev.* **2012**, *112*, 1232.

(139) Huxford, R. C.; deKrafft, K. E.; Boyle, W. S.; Liu, D.; Lin, W. *Chem. Sci.* **2012**, *3*, 198.

(140) Liu, D.; Kramer, S. A.; Huxford-Phillips, R. C.; Wang, S.; Della Rocca, J.; Lin, W. *Chem. Commun.* **2012**, *48*, 2668.

(141) Kent, C. A.; Mehl, B. P.; Ma, L.; Papanikolas, J. M.; Meyer, T. J.; Lin, W. *J. Am. Chem. Soc.* **2010**, *132*, 12767.

(142) Kent, C. A.; Liu, D.; Ma, L.; Papanikolas, J. M.; Meyer, T. J.; Lin, W. *J. Am. Chem. Soc.* **2011**, *133*, 12940.

(143) Wang, C.; Lin, W. *J. Am. Chem. Soc.* **2011**, *133*, 4232.

(144) Wang, C.; Xie, Z.; deKrafft, K. E.; Lin, W. *J. Am. Chem. Soc.* **2011**, *133*, 13445.

(145) Wang, C.; deKrafft, K. E.; Lin, W. *J. Am. Chem. Soc.* **2012**, *134*, 7211.

(146) Cooper, A. I. *Angew. Chem. Int. Ed. Engl.* **2011**, *50*, 996.

(147) Ding, X.; Guo, J.; Feng, X.; Honsho, Y.; Seki, S.; Maitarad, P.; Saeki, A.; Nagase, S.; Jiang, D. *Angew. Chem. Int. Ed. Engl.* **2011**, *50*, 1289.

(148) Jiang, J. X.; Wang, C.; Laybourn, A.; Hasell, T.; Clowes, R.; Khimyak, Y. Z.; Xiao, J. L.; Higgins, S. J.; Adams, D. J.; Cooper, A. I. *Angew. Chem. Int. Ed. Engl.* **2011**, *50*, 1072.

(149) Thomas, A. *Angew. Chem. Int. Ed. Engl.* **2010**, *49*, 8328.

(150) Trewin, A.; Cooper, A. I. *Angew. Chem. Int. Ed. Engl.* **2010**, *49*, 1533.

(151) Yuan, S. W.; Kirklin, S.; Dorney, B.; Liu, D. J.; Yu, L. P. *Macromolecules* **2009**, *42*, 1554.

(152) Ma, L.; Wanderley, M. M.; Lin, W. *ACS Catalysis* **2011**, *1*, 691.

Chapter 2

Doping Metal-Organic Frameworks for Water Oxidation, Carbon Dioxide Reduction, and Organic Photocatalysis

2.1 Doping as a strategy to incorporate functionality into Metal-organic frameworks

2.1.1 Introduction to doping in MOFs and the questions to answer in this study

As mentioned in the introduction, metal-organic frameworks (MOFs) have recently emerged as a new class of functional porous materials that are tunable at molecular level. The art of systematic structural engineering and property tuning can be best represented by isoreticular MOFs,[1-5] which are constructed by linking metal-coordinated secondary building units (SBUs) with bridging ligands of varied length or functional groups, yielding the same framework topology but tunable pore sizes and properties. However, it is not always possible for the building ligand to be assembled into the predesigned framework structure, especially when substantial steric requirement has been imposed from the functional entities. Postsynthetic modifications (PSM)[6-8] of the interior MOF channels have recently been utilized to successfully introduce functional groups that cannot be directly incorporated, but this method tends to reduce the open channel sizes during the PSM processes, thus negatively affecting the material properties in many cases. Here we propose an attractive alternative, to dope a fraction of the ligand with functional groups into a known crystalline system built from ligands of similar shape and length but simpler structures, thus constructing materials possessing both the functionality and the desired crystal structures.[9] This mix-and-match approach mimicking the widely applied metal ion doping in traditional inorganic materials such as metal

oxides, can not only allow the incorporation of sterically demanding functional ligands into the parent framework but also retains the porosity of the framework for various applications.

In the conventional doped metal oxides (or solid solution), the two most significant parameters dictating the degree of doping have been well established to be 1) the degree of size match between doped metal ions and the parent lattice, 2) the requirement of charge balance of the doped lattice. In our proposed mix-and-match strategy in MOF synthesis, it is interesting to test if size and charge of the doped ligands are also controlling factors to determine the doping level in a certain structure.

In our first trial, we prepared three sterically demanding Ir/Ru-phosphor based linear dicarboxylate ligands $H_2\mathbf{L_1}$ to $H_2\mathbf{L_3}$ with similar structures and 0 to +2 charges (dicarboxylate-$[Ir(ppy)_3]$, di-carboxylate-$[Ir(bpy)(ppy)_2]^+$ and dicarboxylate-$[Ru(bpy)_3]^{2+}$, see Scheme 2.1), and successfully doped them into the known IRMOF-9/10 structures to systematically address the aforementioned questions in doping MOFs.

Scheme 2.1

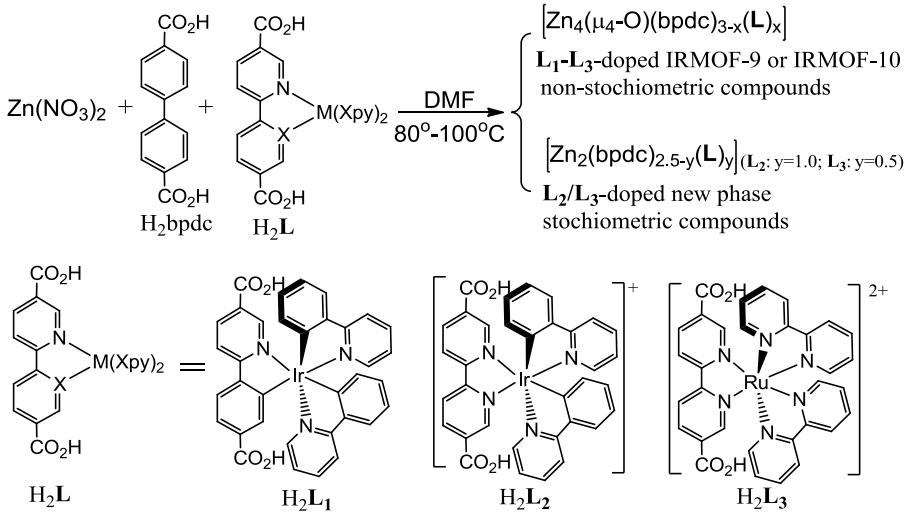

The Ir-based cyclometalated complexes $H_2\mathbf{L_1}$ and $H_2\mathbf{L_2}$ were synthesized by reacting $[Ir(ppy)_2Cl_2]_2$ (ppy = 2-phenylpyridinato, N, $C_{2'}$) with 5,5'-$(MeO_2C)_2$-ppy [methyl 6-(4-(methoxycarbonyl)phenyl)nicotinate] or 5,5'-$(EtO_2C)_2$-bpy [diethyl(2,2'-bipyridine)-5,5'-dicarboxylate], followed by base-promoted hydrolysis.[10] The Ru-complex $H_2\mathbf{L_3}$ was synthesized following the published procedure by directly reacting cis-$[Ru(bpy)_2Cl_2]$ with 5,5'-$(HO_2C)_2$-bpy (2,2'-bipyridine 5,5'-dicarboxylated acid).[11] They are all highly efficient phosphorescent molecules, with long lifetimes of the ^{3}MLCT states. Extensive research efforts have been focused on developing light-emitting devices based on related molecules. The ^{3}MLCT phosphorescence can also be quenched through energy transfer to molecules with triplet ground state such as oxygen, or redox reactions between the ^{3}MLCT state and the quenchers. These phosphorescent Ir and Ru based molecules are thus also suitable for applications in chemical sensing and photosensitization.

The frameworks that are used to host these Ir/Ru phosphor ligands have the IRMOF-9/10 structures. IRMOF-9/10 are a pair of catenation isomers constructed from the BPDC ligand (4,4'-bisphenyl-dicarboxylic acid) and $[Zn_4(\mu_4\text{-}O)(O_2CR)_6]$ SBUs, forming 3D structures of the **pcu** topology (Figure 2.1). Dicarboxylate ligand BPDC possesses the matching length to the phosphor based ligands $H_2\mathbf{L_1}$ to $H_2\mathbf{L_3}$. IRMOF-10 was non-interpenetrated while IRMOF-9 adopted a 2-fold interpenetrated structure of the former framework.

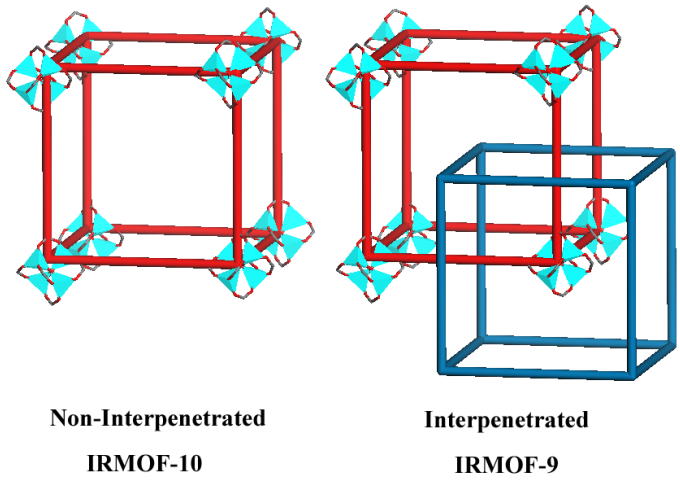

Figure 2.1 structures of interpenetrated IRMOF-9 vs. non-interpenetrated IRMOF-10

2.1.2 General Synthesis and characterization of L/BPDC mixed Zn-MOF series.

Mixtures of H_2**L** and H_2bpdc (4,4'-biphenyldicarboxylic acid) with varying molar ratios were reacted with $Zn(NO_3)_2 \cdot 6H_2O$ in DMF (N,N'-dimethylformamide) under solvothermal conditions. The molar ratio of $Zn(NO_3)_2$: (H_2**L** + H_2bpdc): DMF was 0.5~3: 1 : 2000. The resulting mixtures were placed in an oven at 100 ^oC for 1~2 days. Yellow-red crystals with thin plate or feather-like shapes (depending on the resulting phases) were obtained after filtration. Phases of the obtained MOFs were determined by Powder X-Ray Diffraction (PXRD). Phases of the interpenetrated IRMOF-9 and the non-interpenetrated IRMOF-10 can be differentiated by examining the crystals under polarized lights. IRMOF-9, crystallizing in orthorhombic crystal system, exhibited anisotropic birefringent behavior under polarized lights, while IRMOF-10, crystallizing in cubic crystal system, was optically isotropic. Thermogravimetric analysis (TGA) measuring the solvent weight loss was used to support the above identification of interpenetrated vs non-interpenetrated phases. The Ir/Ru-complex (**L**$_1$ to **L**$_3$) contents in all the MOFs were determined by dissolving a known amount of MOFs in 3 mL basic

water/ethanol mixture and taking quantitative UV-Vis measurements of the solution at 375.5 nm. The **L** contents per mass could be determined from the standardized curve, and the molar doping levels [mol **L**/(mol bpdc+ mol **L**)] were then calculated, based on the framework formulae of different phases. Whenever mixed phases were encountered, estimations based on average formula were adopted. Framework formulae of the stochiometric phases **1** to **3** were deduced from the X-ray crystal structure and the determined doping level, while the solvent contents were established from a combination of ^{1}H NMR and TGA.

2.1.3. Doping neutral H_2L_1 ligand to IRMOF: steric-controlled interpenetration

H_2**L$_1$** was first tested in the doping study. As a neutral ligand satisfying the charge requirement of the parent $Zn_4O(BPDC)_3$ framework, it can be mixed into the IRMOF-9/10 structure for the whole range of H_2**L$_1$**/H_2BPDC ratios from 0 to 1. As a result of the steric bulk of H_2**L$_1$** ligand, with increasing doping levels of H_2**L$_1$**, the crystals change from interpenetrated IRMOF-9 structure to non-interpenetrated IRMOF-10 structure, showing the size effect of ligand doping. Reaction between the pure cyclometalated Ir phosphor H_2**L$_1$** (the neutral ligand) and $Zn(NO_3)_2\cdot 6H_2O$ in DMF afforded red single crystals of $[Zn_4(\mu_4\text{-}O)(\mathbf{L_1})_3]\cdot 64DMF\cdot 35H_2O$ (**1**). **1** crystallizes in the cubic *Fm-3m* space group, revealed by single crystal X-ray crystallography. In the asymmetric unit, 1/8 of **L$_1$** ligand, 1/24 of $Zn_4(\mu_4\text{-}O)$ clusters which are composed of one Zn atom of 1/6 occupancy and one O atom of 1/24 occupancy, are present. As we expected, the carboxylate groups from six adjacent **L$_1$** ligands coordinate to the four Zn centers to form [$Zn_4(\mu_4$-O)(carboxylate)$_6$] SBUs which link **L$_1$** ligands to form a non-interpenetrated 3D network of the **pcu** topology (IRMOF-10 structure, Figure 2.2). **L$_1$** ligands were disordered over

two positions as a result of the rotation of the C-C bond between the carboxylate groups and the aromatic rings, a common phenomenon observed when 2-connected dicarboxylate acids were employed as linkers. Calculated by PLATON, 79% of void space in the crystal structure was filled by the DMF or water molecules. The precise solvent content cannot be determined by X-ray crystallography, owing to their disordered nature. The solvent contents were instead established by a combination of ^{1}H NMR studies and thermogravimetric analysis (Table 2.1).

Table 2.1 Key crystallographic data for **1**-**3**

Compound	**1**	**2**	**3**
Framework formula	$C_{105}H_{66}N_9O_{13}Ir_3Zn_4$	$C_{55}H_{34}N_4O_{10}IrZn_2$	$C_{44}H_{27}N_3O_{10}Ru_{0.5}Zn_2$
Formula weight	2499.82	1233.84	939.01
Temperature (K)	296	296	296
Wavelength (Å)	1.54178	1.54178	1.54178
Crystal system	Cubic	Orthorhombic	Orthorhombic
Space group	*Fm-3m*	$C222_1$	$C222_1$
Unit cell dimensions	a = 34.0239(15)	a = 18.3559(14)	a = 18.4918(14)
	b = 34.0239(15)	b = 26.314(2)	b = 26.861(2)
	c = 34.0239(15)	c = 42.406(3)	c = 41.776(3)
	α = 90	α = 90	α = 90
	β = 90	β = 90	β = 90
	γ = 90	γ = 90	γ = 90
Volume ($Å^3$)	39387(3)	20483(3)	20751(3)
Z	8	8	8
Density (calcd. g/cm^3)	0.843	0.800	0.601
Absorption coeff. (mm^{-1})	4.512	3.280	1.356
F(000)	6088	4632	3608
Crystal size (mm)	0.10 × 0.10 × 0.10	0.10×0.10×0.10	0.10×0.10×0.10

Crystal color & shape	red cube	red rectangle	red rectangle
θ range data collection	2.25– 38.05	2.08– 38.12	2.90 – 36.31
Limiting indices	-12 < *h* < 24	-8 < *h* < 13	- 13 < h < 13
	-3< *k* < 27	-20 < *k* < 19	- 20 <k < 20
	-9< *l* < 24	-27 < *l* < 33	- 20 < k < 30
Reflections collected	3865	8584	7706
Independent reflections	593 [R_{int}= 0.0763]	4785 [R_{int}= 0.0716]	4641 [R_{int}= 0.0491]
Refinement method	Full-matrix least-square on F^2		
Data/restraints/parameters	593/15/0	8584 / 313 / 290	7706 / 313 / 292
Goodness-of-fit on F^2	1.056	0.976	1.229
Final R indices [I>2σ(I)][a,b]	R1 = 0.1362	R1 = 0.1186	R1 = 0.1388
	wR2 = 0.4570	wR2 = 0.3023	wR2 = 0.3436
R indices (all data)	R1 = 0.1691	R1 = 0.1682	R1 = 0.1781
	wR2 = 0.4954	wR2 = 0.3364	wR2 = 0.3725

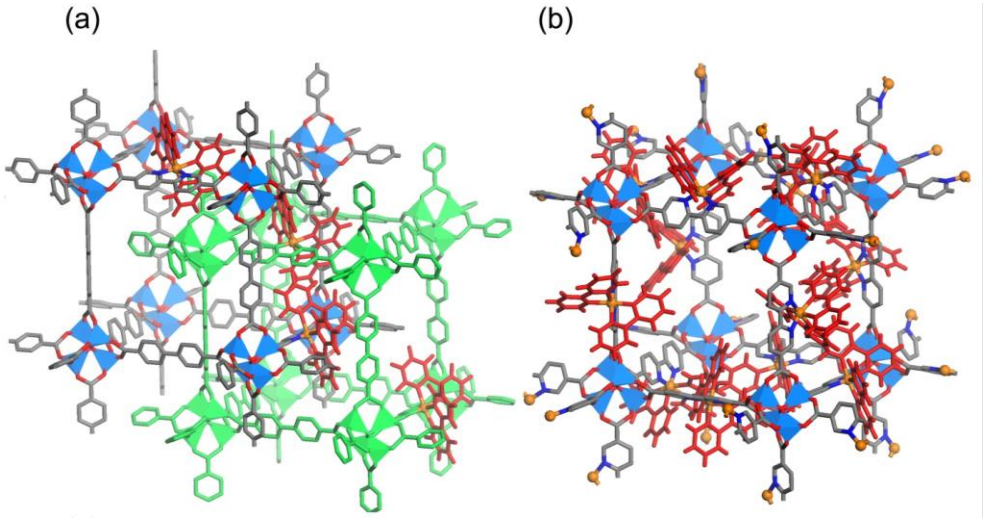

Figure 2.2 (a) stick / polyhedral model for **L_1**-doped interpenetrated IRMOF-9 structure; (b) stick / polyhedral model for **L_1**-doped non-interpenetrated IRMOF-10 structure.

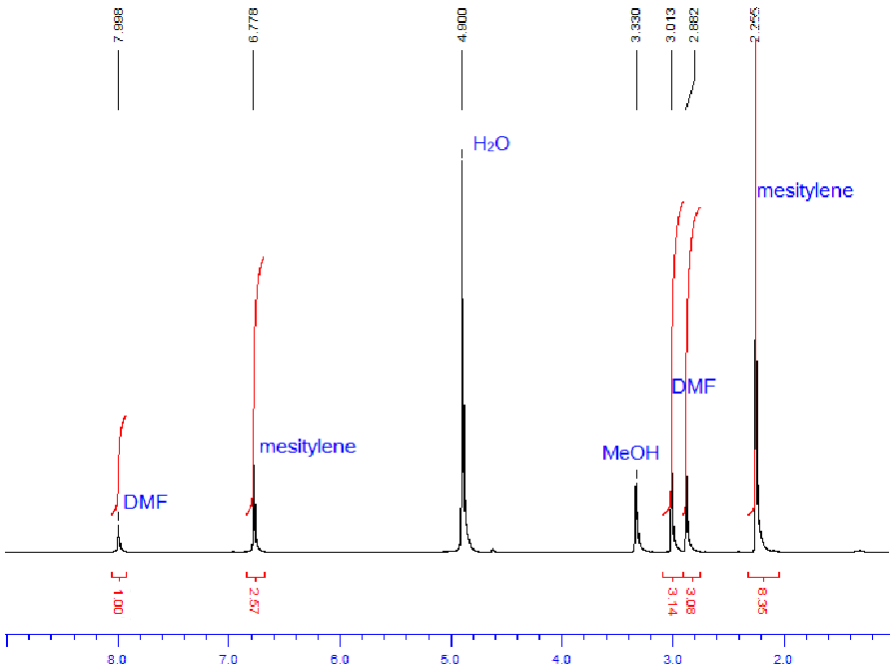

Figure 2.3 ^{1}H NMR spectroscopic determination of solvent content in $Zn_4O(\mathbf{L_1})_3$•$(DMF)_{65}$•$(H_2O)_{35}$ **(1).** 9.12 mg of **1** was used and mesitylene was added as an internal standard.

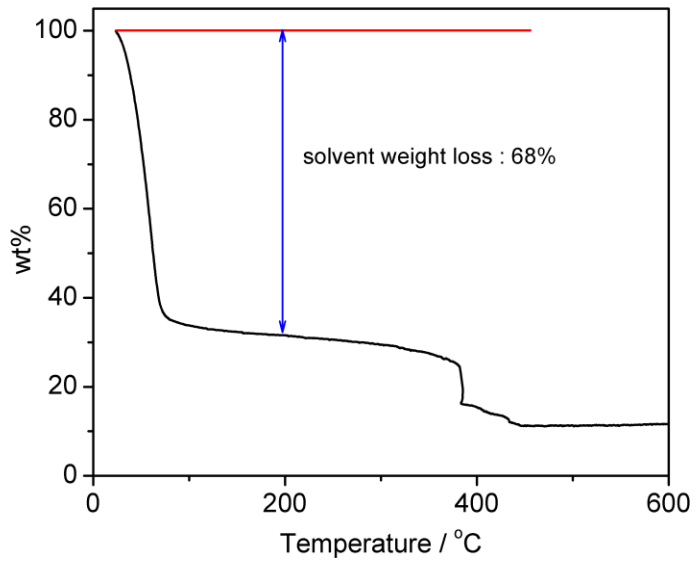

Figure 2.4 Thermogravimetric analysis (TGA) curve for $Zn_4O(\mathbf{L_1})_3 \bullet (DMF)_{64} \bullet (H_2O)_{35}$ (**1**). The sample was heated to 600 ºC at a heating rate of 5 ºC/min.

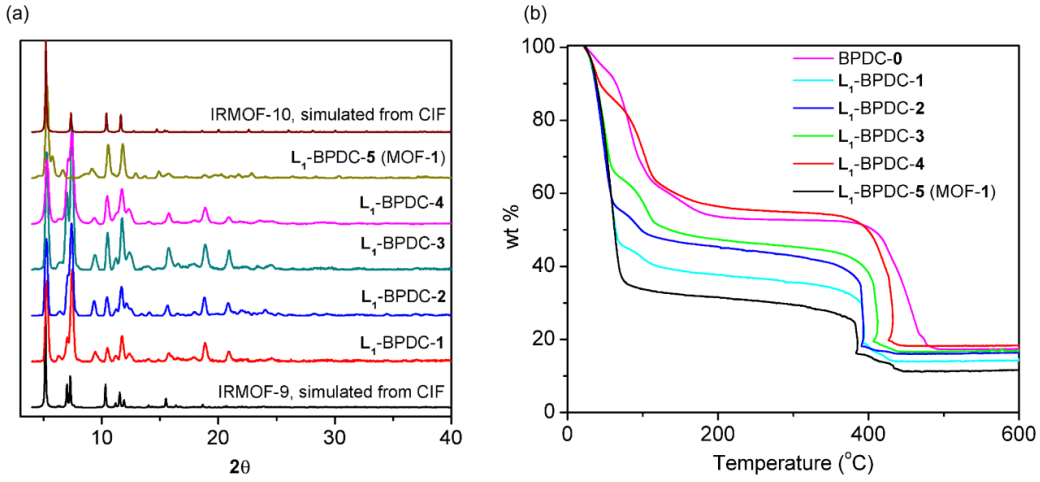

Figure 2.5 (a) Powder X-ray diffraction patterns for $\mathbf{L_1}$-doped IRMOF-9/10 samples; (b) Thermogravimetric analysis of $\mathbf{L_1}$-doped IRMOF-9/10 samples. The preparation conditions / $\mathbf{L_1}$ contents / identified phases of all the samples in (a) and (b) were listed in Table 2.2.

The crystal structure showed that reaction between $H_2\mathbf{L_1}$ and $Zn(NO_3)_2 \cdot 6H_2O$ in DMF afforded non-interpenetrated IRMOF-10 structure, while the originally reported reaction between H_2BPDC and $Zn(NO_3)_2 \cdot 6H_2O$ in DMF yielded interpenetrated IRMOF-9. Considering the similar length of these two ditopic carboxylate ligands, the reason of forming non-interpenetrated structure for the $\mathbf{L_1}$ ligand should be attributed to the steric bulk of the Ir-phosphor core. Furthermore, if systematic doping of the neutral $H_2\mathbf{L_1}$ ligand into the BPDC-Zn system is carried out, a phase transition from interpenetrated IRMOF-9 to non-interpenetrated IRMOF-10 with increasing doping level is expected. With these considerations, $H_2\mathbf{L_1}$ was mixed with H_2BPDC in varying molar ratios and then reacted with $Zn(NO_3)_2 \bullet 6H_2O$ in DMF under solvothermal conditions. Crystalline

samples were obtained from all the vials. Based on PXRD patterns (Figure 2.5a), $\mathbf{L_1}$ can form solid solution with BPDC, adopting IRMOF-9/10 structure in the whole range of $\mathbf{L_1}$/BPDC molar ratios from 0 to 1 (Table 2.2). The PXRD patterns of IRMOF-9 and IRMOF-10 are very similar. However, these two phases can be differentiated by examining the crystals under polarized lights. IRMOF-9, crystallizing in orthorhombic crystal system (space group $C222_1$), exhibited anisotropic birefringent behavior under polarized lights, while IRMOF-10, crystallizing in cubic crystal system (space group *Fm-3m*), was optically isotropic (Figure 2.2(c)). As expected, the crystals change from interpenetrated IRMOF-9 structure to non-interpenetrated IRMOF-10 structure when the doping level of the $\mathbf{L_1}$ ligand increases. Thermogravimetric analysis (TGA) measuring the solvent weight loss supported the above identification of interpenetrated vs non-interpenetrated phases as shown in Figure 2.5b. When going from IRMOF-9 to IRMOF-10 structure (with a mixture of both IRMOF-9 and IRMOF-10 phases in the intermediate range), the solvent weight loss in the TGA of the samples increases continuously, from 44 wt% in the pure IRMOF-9 phase with 4.5% $\mathbf{L_1}$ doped, to 68 wt% in the pure IRMOF-10 built from pure $\mathbf{L_1}$ ligand. Contents of Ir phosphor based ligands in these crystals were quantified by UV-Vis spectroscopy as listed in Table 2.2. This steric effect-governed phase transition from interpenetrated to more porous non-interpenetrated structure highlights the importance of ligand size in systematic ligand doping.

Table 2.2 **L** ligand doping levels determined from quantitative UV-Vis spectroscopy

L *ligand and sample number*	*Added molar ratio of* $Zn(NO_3)_2$ */* H_2***L***/ H_2*bpdc in the synthesis*	*Phases determined from PXRD\optical observation\TGA*	*Doping level* ***L****/(****L****+BPDC)*
BPDC-0	2 / 0 / 1	IRMOF-9	0
$\mathbf{L_1}$ BPDC-**1**	26 / 1 / 12	IRMOF-9	4.5%
$\mathbf{L_1}$ BPDC-**2**	8 / 1 / 3	IRMOF-9 + IRMOF-10 [a]	17%

L_1 BPDC-**3**	4 / 1 / 1	IRMOF-9 + IRMOF-10	39%
L_1 BPDC-**4**	8 / 3 / 1	IRMOF-9 + IRMOF-10	61%
L_1 BPDC-**5**	6 / 1 / 0	IRMOF-10 (**1**)	100%
L_2-BPDC-**1**	26 / 1 / 13	IRMOF-9	6%
L_2-BPDC-**2**	20 / 1 / 9	IRMOF-9	8%
L_2-BPDC-**3**	14 / 1 / 6	IRMOF-9 + **2** [b]	14%
L_2-BPDC-**4**	8 / 1 / 3	IRMOF-9 + **2**	26%
L_2-BPDC-**5**	4 / 1 / 1	IRMOF-9 + **2**	32%
L_2-BPDC-**6**	8 / 3 / 1	**2**	40%
L_2-BPDC-**7**	12 / 5 / 1	**2**	40%
L_2-BPDC-**8**	20 / 9 / 1	**2**	42%
L_2-BPDC-**9**	4 / 1 / 0	unknown phase	100%
L_3-BPDC-**1**	6.5 / 4.4 / 1	IRMOF-9	n.a.
L_3-BPDC-**2**	6.6 / 3 / 1	IRMOF-9	3.8%
L_3-BPDC-**3**	5.9 / 1 / 1	IRMOF-9	6%
L_3-BPDC-**4**	17.7 / 1 / 12	IRMOF-9 + **3** [c]	16.5%
L_3-BPDC-**5**	17.7 / 1 / 18	IRMOF-9 + **3**	17%
L_3-BPDC-**6**	17.7 / 1 / 22	**3**	21%
L_3-BPDC-**7**	17.7 / 1 / 33	**3**	22%

[a]This is a mixture of IRMOF-9 and IRMOF-10 phase, based on optical observation and TGA [b/c]These are mixture of IRMOF-9 and **2/3** phases, based on PXRD, optical observation and TGA

2.1.4. Doping charged H_2L_2 and H_2L_3 ligand to IRMOF: charged-controlled doping and formation of stoichiometric neutral phase

Unlike the neutral H_2**L_1** ligand, pure phosphor-based charged ligands H_2**L_2** and H_2**L_3** do not readily assemble into the predesigned $Zn_4O(L)_3$ open framework. Reactions of many kinds of zinc salts with Ir/Ru complex H_2**L_2** and H_2**L_3** in various mixed solvents at 80-100 °C can only afford amorphous solids or powdery crystalline samples of unknown structure based on PXRD analysis. In spite of these observations, we hypothesized that it might still be possible to dope a small fraction of **L_2** and **L_3** into IRMOF-9 or IRMOF-10 frameworks (built from pure BPDC ligands), taking the advantage of matching ligand lengths between BPDC and **L_2**/**L_3**. This mix-and-match strategy can incorporate these sterically demanding phosphor cores into the IRMOF structure and retain the intrinsic porosity at the same time.

$H_2\mathbf{L_2}$/$H_2\mathbf{L_3}$ were mixed with H_2BPDC and then reacted with $Zn(NO_3)_2$•$6H_2O$ in DMF. Yellow-red crystals with thin plate or feather-like shapes were obtained after placing the reaction mixtures in an oven at 90~100 ^oC for 1~2 days. PXRD analysis showed that doped IRMOF framework had been obtained when reactants were added in certain $Zn(NO_3)_2$/H_2**L**/H_2BPDC molar ratios. Only the interpenetrated IRMOF-9 phase was obtained in both $H_2\mathbf{L_2}$ and $H_2\mathbf{L_3}$ / BPDC doped systems. The preliminary phase identification under polarized light was fully supported by TGA measurement of the samples, showing solvent weight loss ranging from 43% to 47%. Contents of Ir/Ru phosphor-based ligands in the crystals were quantified by UV-Vis spectroscopy, expressed in **L**/(**L**+BPDC) percentages. As listed in Table 2, at least 8% of $\mathbf{L_2}$ and 6% of $\mathbf{L_3}$ can be doped into the IRMOF-9 frameworks.

When increasing the phosphor ligand $H_2\mathbf{L_2}$ to H_2BPDC ratio, or changing the amount of $Zn(NO_3)_2$•$6H_2O$ added, a new phase could be obtained. PXRD patterns of the new phases in both systems ($H_2\mathbf{L_2}$ and $H_2\mathbf{L_3}$) are very similar (Figure 2.7). As shown in Table 2.2, pure phases of the new structures could be obtained under different reactant ratios, formulated as **2** ($Zn_4O(\mathbf{L_2})_3$•$(DMF)_2$•$(H_2O)_7$) for $H_2\mathbf{L_2}$ and **3** ($Zn_4O(\mathbf{L_3})_3$•$(DMF)_9$•$(H_2O)_8$) for $H_2\mathbf{L_3}$, respectively. Single crystal XRD revealed that in both systems the new phases crystallize in *C222₁* space group. Tri-blade paddle wheel [$Zn_2(CO_2)_3$] SBUs were linked by ditopic BPDC or $\mathbf{L_2}$/$\mathbf{L_3}$ ligands to form 3D frameworks (Figure 2.6f). In the asymmetric unit, 5/2 of the dicarboxylate ligands (either BPDC or $\mathbf{L_2}$/$\mathbf{L_3}$) and one Zn_2 tri-blade paddle wheel cluster are present. In the equatorial positions of the tri-blade paddle wheel, three bidentate carboxylate groups of ½ occupancies bridge the two Zn atoms in the SBU, and are linked by the ligand struts into

a 2D graphene net. In the axial positions of the Zn paddle wheel, a dicarboxylate ligand with two monodentate carboxylate groups coordinated to the two Zn atoms, further linking the 2D nets to 3D frameworks of 5-connected **bnn** topology (Figure 2.6b). As a result of the elongated BPDC or $\mathbf{L_2}$/$\mathbf{L_3}$, 2-fold interpenetrated structures were adopted by the two MOFs (Figure 2.6b). There are three crystallographically distinct dicarboxylate ligand positions, among which two of them were in the equatorial positions with respect to the Zn_2 paddle wheel and one of them was in the axial position. Except for one of the equatorial dicarboxylate ligand positions, which is exclusively occupied by BPDCs, the other two positions are mixedly occupied by BPDC or $\mathbf{L_2}$/$\mathbf{L_3}$. The $\mathbf{L_2}$/$\mathbf{L_3}$ ligands in the equatorial positions can further disorder over two orientations resulting from a 180^o rotation along the C-C bond between the carboxylates and aromatic rings. Due to weak diffractions and limited data set qualities, the degree of occupancies of the phosphor based ligands in these mixedly occupied equatorial and axial positions cannot be reliably deduced from the single crystal X-ray diffraction experiment. The Ir/Ru-complex contents in both of the MOFs were obtained by quantitative UV-Vis spectroscopy as shown in Table 2.2. The single crystal structure was then refined against the X-ray data by fixing the $\mathbf{L_2}$/$\mathbf{L_3}$ to BPDC ratio in the mixed ligands positions, based on the result from spectroscopic analysis. In **2**, the determined framework formula was $Zn_2(\mathbf{L_2})(BPDC)_{1.5}$, equaling to ½ $\mathbf{L_2}$ vs ½ BPDC ligands in the mixed ligand positions; in **3**, the determined framework formula turned out to be $Zn_2(\mathbf{L_3})_{0.5}(BPDC)_2$, equaling to 1/3 $\mathbf{L_3}$ vs 2/3 BPDC ligands in the mixed ligand positions. Solvent contents in the channels were determined by a combination of TGA and ^{1}H NMR.

Table 2.3 Rhodamine 6G dye uptake in the doped MOFs

Sample Number[*]	*Structure & phase*	*Doping level L/(L+BPDC)*	*Void space percentage calculated by Platon*	*Dye uptake as wt% of the framework*	*Effective dye concentration inside the MOF channels (mM)*
L_1-BPDC-5	IRMOF-10 (**1**)	100%	79%	11.3%	252
L_1-BPDC-1	IRMOF-9	4.5%	67%	9.8%	213
L_2-BPDC-6	**2**	40%	45%	1.7%	63
L_2-BPDC-1	IRMOF-9	6%	65%	11.1%	254
L_3-BPDC-6	**3**	20%	60%	6.1%	126
L_3-BPDC-3	IRMOF-9	6%	65%	10.3%	231

[*]The preparation condition / **L** content / identified phases of all the samples in (a) and (b) were listed in Table 2.

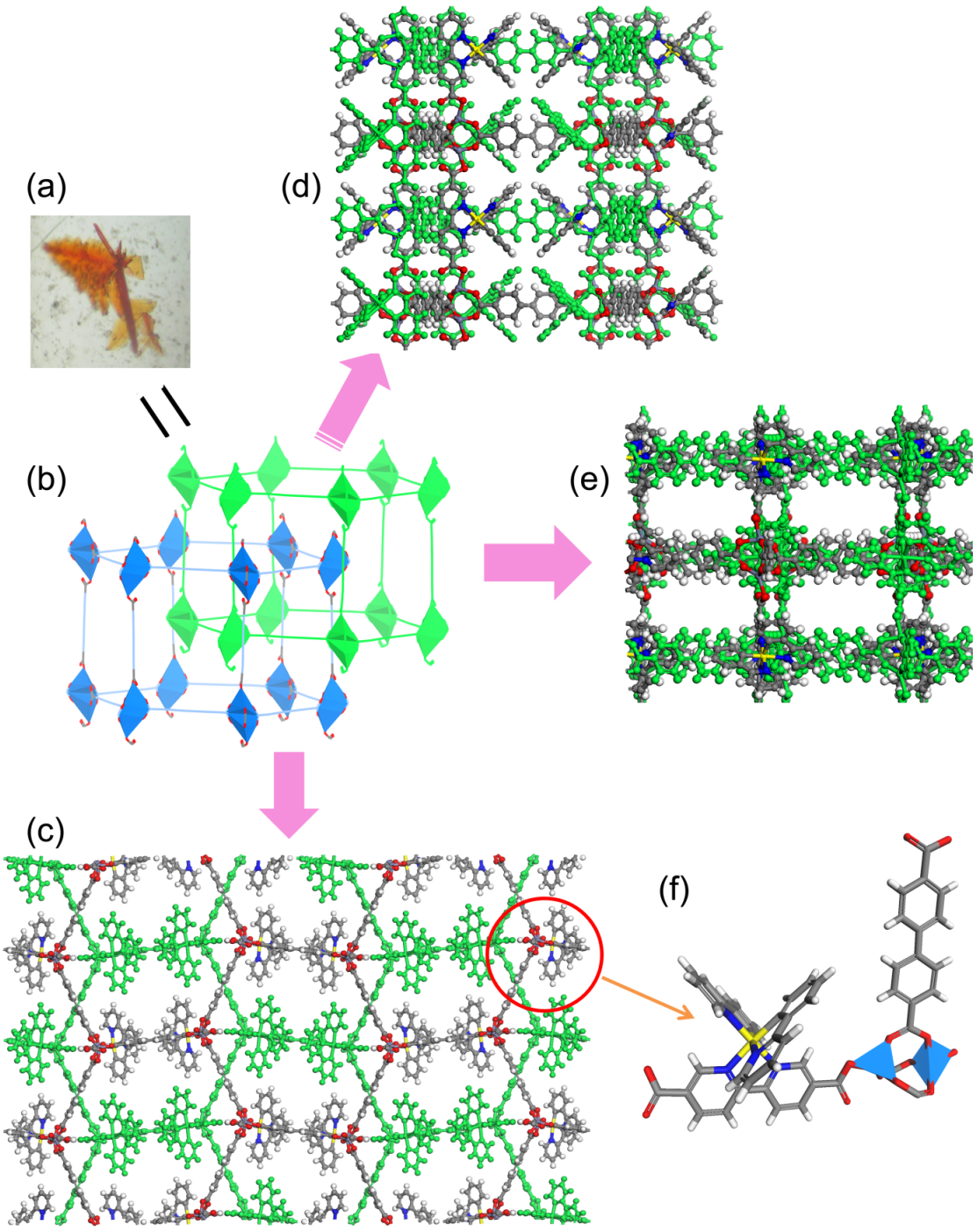

Figure 2.6 (a) photo of crystals of **2** (b) simplified connectivity model showing the interpentrated nets in **bnn** topology of **2**. (c) ball-stick model showing crystal structure of **2** viewed along [001] direction. (d) ball-stick model showing crystal structure of **2** viewed

along [010] direction. (e) ball-stick model showing crystal structure of **2** viewed along [100] direction. (f) Ball-and-stick and polyhedra presentation of asymmetric unit of of **2**.

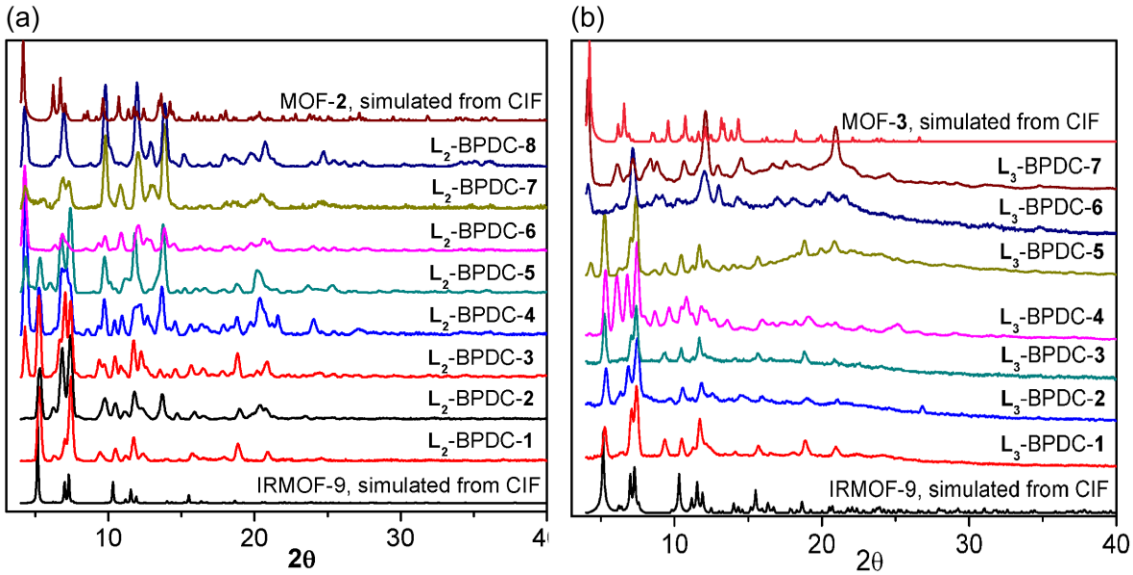

Figure 2.7 Powder X-ray diffractions of (a) $H_2\mathbf{L_2}$ doped BPDC-Zn system (b) $H_2\mathbf{L_3}$ doped BPDC-Zn system. The preparation condition / **L** content / identified phases of all the samples in (a) and (b) were listed in Table 2.2.

It is interesting to note that within the determined formulae for **2** and **3**, both structures obtain neutral frameworks. In **2** ($Zn_2(\mathbf{L_2})(BPDC)_{1.5}$), deprotonated $\mathbf{L_2}$ possesses -1 charge, while deprotonated BPDC ligand holds -2 charge, balancing the positive charges of the Zn^{2+} cations [$(+2)\times2+(-1)\times1+(-2)\times1.5=0$]. The same math holds for **3** ($Zn_2(\mathbf{L_3})_{0.5}(BPDC)_2$), in which case the deprotonated $\mathbf{L_3}$ was actually a neutral ligand [$(+2)\times2+0\times0/5+(-2)\times2=0$]. We thus proposed that the formation of a neutral framework acts as a driving force towards crystallization of the new phase with **bnn** topology.

By doping the Ir/Ru phosphor based ligands $H_2\mathbf{L_1}$ to $H_2\mathbf{L_3}$ into the BPDC-Zn system, we have successfully obtained three series of doped MOFs with different charges of the doping ligand. The ligands $H_2\mathbf{L_2}$ and $H_2\mathbf{L_3}$, with +1 and +2 charges, can only be doped

into the IRMOF-9 structure to a certain doping level, after which the formation of a new phase with neutral framework in **bnn** topology wins over the doped IRMOF-9 structure with positively charged framework. The neutral ligand H_2**L**$_1$, on the other hand, can form solid solution with H_2BPDC in IRMOF-9/10 structure in the whole range of H_2**L**$_1$/ H_2BPDC ratio. The **L**$_1$ doped IRMOF-9/10 possesses neutral framework, and we also need to notice that, for **L**$_1$ ligand in any **L**$_1$/BPDC ratio, it is not possible to form neutral framework in the phase with **bnn** topology. The charge balance in the framework thus comes to be an important argument dictating the degree of doping and phases of the doped structure.

From the crystal structures, all the MOFs contain internal porosities. A dye uptake assay recently developed in our lab was employed to quantify the intrinsic porosity of the MOFs. By soaking the MOFs in a solution of 42 mM Rhodamine 6G dye in ethanol for 16 hours, significant fractions of the Rhodamine 6G can be absorbed into the internal channels of the MOFs, taking advantage of the hydrophobic nature of the MOF channels. The dye solution was then decanted and the MOFs were quickly washed with water three times to remove dye molecules adsorbed on the external surfaces of the crystals. The dye-loaded MOFs were then digested with disodium ethylenediaminetetraacetic acid (Na_2EDTA) and NaOH. The amounts of released Rhodamine 6G were quantified by ultraviolet-visible spectroscopy after acidifying the solution to pH 1.1. As shown in Table 2.3, the MOFs exhibit dye uptake capacities (ranging from 1.7 wt% to 11.3 wt% of the framework) dependent upon the open channels, corresponding to the effective dye concentration of 63 to 254 mM in the channels of the MOFs which is equivalent to1.5 to

6.0 times of the original dye concentration in the EtOH solution. These results unambiguously prove the accessibility of the open channels of the MOFs.

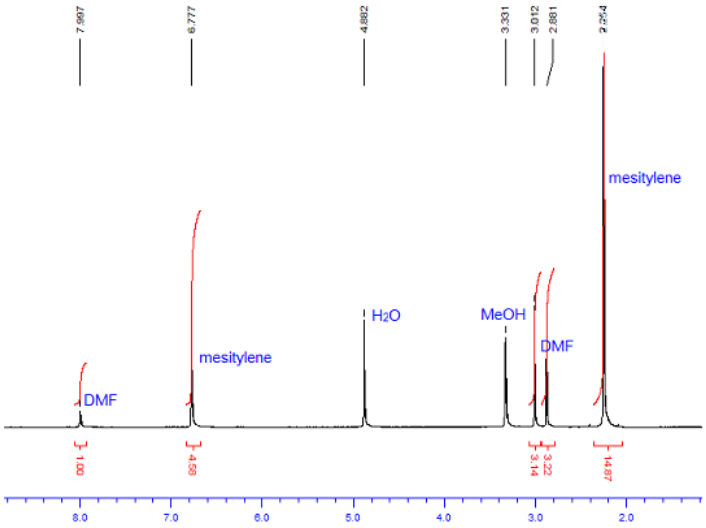

Figure 2.8 ^{1}HNMR spectroscopic determination of solvent content in $Zn_4O(\mathbf{L_2})_3\bullet(DMF)_2\bullet(H_2O)_7$ **(2).** 10.9 mg of **2** was used and mesitylene was added as an internal standard.

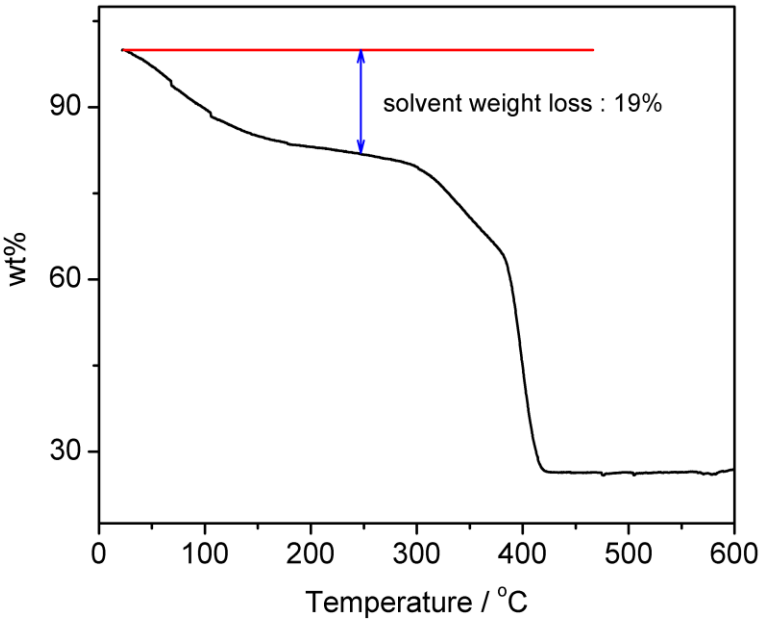

Figure 2.9 Thermogravimetric analysis (TGA) curve for $Zn_4O(\mathbf{L_2})_3$•$(DMF)_2$•$(H_2O)_7$ (**2**). The sample was heated to 600 ºC at a heating rate of 5 ºC/ min.

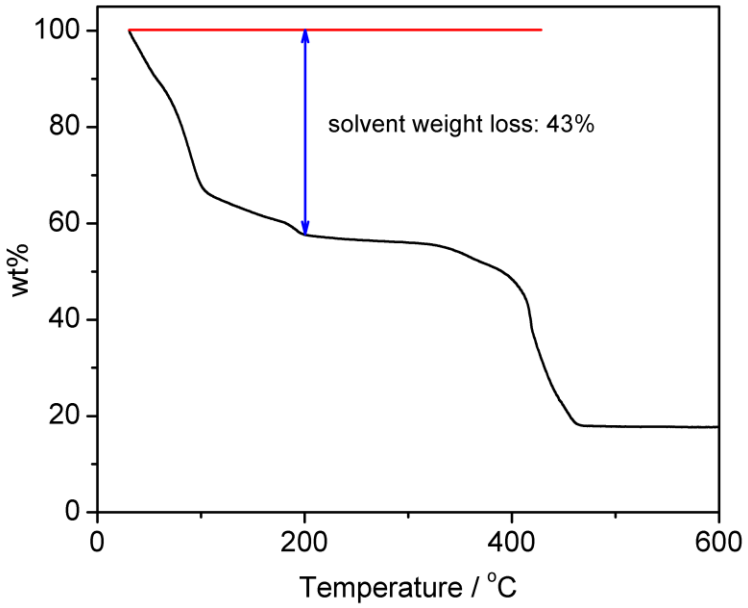

Figure 2.10 Thermogravimetric analysis (TGA) curve for sample $\mathbf{L_2}$-BPDC-**1** in IRMOF-9 structure with 6% $\mathbf{L_2}$ doping. The sample was heated to 600 ºC at a heating rate of 5 ºC/ min.

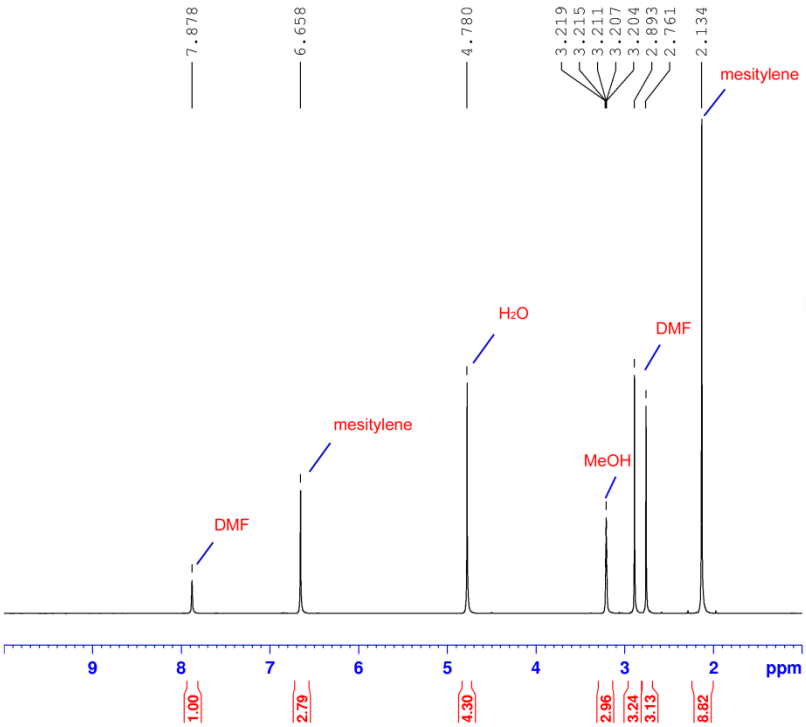

Figure 2.11 ^{1}H-NMR spectroscopic determination of solvent content in $Zn_4O(\mathbf{L_3})_3\bullet(DMF)_9\bullet(H_2O)_8$ **(3).**

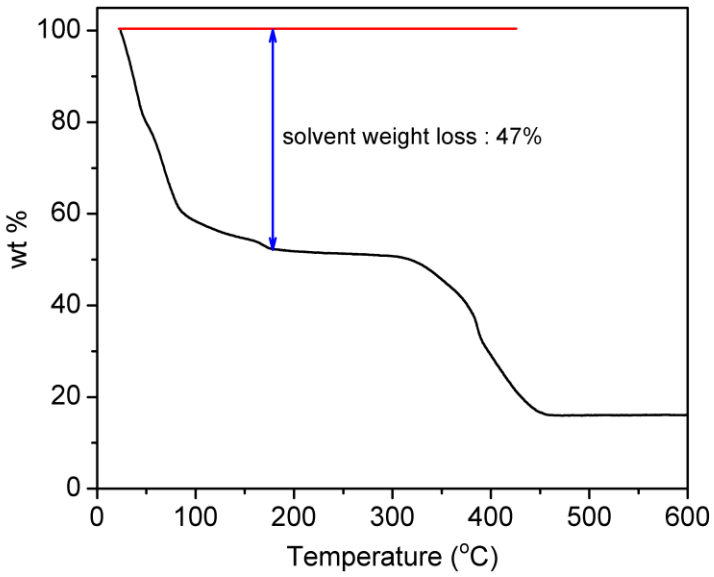

Figure 2.12 Thermogravimetric analysis (TGA) curve for $Zn_4O(\mathbf{L_3})_3\bullet(DMF)_9\bullet(H_2O)_8$ (**3**). The sample was heated to 600 ºC at a heating rate of 5 ºC/min.

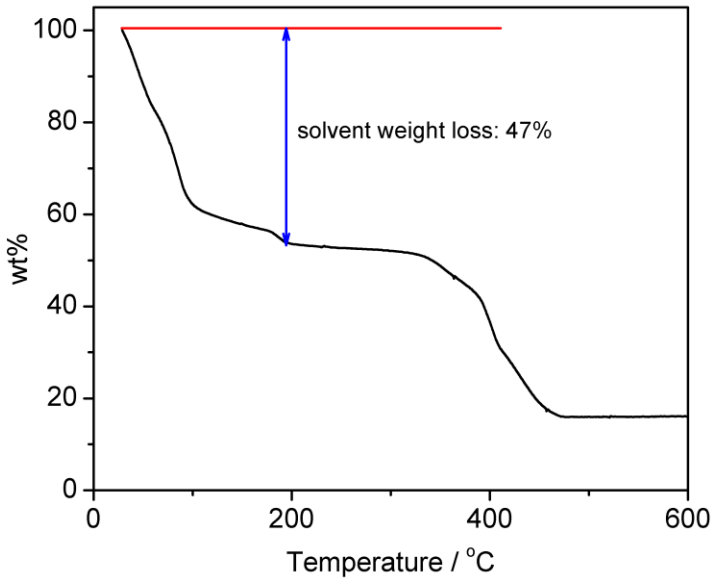

Figure 2.13 Thermogravimetric analysis (TGA) curve for sample $\mathbf{L_3}$-BPDC-**3** in IRMOF-9 structure with 6% $\mathbf{L_3}$ doping. The sample was heated to 600 ºC at a heating rate of 5 ºC/ min.

2.2 Doping Metal-Organic Frameworks for Water Oxidation, Carbon Dioxide Reduction, and Organic Photocatalysis[12]

2.2.1 Introduction to Water Oxidation, Carbon Dioxide Reduction and Organic Photocatalysis and UiO MOFs

Catalytic water oxidation constitutes a key half reaction in artificial photosynthesis.[13,14] A large number of homogeneous water oxidation catalysts (WOCs) have recently been developed based on dimeric Ru complexes,[15,16] monomeric Ru and Fe complexes,[17-19] monomeric Ir complexes,[20-22] and polyoxometalates with a Ru_4O_4 or a Co_4O_4 core.[23,24] These molecular WOCs are highly tunable with high catalyst activity and stability. On the other hand, heterogeneous WOCs based on iridium oxide[25-27] and cobalt

oxide/phosphate[28,29] particles can be readily interfaced with electrodes or photosensitizers to achieve electrocatalytic or photocatalytic water oxidation. We believe it is beneficial to incorporate the molecular WOCs into framework structures. Unfortunately, most MOF structures tend to lack stability under water oxidation reaction conditions.[30] The UiO family of MOFs based on $Zr_6O_4(OH)_4(CO_2)_{12}$ secondary building units (SBUs) and dicarboxylate bridging ligands represent an interesting exception and are very stable in water.[1,31] We successfully incorporated three iridium-based WOCs, $[Ir^{III}(Cp^*)(dcppy)]$ ($H_2\mathbf{L_4}$, where Cp* = pentamethylcyclopentadienyl, dcppy = 2-phenylpyridine-5,4'-dicarboxylic acid) $[Ir^{III}(Cp^*)(dcbpy)]^+$ (dcbpy = 2,2'-bipyridine-5,5'-dicarboxylic acid) ($H_2\mathbf{L_5}$), and $[Ir^{III}(dcppy)_2(H_2O)]^+$ ($H_2\mathbf{L_6}$), into the $Zr_6O_4(OH)_4(bpdc)_6$ (UiO-67, bpdc = *para*-biphenyldicarboxylate) framework (**4**-**6**), and demonstrated catalytic water oxidation by these highly stable MOFs.

In photosynthesis, the reducing equivalents resulting from water oxidation reactions in Photosystem II are used to drive CO_2 reduction in Photosystem I.[32] Photochemically reducing CO_2 into a source of fuel offers an attractive way to both harvest energy from sunlight and alleviate the rise of atmospheric CO_2 concentrations.[33] A number of molecular photocatalysts, including cobalt/nickel tetraaza-macrocyclic compounds,[34-38] iron/cobalt metalloporphyrins,[39-43] and $Re^I(CO)_3(bpy)X$ complexes,[44-48] have been examined for CO_2 reduction in recent years. We successfully incorporated $Re^I(CO)_3(dcbpy)Cl$ ($H_2\mathbf{L_7}$) into the UiO-67 framework to afford a heterogeneous photocatalyst for CO_2 reduction using visible light.

Organic transformations driven by visible light are gaining increasing interest from synthetic chemists, because of generally mild reaction conditions, atom efficiency, and

the potential to mediate thermodynamically uphill reactions.[49] Photocatalysts are often required in visible light-driven organic reactions since the majority of organic substrates in these reactions do not readily absorb photons in the visible region. $[Ru(bpy)_3]^{2+}$ and $[Ir(ppy)_2(bpy)]^+$ have been reported recently as photoredox catalysts in a variety of new photocatalytic organic reactions, such as [2+2] cycloaddition,[50] tin-free dehalogenation,[51] aza-Henry reactions,[52] aerobic amine-coupling,[53,54] sulfide and alcohol oxidation,[55,56] olefin epoxidation,[57] functional group transformation,[58] asymmetric organophotoredox catalysis,[59] and radical chemistry.[60] Because these photocatalysts contain precious metals, it is highly desirable to develop recyclable and reusable heterogeneous photocatalytic systems based on molecular phosphors. We incorporated $[Ir^{III}(ppy)_2(dcbpy)]Cl$ ($H_2\mathbf{L_2}$) and $[Ru^{II}(bpy)_2(dcbpy)]Cl_2$ ($H_2\mathbf{L_3}$) into the UiO-67 framework and demonstrated the applications of these doped MOFs as highly active heterogeneous catalysts for photochemical aza-Henry reactions between tertiary amines and nitroalkanes, aerobic amine coupling, and sulfide photo-oxidations.

2.2.2 Synthesis of metal complex derivatized MOFs by doping the UiO-67 framework

The Ir complexes [IrCp*Cl(dcppy)] ($H_2\mathbf{L_4}$) and [IrCp*Cl(dcbpy)]Cl ($H_2\mathbf{L}_5$) were synthesized by allowing $[IrCp^*Cl_2]_2$ to react with 4,4'-$(EtO_2C)_2$-ppy or 4,4'-$(EtO_2C)_2$-bpy, followed by base-catalyzed hydrolysis. The complex $[Ir(dcppy)_2(H_2O)_2](OTf)$ ($H_2\mathbf{L}_6$) was synthesized by treating $[Ir(dcppy)_2]_2Cl_2$ with AgOTf. The Re complex $[Re(CO)_3(dcbpy)Cl]$ ($H_2\mathbf{L_7}$) was synthesized by a reaction between (2,2'-bipyridine)-5,5'-dicarboxylic acid and pentacarbonylchloro rhenium(I). Complexes $H_2\mathbf{L_4}$-$H_2\mathbf{L_7}$ were

characterized by NMR spectroscopy, and the new compounds $H_2\mathbf{L_4}$, $H_2\mathbf{L_5}$, and $H_2\mathbf{L_6}$ were also characterized by mass spectrometry.[12]

Reactions of $ZrCl_4$ and metal complexes $H_2\mathbf{L_2}$-$H_2\mathbf{L_7}$ in N,N'-dimethylformamide (DMF) failed to produce crystalline UiO frameworks, presumably due to the steric demand of the $\mathbf{L_2}$-$\mathbf{L_7}$ ligands. Structure modeling studies indicated that the steric bulk of the $\mathbf{L_2}$-$\mathbf{L_7}$ ligands precluded the formation of UiO frameworks based on $Zr_6O_4(OH)_4(CO_2)_{12}$ SBUs and pure $\mathbf{L_2}$-$\mathbf{L_7}$ ligands. We hypothesized that the $\mathbf{L_2}$-$\mathbf{L_7}$ ligands could instead be doped into the framework of UiO-67 ($Zr_6(\mu_3\text{-}O)_4(\mu_3\text{-}OH)_4(bpdc)_6$) by taking advantage of matching ligand lengths between bpdc and $\mathbf{L_2}$-$\mathbf{L_7}$. Such a substitution strategy can not only allow for the incorporation of a sterically demanding bridging ligand into a parent framework but also allows for retention of the porosity of the parent framework to facilitate substrate diffusion for efficient catalysis.

Scheme 2.2

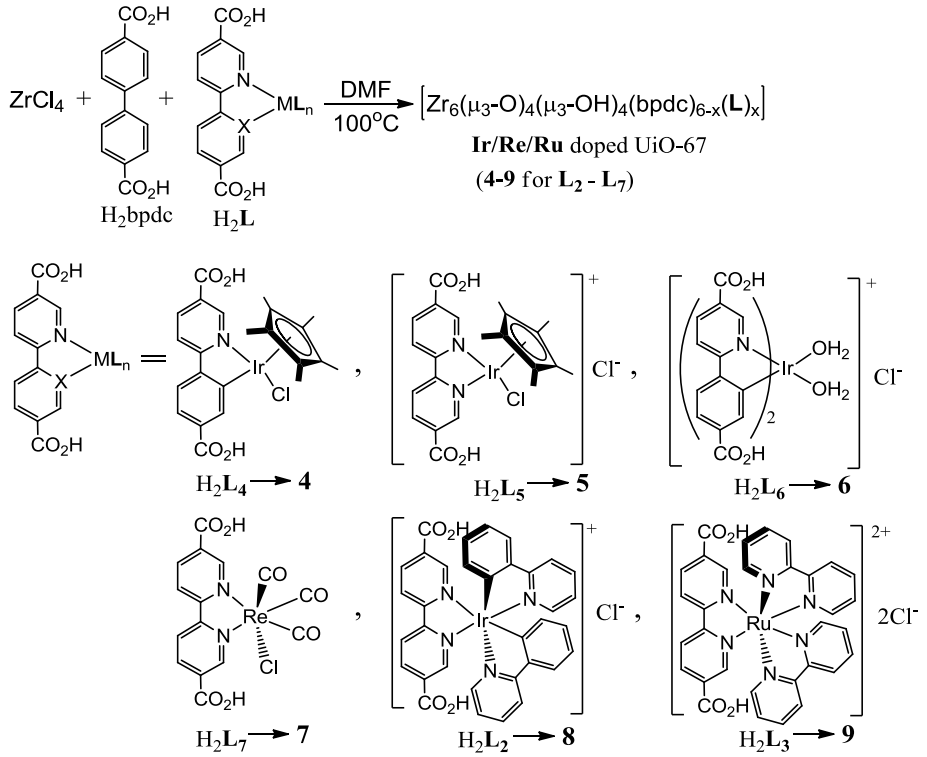

(Reprinted with permission from ref [12], copyright American Chemical Society 2011)

Metal complex doped UiO-67 (**4**-**9**) with the $Zr_6(\mu_3\text{-}O)_4(\mu_3\text{-}OH)_4(bpdc)_{6-x}(\mathbf{L})_x$ formula were synthesized by treating $ZrCl_4$ with a combination of H_2bpdc and ligands $H_2\mathbf{L_2}$-$H_2\mathbf{L_7}$ in DMF at 100˚C (Scheme 2.2). Crystallinity of the MOFs could be enhanced by adding acetic acid to the reaction mixture, which presumably stabilized soluble Zr^{4+} species by acetate coordination and slowed down the formation of amorphous zirconium oxides/hydroxides. Synthetic conditions were optimized to obtain highly crystalline powdery samples of **4**-**9**, which are isostructural with the parent framework UiO-67, based on the similarity of their powder X-ray diffraction (PXRD) patterns (Figures 2.14a and 2.14c). SEM images of the samples showed intergrown nanocrystals of ~200 nm in dimensions (Figure 2.14b). Metal complex contents in MOFs **4**-**9** were established by

inductively coupled plasma mass spectrometry (ICP-MS) analysis. **4-9** were found to contain 2-8 wt% of the $\mathbf{L_2}$-$\mathbf{L_7}$ ligands (Table 2.4). The formulae $Zr_6(\mu_3\text{-}O)_4(\mu_3\text{-}OH)_4(bpdc)_{6-x}(\mathbf{L})_x$ of MOFs **4-9** were supported by thermogravimetric analysis (TGA), showing 61-63% weight loss for the organic linkers. Permanent porosities of MOFs **4-9** were demonstrated by N_2 adsorption at 77 K (Figure 2.14d). Type I isotherms were obtained for all of the six MOFs with BET surface areas ranging from 1092 to 1497 m^2/g, indicating microporous structures (Table 2.4). Pore size distribution (calculated by the HK method) centering at 6.7 Å perfectly agrees with that of the structure model.

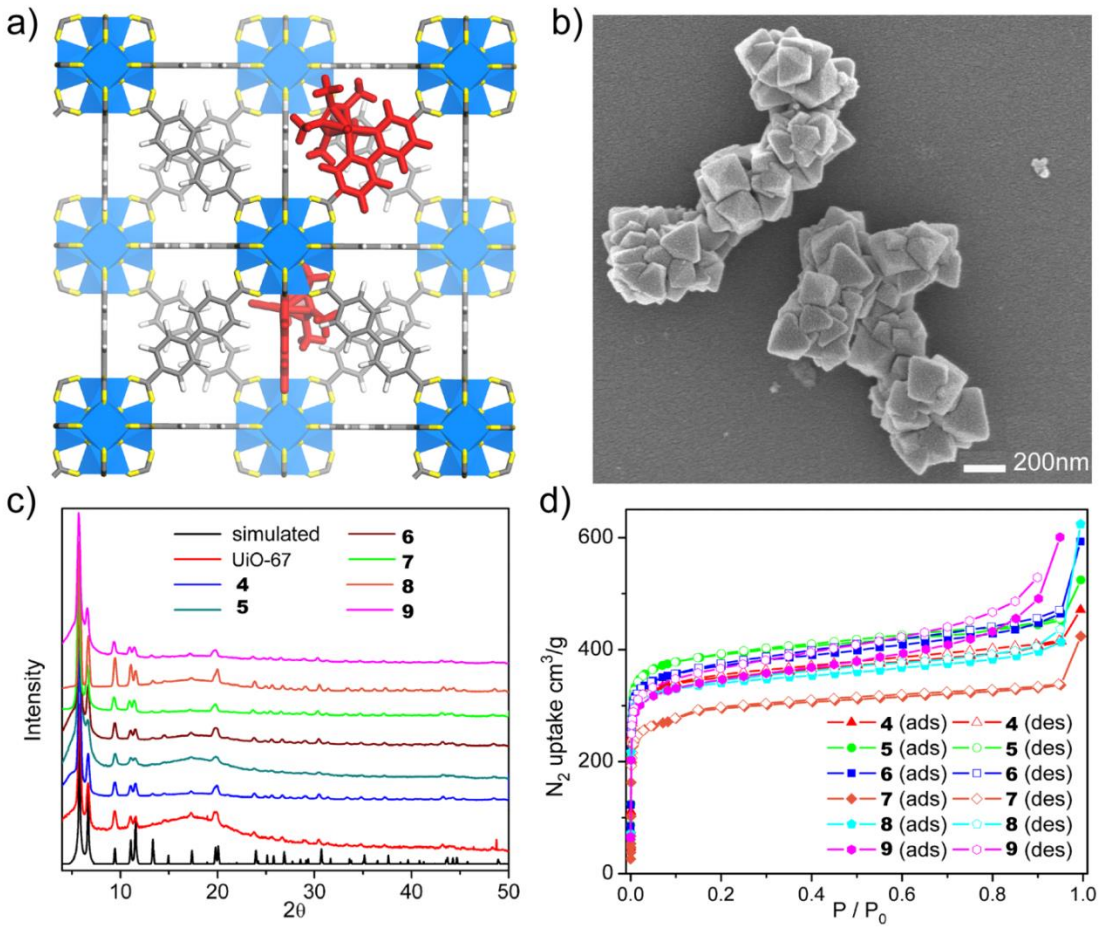

Figure 2.14 a) Structure model of **4** showing doping of $\mathbf{L_4}$ ligand into the UiO-67 framework. b) SEM micrograph of intergrown nanocrystals of **4**. c) PXRD patterns for

UiO-67 and **4-9**. d) Nitrogen adsorption isotherms of **4-9** at 77 K. (Reprinted with permission from ref [12]. Copyright American Chemical Society 2011)

Table 2.4 Ligand doping level and BET surface area of MOFs **4-9**

MOF-**x**	$\mathbf{L_x}$ ligand wt%[a]	BET surface area (m^2/g)[b]
4	7.7	1254
5	8.1	1497
6	6.0	1410
7	4.2	1092
8	2.0	1194
9	3.0	1277

[a]Determined by ICP-MS. [b]BET surface area calculations were based on the adsorption isotherms using P/P_0 from 0.005 to 0.1.

2.2.3 Water oxidation catalysis using 4-6

Water oxidation catalytic activities of **4-6** were examined with Ce^{4+} (cerium ammonium nitrate, CAN) as an oxidant (Figure 2.15a). As shown in Table 2.5, MOFs **4-6** are highly effective water oxidation catalysts with turnover frequencies (TOFs) as high as 4.8 h^{-1}. The catalytic activity must come from the doped $\mathbf{L_4}$-$\mathbf{L_6}$ since the parent UiO-67 did not catalyze water oxidation. The heterogeneous nature of **4-6** was verified by the re-usability of **4-6** for water oxidation (Figure 2.15b) and the lack of catalytic activity for the supernatants of the water oxidation mixtures (Figure 2.15c), which contained no Ir as determined by ICP-MS. Furthermore, the solids recovered from the reactions exhibited the same PXRD patterns as those of the pristine **4-6** (Figure 2.15d), supporting the stability of the UiO-67 framework under the present water oxidation conditions.

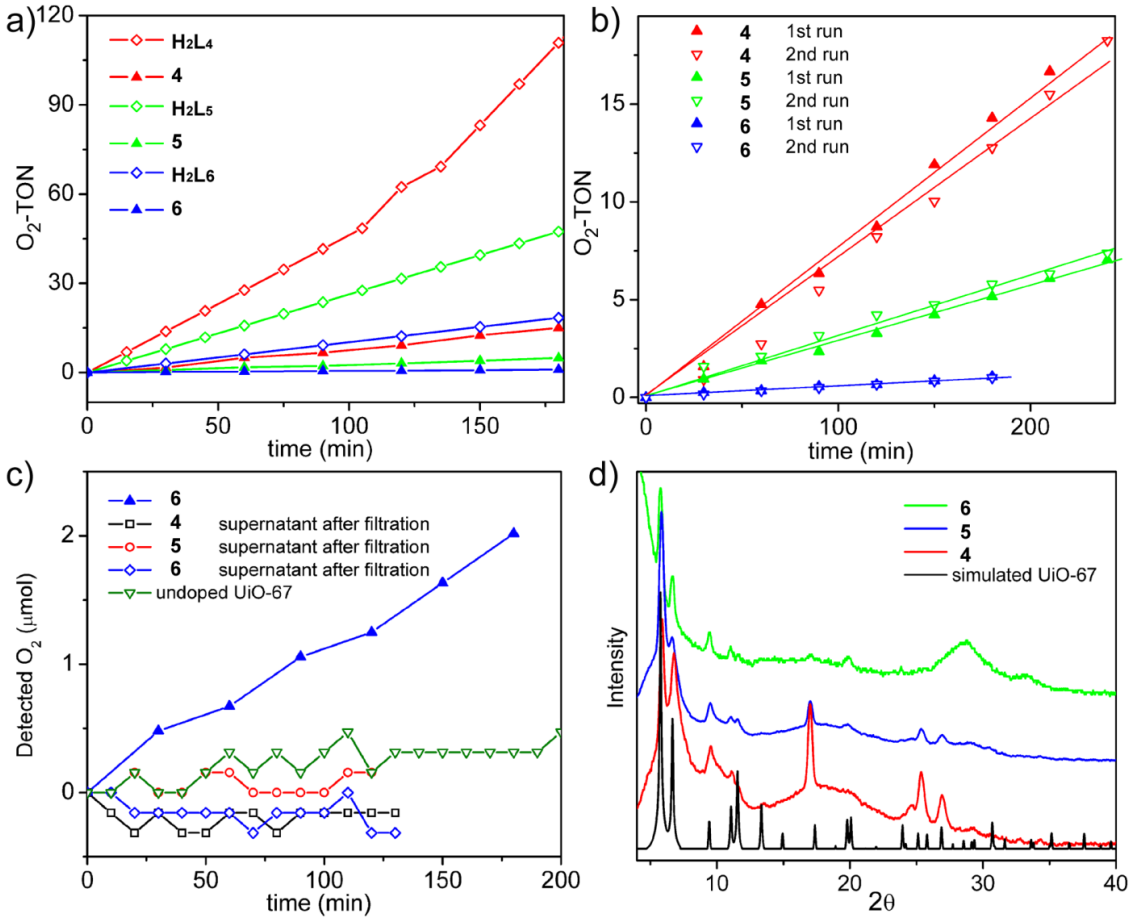

Figure 2.15 a) Plots of O_2 evolving turnover number (O_2-TON) vs. time for **4-6** and the homogeneous H_2**L**$_4$-H_2**L**$_6$. b) Plots of O_2-TON vs. time for reuse experiments of **4-6**. c) The amount of detected O_2 vs. time with undoped UiO-67, and supernatant solutions of **4-6** reaction mixtures; The amount of O_2 generated by **6** was also plotted for comparison. d) PXRD patterns of **4-6** after catalytic reaction and that simulated from the UiO-67 structure. (Reprinted with permission from ref [12]. Copyright American Chemical Society 2011)

Table 2.5 TOFs for **4-6** catalyzed water oxidation[a]

Catalyst	*TOF (h^{-1})*	*Catalyst*	*TOF (h^{-1})*
4[b]	4.8	H_2**L**$_4$[c]	37.0
5[b]	1.9	H_2**L**$_5$[c]	15.7
6[b]	0.4	H_2**L**$_6$[c]	6.2

[a]TOF is defined as the number of evolved oxygen molecules per catalytic site per hour over the first 3 hours. CAN concentration 62.3-67.1 mM, pH = 1. [b]Heterogeneous catalysis was carried out with 3.2-7.4

mg **4**-**6** (equiv. to 0.5 – 1.0 μmol of Ir WOCs). TOFs were calculated based on the Ir-complex doping levels determined by ICP-MS. [c]Homogeneous catalysis with H_2**L**$_4$-H_2**L**$_6$ was carried out with 1.5-7.5×10^{-5} M catalyst.

Comparisons of water oxidation TOFs for **4**-**6** to those of corresponding homogeneous catalysts H_2**L**$_4$-H_2**L**$_6$ provide important insights into the reaction processes. MOFs gave lower TOFs than their homogeneous counterparts (only 6.4-12.9% of the homogeneous catalyst activities, Table 2.5). This level of activity can be accounted for by the Ir catalysts on the MOF particle surface. CAN is apparently too large (~11.3 Å in diameter for the cerium nitrate anions from the crystal structure of CAN) to enter the MOF channels (~6.7 Å in diameter).

A surface poisoning experiment was performed to further prove the assumption of surface catalysis. We first found that reacting the homogeneous [Ir(Cp*)(ppy)Cl] catalyst with triphenylphosphine can effectively suppress its WOC activity. [Ir(Cp*)(ppy)Cl] and 20. eq. of triphenylphosphine were dissolved in ethylacetate and allowed to react at room temperature for 6h. [Ir(Cp*)(ppy)(PPh_3)]Cl was then isolated, which exhibited WOC TOF only 1/30 of that of the parent [Ir(Cp*)(ppy)Cl] complex. We reasoned that it was because of the high coordination strength of triphenylphosphine which may block the open site that is vital in the catalytic cycle. We then proceeded to do the poisoning experiment on **4** with triphenylphosphine. Considering the much larger dynamic size of triphenylphosphine than the pore size of the MOF, the triphenylphosphine molecules can only have access to the Ir sites near the surface of the MOF particles. In other words, the poisoning should be restricted to the MOF surface. The experiment, however, showed complete loss of WOC activity of the **4** after treating it with 20 eq. of triphenylphosphine

in ethylacetate at room temperature. This can only happen if the Ce^{4+}-driven WOC reactions also exclusively took place near the surface of those particles.

Total WOC turn-over numbers of **4**-**6** were estimated from UV-Vis determinations of the residue Ce^{4+} ion concentration after WOC reactions of 12 days (the oxygen sensor can only work for a few hours detecting O_2 in the gas phase, not suitable for the time-scale of those experiments). Control experiment using undoped UiO67 MOF in the 12-day reactions showed no significant change of the concentration of Ce^{4+} ion, confirming the validity of this method. The estimated total TONs obtained in this way are 1513, 1312, 2152 for **4**-**6** respectively. We do not believe that the water oxidation activity of **4**-**6** comes from IrO_2 nanoparticles that could result from the decomposition of $H_2\mathbf{L_4}$-$H_2\mathbf{L_6}$. Control experiments using pre-synthesized IrO_2 nanoparticles under the same conditions used with the MOFs indicated that the IrO_2 nanoparticles were a highly active WOC with a TOF of ~150 h^{-1}. However, the IrO_2 nanoparticles were unstable under the reaction conditions with their catalytic activity lasting for less than 30 mins. The addition of more Ce^{4+} to the reaction mixture did not produce more O_2. The facts that the MOF catalysts could be reused and **4**-**6** each exhibited different water oxidation activity also argue against the possibility that *in situ* generated IrO_2 nanoparticles are responsible for water oxidation. The fact that **4** can be poisoned by triphenylphosphine also supported the molecular origin of the WOC activity from the MOF. X-ray photoelectron spectroscopic analyses of the fresh and recovered MOFs were inconclusive as the Ir 4f binding energies of the $\mathbf{L_4}$-$\mathbf{L_6}$ ligands were too close to those of IrO_2.

2.2.4 Photocatalytic CO_2 reduction using 7

The Re-based $\mathbf{L_7}$ ligand can serve as an active catalyst for photochemical CO_2 reduction. Photocatalytic CO_2 reduction activity of **7** was examined in CO_2-saturated acetonitrile (MeCN), using triethylamine (TEA) as a sacrificial reducing agent. Immediately after irradiating the reaction mixture, the **7** color changed from orange to green, suggestive of catalytic turnovers. As shown in Table 2.6, the MOF catalyst selectively reduced CO_2 to CO under light, as determined by gas chromatography (GC). Under the reaction conditions (MeCN/TEA =20/1, regular MeCN and TEA, saturated with CO_2 gas), the molar ratio of the CO and H_2 production was around 10 during the first six hours. When the photocatalytic CO_2 reduction was carried out with CD_3CN as the solvent, no formic acid or methanol product was detected by ^1H NMR spectroscopy. The CO-TONs reached 5.0 after the first six hours (Table 2.6, entry 1). No CO generation was observed in the absence of CO_2 under the same reaction conditions (Table 2.6, entry 12), ruling out the possibility that the detected CO could have resulted from the decomposition of $\mathbf{L_7}$ ligand. The photocatalytic nature of the reaction was proved by the fact that no CO was generated in the dark (Table 2.6, entry 13). The inactivity of the parent UiO-67 framework in this reaction confirmed that the $[Re^{I}(dcbpy)(CO)_3Cl]$ moiety was responsible for the catalytic CO_2 reduction (Table 2.6, entry 14).

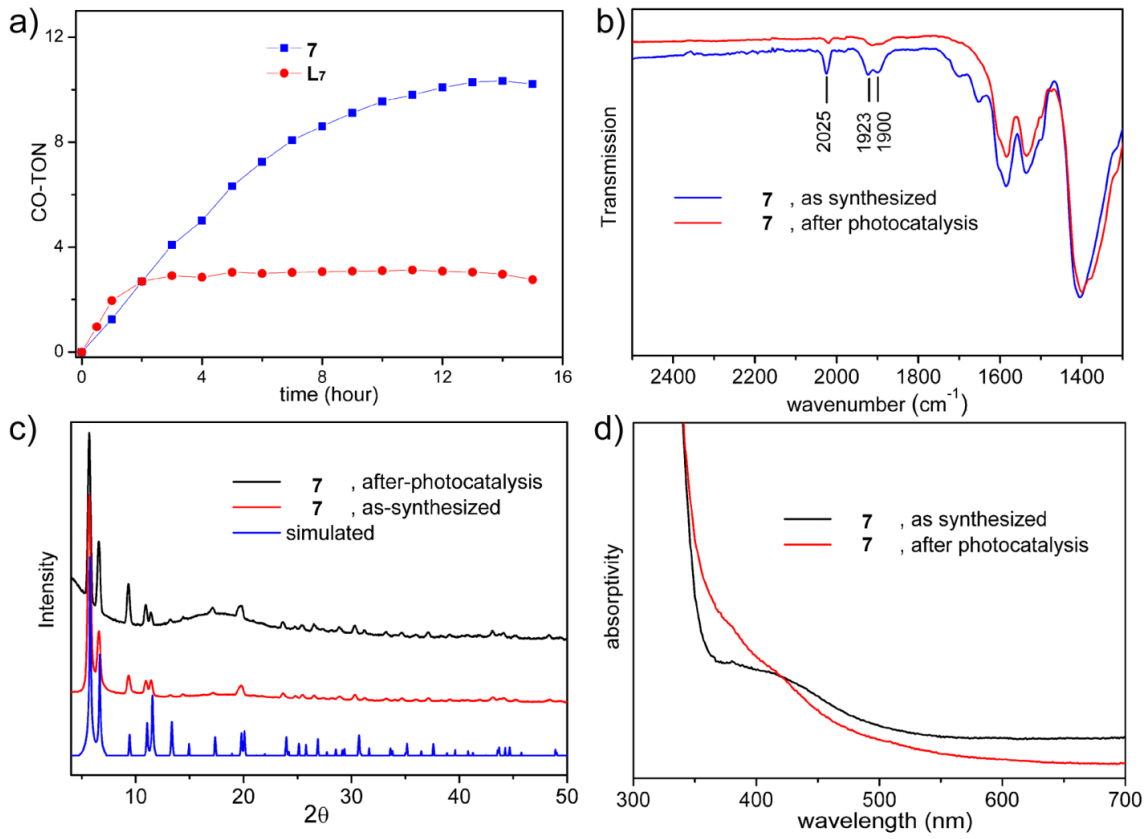

Figure 2.16. (a) Plots of CO evolution turnover number (CO-TON) versus time in the photocatalytic CO_2 reduction with **7** (blue square) and homogeneous $\mathbf{L_7}$ (red circle). (b) FT-IR of as-synthesized **7** (blue) and **7** after photocatalysis (red). (c) PXRD patterns of **7** after catalysis (black), as-synthesized (red) and simulated from the UiO-67 structure (blue). (d) UV-Vis diffuse reflectance spectra of as-synthesized **7** (black) and **7** after photocatalysis (red). (Reprinted with permission from ref [12]. Copyright American Chemical Society 2011)

Table 2.6 Investigations of **7** as a photocatalyst for light-driven CO_2 production.[a]

Entry	*Photocatalyst*	*Reaction time (h)*	*H_2-TON*[b]	*CO-TON*[c]
1	**7**	6	0.5	5.0
2 (reuse1)[d]	**7**	6	0.5	6.9
3 (reuse2)[d]	**7**	6	0.6	0
4	Supernatant after MOF filtration	6	0.1	0
5	**7**	20	2.5	10.9

6	$\mathbf{L_7}$	6	0.5	2.5
7 (reuse1)[e]	$\mathbf{L_7}$	6	0.8	0.07
8 (reuse2)[f]	$\mathbf{L_7}$	6	0.1	0
9	$\mathbf{L_7}$	20	0.6	3.5
10	$Re(CO)_3Cl(bpy)$	6	0.3	5.6
11	$Re(CO)_3Cl(bpy)$	20	1.0	7.0
12[g]	**7**	6	0.02	0
13[h]	**7**	6	0	0
14	undoped-UiO67	6	0	0

[a]The reaction vials were placed 10 cm in front of a 450 W Xe-lamp with a 300 nm cut-off filter, with magnetic stirring. [b]H_2-TON is defined as the number of evolved hydrogen molecules per catalytic site. [c]CO-TON is defined as the number of evolved CO molecules per catalytic site. [d]The MOF solids were recovered by centrifugation for reuse in new catalytic runs. [e]The reaction solution was degassed with CO_2 before a second photocatalytic run. [f]100 μL TEA was added to the reaction solution and the solution was then degassed with CO_2 before a third photocatalytic run. [g]without CO_2 [h]without light.

We also tested the recyclability of the **7** catalyst in light-driven CO_2 reduction. The solid in the reaction mixture was recovered via centrifugation and reused in additional runs of catalytic reactions. However, after two six-hour reaction runs, the catalyst became inactive in CO generation, but a small amount of H_2 was still detected (Table 2.6, entries 2-3). The supernatant of the **7** reaction mixture showed no CO generation activity but slight H_2 generation activity (Table 2.6, entry 4). The total CO-TON of the **7** catalyst was estimated to be 10.9 from the 20 hour reaction (Table 2.6, entry 5). During the 20-hour reaction, 43.6% of the Re had leached into the supernatant, as determined by ICP-MS. In contrast, only 3.5% of the Zr was detected in the supernatant by ICP-MS. PXRD of the recovered solid indicated that the framework structure of **7** remained intact (Figure 2.16c). These results suggest that the Re leached into solution via the detachment of Re-carbonyl moieties from the dcbpy group in the **7** framework, and not by dissolution of **7**. Consistent with this, the recovered **7** lost the UV-Vis peak at 412 nm that is characteristic of the ^{1}MLCT absorption of the $Re(CO)_3(bpy)Cl$ species (Figure 2.16d). The intensities of the IR peaks corresponding to the CO stretching vibrations of the $\mathbf{L_7}$ ligand at ~2025

cm^{-1}(A'), ~1923 cm^{-1}(A'), and ~1900 cm^{-1} (A'') significantly decreased in the recovered solid when compared to those of the as-synthesized **7** (Figure 2.16b), further supporting the decomposition of the $\mathbf{L_7}$ ligand by losing the Re-carbonyl moieties.

Photocatalytic CO_2 reduction was also conducted with the homogeneous ligand $\mathbf{L_7}$ under the same conditions. Upon irradiation, the reaction mixture also turned from orange to green color immediately. After a six-hour reaction, the solution color turned to yellowish gray and GC analysis indicated a moderate CO-TON of 2.5 (Table 2.16, entry 6). The reaction mixture was almost inactive in the second photocatalytic run, even after re-saturating the solution with CO_2 (Table 2.6, entry 7). Adding more TEA to the solution did not regenerate the catalytic activity (Table 2.6, entry 8). All of these observations indicated that the Re $\mathbf{L_7}$ ligand decomposed during the catalytic turnovers. The overall CO-TON for the homogeneous $H_2\mathbf{L_7}$ ligand was estimated to be 3.5 based on the 20 hour reaction (Table 2.6, entry 9). A time-dependent catalytic activity experiment was performed by analyzing the CO production at different time points by GC (Figure 2.16a). Although the homogeneous $H_2\mathbf{L_7}$ was more active than the **7** catalyst in the first two hours, the **7** catalyst retained activity over a longer reaction time to yield a higher total TON. The **7** catalyst thus exhibited much higher total TONs than the homogeneous system, presumably as a result of the catalyst stabilization by the MOF framework. Reactions using $Re(CO)_3(bpy)Cl$ as catalyst were performed to test our experimental set up and reaction conditions (Table 2.6, entries 12 and 13). A total TON of 7.0 was obtained after 20 hours of irradiation, which is comparable to the previously reported value.[69]

Previous mechanistic studies on the $[Re(CO)_3(bpy)Cl]$-catalyzed CO_2 reduction suggested both a unimolecular pathway involving a $[Re^{I}(bpy)(CO)_3(COOH)]$ intermediate[61] and a bimolecular pathway involving a CO_2 bridged Re dimer $[(CO)_3(bpy)Re^{I}](CO_2)[Re^{I}(bpy)(CO)_3]$[62,63] or outer-sphere redox reactions between two Re molecules[69] in the catalytic cycle. The present **7** catalyzed CO_2 reduction can only occur via the unimolecular mechanism as a result of the immobilization of the $\mathbf{L_7}$ catalyst in the MOF framework. Interestingly, the incorporation of $\mathbf{L_7}$ into the **7** framework not only led to higher CO_2 reduction TONs, but also shed light on the CO_2 reduction reaction mechanisms and photocatalyst decomposition pathways.

2.2.5 Photocatalytic Organic Transformations using 8 and 9

Catalytic activities of $Ir(ppy)_2(bpy)^{+}$-based **8** and $Ru(bpy)_3^{2+}$-based **9** toward photocatalytic aza-Henry reactions were evaluated with tetrahydroisoquinoline (**1a**) as the amine substrate and CH_3NO_2 as solvent. The reaction was carried out in the presence of air with a common fluorescent lamp (26 W) as the light source. The reaction was stopped after 12 hours and the MOF catalysts were filtered off. Conversions of the reactions were determined by integrating the peaks of ^{1}H NMR spectra of the crude reaction mixtures. As shown in Table 2.7 (entry 1), both **8** and **9** were highly effective photocatalysts for the aza-Henry reaction between **1a** and nitromethane, with 59% and 86% conversions, respectively. The **8** and **9** catalysts also effectively catalyzed the aza-Henry reactions between nitromethane and bromo- and methoxy-substituted tetrahydroisoquinoline (**2a** and **3a**) with high efficiency (Table 2.7, entries 2 and 3). A number of control experiments were carried out to demonstrate the heterogeneous and

photocatalytic nature of the reactions. The reaction of **1a** in the dark yielded negligible amounts of aza-Henry products (<5%), demonstrating the necessity of light in this reaction. On the other hand, the background reaction in the absence of the catalysts but in the presence of light showed only 19% conversion after 12 hours (Table 2.7, entry 1), indicating that the MOF played a catalytic role in the reactions. These observations are consistent with those of the homogeneous catalytic system reported by Stephenson and co-workers.[74] In addition, a cross-over experiment was carried out to prove the heterogeneity of the MOF catalyst. Substrate **3a** was first used in the **9** catalyzed aza-Henry reaction, and 95% conversion was achieved after 12 hours. The MOF catalyst was then removed by filtering through Celite, and another substrate **1a** was added to the supernatant solution. After stirring the solution under light for 12 hours, only 22% conversion was observed for the second substrate. This low conversion, comparable to that of the background reaction, proved that the supernatant of the **9** reaction mixture is inactive in photocatalysis, supporting the heterogeneous nature of the MOF photocatalysts. A further examination of the supernatant by ICP-MS showed no observable leaching of Ru to the solution during the reaction. The **8** and **9** catalysts were also recovered from the reaction mixture by centrifugation, and reused three times without loss of activity (Table 2.8). In addition, PXRD patterns of **8** and **9** after the reactions showed no deterioration of the crystallinity (Figure 2.17).

Table 2.7. **8** and **9** catalyzed aza-Henry reactions[a]

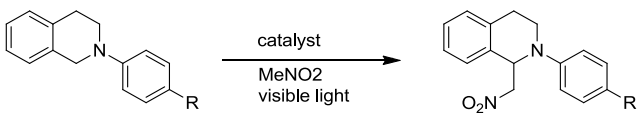

1a, R= H
2a, R= Br
3a, R= OCH_3

1b, R= H
2b, R= Br
3b, R= OCH_3

entry	substrate	Catalyst /Conv. (%) [b]				
		No catalyst	**8**	**L_2-Et_2**[c]	**9**	**L_3-Et_2**[c]
1	**1a**	19	59	99	86	97
2	**2a**	17	62	90	68	88
3	**3a**	28	96	>99	97	>99

[a]The reactions were carried out with 1 mol% catalyst loading, 5 cm in front of a 26 W fluorescent lamp for 12 hours. [b]Conversion yields were determined by ^{1}H NMR. [c] As the acid ligand has very low solubility in nitromethane, the diethyl esters of $\mathbf{L_2}$ and $\mathbf{L_3}$ ligands $\mathbf{L_2}$-Et_2 and $\mathbf{L_3}$-Et_2 were used in the homogeneous control experiments instead.

Table 2.8. Reuse of **8** and **9** in aza-Henry reactions[a]

catalyst	substrate	Conv. (%)[b]		
		1st run	2nd run	3rd run
8	**1a**	59	57	59
8	**2a**	62	68	68
8	**3a**	96	93	95
9	**1a**	86	69	62
9	**2a**	68	71	66
9	**3a**	97	93	95

[a]The reactions were carried out with 1 mol% catalyst loading, 5 cm in front of a 26 W fluorescent lamp for 12 hours. [b]Conversion yields were determined by ^{1}H NMR.

We performed another control experiment to demonstrate the need of MOF permanent porosity in catalyzing the photo-driven aza-Henry reaction. Amorphous nanoparticles were synthesized under similar conditions to those of **8**, except that wet DMF was used in

the synthesis and glacial acetic acid was not added. The resultant material was non-porous as indicated by N_2 adsorption measurement (with a negligible BET surface area of 46 m^2/g) and amorphous by PXRD. The $\mathbf{L_3}$ ligand weight percentage in this material was found to be higher than that of **9** by ICP-MS measurements (7.0 wt%). However, the non-porous nanoparticles did not catalyze the aza-Henry reaction using **1a** as the substrate (18% conversion, corresponding to background reaction) at the same catalyst loading as **9**. This observation unambiguously supported that the photoredox step of the reaction happened inside the channels of **8** and **9**. Although the substrate amines are relatively large compared to the size of channels in these MOFs, it is still possible for them to move through the MOF channels as a result of favorable interactions between the amine substrates and the MOF framework (e.g., π-π stacking interactions).[11] Alternatively, if the aza-Henry reaction is mediated by photochemically generated singlet oxygen, the poresize of the MOF just needs to be large enough to transport O_2 molecules. As surface photocatalytic sites of these systems have minor contributions to the overall photocatalysis (<12% as indicated by the water oxidation activity shown above), micro-porosity is a pre-requisite for the high activity of these doped MOFs.

We also demonstrated the applicability of the $Ru(bpy)_3^{2+}$-based **9** as a photocatalyst in other light-driven reactions. As shown in Table 2.9, **9** efficiently catalyzed aerobic oxidative coupling of a series of primary amines with 46% to 90% conversions in three hours (Table 2.9, entries 1,6,7). The conversion of substrate **1c** using the **9** was comparable to that using the homogeneous molecular catalyst (Table 2.9, entry 4). The recyclability and reusability of **9** were also evaluated in this reaction using **1c** as substrate. The recovered catalyst from simple filtration showed no deterioration of

conversion% (Table 2.9, entry 2), and retained the crystallinity of the pristine sample (Figure 2.17b). The background reaction in the absence of the catalyst but in the presence of light showed only ~8% conversion (Table 2.9, entry 4), verifying that **9** played a catalytic role in the reactions. On the other hand, the reaction of **1c** in the dark yielded negligible amounts of coupling products (Table 2.9, entry 5), demonstrating the necessity of light in this reaction. These observations are consistent with those reported by Lang et al.[75] and Su et al.[76]using carbon nitride and TiO_2 as photocatalysts. Time-dependent conversions of the three substrates have also been monitored by GC analysis at different time points. The initial reaction rate of the three substrates turned out to be quite similar from the experimental data. The reason for the seemingly lower finial conversion of **3c** in the reaction is the slow decomposition of product **3d** on **9**, probably due to intrinsic Lewis acidity of the $[Zr_6(\mu_3\text{-}O)_4(\mu_3\text{-}OH)_4(carboxylate)_6]$ building block. The absence of size-selectivity of the reaction gives the possibility of a singlet oxygen mediated reaction mechanism, in which singlet oxygen generated inside the MOF can diffuse out of the nanocrystal and drive the organic transformation in the solution.

Table 2.9. Photocatalytic aerobic amine coupling reactions[a]

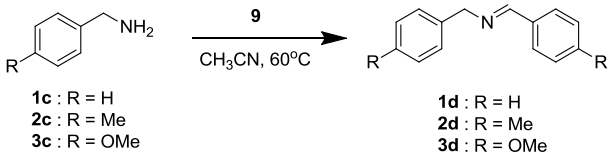

Entry	*catalyst*	*substrate*	*conversion%* [b]
1	**9**	**1c**	83
2	**9** (reuse)	**1c**	80
3	$\mathbf{L_3}$	**1c**	96
4	No catalyst	**1c**	8

5[c]	**9**	**1c**	6
6	**9**	**2c**	90
7	**9**	**3c**	46

[a]Reactions were carried out with 1 mol% catalyst loadings, 5 cm in front of a 300 W Xe lamp for 1 hour. [b]Conversion yields were determined by ^{1}H NMR. [c]without light.

The photocatalyzed aerobic oxidation of thioanisole was also examined, using **9** as the photocatalyst. Photocatalytic aerobic oxidation of sulfide to sulfoxide has been reported before with $Ru(bpy)_3^{2+}$ in acetonitrile but only when a lead ruthenate pyrochlore mineral was added as an electron shuttle.[77] We found that by changing the solvent to methanol, the photocatalyzed sulfide oxidation occurred without an electron relay (Table 2.10, entry 1). It is highly possible that the reaction was mediated by singlet oxygen that is generated photochemically. As shown in Table 2.10, with methanol as the solvent, **9** catalyzed the selective aerobic oxidation of thioanisole to methyl phenyl sulfoxide. No sulfone (the possible over-oxidized by-product) was detected by ^{1}H NMR, demonstrating a high degree of selectivity of this reaction. The conversion% after 22 hours is comparable to that of the corresponding homogeneous catalytic system (Table 2.10, entries 1 and 2). A control experiment with no photocatalyst but with light showed no appreciable conversion of the sulfide (Table 2.10, entry 3). No sulfoxide products were detected when the reactions were carried out in the absence of light but in the presence of **9** or $\mathbf{L_3}$ (Table 2.10, entries 4 and 5). O_2 was shown to be the oxidizing agent since no conversion of sulfide to sulfoxide was observed when the reaction was carried out under N_2 protection (Table 2.10, entries 6 and 7). The PXRD pattern of the **9** catalyst after the reaction was identical to that of the pristine **9**, indicating its stability under the reaction conditions (Figure 2.17).

Table 2.10. Photo-oxidation of thioanisole

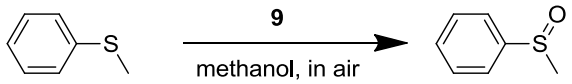

Entry	*Catalyst/reaction condition*	*Time (h)*	*conversion%* [b]
1	**L_3**	22	72
2	**9**	22	73
3	No catalyst, with light	22	0
4	No light, with **L_3**	22	0
5	No light, with **9**	22	0
6	**L_3** under N_2 protection	22	0
7	**9**, under N_2 protection	22	0

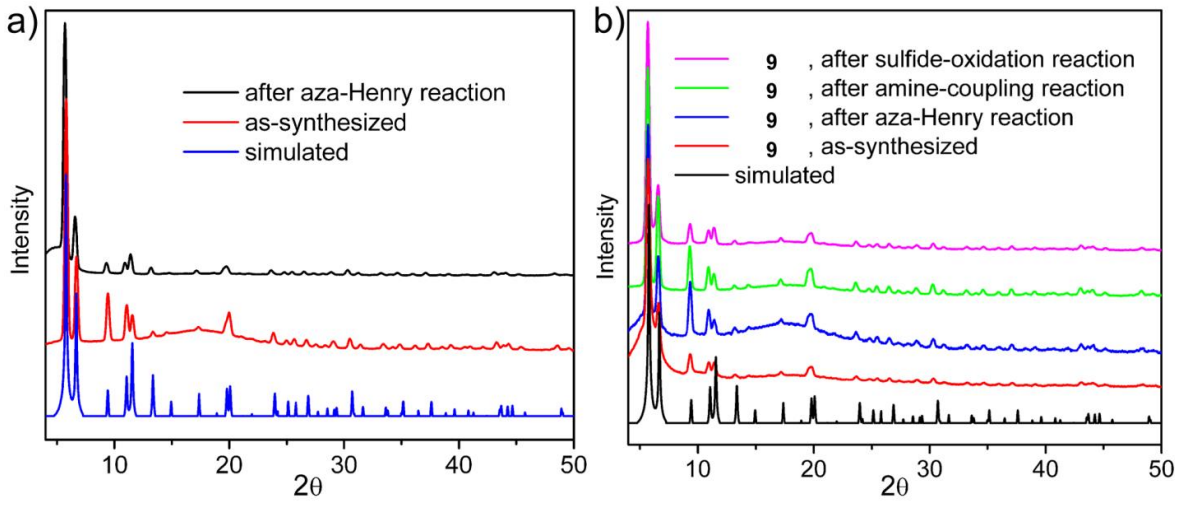

Figure 2.17 (a) PXRD patterns of **8**: as-synthesized (red), after aza-Henry reaction (black), and simulated from the UiO-67 structure (blue). (b) PXRD patterns of **9**: after sulfide-oxidation (pink), after amine-coupling (green), after aza-Henry reaction (blue), as-synthesized (red), and simulated from the UiO-67 structure (black). (Reprinted with permission from ref [12]. Copyright American Chemical Society 2011)

2.2.6 Conclusions

We have successfully incorporated Ir, Re, and Ru complexes into the UiO framework by a mix-and-match strategy. These stable and porous metal complex-derivatized doped MOFs are highly effective catalysts for a range of reactions related to solar energy utilization. **4-6** were used in catalytic water oxidation, while **7** catalyzed photochemical CO_2 reduction. **8** and **9** were used in three photocatalytic organic tranformations: aza-Henry reaction, aerobic amine-coupling, and aerobic thioanisole oxidation. Stability of these MOF catalysts under the reaction conditions was verified by comparing PXRD patterns before and after catalysis. The heterogeneous nature of these catalysts can not only facilitate catalyst recycling and reuse, but can also provide mechanistic insights into the reactions, as in the case of CO_2 reduction using **7**. The modular nature of this synthetic approach should allow further fine-tuning and optimization to lead to highly active heterogeneous catalysts in solar energy utilization.

REFERENCES

(1) Cavka, J. H.; Jakobsen, S.; Olsbye, U.; Guillou, N.; Lamberti, C.; Bordiga, S.; Lillerud, K. P. *J. Am. Chem. Soc.* **2008**, *130*, 13850.

(2) Eddaoudi, M.; Kim, J.; Rosi, N.; Vodak, D.; Wachter, J.; O'Keeffe, M.; Yaghi, O. M. *Science* **2002**, *295*, 469.

(3) Li, Q.; Zhang, W.; Miljanic, O. S.; Sue, C. H.; Zhao, Y. L.; Liu, L.; Knobler, C. B.; Stoddart, J. F.; Yaghi, O. M. *Science* **2009**, *325*, 855.

(4) Ma, L. F., J. M.; Abney, C.; Lin, W. *Nat. Chem.* **2010**.

(5) Song, F.; Wang, C.; Falkowski, J. M.; Ma, L.; Lin, W. *J. Am. Chem. Soc.* **2010**, *132*, 15390.

(6) Banerjee, M.; Das, S.; Yoon, M.; Choi, H. J.; Hyun, M. H.; Park, S. M.; Seo, G.; Kim, K. *J. Am. Chem. Soc.* **2009**, *131*, 7524.

(7) Tanabe, K. K.; Cohen, S. M. *Angew. Chem. Int. Ed. Engl.* **2009**, *48*, 7424.

(8) Wu, C. D.; Hu, A.; Zhang, L.; Lin, W. *J. Am. Chem. Soc.* **2005**, *127*, 8940.

(9) Deng, H.; Doonan, C. J.; Furukawa, H.; Ferreira, R. B.; Towne, J.; Knobler, C. B.; Wang, B.; Yaghi, O. M. *Science* **2010**, *327*, 846.

(10) Barrett, S. M.; Wang, C.; Lin, W. *J. Mater. Chem.* **2012**, *22*, 10329.

(11) Wang, C.; Lin, W. *J. Am. Chem. Soc.* **2011**, *133*, 4232.

(12) Wang, C.; Xie, Z.; deKrafft, K. E.; Lin, W. *J. Am. Chem. Soc.* **2011**, *133*, 13445.

(13) Concepcion, J. J.; Jurss, J. W.; Brennaman, M. K.; Hoertz, P. G.; Patrocinio, A. O. v. T.; Murakami Iha, N. Y.; Templeton, J. L.; Meyer, T. J. *Acc. Chem. Res.* **2009**, *42*, 1954.

(14) Gust, D.; Moore, T. A.; Moore, A. L. *Acc. Chem. Res.* **2009**, *42*, 1890.

(15) Duan, L.; Fischer, A.; Xu, Y.; Sun, L. *J. Am. Chem. Soc.* **2009**, *131*, 10397.

(16) Zong, R.; Thummel, R. P. *J. Am. Chem. Soc.* **2005**, *127*, 12802.

(17) Concepcion, J. J.; Jurss, J. W.; Templeton, J. L.; Meyer, T. J. *J. Am. Chem. Soc.* **2008**, *130*, 16462.

(18) Ellis, W. C.; McDaniel, N. D.; Bernhard, S.; Collins, T. J. *J. Am. Chem. Soc.* **2010**, *132*, 10990.

(19) Tseng, H. W.; Zong, R.; Muckerman, J. T.; Thummel, R. *Inorg. Chem.* **2008**, *47*, 11763.

(20) Blakemore, J. D.; Schley, N. D.; Balcells, D.; Hull, J. F.; Olack, G. W.; Incarvito, C. D.; Eisenstein, O.; Brudvig, G. W.; Crabtree, R. H. *J. Am. Chem. Soc.* **2010**, *132*, 16017.

(21) Hu, A.; Ngo, H. L.; Lin, W. *J. Am. Chem. Soc.* **2003**, *125*, 11490.

(22) McDaniel, N. D.; Coughlin, F. J.; Tinker, L. L.; Bernhard, S. *J. Am. Chem. Soc.* **2008**, *130*, 210.

(23) Geletii, Y. V.; Huang, Z.; Hou, Y.; Musaev, D. G.; Lian, T.; Hill, C. L. *J. Am. Chem. Soc.* **2009**, *131*, 7522.

(24) Yin, Q.; Tan, J. M.; Besson, C.; Geletii, Y. V.; Musaev, D. G.; Kuznetsov, A. E.; Luo, Z.; Hardcastle, K. I.; Hill, C. L. *Science* **2010**, *328*, 342.

(25) Morris, N. D.; Mallouk, T. E. *J. Am. Chem. Soc.* **2002**, *124*, 11114.

(26) Nakagawa, T.; Bjorge, N. S.; Murray, R. W. *J. Am. Chem. Soc.* **2009**, *131*, 15578.

(27) Youngblood, W. J.; Lee, S. H.; Kobayashi, Y.; Hernandez-Pagan, E. A.; Hoertz, P. G.; Moore, T. A.; Moore, A. L.; Gust, D.; Mallouk, T. E. *J. Am. Chem. Soc.* **2009**, *131*, 926.

(28) Jiao, F.; Frei, H. *Angew. Chem. Int. Ed. Engl.* **2009**, *48*, 1841.

(29) Kanan, M. W.; Nocera, D. G. *Science* **2008**, *321*, 1072.

(30) Low, J. J.; Benin, A. I.; Jakubczak, P.; Abrahamian, J. F.; Faheem, S. A.; Willis, R. R. *J. Am. Chem. Soc.* **2009**, *131*, 15834.

(31) Guillerm, V.; Gross, S.; Serre, C.; Devic, T.; Bauer, M.; Ferey, G. *Chem. Commun.* **2010**, *46*, 767.

(32) Jordan, P.; Fromme, P.; Witt, H. T.; Klukas, O.; Saenger, W.; Krausz, N. *Nature* **2001**, *411*, 909.

(33) Morris, A. J.; Meyer, G. J.; Fujita, E. *Acc. Chem. Res.* **2009**, *42*, 1983.

(34) Beley, M.; Collin, J. P.; Ruppert, R.; Sauvage, J. P. *J. Am. Chem. Soc.* **1986**, *108*, 7461.

(35) Craig, C. A.; Spreer, L. O.; Otvos, J. W.; Calvin, M. *J. Phys. Chem.* **1990**, *94*, 7957.

(36) Matsuoka, S.; Yamamoto, K.; Ogata, T.; Kusaba, M.; Nakashima, N.; Fujita, E.; Yanagida, S. *J. Am. Chem. Soc.* **1993**, *115*, 601.

(37) Ogata, T.; Yamamoto, Y.; Wada, Y.; Murakoshi, K.; Kusaba, M.; Nakashima, N.; Ishida, A.; Takamuku, S.; Yanagida, S. *J. Phys. Chem.* **1995**, *99*, 11916.

(38) Tinnemans, A. H. A.; Koster, T. P. M.; Thewissen, D. H. M. W.; Mackor, A. *Recl.: J. R. Neth. Chem. Soc.* **1984**, *103*, 288.

(39) Behar, D.; Dhanasekaran, T.; Neta, P.; Hosten, C. M.; Ejeh, D.; Hambright, P.; Fujita, E. *J. Phys. Chem. A* **1998**, *102*, 2870.

(40) Grodkowski, J.; Behar, D.; Neta, P.; Hambright, P. *J. Phys. Chem. A* **1997**, *101*, 248.

(41) Grodkowski, J.; Dhanasekaran, T.; Neta, P.; Hambright, P.; Brunschwig, B. S.; Shinozaki, K.; Fujita, E. *J. Phys. Chem. A* **2000**, *104*, 11332.

(42) Grodkowski, J.; Neta, P. *J. Phys. Chem. A* **2000**, *104*, 1848.

(43) Grodkowski, J.; Neta, P.; Fujita, E.; Mahammed, A.; Simkhovich, L.; Gross, Z. *J. Phys. Chem. A* **2002**, *106*, 4772.

(44) Doherty, M. D.; Grills, D. C.; Fujita, E. *Inorg. Chem.* **2009**, *48*, 1796.

(45) Hawecker, J.; Lehn, J. M.; Ziessel, R. *J. Chem. Soc., Chem. Commun.* **1983**, 536.

(46) Hori, H.; Johnson, F. P. A.; Koike, K.; Ishitani, O.; Ibusuki, T. *J. Photochem. Photobiol., A* **1996**, *96*, 171.

(47) Hori, H.; Koike, K.; Suzuki, Y.; Ishizuka, M.; Tanaka, J.; Takeuchi, K.; Sasaki, Y. *J. Mol. Catal. A: Chem.* **2002**, *179*, 1.

(48) Takeda, H.; Koike, K.; Inoue, H.; Ishitani, O. *J. Am. Chem. Soc.* **2008**, *130*, 2023.

(49) Narayanam, J. M.; Stephenson, C. R. *Chem. Soc. Rev.* **2011**, *40*, 102.

(50) Ischay, M. A.; Anzovino, M. E.; Du, J.; Yoon, T. P. *J. Am. Chem. Soc.* **2008**, *130*, 12886.

(51) Narayanam, J. M.; Tucker, J. W.; Stephenson, C. R. *J. Am. Chem. Soc.* **2009**, *131*, 8756.

(52) Condie, A. G.; Gonzalez-Gomez, J. C.; Stephenson, C. R. *J. Am. Chem. Soc.* **2010**, *132*, 1464.

(53) Lang, X.; Ji, H.; Chen, C.; Ma, W.; Zhao, J. *Angew. Chem. Int. Ed. Engl.* **2011**, 50, 3934.

(54) Su, F.; Mathew, S. C.; Mohlmann, L.; Antonietti, M.; Wang, X.; Blechert, S. *Angew. Chem. Int. Ed. Engl.* **2011**, *50*, 657.

(55) Chen, W.; Rein, F. N.; Rocha, R. C. *Angew. Chem. Int. Ed. Engl.* **2009**, *48*, 9672.

(56) Zen, J. M.; Liou, S. L.; Kumar, A. S.; Hsia, M. S. *Angew. Chem. Int. Ed. Engl.* **2003**, *42*, 577.

(57) Fukuzumi, S.; Kishi, T.; Kotani, H.; Lee, Y.-M.; Nam, W. *Nat. Chem.* **2011**, *3*, 38.

(58) Dai, C.; Narayanam, J. M.; Stephenson, C. R. *Nat. Chem.* **2011**, *3*, 140.

(59) Nicewicz, D. A.; MacMillan, D. W. *Science* **2008**, *322*, 77.

(60) Tucker, J. W.; Nguyen, J. D.; Narayanam, J. M.; Krabbe, S. W.; Stephenson, C. R. *Chem. Commun.* **2010**, *46*, 4985.

(61) Gibson, D. H.; Yin, X.; He, H.; Mashuta, M. S. *Organometallics* **2003**, *22*, 337.

(62) Gibson, D. H.; Yin, X. *J. Am. Chem. Soc.* **1998**, *120*, 11200.

(63) Hayashi, Y.; Kita, S.; Brunschwig, B. S.; Fujita, E. *J. Am. Chem. Soc.* **2003**, *125*, 11976.

Chapter 3

Pt Nanoparticles@Photoactive Metal-Organic Frameworks: Efficient Hydrogen Evolution via Synergistic Photo-excitation and Electron Injection[1]

3.1 Introduction to nanoparticle deposition in Metal-Organic Frameworks

Functional entities can be built into MOF frameworks (walls) either as organic building blocks[2] or as metal cluster secondary building units (SBUs).[3] Alternatively, functional groups can be tethered onto MOF walls via postsynthetic modifications.[4,5] Functional entities can also be assembled inside the internal channels or cavities of MOFs as counter ions or as trapped nanoparticles which are not covalently linked to the MOF walls.[6-8] In particular, metal nanoparticles have been incorporated into MOFs through chemical vapor deposition,[9-11] liquid/incipient wetness impregnation[12-17], solid grinding,[18,19] and microwave irradiation[20] to form metal@MOF hierarchical assemblies. Such a versatile variety of functionalization methods makes it possible to incorporate multiple functional entities into the same MOF to enable synergistic functions.[21]

We are interested in using photoactive framework materials as a new platform to integrate different functional components that are needed for solar energy conversion.[22-24] Photocatalytic hydrogen generation is an essential half reaction in water splitting, which converts sunlight energy into the chemical potential of hydrogen molecules.[25-28] A visible light-driven photocatalytic hydrogen evolution system often requires two components—the phosphor to harvest sunlight and the catalyst to produce hydrogen using the harvested energy. Bernhard et al. pioneered the use of $[Ir(ppy)_2(bpy)]^+$ (ppy=2-phenylpyridine;

bpy=2,2'-bipyridine) and its derivatives as photosensitizers to drive photocatalytic hydrogen evolution with Pt nanoparticles.[29-33] In this chapter, I will describe the design of synergistic hydrogen evolution photocatalysts based on Pt nanoparticle@MOF assemblies. Pt nanoparticles were loaded to the cavities of phosphorescent MOFs (**8** and **10**) to enable efficient photocatalytic H_2 evolution via photo-injection of electrons from the light-harvesting MOF frameworks into the Pt nanoparticles. The Pt@**10** assembly showed a much enhanced (~five times) hydrogen evolution efficiency compared to the homogeneous control, and could be readily recycled and reused by centrifugation.

3.2 Pt Nanoparticles@Photoactive Metal-Organic Frameworks for hydrogen evolution

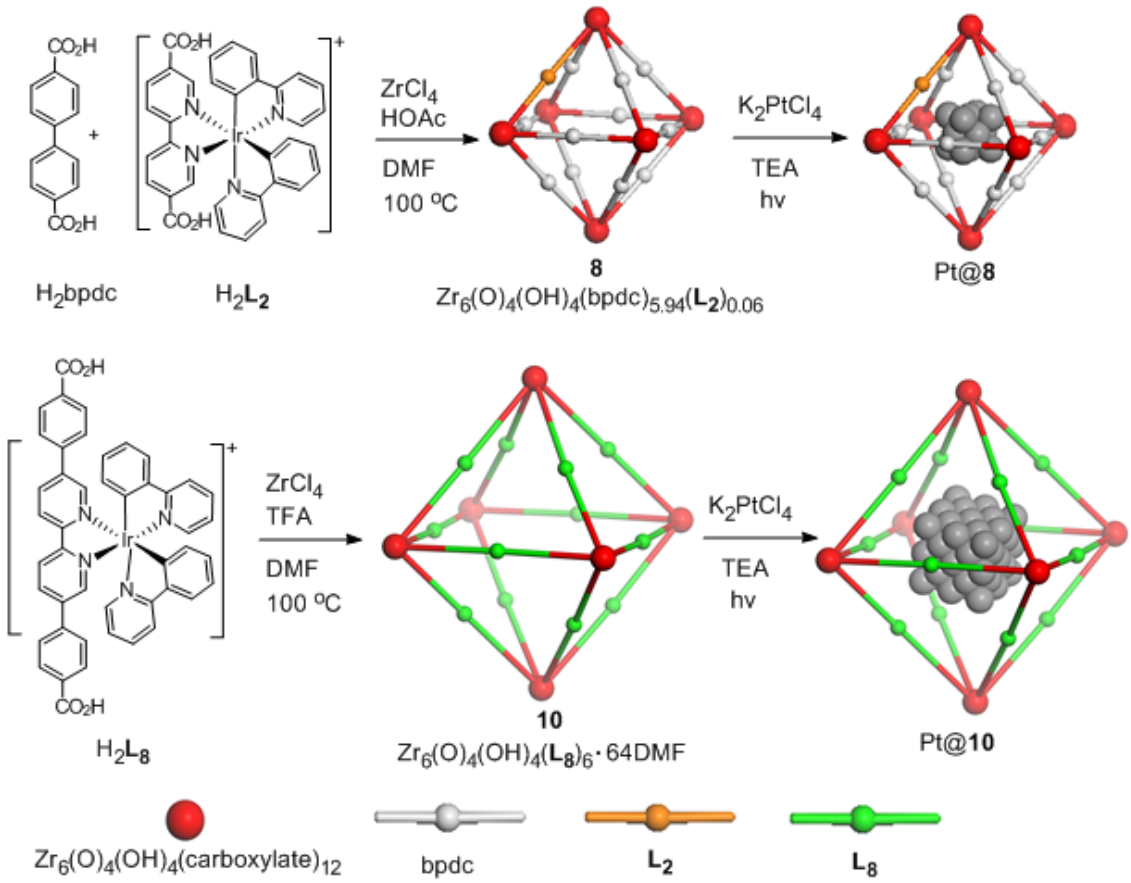

Scheme 3.1. Synthesis of phosphorescent Zr-carboxylate MOFs (**8** and **10**) of the **fcu** topology and subsequent loading of Pt nanoparticles inside MOF cavities via MOF-

mediated photo-reduction of K_2PtCl_4 to form the Pt@**8** and Pt@**10** assemblies. (Reprinted with permission from ref [1]. Copyright American Chemical Society 2012)

The $[Ir(ppy)_2(bpy)]Cl$-derived dicarboxylic acid $H_2\mathbf{L_8}$ was synthesized by treating $[Ir(ppy)_2Cl]_2$ with dimethyl (2,2'-bipyridine)-5,5'-dibenzoate ($Me_2\mathbf{L_8}$), followed by base-catalyzed hydrolysis.[22] We targeted the synthesis of UiO frameworks built from a linear dicarboxylate ligand and the $Zr_6(\mu_3\text{-}O)_4(\mu_3\text{-}OH)_4(carboxylate)_{12}$ SBU in this work because of their high chemical stability.[34-39] As shown in chapter 2,[22] $Zr_6(\mu_3\text{-}O)_4(\mu_3\text{-}OH)_4(bpdc)_{5.94}(\mathbf{L_2})_{0.06}$ (**8**) was prepared by doping the $\mathbf{L_2}$ ligand into the UiO-67 framework with biphenyldicarboxylate (BPDC) as the bridging ligand at ~2 wt% loadings, by taking advantage of the matching length of $\mathbf{L_2}$ and BPDC (Scheme 3.1). Intergrown octahedral nanocrystals of **8** of ~200 nm in dimensions (Fig. 3.2a) were used for hydrogen evolution studies. **8** is highly porous with a BET surface area of 1194 m^2/g and an average pore size of 6.7 Å.

10 was synthesized by treating $H_2\mathbf{L_8}$ with $ZrCl_4$ in DMF at 100 ^oC for 3 days. A small amount of trifluoroacetic acid was added to improve the crystallinity of **10**.[37] Cuboctahedron-shaped single crystals of **10,** approximately 0.02 mm in each dimension, were obtained and used for X-ray diffraction studies.[40] **10** adopts the UiO framework structure of the **fcu** topology by connecting the $Zr_6(\mu_3\text{-}O)_4(\mu_3\text{-}OH)_4(carboxylate)_{12}$ SBUs with the linear dicarboxylate $\mathbf{L_8}$ linker (Figures 3.1a-d).[41] Because of the steric bulk of the $\mathbf{L_8}$ ligand, a non-interpenetrated structure was obtained, with 71.4% void space as calculated by PLATON and a triangular open channel with 1.6 nm edge length and an octahedral cavity with a diameter of 1 nm. The disordered nature of the solvent molecules and counterions in the MOF channels prevents their identification by X-ray

crystallography. The solvent molecules and counterions were instead determined by a combination of TGA and NMR studies, which gave the overall formula of $Zr_6(\mu_3\text{-}O)_4(\mu_3\text{-}OH)_4(\mathbf{L_8})_6 \cdot 64DMF$ for **10**.[42] Nitrogen adsorption measurements on **10** indicated zero surface area. Powder X-ray diffraction (PXRD) studies indicated severe framework distortion for **10** upon solvent removal, a process that is common for MOFs with large open channels.[43] The porosity of **10** was instead ascertained by dye uptake measurements. **10** exhibited approximately 75 wt% uptake of both Brilliant Blue R-250 and Crystal Violet.

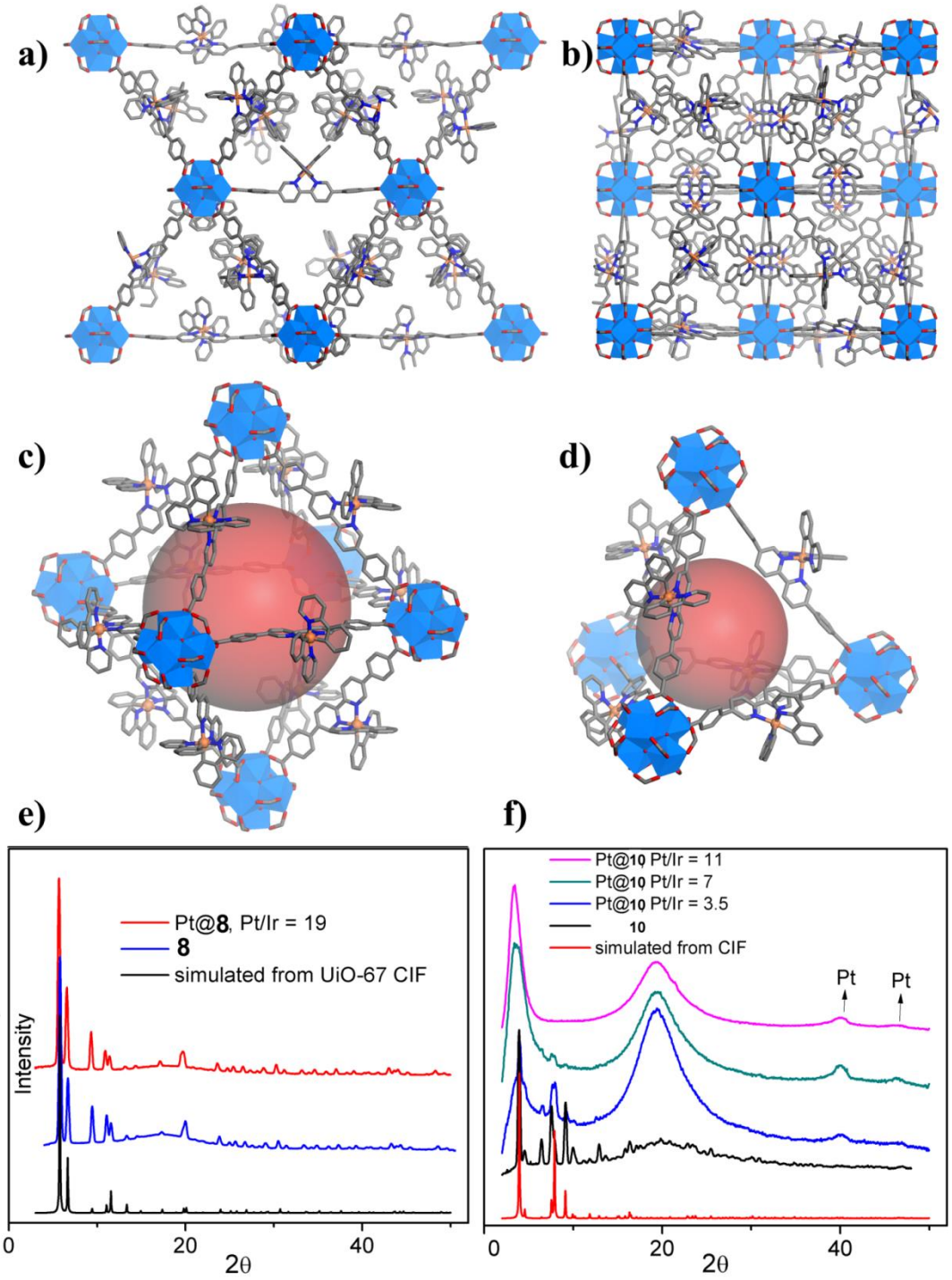

Figure 3.1 Stick-polyhedron model of the crystal structure of **10** (a) viewed along the [110] direction; (b) viewed along the [100] direction; (c) showing an octahedral cavity, represented by a red ball with the diameter of 1 nm; and (d) showing a tetrahedral cavity, represented by a red ball with a diameter of 0.6 nm. PXRD patterns of (e) Pt@**8**(red), **8** (blue), the idealized UiO-67 framework (black), and (f) **10** (black), Pt@**10** with different

Pt/Ir ratios (3.5-blue, 7-green, 11-purple), and the idealized framework of **10** (red). (Reprinted with permission from ref [1]. Copyright American Chemical Society 2012)

The $[Ir^{III}(ppy)_2(bpy)]^+$ core in **8** and **10** can be excited by visible light to a ^{1}MLCT excited state, which efficiently transitions to a ^{3}MLCT state through intersystem crossing. The long-lived ^{3}MLCT state then returns to the ground state to lead to phosphorescence emission (Fig. 3.3b inset). Time-resolved emission measurements revealed the weighted lifetime of the ^{3}MLCT state of **8** to be 51.8 ns (vs. 11.1 ns for $Et_2\mathbf{L_2}$) and that of **10** to be 110.3 ns (vs. 89.0 ns for $Me_2\mathbf{L_8}$) (Fig. 3.3b). We believe the longer emission lifetime of MOFs than that of corresponding ligands is due to rigidity of the MOF framework.

Pt nanoparticles were loaded to the cavities of **8** and **10** by *in situ* photoreduction of K_2PtCl_4. A mixture of K_2PtCl_4 and the MOF powder in a mixed solvent of tetrahydrofuran (THF)/triethylamine (TEA)/H_2O (20/1/1 v/v/v) was degassed by bubbling N_2 through for 10 min before being placed in front of a 450 W Xe-lamp with a 420 nm cut-off (long pass) filter. It is established that TEA can reductively quench the photo-excited $[Ir^{III}(ppy)_2(bpy)]^{+*}$ to generate the reduced radical $[Ir^{III}(ppy)_2(bpy^{\cdot-})]$ which can in turn reduce K_2PtCl_4 to form Pt nanoparticles in the homogeneous systems.[29-31] We found that K_2PtCl_4 could be photoreduced by the ultraviolet (UV) light from the Xe-lamp in the absence of Ir-phosphors via direct UV light absorption by K_2PtCl_4. We placed a 420 nm cut-off filter in front of the Xe-lamp to reliably control the formation of Pt nanoparticles only inside MOF cavities.

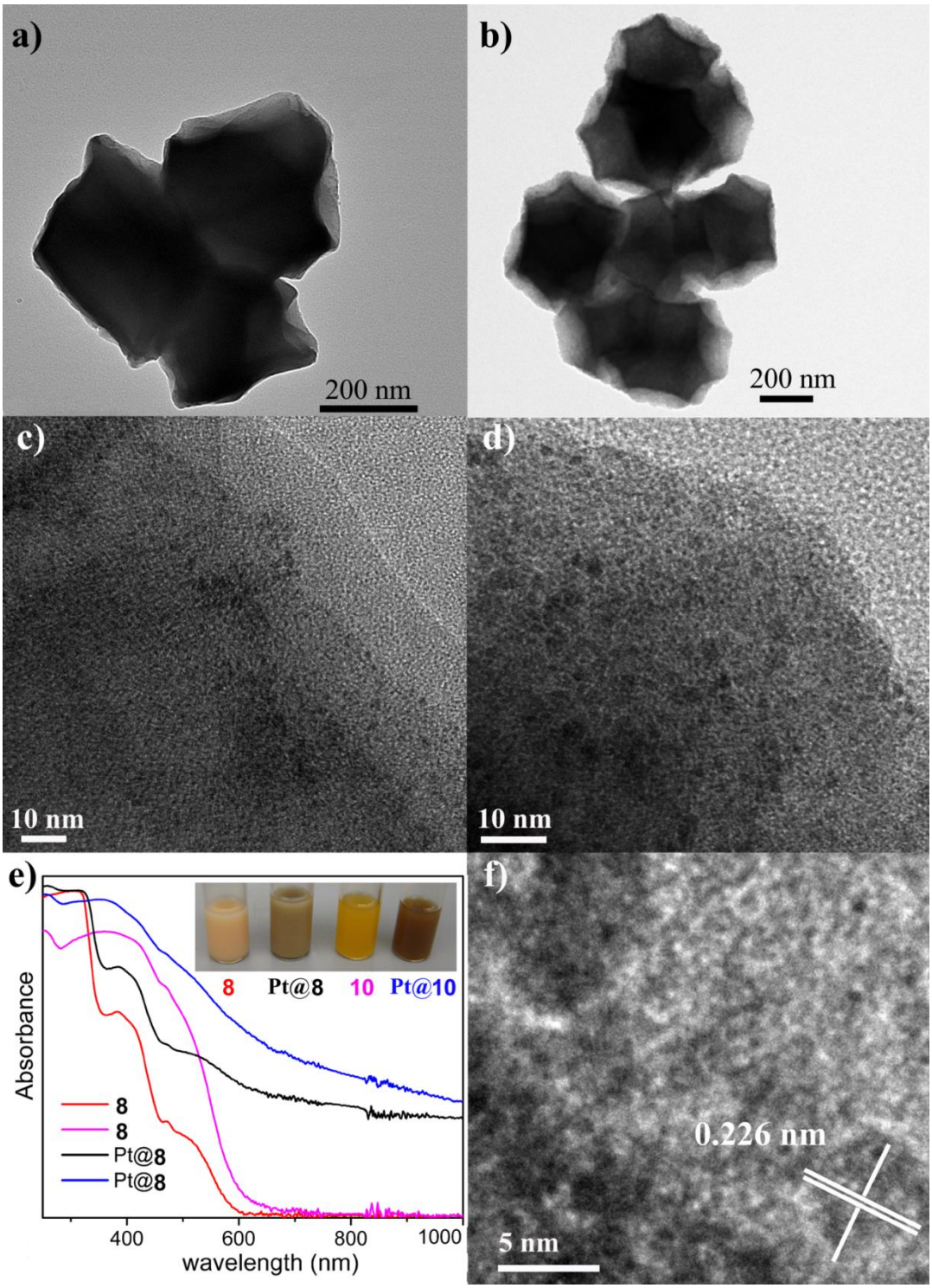

Figure 3.2 TEM images of Pt@**8** (a and c) and Pt@**10** (b, d and f). The black dots in (c) and (d) are Pt nanoparticles, and (f) shows the lattice fringes of the Pt particles, with d-spacing matching that of the Pt{111} plane. (e) Diffuse reflectance spectra of **8** (red), Pt@**8** (black), **10** (purple), and Pt@**10** (blue). A photograph of suspensions of these

samples is shown in the inset. (Reprinted with permission from ref [1]. Copyright American Chemical Society 2012)

The formation of Pt@MOF assemblies is supported by the following observations. Upon Pt loading, the color of the MOF powders changed from reddish-orange to brown or black due to the plasmonic absorption of Pt nanoparticles.[44,45] Diffuse reflectance spectra of the Pt@MOF samples are shown in Fig. 3.2e. Pt nanoparticle with diameters of 2-3 nm and 5-6 nm were formed inside the cavities of **8** and **10**, respectively, as revealed by high-resolution transmission electron microscopy (HRTEM) (Fig. 3.2). The fact that the Pt nanoparticle sizes are larger than those of the MOF cavities indicates partial MOF framework distortion/degradation during Pt particle formation; this phenomenon has been commonly observed for metal@MOFs.[9] Energy dispersive X-ray spectroscopy (EDS) confirmed the presence of Pt in the samples. The amounts of Pt nanoparticles in the samples were quantitatively determined by inductively coupled plasma-mass spectrometry (ICP-MS). As **10** possesses a more open framework structure and contains a much higher concentration of Ir-phosphor than **8**, much higher loadings of Pt were incorporated into **10** when the same amount of K_2PtCl_4 was used in the reactions. The Pt@**10** samples reached a plateau Pt/Ir molar ratio of 40, corresponding to 240 Pt atoms per $Zr_6(\mu_3\text{-}O)_4(\mu_3\text{-}OH)_4(\text{carboxylate})_{12}$ SBU and a filling of 47% of the void volume of **10**. In comparison, the Pt@**8** samples showed a maximum Pt/Ir ratio of 53 in the experiments (corresponding to 3 Pt atoms per SBU). The drastically different Pt loadings in **8** and **10** correlate well with the different Ir-phosphor loadings of the two MOFs.

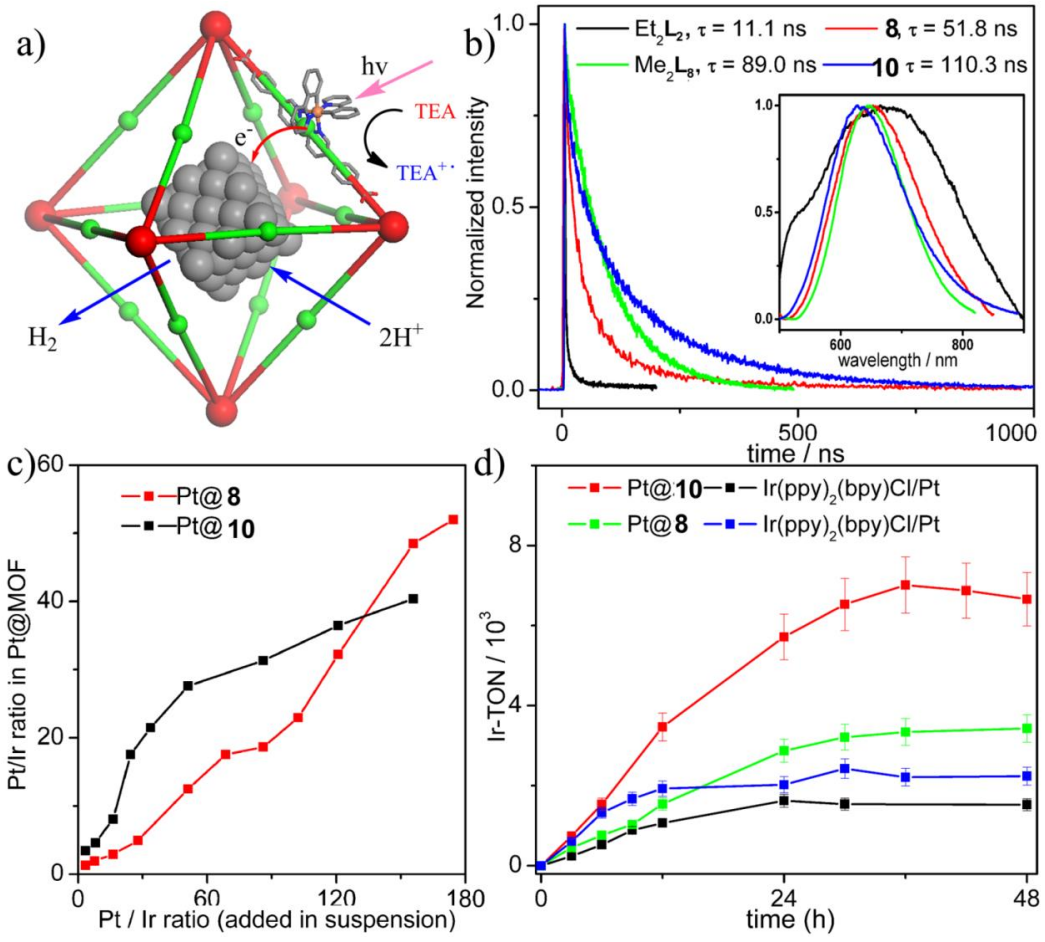

Figure 3.3 (a) Scheme showing the synergistic photocatalytic hydrogen evolution process via photo-injection of electrons from the light-harvesting MOF frameworks into the Pt nanoparticles. The red balls represent $Zr_6(O)_4(OH)_4(carboxylate)_{12}$ cores, while the green balls represent the Ir-phosphor ligand of the MOF. (b) Decay transients measured at 640 nm (with 445 nm excitation) in THF for $Et_2\mathbf{L_2}$ (black), **8** (red), $Me_2\mathbf{L_{10}}$ (green) and **10** (blue); The emission decays were fit to bi-exponential expression $A = A_1e^{-t/\tau1} + A_2e^{-t/\tau2}$. The reported lifetime τ is the weighted lifetime $\tau = (A_1\tau_1^2 + A_2\tau_2^2)/(A_1\tau_1 + A_2\tau_2)$. Insert: Steady-state emission spectra of $Et_2\mathbf{L_2}$ (black), **8** (red), $Me_2\mathbf{L_8}$ (green) and **10** (blue) with excitation at 485 nm. (c) Relationship between the amount of K_2PtCl_4 added in the reaction solution and the amount of Pt deposited inside the MOF (normalized to the amount of Ir in the sample) for Pt@**8** (red) and Pt@**10** (black). (d) Time-dependent hydrogen evolution curves of Pt@**8** (green), Pt@**10** (red), and homogeneous control $[Ir(ppy)_2(bpy)]Cl/K_2PtCl_4$ (blue and black for different Pt/Ir ratios) under optimized conditions (Pt/Ir ratios in solution/suspension for Pt@**8** and its homogeneous control is

86.0; Pt/Ir ratios in solution/suspension for Pt@**10** and its homogeneous control is 24.2; stirring rate for all reactions was 1000 rpm). (Reprinted with permission from ref [1]. Copyright American Chemical Society 2012)

PXRD patterns of Pt@**8** showed that the framework structure of **8** was retained upon the loading of Pt nanoparticles (Fig. 3.1e). On the other hand, peaks in the PXRD patterns of Pt@**10** gradually broadened with increasing Pt loadings, indicating significant structural distortion caused by the nanoparticles in the MOF channels (Fig. 3.1f). Peaks due to Pt nanoparticles at 39.7^{o} and 46.4^{o} also became more prominent in the PXRD patterns as the Pt loadings increased. Different structural impacts of Pt nanoparticles on **8** and **10** are consistent with the higher Pt loadings and larger MOF cavity/Pt particle sizes of Pt@**10** compared to those of Pt@**8**.

The *in situ* generated Pt@MOF assemblies were examined for their photocatalytic activities for hydrogen evolution using visible light (>420 nm). The $[Ir^{III}(ppy)_2(bpy^{\cdot-})]$ radicals generated by TEA-mediated photoreduction can transfer electrons to the Pt nanoparticles to reduce protons for hydrogen production. The amounts of hydrogen generated in the experiments were quantified by GC analysis of the headspace gas in the reactor using methane gas as the internal standard. The amount of K_2PtCl_4 added in the suspension was optimized for the Pt@MOFs to generate the largest amount of hydrogen in 6 hours. Under the optimized conditions, the Pt/Ir ratio in the MOF sample was determined by ICP-MS to be 18.6 and 17.8 for Pt@**8** and Pt@**10**, respectively. The highest hydrogen evolution turnover number (TON) for each MOF based on Ir phosphors (Ir-TON) in 6 hours is 730 and 1620 for Pt@**8** and Pt@**10**, respectively. The assembled Pt@MOFs can be recovered from the solution by centrifugation after the reaction and used again for hydrogen evolution in a fresh solution without adding additional K_2PtCl_4.

The Ir-TONs of the recovered catalysts are only slightly lower than those of the first run (Table 3.1). The catalysts could be recycled and re-used at least three times. ICP-MS analysis of the supernatant solution in the second reaction run of the recovered Pt@**10** sample showed only 2.0% of the Ir and 0.5% of the Pt leaching into the solution during the run. A control experiment without addition of the Ir-phosphor MOF or K_2PtCl_4 in the solution showed no hydrogen evolution under the same experimental conditions (Table 3.1, entry 9 and 12), although K_2PtCl_4 solution alone under UV light did exhibit very modest photocatalytic activity for hydrogen production (Table 3.1, entry 13). TEA was also proved to be a necessary sacrificial reductant in the reaction (Table 3.1, entry 10), and the absence of hydrogen in the headspace of the reaction in the dark confirmed the photocatalytic nature of the reaction (Table 3.1, entry 11).

Table 3.1 Pt@MOFs as photocatalyst for hydrogen evolution[a]

Entry	Catalyst	Ir-TON[b]	Pt-TON[c]
1	Pt@**8** (1st run)	730	39.2
2[d]	Pt@**8** (2nd run)	633	34.0
3	Pt@**8** (3rd run)	624	33.5
4	Pt@**8** (4th run)	740	39.8
5	Pt@**10** (1st run)	1620	90.9
6	Pt@**10** (2nd run)	1500	84.1
7	Pt@**10** (3rd run)	990	55.6
8	Pt@**10** (4th run)	1380	77.5
9[e]	**8**	0	N/A
10[f]	K_2PtCl_4+**8**	0	0
11[g]	K_2PtCl_4+**8**	0	0
12[h]	K_2PtCl_4	N/A	0
13[i]	K_2PtCl_4	N/A	4.3

[a] Hydrogen evolution reactions were carried out for 6 hours using a 450 W Xe-lamp with a 420 nm cut-off filter. [b] Ir-based turnover number (Ir-TON) is defined as $n(1/2H_2)/n(Ir)$. [c] Pt-based turnover number (Pt-TON) is defined as $n(1/2H_2)/n(Pt)$. [d]The solids were recovered from the reaction mixtures via centrifugation and added to 2 mL fresh THF/H_2O/TEA (20/1/1). The mixture was degassed before reuse tests without adding K_2PtCl_4. [e] without adding K_2PtCl_4. [f] without adding TEA. [g]in the dark. [h] without adding Ir-phosphor using 420 nm cut-off filter. [i] without adding Ir-phosphor using 300 nm cut-off filter.

To determine the total turnover number of the Pt@MOFs, time-dependent hydrogen

evolution experiments were carried out over 48 hours. As shown in Fig. 3.3d, Pt@**8** and Pt@**10** samples gave a total Ir-TON of 3400 and 7000, respectively. These Ir-TONs are 1.5 and 4.7 times the values afforded by the homogeneous controls **[**$Ir(ppy)_2(bpy)]Cl/K_2PtCl_4$ under their respective conditions (2200 and 1500, respectively). We believe that the enhanced photocatalytic hydrogen evolution activities of Pt@MOFs are due to more efficient electron transfer from the unstable $[Ir^{III}(ppy)_2(bpy^{\cdot-})]$ species to Pt nanoparticles which not only increased hydrogen reduction rates but also slowed down the decomposition of the Ir complexes.[33] ICP-MS of the supernatant solution of the Pt@**10**-catalyzed reaction after the 48 hour showed that 25.6% of the Ir leached into the solution, indicating the decomposition of the Ir-complex during the 48 h reaction. The photochemical quantum yield of the Pt@**10**-catalyzed reaction driven with 440 nm light was determined to be $(5.6\pm0.4)\times10^{-4}$, much higher than that of the homogeneous control $[(3.0\pm0.4)\times10^{-4}]$.

3.3 Conclusion

In summary, we have successfully loaded Pt nanoparticles into the cavities of two stable, porous, phosphorescent UiO MOFs built from Ir-phosphor-derived linear dicarboxylate linkers and $Zr_6(\mu_3\text{-}O)_4(\mu_3\text{-}OH)_4(carboxylate)_{12}$ SBUs. The Pt@MOF assemblies serve as highly efficient photocatalysts for hydrogen evolution with both higher turnover frequencies and higher turnover numbers than the homogeneous analogues, as a result of facile electron transfer from the photo-reduced Ir phosphor to the entrapped Pt nanoparticles. This work highlights the opportunity to use MOFs as a versatile and tunable platform to hierarchically integrate different functional components for solar energy utilization.

References

(1) Wang, C.; deKrafft, K. E.; Lin, W. *J. Am. Chem. Soc.* **2012**, *134*, 7211.

(2) Song, F.; Wang, C.; Falkowski, J. M.; Ma, L.; Lin, W. *J. Am. Chem. Soc.* **2010**, *132*, 15390.

(3) Horike, S.; Dincă, M.; Tamaki, K.; Long, J. R. *J. Am. Chem. Soc.* **2008**, *130*, 5854.

(4) Wu, C.-D.; Lin, W. *Angew. Chem. Int. Ed. Engl.* **2005**, *44*, 1958.

(5) Tanabe, K. K.; Cohen, S. M. *Chem. Soc. Rev.* **2011**, *40*, 498.

(6) Song, J.; Luo, Z.; Britt, D. K.; Furukawa, H.; Yaghi, O. M.; Hardcastle, K. I.; Hill, C. L. *J. Am. Chem. Soc.* **2011**, *133*, 16839.

(7) Meilikhov, M.; Yusenko, K.; Esken, D.; Turner, S.; Van Tendeloo, G.; Fischer, R. A. *Eur. J. Inorg. Chem.* **2010**, *2010*, 3701.

(8) Jiang, H. L.; Xu, Q. *Chem. Commun.* **2011**, *47*, 3351.

(9) Hermes, S.; Schröter, M.-K.; Schmid, R.; Khodeir, L.; Muhler, M.; Tissler, A.; Fischer, R. W.; Fischer, R. A. *Angew. Chem. Int. Ed. Engl.* **2005**, *44*, 6237.

(10) Proch, S.; Herrmannsdörfer, J.; Kempe, R.; Kern, C.; Jess, A.; Seyfarth, L.; Senker, J. *Chem.– Euro. J.* **2008**, *14*, 8204.

(11) Müller, M.; Hermes, S.; Kähler, K.; van den Berg, M. W. E.; Muhler, M.; Fischer, R. A. *Chem.Mater.* **2008**, *20*, 4576.

(12) Sabo, M.; Henschel, A.; Frode, H.; Klemm, E.; Kaskel, S. *Chem.Mater.* **2007**, *17*, 3827.

(13) Yuan, B.; Pan, Y.; Li, Y.; Yin, B.; Jiang, H. *Angew. Chem. Int. Ed. Engl.* **2010**, *49*, 4054.

(14) Jiang, H. L.; Akita, T.; Ishida, T.; Haruta, M.; Xu, Q. *J. Am. Chem. Soc.* **2011**, *133*, 1304.

(15) Gu, X. J.; Lu, Z. H.; Jiang, H. L.; Akita, T.; Xu, Q. *J. Am. Chem. Soc.* **2011**, *133*, 11822.

(16) Moon, H. R.; Kim, J. H.; Suh, M. P. *Angew. Chem. Int. Ed. Engl.* **2005**, *44*, 1261.

(17) Suh, M. P.; Moon, H. R.; Lee, E. Y.; Jang, S. Y. *J. Am. Chem. Soc.* **2006**, *128*, 4710.

(18) Ishida, T.; Nagaoka, M.; Akita, T.; Haruta, M. *Chem.– Euro. J.* **2008**, *14*, 8456.

(19) Jiang, H.-L.; Liu, B.; Akita, T.; Haruta, M.; Sakurai, H.; Xu, Q. *J. Am. Chem. Soc.* **2009**, *131*, 11302.

(20) El-Shall, M. S.; Abdelsayed, V.; Khder, A. E. R. S.; Hassan, H. M. A.; El-Kaderi, H. M.; Reich, T. E. *J. Mater. Chem.* **2009**, *19*, 7625.

(21) Song, F. J.; Wang, C.; Lin, W. B. *Chem. Commun.* **2011**, *47*, 8256.

(22) Wang, C.; Xie, Z. G.; deKrafft, K. E.; Lin, W. L. *J. Am. Chem. Soc.* **2011**, *133*, 13445.

(23) Kent, C. A.; Mehl, B. P.; Ma, L.; Papanikolas, J. M.; Meyer, T. J.; Lin, W. *J. Am. Chem. Soc.* **2010**, *132*, 12767.

(24) Kent, C. A.; Liu, D.; Ma, L.; Papanikolas, J. M.; Meyer, T. J.; Lin, W. *J. Am. Chem. Soc.* **2011**, *133*, 12940.

(25) Esswein, M. J.; Nocera, D. G. *Chem. Rev.* **2007**, *107*, 4022.

(26) Dubois, M. R.; Dubois, D. L. *Acc. Chem. Res.* **2009**, *42*, 1974.

(27) Hammarström, L.; Hammes-Schiffer, S. . *Acc. Chem. Res.* **2009**, *42*, 1859.

(28) Youngblood, W. J.; Lee, S. H.; Maeda, K.; Mallouk, T. E. *Acc. Chem. Res.* **2009**, *42*, 1966.

(29) Goldsmith, J. I.; Hudson, W. R.; Lowry, M. S.; Anderson, T. H.; Bernhard, S. *J. Am. Chem. Soc.* **2005**, *127*, 7502.

(30) Tinker, L. L.; McDaniel, N. D.; Curtin, P. N.; Smith, C. K.; Ireland, M. J.; Bernhard, S. *Chem.– Euro. J.* **2007**, *13*, 8726.

(31) Curtin, P. N.; Tinker, L. L.; Burgess, C. M.; Cline, E. D.; Bernhard, S. *Inorg. Chem.* **2009**, *48*, 10498.

(32) Metz, S.; Bernhard, S. *Chem. Commun.* **2010**, *46*, 7551.

(33) DiSalle, B. F.; Bernhard, S. *J. Am. Chem. Soc.* **2011**, *133*, 11819.

(34) Cavka, J. H.; Jakobsen, S.; Olsbye, U.; Guillou, N.; Lamberti, C.; Bordiga, S.; Lillerud, K. P. *J. Am. Chem. Soc.* **2008**, *130*, 13850.

(35) Gomes Silva, C.; Luz, I.; Llabrés i Xamena, F. X.; Corma, A.; García, H. *Chem.– Euro. J.* **2010**, *16*, 11133.

(36) Kandiah, M.; Nilsen, M. H.; Usseglio, S.; Jakobsen, S.; Olsbye, U.; Tilset, M.; Larabi, C.; Quadrelli, E. A.; Bonino, F.; Lillerud, K. P. *Chem. Mate.* **2010**, *22*, 6632.

(37) Schaate, A.; Roy, P.; Godt, A.; Lippke, J.; Waltz, F.; Wiebcke, M.; Behrens, P. *Chem.– Euro. J.* **2011**, *17*, 6643.

(38) Schaate, A.; Roy, P.; Preuße, T.; Lohmeier, S. J.; Godt, A.; Behrens, P. *Chem.– Euro. J.* **2011**, *17*, 9320.

(39) Kim, M.; Cohen, S. M. *CrystEngComm* **2012**.

(40) As a result of small crystal size, X-ray diffraction data collection only leads to a dataset with the resolution of 2.1 Å.

(41) As trifluoacetic acid was added in the crystal growth step, the chloride counter ion on the $\mathbf{L_8}$ ligand was replaced by trifluoacetate as revealed by ^{19}F-NMR.

(42) The complete formula is $[Zr_6(\mu_3\text{-}O)_4(\mu_3\text{-}OH)_4(IrC_{46}H_{32}O_4N_4)6(O_2CCF_3)_6\bullet 64DMF]$

(43) Ferey, G.; Serre, C. *Chem. Soc. Rev.* **2009**, *38*, 1380.

(44) Chen, J.; Herricks, T.; Geissler, M.; Xia, Y. *J. Am. Chem. Soc.* **2004**, *126*, 10854.

(45) Sun, Y.; Xia, Y. *Science* **2002**, *298*, 2176.

Chapter 4

Diffusion-Controlled Luminescence Quenching in Metal-Organic Frameworks[1]

4.1 Introduction to the study of diffusion in MOFs

In many of the potential applications of MOFs such as liquid phase separation,[2,3] chemical sensing,[4-7] and particularly selective catalysis of various organic transformations,[8-12] mass transport properties of MOFs play a dominant role on their performances. Diffusion coefficient (or diffusivity) of MOFs, a key parameter characterizing the transport process, is thus an important physical quantity to be determined.

Guest molecule diffusivity in MOFs was first computationally studied using molecular dynamics (MD) simulations. Sarkisov et al. first reported theoretical predictions of self-diffusion coefficient D_s of several alkanes in MOF-**5**.[13] Sholl, Johnson, Schmid, and others also examined self-diffusion coefficient D_s and transport diffusion coefficient D_t of simple alkanes, hydrogen, carbon dioxide, benzene and other small molecules in several MOFs including the IRMOF series and HKUST-**1**.[14-18]

In contrast to a wealth of literature on simulation efforts, there are only a few published experimental studies of measuring diffusivity in MOFs. Stallmach et al. first reported self-diffusivity of hydrocarbons in MOF-**5**,[19] and more recently in HKUST-**1**,[20] using the pulsed-field gradient (PFG) NMR technique. Jobic and Maurin used quasi-elastic neutron scattering (QUENS) method to study self-diffusion of H_2, CO_2, and alkanes in MIL-47(V) and MIL-53(Cr).[21-24] In another direction, Kärger and coworkers

used interference microscopy[25] and infrared microscopy[26] to study transport diffusion of methanol into vacuum-activated manganese formate and alkanes into vacuum-activated HKUST-**1**, respectively. Quartz crystal microbalance (QCM) measurement of thin films was also employed by Zybaylo et al. to estimate the diffusivity of pyridine in vacuum-activated HKUST-**1**.[27]

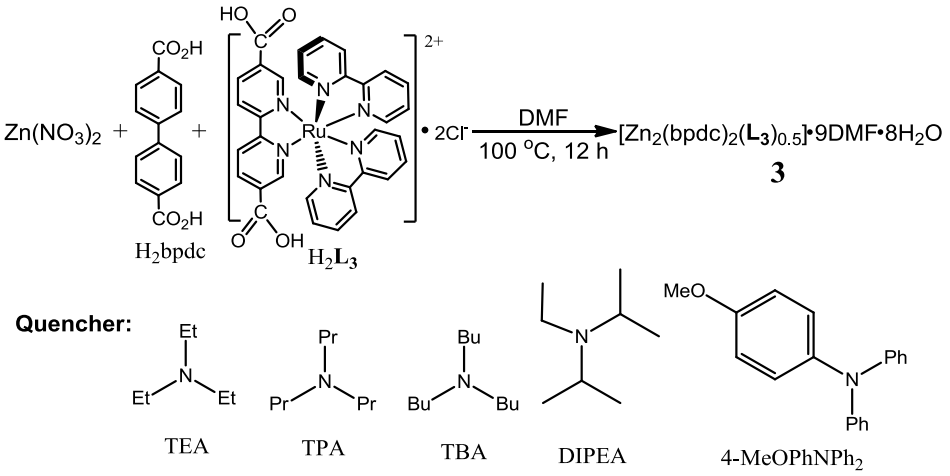

Scheme 4.1 Synthesis of phosphorescent **3** and chemical structures of amine quenchers of varying sizes. (Reprinted with permission from ref [1]. Copyright American Chemical Society 2011)

These measurements provide invaluable information for the applications of MOFs in gas phase adsorption and separation. However, many of interesting applications of MOFs, such as heterogeneous catalysis, involve liquid suspensions of MOFs. In these cases, diffusion occurs when MOF channels are already filled with solvent molecules. The realistic physical picture involves continuous exchange of diffusant molecules (*e.g.* substrate or product molecules in MOF catalysis) with solvent molecules during their transport through MOF channels, instead of self-diffusion or transport diffusion into vacuum-activated MOFs. This kind of diffusion process is expected to be much slower than self-diffusion or transport diffusion. There were two studies on molecular diffusion

into solvent-filled MOF channels,[28,29] but quantitative diffusivities could not be determined in these experiments.

In our exploration of photoactive MOFs, we encountered an interesting diffusion-controlled quenching phenomenon, in which amine quenchers in solution diffuse into MOF channels and gradually quench the MOF emission from the $Ru(bpy)_3^{2+}$ derived bridging ligand via a redox quenching mechanism.[30] We proposed that such time-dependent luminescence quenching behaviors can be utilized to model the diffusion processes of different quenchers in MOFs in solution. In a related study, diffusion coefficients of fluorescein in lysozyme crystals were obtained by modeling the fluorescence intensities determined by confocal laser scanning microscopy.[31]

4.2 Diffusion-Controlled Luminescence Quenching

The phosphorescent MOF (**3**) used in this study contains a $Ru(bpy)_3^{2+}$ derivative $H_2\mathbf{L_3}$, which was synthesized as described in Chapter 2 (Scheme 4.1). The detailed description of crystal structure can be found in Chapter 2

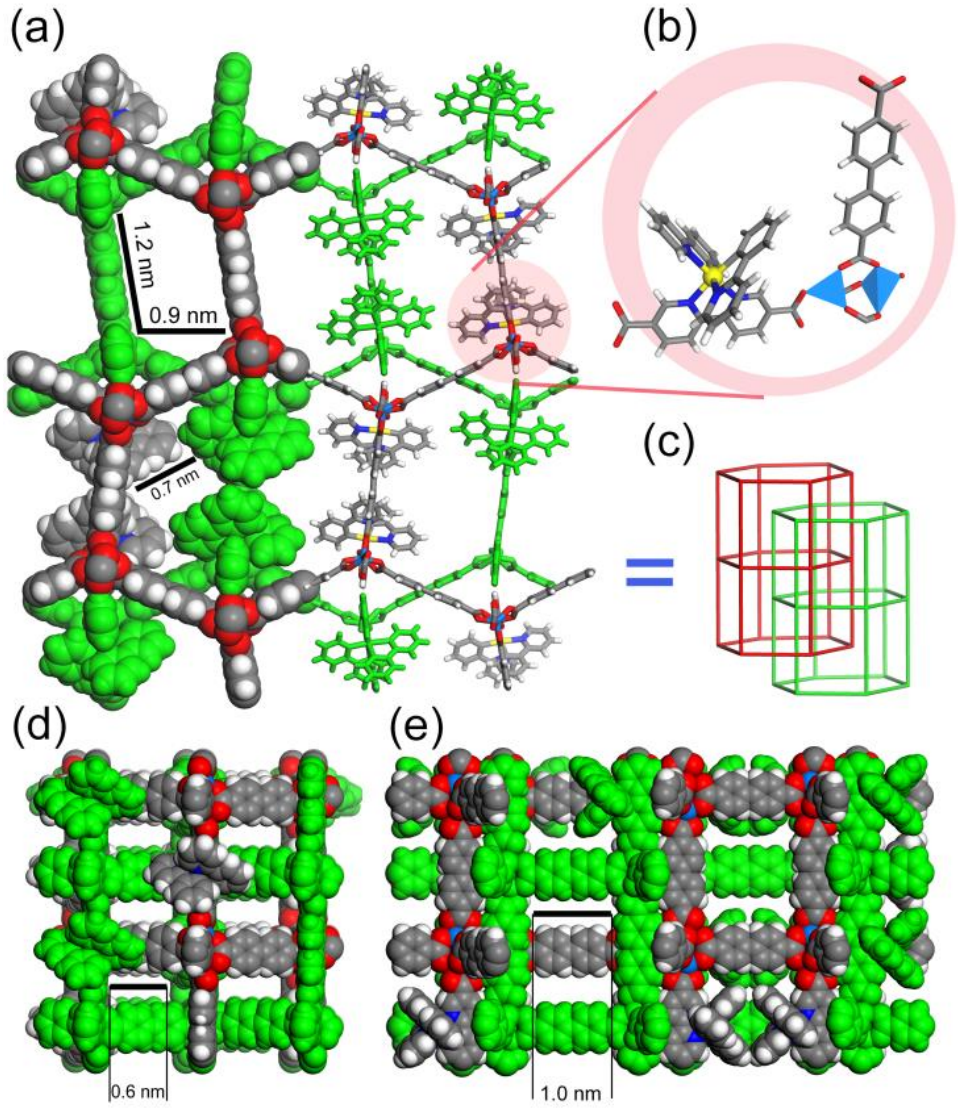

Figure 4.1 Structure model of **3**. (a) Space-filling and stick model viewed along the [001] direction, showing different channel sizes due to different local distributions of $\mathbf{L_3}$ ligands. (b) Building blocks of **3**. (c) Schematic showing 2-fold interpenetrating frameworks of the **bnn** topology. (d) Space-filling model viewed along the [100] direction. (e) Space-filling model viewed along the [010] direction. (Reprinted with permission from ref [1]. Copyright American Chemical Society 2011)

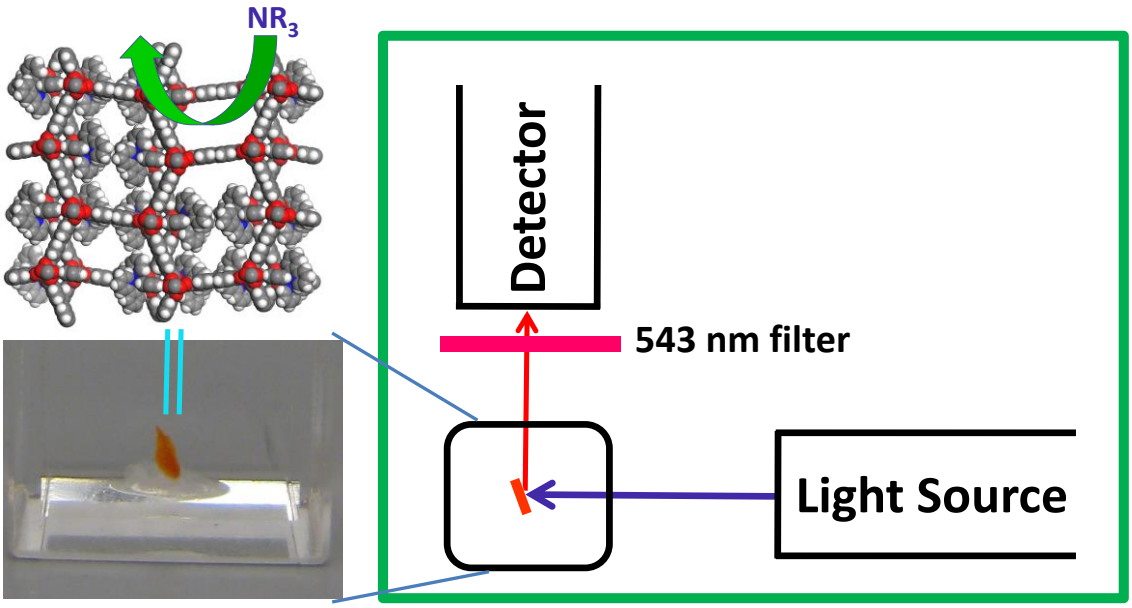

Scheme 4.2 Schematic of the experimental set-up used for luminescence quenching measurements. (Reprinted with permission from ref [1]. Copyright American Chemical Society 2011)

Luminescence quenching experiments were performed on plate-like single crystals of **3** affixed to the bottom of a quartz fluorescent cuvette, with their faces perpendicular to the cuvette bottom and immersed in cyclohexane (Scheme 4.2). The original DMF/H_2O solvent molecules inside the channels of **3** were first exchanged with CH_2Cl_2 and then with cyclohexane. The O_2 molecules inside the channels were removed by keeping the crystal in degassed cyclohexane overnight. The thicknesses of plate-like crystals of **3** were measured using a microscope with a built-in ruler. In the quenching experiment, a **3** crystal was excited at a wavelength of 452 nm and the emission intensity at 627 nm was recorded at different time points after the addition of a pre-determined amount of amine quenchers. The amines or solutions of amines were fully degassed before use. Structures of the amines are shown in Scheme 4.1. Excitation light was blocked from impinging on the crystal during the intervals between different emission measurements to avoid

photodecomposition of the amine and other irreversible photochemical processes. A typical emission measurement took about 2 to 3 seconds, during which time the crystal and quenchers were exposed to light. The average value of the emission signals was recorded, and the experimental error for each time point was estimated from the signal fluctuations within the 2 to 3 seconds. Spectra of the crystals were taken before and after the quenching studies to ensure that no substantial spectra change has occurred.

The time-dependent intensity $I(t)$ was normalized against the equilibrium intensity after a long time $I(\infty)$. A plot of $u(t)=[I(t)-I(\infty)]/I(\infty)$ vs. time is shown in Figure 4.2a. Exponential decay of the emission intensities over time to 80 to 85% of their initial values were observed in solutions of 0.433 M triethylamine (TEA), tripropylamine (TPA), tributylamine (TBA) and 0.024 M 4-methoxylphenyldiphenylamine (4-MeOPhNPh$_2$), as a result of diffusion-controlled luminescence quenching of **3** by these amines. The amount of time required for the emission to reach equilibrium after adding TEA, TPA, TBA, and 4-MeOPhNPh$_2$ is approximately 10 min, 30 min, 30 min and 120 min, respectively. This order of increase in time required to reach equilibrium correlates well with the sizes of these amines.

For diisopropylethylamine (DIPEA) quenching, however, the intensity dropped instantaneously to 96% of its original value and remained unchanged after that. This behavior is likely a result of surface quenching only, suggesting that DIPEA cannot enter the MOF channels. To confirm this, we investigated the reverse process of amine diffusing out of the MOF channels. Crystals fully soaked in amine solutions were put back into freshly degassed cyclohexane under N_2 protection, and the changes in emission intensities were monitored. An increase of signal over time was observed for TPA- and 4-

MeOPhNPh$_2$-treated MOFs, indicating the release of absorbed quenchers (Figure 4.3). In contrast, for the MOFs soaked in DIPEA, no signal increase was detected. This result supports the notion that no DIPEA can enter in MOF channels, presumably owing to its large size. Further evidence comes from GC analysis of the absorbed amine in the MOF channels. Amine-treated **3** released substantial amounts of TPA, TBA, and 4-MeOPhNPh$_2$, but no DIPEA (Table 4.1). These results unambiguously prove the accessibility of the MOF channels to all the amines except DIPEA.

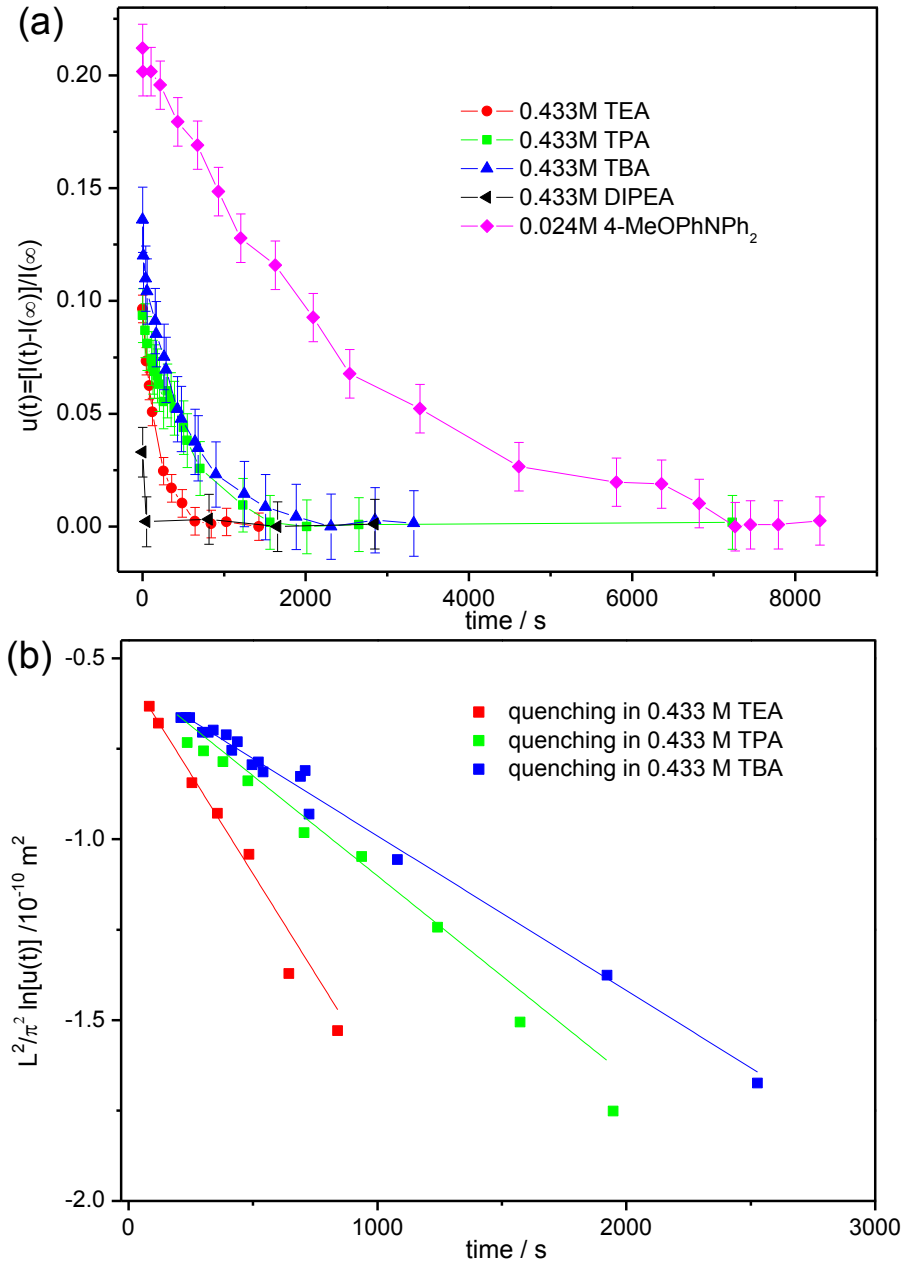

Figure 4.2 (a) Plots of $u(t)=[I(t)-I(\infty)]/I(\infty)$ vs t for different amine quenchers: TEA (red), TPA (green), TBA (blue), DIPEA (black), and 4-MeOPhNPh$_2$ (purple) (see supporting information for more detailed plots). (b) Linear fitting of $(L^2/\pi^2)\text{Ln}[u(t)]$ vs. t of TEA (red), TPA (green), and TBA (blue). Only the data points of t > 100 s for TEA

and t > 200s for TPA and TBA were used in these fits. (Reprinted with permission from ref [1]. Copyright American Chemical Society 2011)

Geometry-optimized structure of 4-MeOPhNPh$_2$ is much larger than that of DIPEA, so their different uptake behaviors by **3** cannot be explained simply based on their sizes. Instead, we believe that different uptake behaviors of the two amines stem from their disparate affinities towards the MOF channels. 4-MeOPhNPh$_2$, as an aromatic amine, can strongly interact with the MOF channel wall via π-π interactions, whereas aliphatic chains of DIPEA do not provide such a driving force for inclusion. PXRD patterns of amine-treated crystals of **3** were taken to provide insights into these different uptake behaviors. While the PXRD patterns of all the aliphatic amine-treated MOFs closely resemble that of the as-synthesized **3**, the pattern of 4-MeOPhNPh$_2$–treated MOF crystals lose all of the diffraction peaks due to **3** (Figure 4.4). The severe framework structure distortion of 4-MeOPhNPh$_2$–treated **3** suggests that 4-MeOPhNPh$_2$ enters the MOF by intercalating into the framework via π-π interactions instead of simple Fickian diffusion.

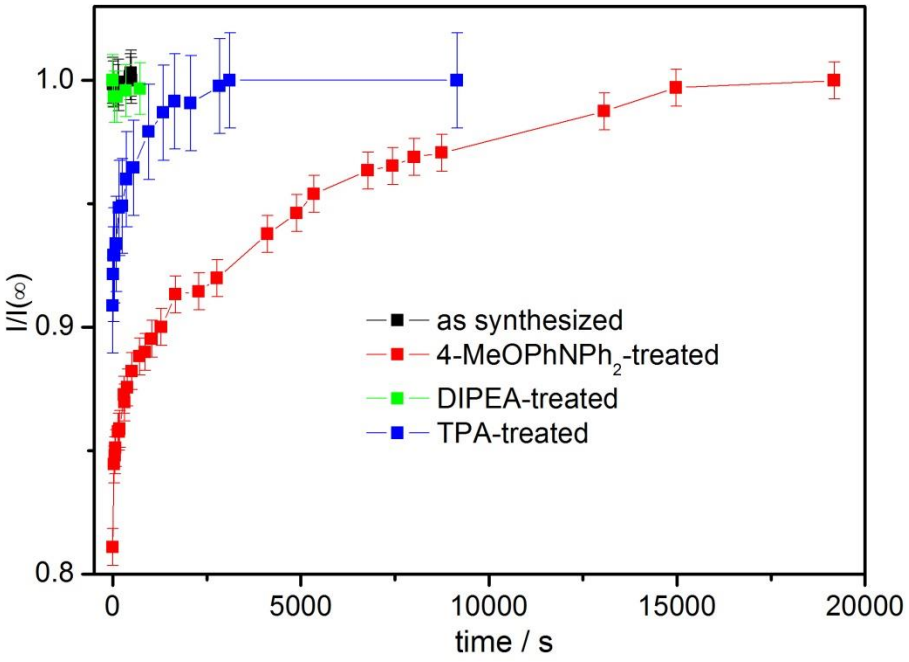

Figure 4.3 Quencher release experiment for **3** after being soaked in solutions of TPA (blue), DIPEA (green), 4-MeOPhNPh$_2$ (red) and as synthesized (black). The crystals were excited at a wavelength of 452 nm, and the emission signal is detected at the wavelength of 627 nm. (Reprinted with permission from ref [1]. Copyright American Chemical Society 2011)

Table 4.1 Determination of the amount of amine in MOF channels

Amine Symbol	Amine Concentration in solution (M)	Amount of amine detected by GC (nmol)	Amount of Zn detected by ICP-MS (nmol)	Number of absorbed amine molecules per unit-cell	Effective concentration of amine inside MOF channels (M)
TPA	0.433	166	516	5.15	0.657
TBA	0.433	268	487	8.81	1.12
DIPEA	0.433	0	267	0	0
4-MeOPhNPh$_2$	0.024	47	937	0.80	0.102

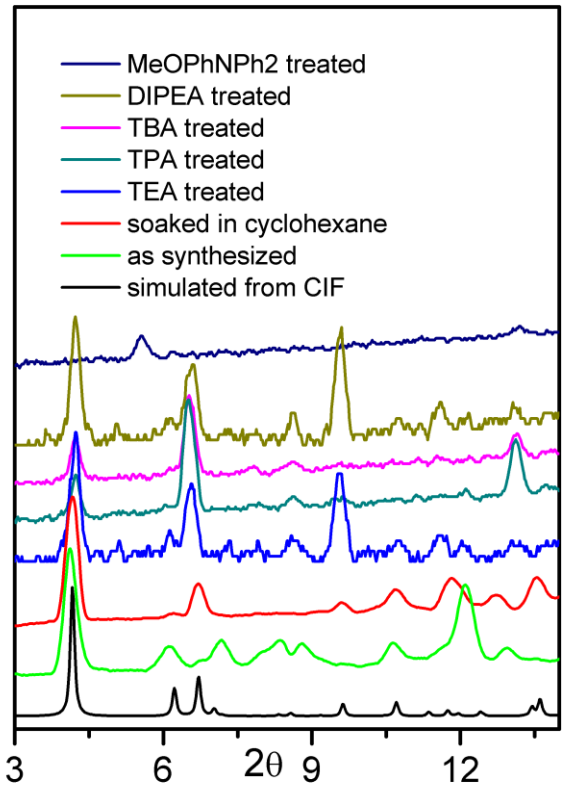

Figure 4.4 PXRD patters of **3** as synthesized (green), and after being soaked in pure cyclohexane (red), in solutions of TEA (blue), TPA (green), TBA (purple), DIPEA (yellow), 4-MeOPhNPh$_2$ (dark blue). (Reprinted with permission from ref [1]. Copyright American Chemical Society 2011)

We quantitatively analyze the diffusion of TEA, TPA and TBA in the frame of Fickian diffusion. In other words, we assume a constant diffusivity, D, independent of local concentration of amine quenchers. By taking advantage of thin plate morphology of the MOF crystals, we further simplify the diffusion process into a one-dimensional diffusion described by Fick's Second Law (Eq. 4.1) with the boundary conditions and initial conditions expressed in Eq. 4.2 and Eq. 4.3, respectively:

$$\begin{cases} \frac{\partial c(x,t)}{\partial t} = D\frac{\partial^2 c(x,t)}{\partial x^2} & \text{(Eq.4.1)} \\ c(0,t) = c(L,t) = c_0 & \text{(Eq.4.2)} \end{cases}$$

$$c(x,0) = 0 \ \ (0 < x < L) \qquad \text{(Eq.4.3)}$$

For the emission quenching, we assume a rapid, reversible quenching behavior that can be described by the Stern-Volmer equation. In addition, activity correction for amine concentration inside MOF channels, the sample dependent crystal geometry and position factor, and the contribution from surface emission have also been considered. Using this model, the time-dependent normalized emission intensity was derived (see section 4.3), and can be expressed with Eq. 4.4:

$$u(t) \approx Ae^{-\pi^2 Dt/L^2} \qquad \text{(Eq.4.4)}$$

where A is a term independent of time t and is expressed by $A = \frac{1}{1+\delta} \times \frac{4\alpha\beta c_0}{1+\alpha\beta c_0} \times \frac{\frac{\in L}{cos\theta}}{(\frac{\in L}{cos\theta})^2+\pi^2}$ (β, α, ∈, θ, and δ are introduced to account for Stern-Volmer quenching, activity correction, crystal absorption, crystal positioning, and surface emission, respectively, section 4.3); L is thickness of the crystal; and D is the Fickian diffusivity.

Plots of $(L^2/\pi^2)\text{Ln}[u(t)]$ vs. t gave straight lines (Figure 4.2b), indicating the validity of the Fickian diffusion model as described by Eq 4.4. Diffusivities of TEA, TPA, and TBA in **3** could be obtained from the slopes of these linear fits, and were determined to be $(1.1\pm0.2)\times10^{-13}$, $(4.8\pm1.2)\times10^{-14}$, and $(4.0\pm0.4)\times10^{-14}$ m^2/s, respectively. These values are one to two orders of magnitude smaller than the transport diffusivity reported for methanol into vacuum-activated porous manganese formate crystals,[25] a system that has a similar diffusant/channel size ratio as our present case. This discrepancy is expected since the two diffusion processes are of very different nature. The diffusivity derived in our present study is much more relevant to many applications that involve liquid suspensions of MOFs.

4.3. Detailed derivation of diffusivity equations and related approximations

List of symbols used in this section

I_0 : emission of the crystal in the absence of quenchers

i_0 : the excitation light density

I(t) : detected emission as a function of time

I(∞) : equilibrium emission intensity after adding quenchers for a long time

u(t) : normalized emission intensity $u(t) = \frac{I(t)-I(\infty)}{I(\infty)}$

D : diffusivity within the crystals,

c_0 : the concentration of a diffusant in the bulk solution surrounding the crystal

L : the thickness of the crystal

β : activity coefficient correction for quencher concentration within the MOF channels

$\emptyset_0$: quantum yield of MOF in the absence of quencher

∈ : absorption parameter of MOF. $\in = 2.303\ \varepsilon n$. ε is the extinction coefficient, while n is the effective dye concentration in MOFs.

δ : fraction of surface emission contribution to total emission of the crystal

θ : tilting angle of the crystal with respect to the direction of excitation light

γ : crystal geometry and position coefficient

α : Stern-Volmer constant for the particular quencher in cyclohexane

Scheme 4.3

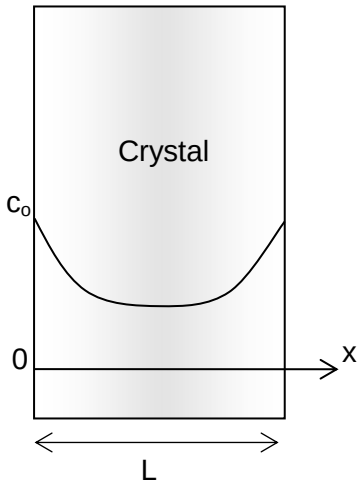

4.3.1 Diffusion model

We plan to construct a working model for TEA, TPA and TBA diffusion inside **3** in the frame of Fickian diffusion. The diffusion process for 4-MeOPhNPh$_2$ is more complicated than simple Fickian diffusion,[32] and is not included in this analysis. For molecules to diffuse into plate-like MOF crystals, the problem is simplified to one-dimensional diffusion by ignoring contributions from the other two longer dimensions.

As shown in scheme 4.3, during the process of diffusion, the local concentration of a diffusant within the MOF crystal at a given time t is different for different position x in the crystal. We can then represent the diffusant concentration as a function of both time and position c(x,t). This one dimensional diffusion problem can then be described by Fick's Second Law of diffusion, combined with the boundary conditions and initial conditions as follows.

$$\begin{cases} \frac{\partial c(x,t)}{\partial t} = D\frac{\partial^2 c(x,t)}{\partial x^2} & \text{(eq.4.1)} \\ c(0,t) = c(L,t) = c_0 & \text{(eq.4.2)} \\ c(x,0) = 0 \ \ (0 < x < L) & \text{(eq.4.3)} \end{cases}$$

D is the diffusivity within the crystals,

c_0 is the concentration of a diffusant in the bulk solution surrounding the crystal

L is the thickness of the crystal

A solution to this differential equation is

$$c(x,t) = c_0\left(1 - \frac{4}{\pi}\sum_{n=0}^{\infty}\frac{1}{2n+1}e^{-\pi^2(2n+1)^2Dt/L^2}\sin\frac{(2n+1)\pi x}{L}\right) \qquad \text{(eq.4.5)}$$

This is the standard mathematical solution of the diffusion equation in a plane sheet with uniform initial distribution.

It is easy to see that $c(x,\infty) = c_0$, which simply means that after waiting for infinite amount of time, the diffusant concentration all through the MOF crystal will be equal to the concentration in the bulk solution. In the above equation, we totally ignored the fact that interactions between the particular diffusant molecules and MOF channels may cause the equilibrium to favor or disfavor molecules entering MOFs, leading to different effective equilibrium diffusant concentration within MOFs from that in the outside solution. As a first order correction to this error, we can introduce a diffusant dependent parameter β to represent the correction to equilibrium diffusant concentration in MOFs. (This correction is equivalent to using activity to replace concentration. The β parameter corresponds to activity coefficient.)

We hereby reformulate c(x,t) as

$$c(x,t) = \beta c_0\left(1 - \frac{4}{\pi}\sum_{n=0}^{\infty}\frac{1}{2n+1}e^{-\pi^2(2n+1)^2 Dt/L^2}\sin\frac{(2n+1)\pi x}{L}\right) \qquad \text{(eq.4.6)}$$

4.3.2 Model for the phosphorescence from a single crystal

The first thing to notice is that the light is not evenly distributed through the whole crystal. The light intensity is attenuated when penetrating through the MOF crystal according to Lambert-Beer's Law. The simplest situation is that the incoming light is perpedicular to the surface of the crystal like in scheme 4.4.

Scheme 4.4

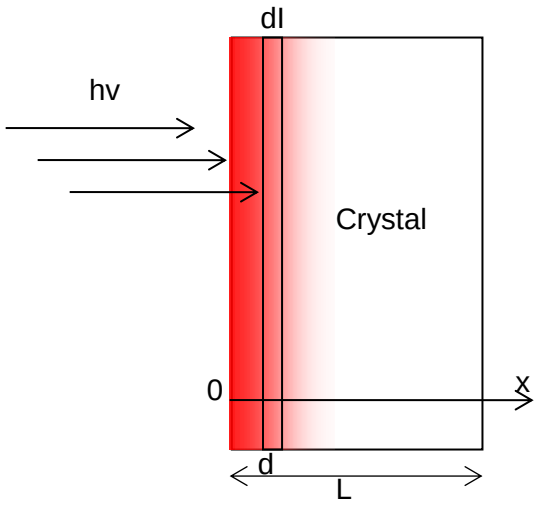

Sectioning the plate-like crystal to several slices parallel to the plate surface and considering the emission from each slice with the width of dx, the emission from this slice in the absence of quencher should be proportional to the local light intensity.

$dI_0 = \emptyset_0 i_0 e^{-\epsilon x} dx$ (eq.4.7)

i_0 is the incoming light density

$\emptyset_0$ is the quantum yield of MOF in the absence of quencher

The term $e^{-\epsilon x}$ accounts for Larmbert-Beer's Law. $\epsilon = 2.303\,\varepsilon n$. ε is the extinction coefficient, while n is the effective dye concentration in MOFs.

So the emission intensity without quenchers is:

$I_0 = \int dI_0 = \int_0^L \emptyset_0 i_0 e^{-\epsilon x} dx = \emptyset_0 i_0 \frac{1-e^{-\epsilon L}}{\epsilon}$ (eq.4.8)

When quenchers inside the MOFs are considered,

emission from each MOF slice is dynamically quenched according to Stern-Volmer equation

$\frac{dI_0}{dI} = 1 + \alpha c(x,t)$ (eq.4.9)

α is Stern-Volmer constant for the particular quencher.

So $I(t) = \int dI = \int \frac{dI_0}{1+\alpha c(x,t)} =$

$\emptyset_0 i_0 \int_0^L \frac{e^{-\epsilon x} dx}{1+\alpha c(x,t)}$ (eq.4.10)

$I(\infty) = \emptyset_0 i_0 \frac{1-e^{-\epsilon L}}{\epsilon} \times \frac{1}{1+\alpha\beta c_0}$

(eq.4.11)

Scheme 4.5

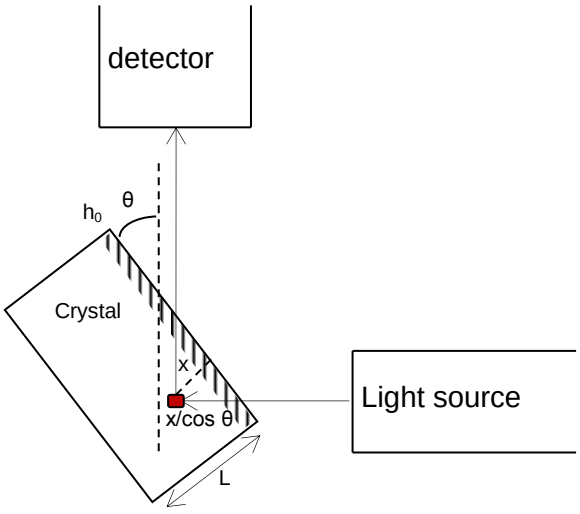

However, the crystal cannot be placed precisely in the perpendicular position to the incoming light, as shown in Scheme 4.5. To

correct this effect, ∈ in the above expressions (eq.4.8 to eq.4.11) should be replaced by $\in/cos\theta$.

Another factor to take into account is that not all the emission light can be detected by the detector. The amount of detectable emission is sensitive to the exact position and geometry of the specific single crystal. Thus, a crystal dependent common coefficient γ should be formulated into the expressions.

In addition, quenching of dye molecules near the surface of MOFs can account for a significant amount of detected emission, when considering the fact that the slices near the surface of the MOF crystal contribute more to the detected emission I_0 because incoming light will attenuate while penetrating deeper into the bulk crystal. Assuming that surface quenching occurs immediately after adding the quencher, and the surface emission accounts for δ fraction of total emission of the crystal. The intensities can then be expressed as the sum of two terms from the surface and the bulk crystals.

With these considerations, the expressions for emission intensities are modified to:

$$I_0 = (1+\delta)\gamma\emptyset_0 i_0 \frac{(1-e^{-\in L/cos\theta})cos\theta}{\in} \quad \text{(eq.4.12)}$$

$$I(t) = \delta\gamma\emptyset_0 i_0 \frac{(1-e^{-\in L/cos\theta})cos\theta}{\in} \times \frac{1}{1+\alpha\beta c_0} + \gamma\emptyset_0 i_0 \int_0^L \frac{e^{-\frac{\in}{cos\theta}x}dx}{1+\alpha c(x,t)} \quad \text{(eq.4.13)}$$

$$I(\infty) = (1+\delta)\gamma\emptyset_0 i_0 \frac{(1-e^{-\in L/cos\theta})cos\theta}{\in} \times \frac{1}{1+\alpha\beta c_0} \quad \text{(eq.4.14)}$$

Because of the possibility of slightly moving the cell when adding a quencher and unpredictable issues related to surface quenching, it is much more reliable to use intensity at infinite time ($I(\infty)$) to normalize the data than using intensity ratio of I/I_0.

The I_0 value is still useful to evaluate the magnitude of the Stern-Volmer constant of the specific quencher in cyclohexane α ,times β, both of which are basically unknown.

$$\alpha\beta c_0 \sim \frac{I_0}{I(\infty)} - 1 \qquad \text{(eq.4.15)}$$

As shown below, from the experimental data, the value of $\alpha\beta c_0$is less than 0.1 for TEA, TPA and TBA diffusion. This piece of information is very useful to simplify the above equations.

Define the observable as $u(t) = \frac{I(t)-I(\infty)}{I(\infty)} \approx \frac{\in}{cos\theta}\frac{(1+\alpha\beta c_0)}{1+\delta}\int_0^L \frac{e^{-\in x/cos\theta}dx}{1+\alpha c(x,t)} - \frac{1}{1+\delta}$ (eq.4.16)

(as $e^{-\in L/cos\theta} \approx 0$)

As a first-order approximation,

$$u(t) = \frac{I(t)-I(\infty)}{I(\infty)} \approx \frac{\in}{cos\theta}\frac{(1+\alpha\beta c_0)}{1+\delta}\int_0^L \frac{e^{-\in x/cos\theta}dx}{1+\alpha c(x,t)} - \frac{1}{1+\delta} =$$

$$\frac{\in}{cos\theta}\frac{(1+\alpha\beta c_0)}{1+\delta}\int_0^L \frac{e^{-\in x/cos\theta}dx}{1+\alpha\beta c_0(1-\frac{4}{\pi}\sum_{n=0}^{\infty}\frac{1}{2n+1}e^{-\pi^2(2n+1)^2Dt/L^2}\sin\frac{(2n+1)\pi x}{L})} - \frac{1}{1+\delta} =$$

$$\frac{\in}{cos\theta}\frac{1}{1+\delta}\int_0^L \frac{e^{-\in x/cos\theta}dx}{1-\frac{\alpha\beta c_0}{1+\alpha\beta c_0}\frac{4}{\pi}\sum_{n=0}^{\infty}\frac{1}{2n+1}e^{-\pi^2(2n+1)^2Dt/L^2}\sin\frac{(2n+1)\pi x}{L}} - \frac{1}{1+\delta} \approx \frac{\in}{cos\theta}\frac{1}{1+\delta}\int_0^L(1 +$$

$$\frac{\alpha\beta c_0}{1+\alpha\beta c_0}\frac{4}{\pi}\sum_{n=0}^{\infty}\frac{1}{2n+1}e^{-\pi^2(2n+1)^2Dt/L^2}\sin\frac{(2n+1)\pi x}{L})\, e^{-\in x/cos\theta}dx - \frac{1}{1+\delta} \approx \frac{1}{1+\delta} \times \frac{\alpha\beta c_0}{1+\alpha\beta c_0} \times$$

$$\frac{4}{\pi}\sum_{n=0}^{\infty}\frac{1}{2n+1}e^{-\pi^2(2n+1)^2Dt/L^2}\int_0^L \sin\frac{(2n+1)\pi x}{L}\frac{\in}{cos\theta}e^{-\in x/cos\theta}dx =$$

$$\frac{1}{1+\delta} \times \frac{4\alpha\beta c_0}{1+\alpha\beta c_0}\sum_{n=0}^{\infty} e^{-\pi^2(2n+1)^2Dt/L^2}\frac{\frac{\in L}{cos\theta}(1+e^{-\frac{\in L}{cos\theta}})}{(\frac{\in L}{cos\theta})^2+(2n+1)^2\pi^2} \approx$$

$$\frac{1}{1+\delta} \times \frac{4\alpha\beta c_0}{1+\alpha\beta c_0}\sum_{n=0}^{\infty} e^{-\pi^2(2n+1)^2Dt/L^2}\frac{\frac{\in L}{cos\theta}}{(\frac{\in L}{cos\theta})^2+(2n+1)^2\pi^2} \qquad \text{(eq.4.17)}$$

If we just use the first term in the summation series:

$$u(t) \approx \frac{1}{1+\delta} \times \frac{4\alpha\beta c_0}{1+\alpha\beta c_0} \times \frac{\frac{\in L}{cos\theta}}{(\frac{\in L}{cos\theta})^2+\pi^2} e^{-\pi^2 Dt/L^2} = Ae^{-\pi^2 Dt/L^2} \quad \text{(eq.4.4)}$$

Here A is a term independent of time t; L is the thickness of the crystal which can be measured for each crystal. Then diffusivity can be obtained by a linear fitting of the plot of ln[u(t)] vs. t.

4.3.3. Assessing the errors introduced in the assumptions and approximations

However, the validity of this truncation is subject to further evaluation. The complete expression (eq.4.17) can be reformulated as

$$u(t) = A(1 + M(t))e^{-\pi^2 Dt/L^2} \quad \text{(eq.4.18)}$$

$$M(t) = \sum_{n=1}^{\infty} e^{-\pi^2[(2n+1)^2-1]Dt/L^2} \frac{1}{1+m[(2n+1)^2-1]} \qquad \left(m = \frac{\pi^2}{\pi^2+\left(\frac{\epsilon L}{cos\theta}\right)^2}\right) \qquad \text{(eq.4.19)}$$

Only when $M(t) \ll 1$ can we use eq.4.4 to replace eq.4.18. We know M(t) will be significant when t is small, but will decay very quickly when t gets large. We can thus minimize this truncation error by cutting off data points from the first 200s.

To quantitatively evaluate the effect of this truncation, we need to know $\epsilon = 2.303\varepsilon n = 2.303 \times 1.04 M^{-1}\mu m^{-1} \times 0.320 M = 0.767 \mu m^{-1}$, which we measured experimentally on the homogeneous compound. If we let $cos\theta \approx 1$, we can estimate the value of m by

$$m = \frac{\pi^2}{\pi^2+(\epsilon L)^2}$$

The fitting was performed in the time scale of t > 100 to 200 s, so we can use t lower limit to calculate the upper limit of this truncation error.

As shown in Table 4.2, the resultant upper limit of M(t) value for TEA, TPA and TBA diffusions are all less than 15%, which are quite acceptable when considering the presence of experimental errors that are much larger than this amount.

To precisely evaluate the effect of residue M(t) on the diffusivity calculation, the M(t) contribution to the diffusivity can be calculated by $D_M(t) = \left|\frac{L^2}{\pi^2}\frac{d}{dt}\ln[1 + M(t)]\right|$. This

$D_M(t)$ is a monotone decreasing function and gets its maximum at the beginning point. $\%E(500) = \frac{D_M(t)}{D}|_{t=500\,s}$ at a selected typical time t = 500 s is used as an estimation of the percent error introduced by the above mathematical truncation.

Table 4.2. Fitting results of diffusion controlled quenching

Quencher	run	Diffusivity ($\times 10^{-13}$ m^2/s)	t lower limit /s	M(t) upper limit	percent error %E(500)
TEA	1	1.11 ± 0.05	84	0.024	<0.01%
	2	1.04 ± 0.05	113	0.010	<0.01%
	3	1.24 ± 0.07	107.6	0.006	<0.01%
TPA	1	4.7 ± 0.6	205	0.022	0.1%
	2	3.6 ± 0.4	207	0.047	0.9%
	3	5.6 ± 0.1	195	0.089	2.4%
	4	5.1 ± 0.3	236	0.071	2.6%
TBA	1	4.1 ± 0.3	201.6	0.153	10.4%
	2	3.9 ± 0.1	262.8	0.018	0.6%

4.4 Conclusion

We have examined diffusion-controlled luminescence quenching of a $Ru(bpy)_3$-incorporated MOF by a series of amines of different sizes. TEA, TPA, and TBA can diffuse through the MOF channels according to the time-dependent quenching data, whereas DIPEA is too large to enter the MOF channels. Despite its large size, 4-$MeOPhNPh_2$ can enter the MOF channels via a slow, complicated framework/guest intercalation process to result in extensive framework distortion as revealed by powder X-ray diffraction (PXRD). The time-dependent quenching curves of TEA, TPA, and TBA were fitted quantitatively with a one-dimensional Fickian diffusion model to afford diffusivities on the order of 10^{-14} to 10^{-13} m^2/s. These diffusivities are one to two orders of magnitude smaller than that of a transport diffusion system of a similar diffusant/channel size ratio. The dynamics of molecular diffusion into solvent-filled MOF channels reported herein is of fundamental importance to many MOF applications in solution.

REFERENCES

(1) Wang, C.; Lin, W. *J. Am. Chem. Soc.* **2011**, *133*, 4232.

(2) Alaerts, L.; Maes, M.; Giebeler, L.; Jacobs, P. A.; Martens, J. A.; Denayer, J. F. M.; Kirschhock, C. E. A.; De Vos, D. E. *J. Am. Chem. Soc.* **2008**, *130*, 14170.

(3) Maes, M.; Alaerts, L.; Vermoortele, F.; Ameloot, R.; Couck, S.; Finsy, V.; Denayer, J. F. M.; De Vos, D. E. *J. Am. Chem. Soc.* **2010**, *132*, 2284.

(4) Allendorf, M. D.; Houk, R. J.; Andruszkiewicz, L.; Talin, A. A.; Pikarsky, J.; Choudhury, A.; Gall, K. A.; Hesketh, P. J. *J. Am. Chem. Soc.* **2008**, *130*, 14404.

(5) Chen, B.; Wang, L.; Xiao, Y.; Fronczek, F. R.; Xue, M.; Cui, Y.; Qian, G. *Angew. Chem. Int. Ed. Engl.* **2009**, *48*, 500.

(6) Lan, A.; Li, K.; Wu, H.; Olson, D. H.; Emge, T. J.; Ki, W.; Hong, M.; Li, J. *Angew. Chem. Int. Ed. Engl.* **2009**, *48*, 2334.

(7) Xie, Z.; Ma, L.; deKrafft, K. E.; Jin, A.; Lin, W. *J. Am. Chem. Soc.*, **2010**, *132*, 922.

(8) Lee, J.; Farha, O. K.; Roberts, J.; Scheidt, K. A.; Nguyen, S. T.; Hupp, J. T. *Chem. Soc. Rev.* **2009**, *38*, 1450.

(9) Lin, W. B. *MRS Bulletin* **2007**, *32*, 544.

(10) Ma, L.; Abney, C.; Lin, W. *Chem. Soc. Rev.* **2009**, *38*, 1248.

(11) Ma, L. F., J. M.; Abney, C.; Lin, W. *Nat. Chem.* **2010**.

(12) Song, F.; Wang, C.; Falkowski, J. M.; Ma, L.; Lin, W. *J. Am. Chem. Soc.* **2010**, *132*, 15390.

(13) Sarkisov, L. D., T.; Snurr, Q.R. *Mol. Phys.* **2004**, *102*, 211.

(14) Amirjalayer, S.; Schmid, R. *Micropor. Mesopor. Mater.* **2009**, *125*, 90.

(15) Amirjalayer, S.; Tafipolsky, M.; Schmid, R. *Angew. Chem. Int. Ed. Engl.* **2007**, *46*, 463.

(16) Keskin, S.; Sholl, D. S. *Langmuir* **2009**, *25*, 11786.

(17) Seehamart, K.; Nanok, T.; Karger, J.; Chmelik, C.; Krishna, R.; Fritzsche, S. *Micropor. Mesopor. Mater.* **2010**, *130*, 92.

(18) Skoulidas, A. I.; Sholl, D. S. *J. Phys. Chem. B* **2005**, *109*, 15760.

(19) Stallmach, F.; Groger, S.; Kunzel, V.; Karger, J.; Yaghi, O. M.; Hesse, M.; Muller, U. *Angew. Chem. Int. Ed. Engl.* **2006**, *45*, 2123.

(20) Wehring, M.; Gascon, J.; Dubbeldam, D.; Kapteijn, F.; Snurr, R. Q.; Stallmach, F. *J. Phys. Chem. C* **2010**, *114*, 10527.

(21) Jobic, H.; Rosenbach, N.; Ghoufi, A.; Kolokolov, D. I.; Yot, P. G.; Devic, T.; Serre, C.; Ferey, G.; Maurin, G. *Chem.-Eur. J.* **2010**, *16*, 10337.

(22) Rosenbach, N.; Jobic, H.; Ghoufi, A.; Salles, F.; Maurin, G.; Bourrelly, S.; Llewellyn, P. L.; Devic, T.; Serre, C.; Ferey, G. *Angew. Chem. Int. Ed. Engl.* **2008**, *47*, 6611.

(23) Salles, F.; Jobic, H.; Ghoufi, A.; Llewellyn, P. L.; Serre, C.; Bourrelly, S.; Ferey, G.; Maurin, G. *Angew. Chem. Int. Ed. Engl.* **2009**, *48*, 8335.

(24) Salles, F.; Jobic, H.; Maurin, G.; Koza, M. M.; Llewellyn, P. L.; Devic, T.; Serre, C.; Ferey, G. *Phys. Rev. Lett.* **2008**, *100*.

(25) Kortunov, P. V.; Heinke, L.; Arnold, M.; Nedellec, Y.; Jones, D. J.; Caro, J.; Karger, J. *J. Am. Chem. Soc.* **2007**, *129*, 8041.

(26) Chmelik, C.; Karger, J.; Wiebcke, M.; Caro, J.; van Baten, J. M.; Krishna, R. *Micropor. Mesopor. Mater.* **2009**, *117*, 22.

(27) Zybaylo, O.; Shekhah, O.; Wang, H.; Tafipolsky, M.; Schmid, R.; Johannsmann, D.; Woll, C. *Phys. Chem. Chem. Phys.* **2010**, *12*, 8092.

(28) Choi, H. J.; Suh, M. P. *J. Am. Chem. Soc.* **2004**, *126*, 15844.

(29) Han, S. B.; Wei, Y. H.; Valente, C.; Lagzi, I.; Gassensmith, J. J.; Coskun, A.; Stoddart, J. F.; Grzybowski, B. A. *J. Am. Chem. Soc.* **2010**, *132*, 16358.

(30) Kalyanasundaram, K. *Coord. Chem. Rev.* **1982**, *46*, 159.

(31) Cvetkovic, A.; Picioreanu, C.; Straathof, A. J. J.; Krishna, R.; van der Wielent, L. A. M. *J. Am. Chem. Soc.* **2005**, *127*, 875.

(32) Han, S.; Hermans, T. M.; Fuller, P. E.; Wei, Y.; Grzybowski, B. A. *Angew. Chem. Int. Ed. Engl.* **2012**, *51*, 2662.

Chapter 5

Elucidating Molecular Iridium Water Oxidation Catalysts Using Metal-Organic Frameworks: A Comprehensive Structural, Catalytic, Spectroscopic, and Kinetic Study[1]

5.1 Introduction

The oxidation of water to oxygen is the key half-reaction in both natural photosynthesis and the proposed water splitting scheme for solar energy harvesting/storage.[2,3] Considerable progress has been made on developing water oxidation catalysts (WOCs) over the past few decades. For example, a number of metal oxides, metal nitrides, and other metal salts have been shown by Domen, Nocera, Mallouk, Frei, and others as efficient catalysts to perform water oxidation both electrochemically and photochemically.[4-10] Compared to inorganic solid catalysts, molecular catalysts are more amenable to mechanistic studies and fine-tuning using synthetic chemistry to optimize their performances. Following the pioneering work of Meyer and co-workers on water oxidation reaction (WOR) with the Ru-based blue dimer,[11] molecules containing a variety of transition metals (Ru, Ir, Mn, Fe, Co, Cu) have been identified as WOCs in recent years.[12-22]

Crabtree and Brudvig and coworkers have extensively studied half-sandwich Cp*Ir complexes (Cp* is the pentamethylcyclopentadienyl ligand) as potential molecular WOCs.[23,24] However, due to the high oxidation power of catalytic intermediates generated in the water oxidation process, at least some of these catalysts can undergo oxidative degradation during WORs.[23,25-27] The ultimate decomposition products in Ce^{4+}-

driven and electrochemically driven reactions were suggested to be iridium oxides/iridium hydroxides, which have been proven to be efficient WOCs.[5,8,28,29] These observations raised concerns about the molecular nature of the active catalysts based on the Cp*Ir complexes.

A number of elegant experiments have been performed by Crabtree and Brudvig and coworkers as well as other research groups to elucidate the nature of the active catalytic species. $IrCl_3(H_2O)_3$ and $IrCl_6^{3-}$ were first ruled out by Crabtree and Brudvig and coworkers to be the active catalysts, due to their insignificant water oxidation activity in the beginning stage of Ce^{4+}-driven reactions at pH=1. IrO_2 nanoparticles were also not likely to be the active catalysts due to their drastically different kinetic isotope effect from Ir complexes when D_2O was used as the solvent.[23] By carefully studying various Cp*Ir complexes as well as their CpIr analogs (Cp is the cyclopentadienyl ligand), Crabtree and Brudvig and co-workers showed that these compounds decomposed to varying degrees under the catalytic conditions (pH =1 and $[Ce^{4+}]$ = 78 mM). For catalysts with only Cp* but no other chelating ligand, the complexes decomposed and formed nanoparticles under Ce^{4+}-driven reaction conditions [30] and a blue deposit on electrode under electrochemical conditions.[25] The resultant nanoparticles/films from these reactions behaved similarly to iridium oxide / hydroxide but might contain organic residues. In contrast, Cp*Ir complexes with chelating ligands were stable at least during the beginning stage of the reaction.[23] At longer reaction times, the activity of these catalysts decreased, but no nanoparticle formation in Ce^{4+}-driven reactions[30] or film formation during electrochemical catalysis[31] was unambiguously observed. The catalyst decomposition pathway was likely related to the oxidation of Cp* since the Cp analogs

appeared to be more stable.[23] Moreover, some of the catalysts that were previously reported to decompose to form nanoparticles with Ce^{4+} as the oxidant were found to remain molecular when IO_4^- was used as the oxidant.[32,33] The experimental evidences provided by Crabtree and Brudvig and coworkers support that Cp*Ir complexes with chelating ligands are molecular catalysts.

Grotjahn and co-workers carried out comprehensive studies on the degradation of Cp*Ir complexes. They sequentially added Ce^{4+} to the catalyst solution and followed the generation of oxygen both in solution and in the gas phase.[26] An induction period was observed before the detection of O_2 after the addition of the first <15 equivalents of Ce^{4+} (initial $[Ce^{4+}]$ = 78 mM). This observation was interpreted as initial oxidation of the Cp* groups before water oxidation took place, which were supported by careful NMR and MS studies. They also provided some evidences for nanoparticle formation, but the TEM images and PXRD patterns were taken after the solvents were evaporated, which complicates the analysis because of crystallization of solution species. Their observation of an absorption peak in the 500 nm – 600 nm region, which was assigned as a signature absorption of IrO_x nanoparticles, can be alternatively explained by the formation of Ir(IV) molecular species, as pointed out by Crabtree and Brudvig and coworkers.[30] Macchioni and co-workers also performed detailed studies on the degradation pathway of Cp*Ir catalysts. By careful NMR studies, they found that oxidative degradation proceeds with an initial attack at the Cp* rings to form HCO_2H, CH_3CO_2H, and CH_2OHCO_2H.[27,34] Fukuzumi investigated the effects of bpy substituents on the stability of the Cp*Ir complexes in Ce^{4+}-driven water oxidation.[35] While the -OMe, -Me, and $–CO_2H$ substituents at the 4,4'-positions of 2,2'-bipyridine (bpy) do not have a significant effect

on catalyst degradation, the –OH groups at the 4,4'-positions of bpy significantly accelerate ligand decomposition. This substituent effect was attributed to the oxidative susceptibility of the 4,4'-$(OH)_2$-bpy ligand.

The large body of experimental results indicates that the Cp* rings of these Ir complexes are easily oxidized during WORs, but it is likely that the active WOCs are molecular in nature. However, true identities of these molecular WOCs remain elusive to date, at least partly owing to the use of highly potent oxidants and the involvement of the complex $4e^-/4H^+$ process during WORs.

With the goal of building water splitting devices using molecular components, we became interested in using metal-organic frameworks (MOFs) and surface assemblies to study Cp*Ir-based WOCs. There are two distinct advantages in studying WOCs immobilized in MOF frameworks or on surfaces: 1) as the catalysts are isolated from each other in these assemblies, degradation pathways involving multiple molecules are prohibited, which greatly simplifies the mechanistic scenarios; 2) solid materials or surface-grafted moieties can easily be separated from solutions, which facilitates further characterization of the catalysts after WORs. We have previously grafted the $[Cp^*Ir(bpy)Cl]^+$ and Cp*Ir(ppy)Cl (ppy is 2-phenylpyridine) catalysts onto the glassy carbon surface via diazonium coupling, and studied their electrochemical water oxidation activities.[36] Although partially complicated by oxidation of glassy carbon electrode during catalysis, careful analyses of these immobilized complexes after WORs support the molecular nature of these catalysts.

MOFs have provided a great platform to engineer single-site solid catalysts with tunable molecular functionalities, open channels, and other important attributes. I have

described in Chapter 2 of water oxidation using MOFs that contain Cp*Ir catalysts. These MOFs were synthesized by doping Cp*Ir complexes with 5,5'-dicarboxylate-substituted bpy or ppy chelating ligands into the UiO-67 framework that is composed of $Zr_6O_4(OH)_4(CO_2)_{12}$ SBUs and *p*-biphenyldicarboxylate bridging ligands. The open channel sizes of those MOFs are however too small to allow hydrated Ce^{4+} ions to diffuse through, and consequently, only a minute fraction of the WOCs on the surfaces of these MOF particles is involved in water oxidation. It is of great interest to increase MOF channel sizes to allow all the catalytic struts to engage in water oxidation.

In this chapter, I will describe the synthesis and characterization of two new highly porous and stable Zr-carboxylate MOFs, **11** and **12**, built with elongated bpy or ppy ligands attached to the Cp*Ir moieties. We performed detailed kinetic studies of Ce^{4+}-driven WORs catalyzed by **11** and **12** using a combination of UV-Vis spectroscopy, phosphorescent oxygen detection, and GC analysis. The recovered MOFs were then carefully studied for possible oxidative modification of the Cp* rings during WORs. After careful NMR and MS studies of the digested sample of **11**, (**bpy-dc**)$Ir(H_2O)_2XCl$ (X is likely formic acid or acetic acid), formed by oxidative degradation of the Cp* rings, was identified as an active catalyst for water oxidation. The identity of the active WOC was further supported by X-ray photoelectron, diffuse-reflectance UV-Vis absorption, luminescence, and infrared spectroscopies. With these mechanistic details in hand, a reaction-diffusion model was developed to describe the kinetics of MOF-catalyzed WORs. An understanding of the competition between reaction and diffusion rates provides important insights into these MOF-catalyzed WORs.

5.2 Synthesis and Characterization of 11 and 12

The elongated dimethyl esters of 2,2'-bipyridine and 2-phenylpyridine (**bpy-de** and **ppy-de**) were prepared in high yields by Pd-catalyzed Suzuki coupling reactions between 4-(methoxycarbonyl)phenylboronic acid and 5,5'-dibromo-2,2'-pyridine or 5-bromo-2-(4-bromophenyl)pyridine, respectively. The corresponding dicarboxylic acids of **bpy-de** or **ppy-de** are denoted **bpy-dc** and **ppy-dc**, respectively. The dicarboxylic methyl ester-containing Ir complexes $\mathbf{L_9}$-Me_2 and $\mathbf{L_{10}}$-Me_2 were synthesized by treating $[Cp^*IrCl_2]_2$ with **bpy-de** or **ppy-de** in DMF at 70 ^oC. $\mathbf{L_9}$-Me_2 and $\mathbf{L_{10}}$-Me_2 were isolated in 92% and 57% yields, respectively, and then converted to dicarboxylic acids $\mathbf{L_9}$-H_2 or $\mathbf{L_{10}}$-H_2 by base-catalyzed hydrolysis in 80% and 87% yield, respectively (Scheme 5.1). All of the new compounds were characterized by NMR spectroscopy and electrospray ionization-mass spectrometry.

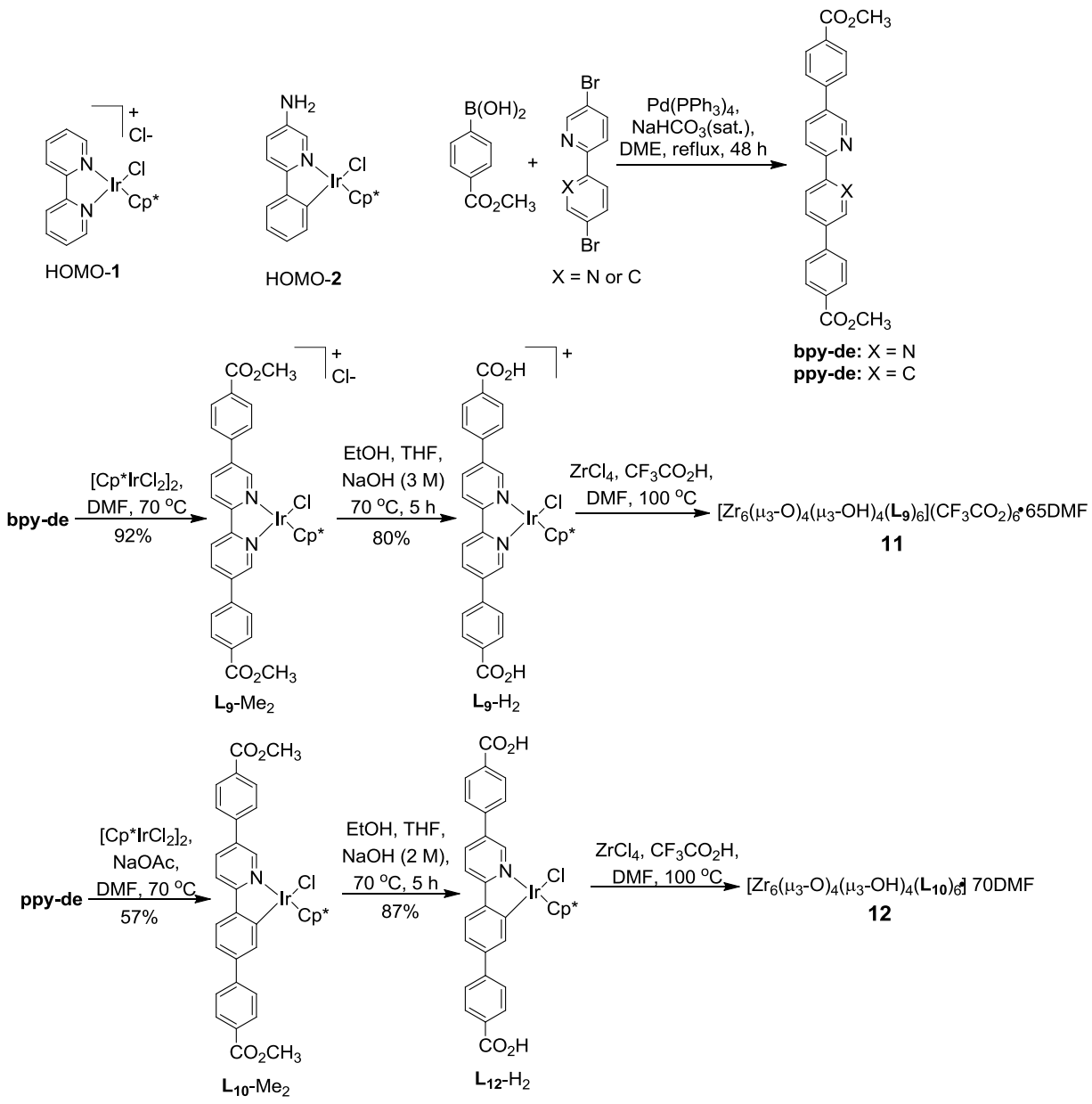

Scheme 5.1. Chemical structures of homogeneous control catalysts and synthesis of Zr-carboxylate **11** and **12** of the fcu topology. (Reprinted with permission from ref [1]. Copyright American Chemical Society 2012)

Highly stable **11** and **12** were synthesized by heating mixtures of $\mathbf{L_9}$–H_2 or $\mathbf{L_{10}}$–H_2 with $ZrCl_4$ and trifluoroacetic acid in DMF at 100 ^oC for 48 h. The resulting yellow crystalline solids were washed with copious amounts of DMF, methanol, and water. **11** and **12** were

characterized by powder X-ray diffraction (PXRD), thermogravimetric analysis (TGA), scanning electron microscopy (SEM), transmission electron microscopy (TEM), X-ray photoelectron spectroscopy (XPS), inductively coupled plasma-mass spectroscopy (ICP-MS). The crystals of **11** and **12** were not suitable for single-crystal X-ray diffraction analysis owing to their small sizes (in micrometers). Fortunately, as we expected, they are isostructural to the UiO MOF **10** (in Chapter 3) with a similar bridging ligand $\mathbf{L_8}$ (of the identical length to $\mathbf{L_9}$ and $\mathbf{L_{10}}$) based on the similarity of their powder X-ray diffraction patterns (Figure 5.1d). **11** and **12** thus adopt the UiO framework structure of the **fcu** topology by connecting the $Zr_6(\mu_3\text{-}O)_4(\mu_3\text{-}OH)_4(\text{carboxylate})_{12}$ SBUs with the $\mathbf{L_9}$ or $\mathbf{L_{10}}$ linkers (Figure 5.1a). Because of the steric bulk of $\mathbf{L_9}$ and $\mathbf{L_{10}}$, **11** and **12** adopt non-interpenetrated structures, as confirmed by the systematic absences and relative peak intensities of their PXRD patterns. Based on PLATON calculations, **11** and **12** possess 66.0% and 69.5% of void spaces, respectively. Both **11** and **12** exhibit a triangular open channel with an edge length of 1.6 nm and an octahedral cavity with a diameter of 1 nm (Figure 5.1b).

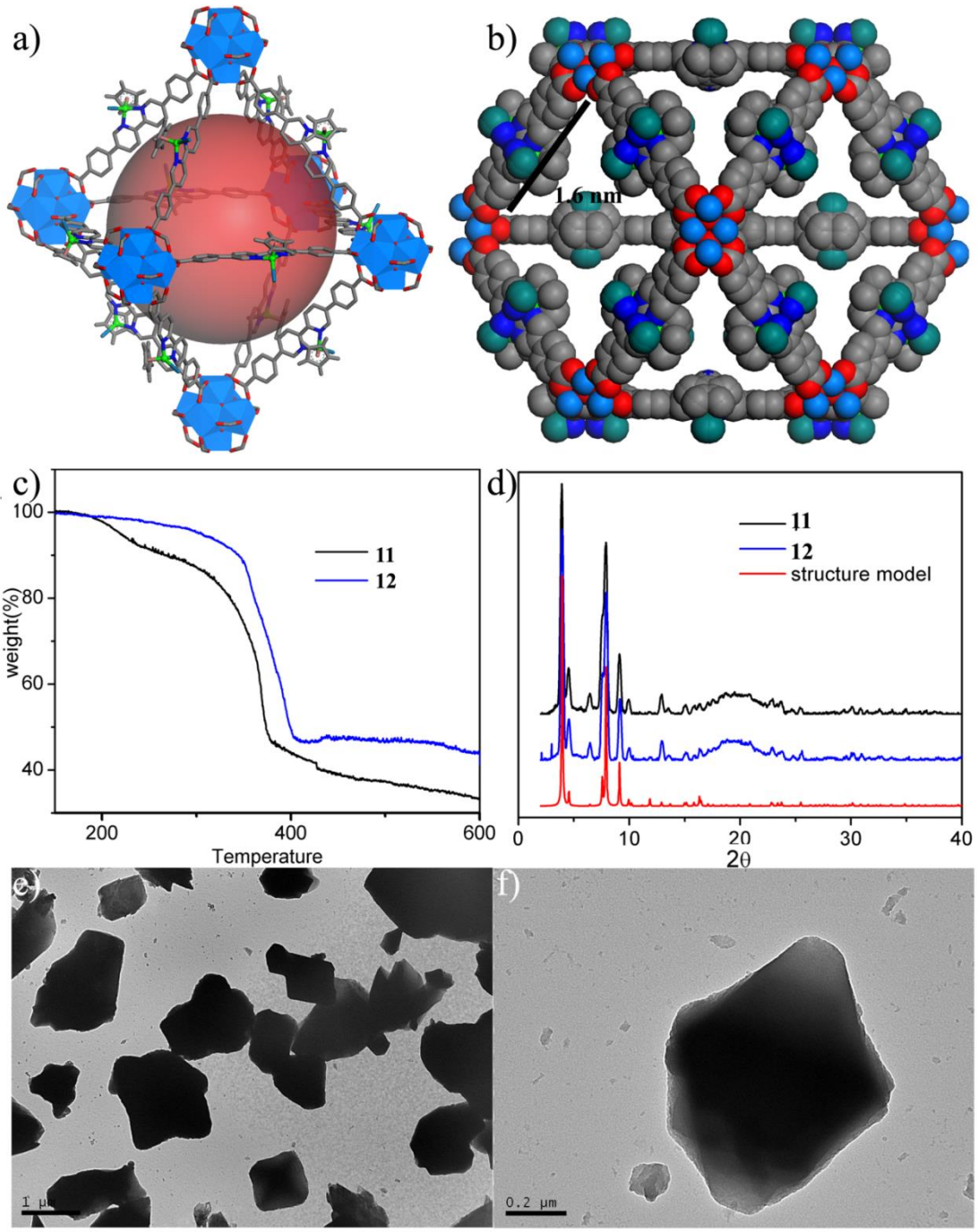

Figure 5.1. (a) Structure model for **11** showing an octahedral cage of 1 nm in diameter. Zr, blue polyhedron; Ir, green ball; Cl, dark green; C, grey; N, blue. The red ball in the middle represents the cage cavity. (b) Space-filling model of **11** as viewed along [110] direction. The triangular channel has an edge length of 1.6 nm. (c) TGA of solvent-free **11** (black) and **12** (blue). (d) PXRD patterns of **11** (blue) and **12** (black) along with the simulated PXRD pattern based on the structure model (red). (e) TEM images of

microcrystals of **11**. (f) TEM image of one microcrystal of **11** showing the octahedral shape. (Reprinted with permission from ref [1]. Copyright American Chemical Society 2012)

TEM images of **11** showed octahedral microcrystals of ~1 μm in dimensions (Figures 5.1e and 5.1f), while SEM images of **12** showed aggregated microcrystals of 1-2 μm in dimensions. We used a combination of ^{1}H and ^{19}F NMR, TGA, and ICP-MS to establish the complete formulae of **11** and **12** to be $[Zr_6(\mu_3\text{-}O)_4(\mu_3\text{-}OH)_4(\mathbf{L_9})_6](CF_3CO_2)_6\cdot 65DMF$ and $[Zr_6(\mu_3\text{-}O)_4(\mu_3\text{-}OH)_4(\mathbf{L_{10}})_6]\cdot 70DMF$, respectively. The solvent contents of **11** and **12** are thus 35% and 40%, respectively. Freeze-dried samples of **11** exhibited negligible surface areas based on nitrogen adsorption measurements.[37] PXRD studies indicated severe framework distortion for **11** upon solvent removal, a phenomenon that has been observed for many MOFs with very large open channels. We also demonstrated the porosity of **11** by dye uptake measurements; **11** exhibited substantial amount (>20 wt%) of Brilliant Blue R-250 uptake.

5.3 Water oxidation activity of 11 and 12

We performed Ce^{4+}-driven WORs using **11** and **12** as catalysts. The WORs were studied by three different methods: 1) using a phosphorescent oxygen sensor to detect the amount of O_2 in solution; 2) using UV-Vis absorption at 420 nm to monitor Ce^{4+} consumptions; and 3) using gas chromatography (GC) to analyze the gas compositions in the headspace. The experiments were performed with 10 μM MOFs based on Ir in aqueous solutions of HNO_3 with pH = 1. The initial $[Ce^{4+}]$ was 3 mM for the WORs catalyzed by **11**.

As shown in Figure 5.2a, by quantifying the time-dependent oxygen generation using a phosphorescent sensor, an water oxidation turnover frequency (TOF) of 0.48 ± 0.02 min^{-1} (based on ¼ O_2 or 1 e^-) was obtained for **11** during the first 10 minutes of WOR (Table 5.1). At later time points, the oxygen generation appeared to slow down, owing to the formation of oxygen bubbles but not because of the deceleration of the WOR. The formation of oxygen bubbles reduced the percentage of generated O_2 that was detected by the phosphorescent sensor, and caused significant fluctuations in the O_2 generation curves.

By monitoring the absorption peak intensity at 420 nm, the Ce^{4+} consumption rate was determined to be 0.52 ± 0.06 min^{-1} for **11** in the first 10 minutes of WOR (Figure 5.2c and Table 5.1). Comparisons of oxygen evolution rates determined by phosphorescent sensor (0.48 ± 0.02 min^{-1}) to this Ce^{4+} consumption rates, gave an oxygen-generation efficiency of >90% in the first 10 minutes of WORs. 16 equivalents of Ce^{4+} would have been consumed to oxidize one equivalent of Cp* groups to acetic acid. Considering a total turnover number of 300 based on the amount of Ir, the consumption of 16 equivalents of Ce^{4+} for ligand oxidation still gives a high oxygen-generation efficiency of >94.7%. The oxygen-generation efficiency is thus not a sensitive indicator for ligand oxidation.

The headspace gas of the **11**-catalyzed WOR was also analyzed by GC to quantify the amount of O_2 generated from the WOR. The amount of CO_2 detected in the gas phase after water oxidation was not significantly different from the background signal. The O_2 generation TOF was calculated by analyzing the headspace during the first 4 hours of the WOR to be 0.40 ± 0.06 min^{-1} (Table 5.1). This TOF is slightly smaller than those

obtained during the first 10 minutes of WORs, which again can be attributed to the O_2 bubble formation at later times of WORs.

To further examine the stability of the WOC derived from **11** under reaction conditions, we attempted to reuse **11** for water oxidation by adding fresh Ce^{4+} solutions to the recovered **11**. As shown in Figures 5.2a and 5.2c, **11** retained high catalytic activity for at least two consecutive reuses; the TOFs for the first and second reuse were slightly higher than that of the first use. Moreover, the supernatant from the reaction showed negligible water oxidation activity. ICP-MS analysis of the supernatant after water oxidation indicated that <1% of the Ir had leached into the solution. This is consistent with our assumption that at low [Ce^{4+}]'s, the active WOC derived from **11** is molecular in nature and does not dissociate from the MOF framework.

We also examined O_2 evolution from **12**-catalyzed water oxidation. PXRD and UV-Vis studies indicated that the structure of **12** can be preserved at [Ce^{4+}] = 0.3 mM, but will degrade quickly at higher [Ce^{4+}]'s. Unfortunately, we cannot accurately quantify oxygen at a [Ce^{4+}] of 0.3 mM due to the limited sensitivity of the oxygen sensor. The supernatants of the water oxidation mixtures with 0.3 mM Ce^{4+} contained less than 1 % of Ir as revealed by ICP-MS studies. In an effort to confirm the water oxidation activity of **12**, we increased the [Ce^{4+}] to 3 mM, the same condition as that was used in the O_2 generation experiment for **11**. As shown in Figure 5.2b, **12** exhibited increasing O_2 generation rates with time. The initial O_2 generation TOF was 0.21 ± 0.02 min^{-1} (based on ¼ O_2 or 1 e^-). Based on UV-Vis measurements, a Ce^{4+} consumption rate was calculated to be 6.3 ± 1.0 min^{-1} for **12** in the first 10 minutes of WORs (Figure 5.2d). **12** thus has a 5%

O_2 generation efficiency at the beginning state of WOR, with a significant amount of Ce^{4+} used for the oxidative degradation of **12**. We have also reused **12** as water oxidation catalyst twice after Ce^{4+} was depleted. The TOFs of second and third runs were significantly higher than that of the first run, indicating that the **12** decomposed to more active species during the WORs. Moreover, about 6% of Ir was leached into the supernatants as revealed by ICP-MS studies. The drastically different behaviors of **11** and **12** under the same WOR conditions indicate that **12** is more prone to oxidative degradation than **11**, consistent with the fact that the electron-donating nature of the ppy chelator facilitates oxidative degradation of the ligand.

Table 5.1 Turnover frequencies[a] of water oxidation reactions catalyzed by **11** and **12**.

	11 (min^{-1})	***12*** (min^{-1})
by UV-Vis[b] (1^{st} run)	0.52 ± 0.06	6.3 ± 1.0
by UV-Vis[b] (2^{nd} run)	0.54 ± 0.07	9.4 ± 2.0
by UV-Vis[b] (3^{rd} run)	0.53 ± 0.07	-
by O_2 detection[b] (1^{st} run)	0.48 ± 0.02	0.21 ± 0.02
by O_2 detection[b] (2^{nd} run)	0.48 ± 0.02	0.92 ± 0.05
by O_2 detection[b] (3^{rd} run)	0.47 ± 0.02	1.01 ± 0.05
by GC detection	[c]0.40 ± 0.06	[d]1.7 ± 0.4

[a]Turnover frequency is based on ¼ O_2 or 1 Ce^{4+}, in other words 1 e^-.
[b]3 mM Ce^{4+} in pH =1 HNO_3 solution with 10 μM Ir, based on data from the first 10 minutes.
[c]3 mM Ce^{4+} in pH = 1 HNO_3 solution with 10 μM Ir, based on data after reaction of 4 hours.
[d]3 mM Ce^{4+} in pH = 1 HNO_3 solution with 10 μM Ir, based on data after reaction of 2.5 hours.

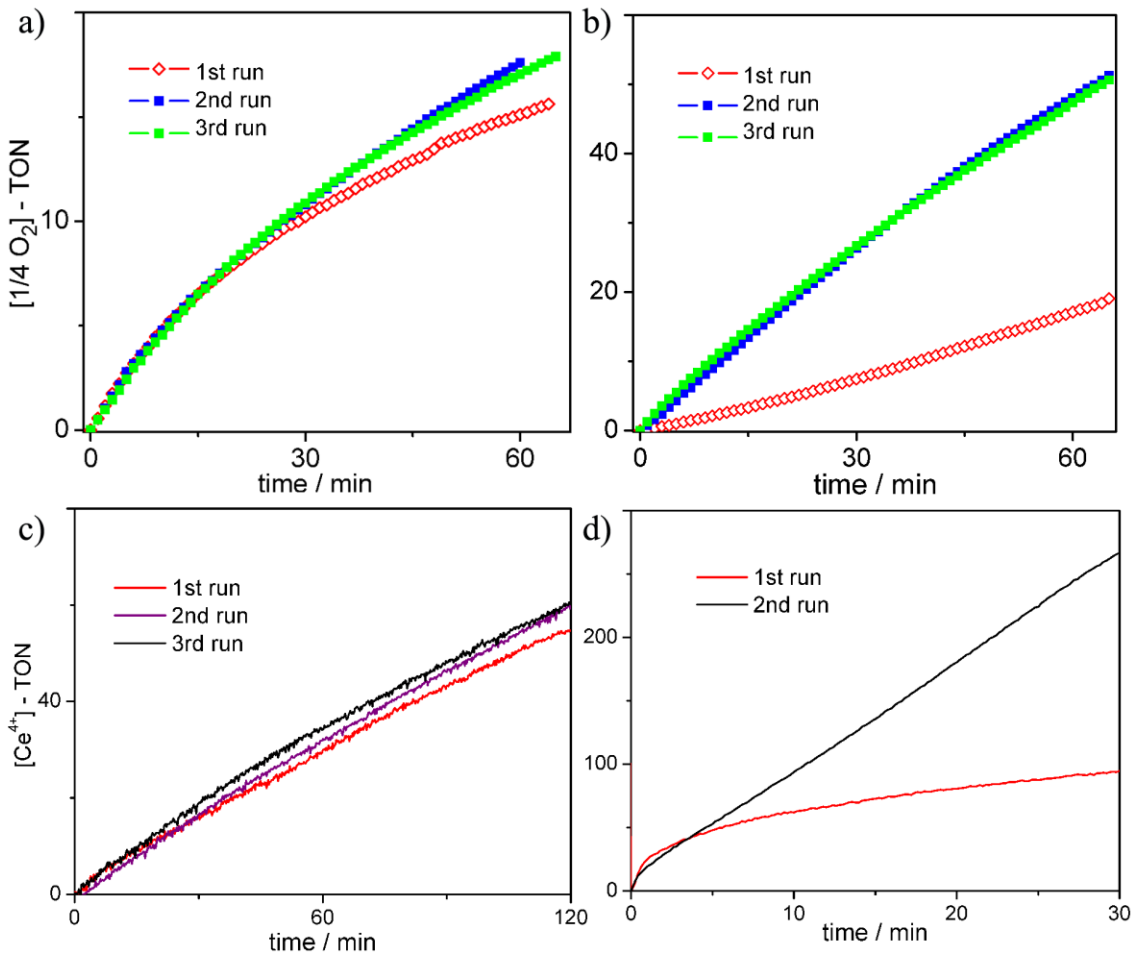

Figure 5.2 (a) Plots of O_2 evolving turnover number (1/4 O_2-TON) vs time for **11**. (b) Plots of O_2 evolving turnover number (1/4 O_2-TON) vs time for **12**. (c) Plots of Ce^{4+} consumption turnover number (1/4 O_2-TON) vs time for **11**. (d) Plots of Ce^{4+} consumption turnover number (1/4 O_2-TON) vs time for **12**. Experimental condition for a-d: 3 mM Ce^{4+} in pH =1 HNO_3 solution with 10 μM Ir. (Reprinted with permission from ref [1]. Copyright American Chemical Society 2012)

5.4 Identification of (bpy-dc)Ir$(H_2O)_2$XCl as an active WOC in 11-catalyzed water oxidation.

As suggested by other researchers in previous studies, significant modifications of the Cp* rings of the Cp*Ir catalysts occur during Ce^{4+}-driven WORs. In MOF-catalyzed WORs, multi-molecular catalyst degradation pathways are shut down as a result of

physical isolation of the catalytic struts. We thus believe that MOFs provide a unique platform to interrogate water oxidation pathways. In particular, we are interested in answering the following questions: (1) Do modifications of the Cp* rings happen in the catalytic struts of **11** during Ce^{4+}-driven WORs? (2) What is the chemical structure of the modified Ir compound? (3) Is the modified compound an active WOC? (4) Are large hydrated Ce^{4+} ions able to diffuse through the MOF channels to reach the active WOCs in the MOF interiors? (5) What roles do Ce^{4+} ion diffusion rates and water oxidation rates play in MOF-catalyzed WORs?

5.4.1 Identification and quantification of acetic acid generated from oxidative modifications of Cp* groups by ^{1}H-NMR

Oxidative degradation of the Cp* rings was previously shown to lead to the formation of acetic acid, formic acid, and other decomposition products. Monitoring the reaction solution by ^{1}H-NMR can thus provide information on the possible degradation of Cp* rings on the Cp*Ir complexes. 0.5 μmol of **11** was dispersed in 0.5 mL of D_2O (1 mM of $\mathbf{L_9}$). Ce^{4+} was added to the suspension successively. Aliquots of 3 equivalents of Ce^{4+} were added to the suspension each time, and ^{1}H-NMR spectrum of the mixture was taken after complete consumption of the added Ce^{4+} in each cycle. Acetic acid and a small amount of formic acid were detected in the solution during the Ce^{4+}-driven WOR with **11**. The acetic acid and formic acid peaks were confirmed by adding acetic acid and formic acid standard to the solution for a peak spiking. The amounts of acetic acid and formic acid generated from oxidative degradation of Cp* rings were quantified by integration of the ^{1}H-NMR peaks with NMe_4^+ as an internal standard. The amount of generated acetic acid steadily increased after each addition of Ce^{4+} into the solution and

plateaued at an amount around 1.8 times of that of the total **L$_9$** after adding 30 equivalents of Ce^{4+}. The amount of formic acid detected was < 5% of that of **L$_9$**.

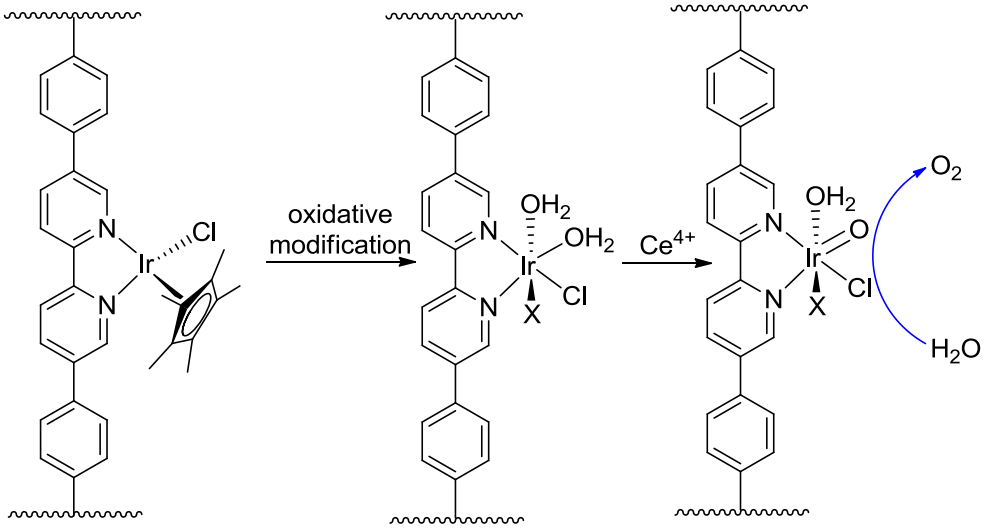

Scheme 5.2 Oxidative modifications of the Cp* ring of the catalytic strut in **11** to form (**bpy-dc**)Ir$(H_2O)_2$XCl (X is likely a formate or acetate ligand) and the proposed oxidation of (**bpy-dc**)Ir$(H_2O)_2$XCl to form the Ir(V)=O species that is responsible for water oxidation. (Reprinted with permission from ref [1]. Copyright American Chemical Society 2012)

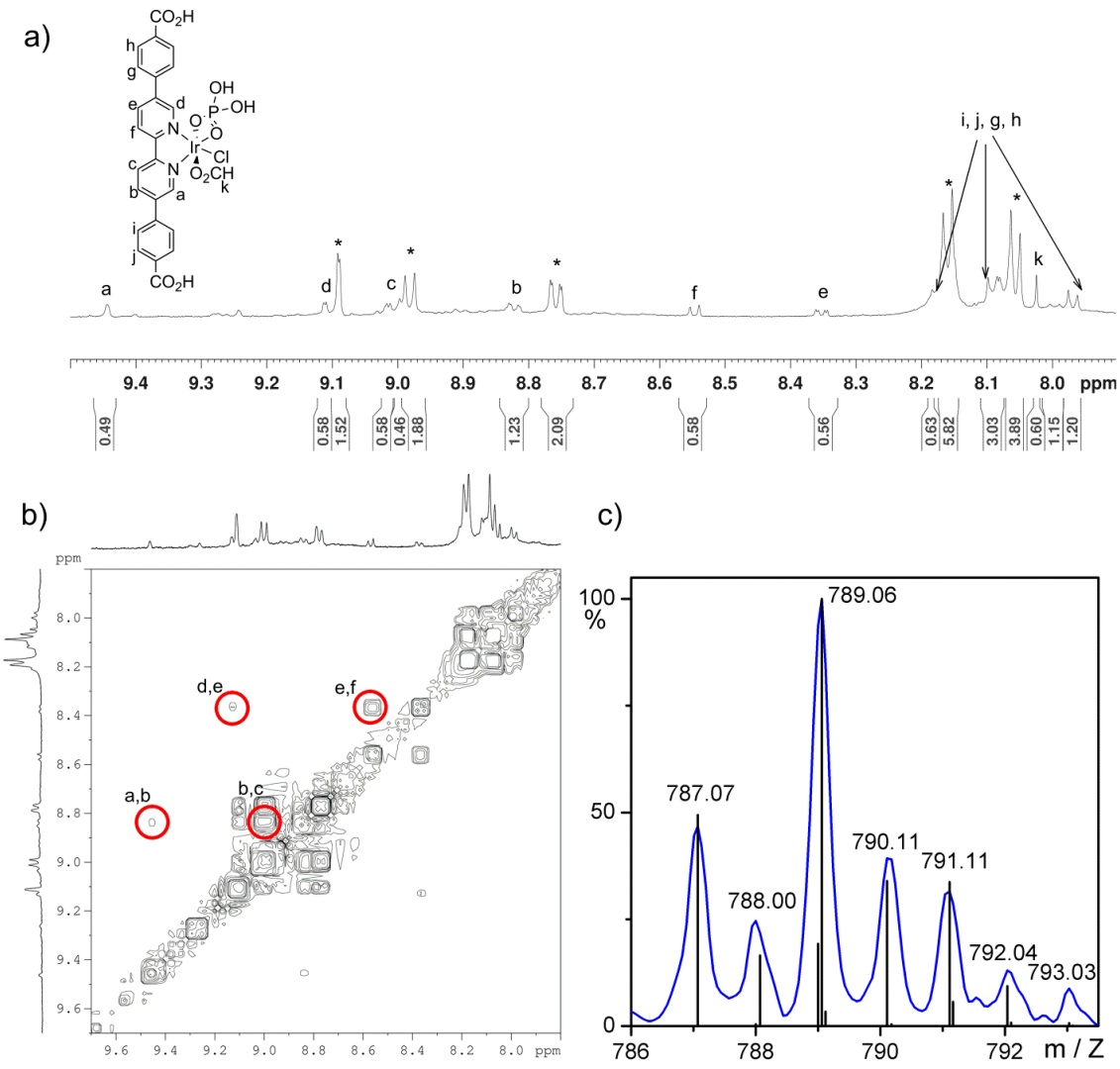

Figure 5.3 (a) ^{1}H-NMR spectrum of digested **11** after WOR. (A total 30 eq. of Ce^{4+} were added successively to the pH =1 HNO_3 / D_2O solution with 1 mM Ir before the MOF is digested for NMR. Each time only 3 eq. of Ce^{4+} were added to give a Ce^{4+} concentration of 3mM. The next aliquot of Ce^{4+} is only added after the complete consumption of the previous aliquot) * denotes peaks due to the original $\mathbf{L_9}$-H_2 ligand. Other major peaks are assigned to the proposed structure. (b) ^{1}H-^{1}H COSY spectrum of digested **11** after WOR. (c) ESI-MS of digested **11** (with phosphoric acid) after water oxidation showing the presence of the $\{[(\mathbf{bpy\text{-}dc})Ir(H_2PO_4)(HCO_2)Cl]+Na\}^{+}$ molecular ion. The black lines show the expected isotopic peaks. (Reprinted with permission from ref [1]. Copyright American Chemical Society 2012)

5.4.2 NMR and Mass spectrometric studies of the recovered 11 after water oxidation reactions

To identify the active Ir catalysts after Cp* ring modifications, we characterized the digested sample of **11** after WORs by NMR and MS. The recovered solid was thoroughly washed with water before being dissolved in a 0.1 M D_3PO_4/d_6-DMSO solution. NMR spectra were taken on the dissolved samples with mesitylene as a standard. After treatment with 30 equivalents of Ce^{4+}, 55% of the $\mathbf{L_9}$ struts were oxidatively modified. Multiple modification products were observed in the ^{1}H-NMR spectra, but the major modified species (28% of the original amount of $\mathbf{L_9}$) was identified as [(**bpy-dc**)Ir(solvent)$_2$XCl]$^+$ based on the unsymmetrical **bpy-dc** coordination to the Ir center (Figure 5.3). The assignment of the proton signals was supported by the ^{1}H-^{1}H COSY spectrum. The X in the formula is likely to be a formate group resulting from the decomposition of the Cp* rings, as shown by a singlet at δ 8.02 in the ^{1}H-NMR.[38-40]

The digested sample of **11** was also characterized by electrospray ionization-mass spectrometry (ESI-MS). The sample was digested either under acidic condition using 0.1 M H_3PO_4/DMSO or under basic condition using 0.1 M NaOH/H_2O, before diluted with 1% formic acid/methanol solution for ESI-MS measurements. For the sample digested with H_3PO_4, molecular ion peaks for [(**bpy-dc**)Ir(H_2PO_4)(HCO_2)Cl] were observed ([M+Na]$^+$, expected: 789.00, observed: 789.06, Figure 5.3c). For the sample digested with NaOH, molecular ion peaks for [(**bpy-dc**)Ir(H_2O)$_2$(HCO_2)Cl]$^+$ were observed (M^+, expected: 705.06, observed:705.14). The assignments of these species are unambiguous because of the ^{1}H NMR spectroscopic data and the unique isotope patterns of the molecular ions in the mass spectra. We believe that [(**bpy-dc**)Ir(H_2O)$_2$(HCO_2)Cl]$^+$ is the

most likely precatalyst in **11**-catalyzed WORs (Scheme 5.2). Presumably, [(**bpy-dc**)Ir(H_2O)$_2$(HCO_2)Cl]$^+$ is oxidized by Ce^{4+} via a proton-coupled electron transfer process to form the corresponding Ir(V)=O species (Scheme 5.2) which initiates the water oxidation catalytic cycle.

Although significant catalyst modification is present for the MOF catalyzed WORs, an O_2 generation curve without initial induction period was obtained. These suggest that the original $\mathbf{L_9}$ ligand is also an active water oxidation with similar activity as that of the oxidatively modified one. It is difficult to further confirm this assumption based our experimental results.

5.4.3 Water oxidation activity of soluble (bpy)Ir(solvent)$_n$X$_m$ species

To support the hypothesis that (**bpy-dc**)Ir(H_2O)$_2$XCl is a true precatalyst for **11**-catalyzed WORs, we synthesized (bpy)Ir complexes containing water and chloride groups but no other ancillary ligands to test their water oxidation activities. Although K[Ir(bpy)Cl_4] was not a competent WOC, its derivatives after treatment with $AgNO_3$ showed water oxidation activities with Ce^{4+} as the oxidant. Upon treating K[Ir(bpy)Cl_4] with four equivalents of $AgNO_3$ in pH = 1 (with added HNO_3), the resultant soluble species showed complicated ^{1}H-NMR spectra, indicating the formation of multiple species due to incomplete Cl removal. Nevertheless, the resulting (bpy)Ir(solvent)$_n$X$_m$ mixture (with water and chloride or nitrate groups in addition to the bpy ligand, 25 μM based on Ir) was highly active for water oxidation in the presence of 10 mM Ce^{4+} at pH = 1. However, the water oxidation activity of this mixture decreased with time with an intractable dark blue solid forming within one hour (Figure 5.4). The solid formation was

due to aggregation of the Ir(IV) or Ir(V) molecular species; such a process was prevented in the MOFs as a result of catalyst site isolation in the frameworks.

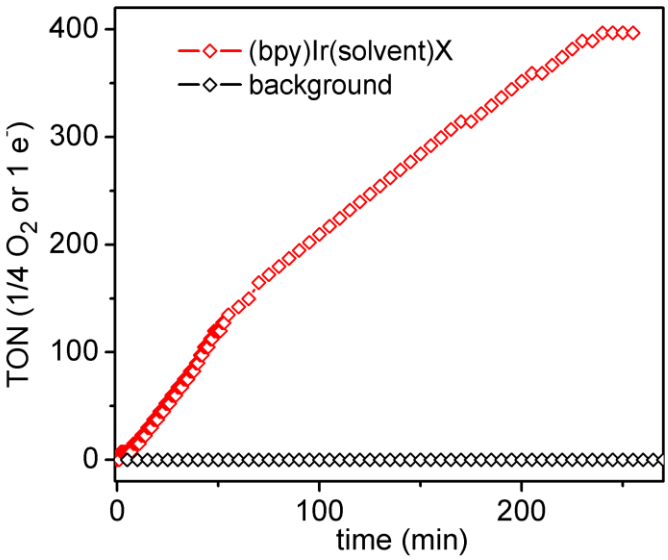

Figure 5.4. O_2 generation using the (bpy)Ir(solvent)$_n$X$_m$ species. The concentration of Ir was 25 µM and the initial [Ce^{4+}] was 10 mM in 10 mL of pH = 1 HNO_3 solution. The O_2 was detected in the gas phase. (Reprinted with permission from ref [1]. Copyright American Chemical Society 2012)

5.5 MOF Stability as revealed by PXRD and ICP-MS studies.

PXRD studies indicated that the structure of **11** was preserved under WOR conditions (Figure 5.5). Since the oxidation of Cp* rings of the **L$_9$** ligands does not affect the MOF connectivity, the PXRD pattern is maintained even after the Cp* groups have been replaced with solvents and anionic ligands. The preservation of the PXRD patterns after WORs is thus consistent with the formation of the (**bpy-dc**)Ir(H_2O)$_2$XCl species. ICP-MS measurements of the supernatant of the reaction mixture further confirmed the stability of **11** under the WOR conditions. After treatment of **11** with 3 mM Ce^{4+} at pH = 1 for 12 hours, <1% of the Ir leached into the solution. In contrast, the framework of **12** can only

be preserved at a [Ce^{4+}] of 0.3 mM The framework structure of **12** is lost within 1 h of treatment with 3 mM Ce^{4+}, suggesting that the putative (**ppy-dc**)Ir(solvent)$_n$X$_m$ species further degrade to lead to even more active non-molecular Ir water oxidation catalysts. Our attempts to isolate and identify the true pre-catalyst for **12**-catalyzed water oxidation have not yet been successful.

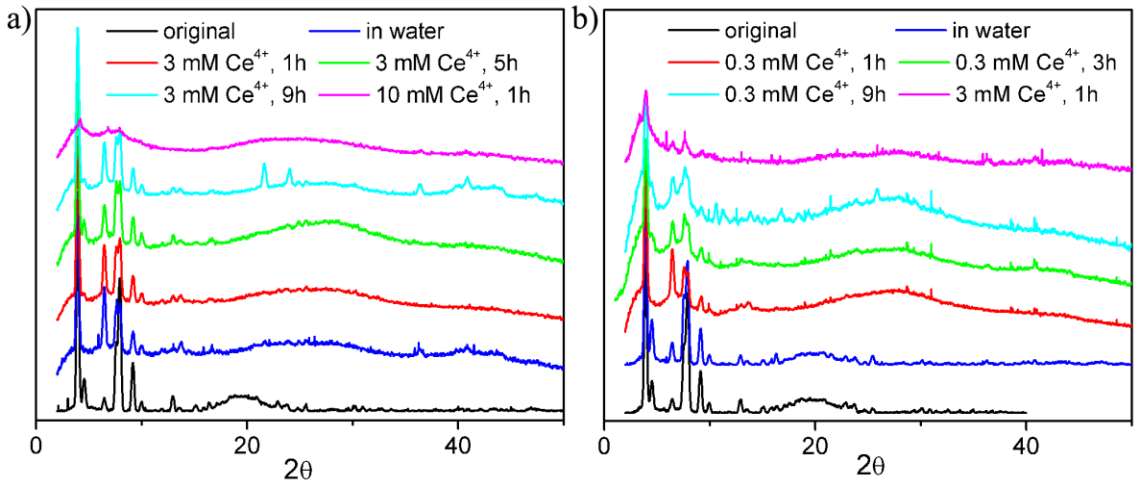

Figure 5.5 (a) PXRD patterns of **11** taken after different times of WORs. (b) PXRD patterns of **12** taken after different times of WORs. Experimental condition: pH =1 HNO_3 solution with 10 μM Ir with different concentration of Ce^{4+} and different reaction time. (Reprinted with permission from ref [1]. Copyright American Chemical Society 2012)

5.6 XPS analyses of 11 and 12 before and after water oxidation reactions.

XPS analysis was performed on the recovered MOF solids (10 μM based on Ir) after treatment with various [Ce^{4+}]'s (0.3, 3, and 200 mM) at pH=1 for 12 h. All the MOF samples were washed with nitric acid and dried on silicon wafer and then kept in vacuum overnight prior to XPS measurements. The spectra were calibrated with respect to the C(1s) peaks in each sample. The Ir(4f) region of the spectra showed no difference in peak positions between the original MOF and the samples treated with different [Ce^{4+}]'s,

indicating the Ir(III) oxidation state in all of these samples. We noticed that the MOFs remained in green color in a pH=1 solution after all of the Ce^{4+} ions were consumed. The green color suggested the Ir(IV) oxidation state for the resting state of the catalysts at low pH. These MOFs however reverted to the original yellow-red color after treatment with neutral water. We believe that the observation of the Ir(III) oxidation state by XPS is owing to the ready reduction of the recovered MOFs either during the drying and vacuum processing prior to XPS measurements or by X-rays or the generated photoelectrons during the XPS measurements. XPS thus cannot be considered a reliable technique for determining the oxidation states of Ir WOCs. The signal intensity of Ir(4f), N(1s), and Zr(3d) peaks all decreased with respect to the C(1s) peak intensity at increasing [Ce^{4+}]'s, presumably caused by adsorbed Ce^{4+} and NO_3^- ions on the MOF surface. The XPS spectra also showed two different N(1s) peaks at binding energies of 398.2 and 404.6 eV for the pyridyl and nitrate nitrogen atoms, respectively (Figure 5.6). The atomic ratios of Ir vs. pyridyl nitrogen in these samples provide useful information on the stability of chelating **bpy-dc** and **ppy-dc** ligands. As shown in Table 5.2, the atomic ratios of Ir vs. pyridyl nitrogen remained constant for both **11** and **12** after treatment with relatively low [Ce^{4+}]'s, suggesting that the Ir atom and pyridine moiety in **bpy-dc** and **ppy-dc** ligands remain intact under these conditions. However, under high [Ce^{4+}]'s, the atomic ratios of Ir vs. pyridyl nitrogen decreased significantly compared to those of the original MOFs, suggesting loss of Ir from the MOFs as a result of partial degradation of the chelating ligands. It is noted that the deviation of Ir vs. pyridyl nitrogen atomic ratios from the ideal atomic ratios is due to different electron collection efficiency for different elements in the samples, which is not uncommon for XPS analyses.

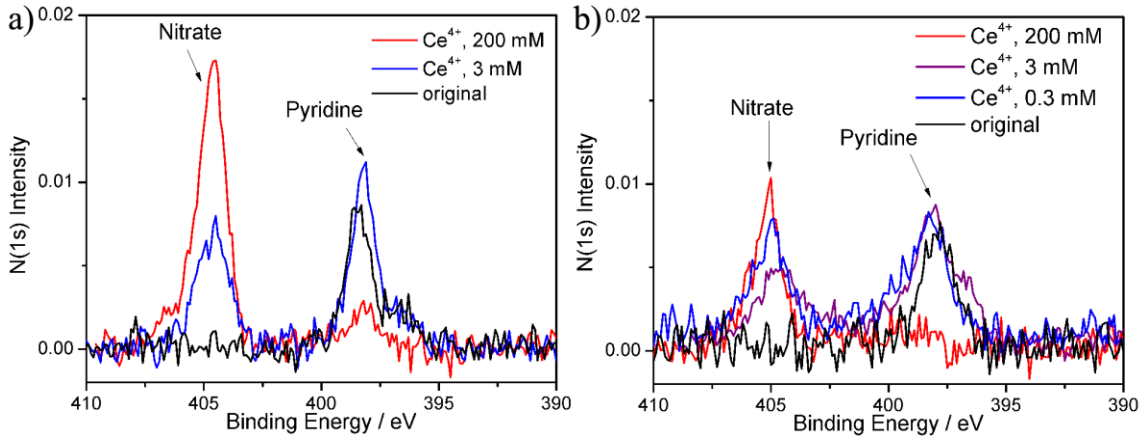

Figure 5.6 (a) N(1s) XPS signals for **11** after treatment with various [Ce^{4+}]'s at pH=1 for 12 h. black, as-synthesized **11**; blue, after treatment with 3 mM Ce^{4+}; red, after treatment with 200 mM Ce^{4+}. (b) N(1s) XPS signals for **12** after treatment with various [Ce^{4+}]'s at pH=1 for 12 h. black, as-synthesized **12**; blue, after treatment with 0.3 mM Ce^{4+}; purple, after treatment with 3 mM Ce^{4+}; red, after treatment with 200 mM Ce^{4+}. All the WOR experiments were done in pH =1 HNO_3 solution with 10 μM Ir. (Reprinted with permission from ref [1]. Copyright American Chemical Society 2012)

Table 5.2. Ir / N (pyridine) and Ir / Zr atomic ratios determined from XPS

	Ce^{4+} concentration (mM)[a]	Ir / N (pyridine) atomic ratio	Ir / Zr atomic ratio
11	0 (original MOF)	0.37	0.35
11	3	0.39	0.49
11	200	0.32	2.73
12	0 (original MOF)	0.50	0.53
12	0.3	0.50	0.61
12	3	0.51	1.09
12	10	0.31	3.89
12	200	Pyridine N not observed	Zr not observed

[a]All the reactions were performed in pH = 1 HNO_3 solution for 12 hours.

5.7 Diffuse-reflectance UV-Vis measurements of 11 after water oxidation reactions.

The recovered **11** after treatment with Ce^{4+} (3 mM) overnight was washed with copious amounts of 0.1 M HNO_3 solution. The recovered solid exhibits a green color, suggesting an Ir(IV) species as the catalyst resting state. Note that if the solid is washed with water (pH=7), the green color will slowly change to the original yellow-red color, suggesting that the Ir(IV) species is not stable at neutral pH. Diffuse-reflectance UV-Vis spectrum of the recovered **11** (after washing with 0.1 M HNO_3 solution) was taken by pressing the solids onto a smooth $BaSO_4$ surface. As shown in Figure 5.7a, an additional peak at ~600 nm appears in the solid when compared to **11**, corresponding to the Ir(IV) species at resting state.[9] Interestingly, the Ir(IV) species of the recovered **11** was readily reduced to Ir(III) species by adding a few drops of ethanol to the pressed solid sample (for diffuse reflectance UV-Vis measurements). The spectrum taken after evaporation of ethanol lost the peak at ~600 nm, suggesting a complete reduction of the Ir(IV) species to Ir(III). This reversible oxidation/reduction of the Ir species is consistent with the molecular nature of water oxidation catalysts. The peak intensities of the diffuse-reflectance spectra cannot be exactly reproduced in each measurement due to different sample positions and other experimental variables.

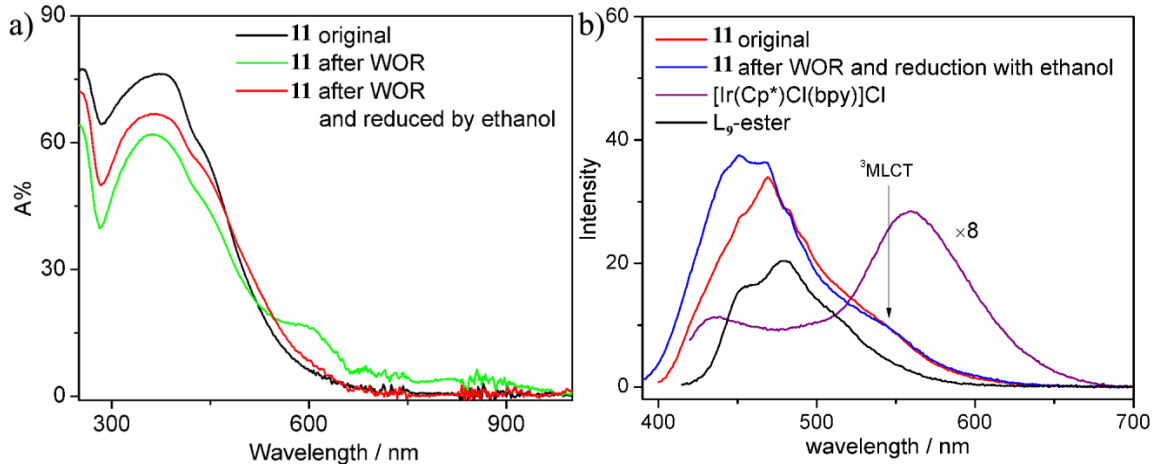

Figure 5.7. (a) Diffuse-reflectance spectra of **11**: original (black), after WOR (green) and after WOR and then reduction with ethanol (red). (b) Fluorescence spectra of **11** before and after WORs. The spectra were taken with an acetonitrile suspension of MOFs with a [Ir] of 0.4 mM. The excitation wavelength was 370 nm and no optical filter was used in the measurement. The **L$_9$**-Me$_2$ and [Ir(Cp*)Cl(bpy)]Cl were dissolved in acetonitrile with a [Ir] of 0.4 mM. WOR condition: 3 mM Ce^{4+} in pH =1 HNO_3 solution with 10 μM Ir. (Reprinted with permission from ref [1]. Copyright American Chemical Society 2012)

5.8 Luminescence spectroscopy of 11 after water oxidation reactions.

$[Cp^*Ir(bpy)Cl]^+$ and its derivatives are weakly luminescent in acetonitrile. Luminescence spectra can sensitively probe the Ir coordination environments. The recovered **11** was reduced to the Ir(III) oxidation state by washing with ethanol and the luminescence spectra were taken with an acetonitrile suspension of the reduced MOF at a [Ir] of 0.4 mM. As shown in Figure 5.7b, the shoulder peak at ~550 nm for **11** before and after WORs was assigned to emission from the triplet metal-to-ligand charge transfer (^{3}MLCT) excited state of the Ir complexes by comparing with the emission spectra of the parent $[Cp^*Ir(bpy)Cl]^+$ complex. The presence of the MLCT emission band after WORs indicated that Ir is still coordinated to the bpy moiety in **11**. The strong emissions at

shorter wavelength are due to the fluorescence of the **bpy-dc** ligand with vibrational fine structures, whereas the different intensities of different vibrational bands of the **bpy-dc** ligand for the samples before and after WORs can be accounted for by modifications of the Cp* ligand during the WOR.

5.9 [Ce^{4+}]-dependent degradation of MOF water oxidation catalysts.

The observed degradation of **12** at 3 mM of Ce^{4+} prompted us to carefully examine the degradation of MOF WOCs during WORs. The degradation of MOF WOCs can be inferred from the kinetic data of WORs as determined by Ce^{4+} consumption rates using UV-Vis spectroscopy. The catalyst decomposition rate is shown to be very sensitive to the [Ce^{4+}].

For **11**-catalyzed reactions, the kinetics of Ce^{4+} consumption becomes much faster when the [Ce^{4+}] exceeds 4.5 mM (Figure 5.8a), suggesting the decomposition of the MOF catalyst to form more active WOCs under these conditions. This decomposition kinetics can be more clearly visualized by plotting [Ce^{4+}]/C_0 vs. t (C_0 is the initial concentration of Ce^{4+}). At $C_0 < 4.5$ mM, [Ce^{4+}]/C_0 decays more slowly as C_0 becomes higher. However, At $C_0 > 4.5$ mM, [Ce^{4+}]/C_0 decays faster as C_0 becomes higher. This [Ce^{4+}]-dependent behavior indicates that MOF decomposition has a high order dependence on [Ce^{4+}].

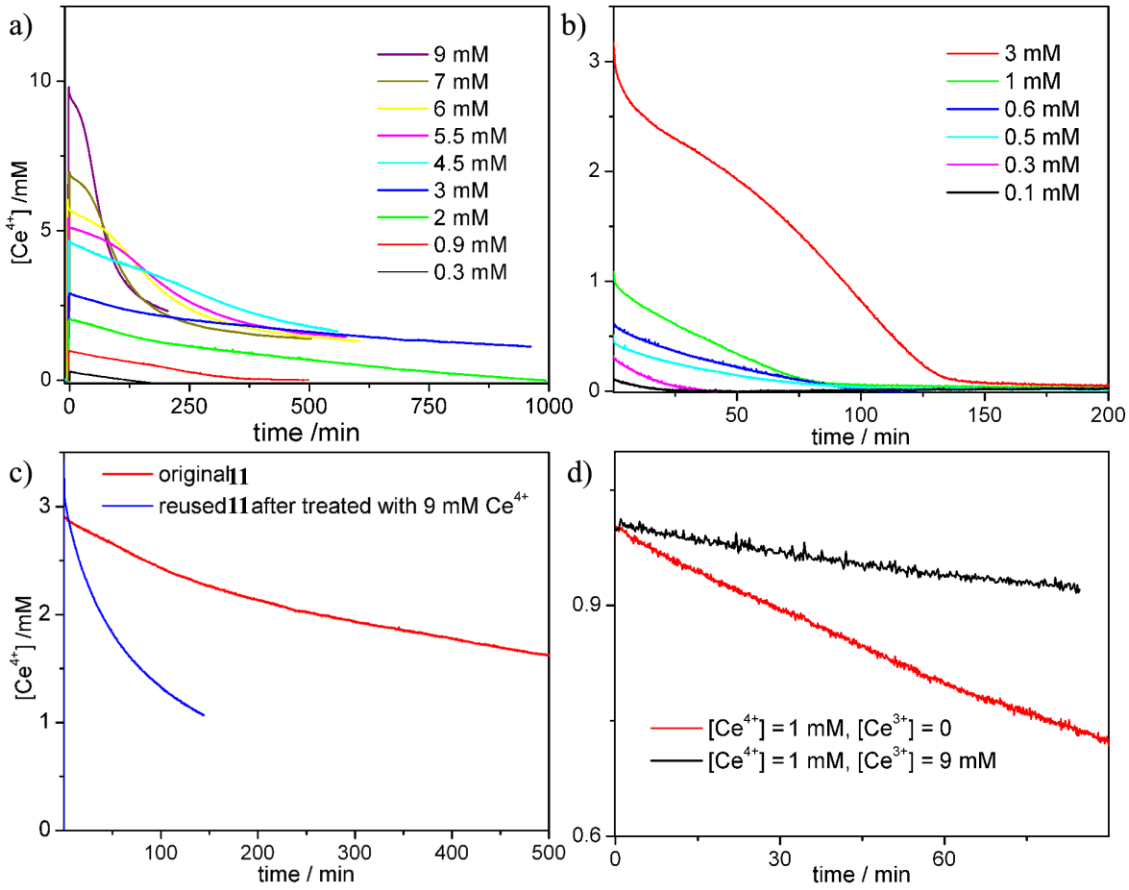

Figure 5.8. (a) $[Ce^{4+}]$-t plots of **11**-catalyzed WORs under different initial $[Ce^{4+}]$'s. (b) $[Ce^{4+}]$-t plots of **12**-catalyzed WORs under different initial $[Ce^{4+}]$'s. (c) $[Ce^{4+}]$-t plots of **11**-catalyzed WORs with an initial $[Ce^{4+}]$ of 3 mM, before and after treatment with 9 mM Ce^{4+}. (d) $[Ce^{4+}]$-t plots of **11** catalyzed-WORs with an initial $[Ce^{4+}]$ of 1.0 mM, in the presence and absence of 9 mM Ce^{3+}. All the WOR experiments were performed in pH =1 HNO_3 solution with 10 μM Ir. (Reprinted with permission from ref [1]. Copyright American Chemical Society 2012)

To further confirm this $[Ce^{4+}]$-dependent decomposition, the MOF after being treated with 9 mM Ce^{4+} was recovered after all of the Ce^{4+} ions were consumed and reused in a new run of water oxidation with 3 mM Ce^{4+}. The recovered MOF showed much faster Ce^{4+} consumption as shown in Figure 5.8c, supporting the decomposition of the MOF at

high [Ce^{4+}]'s. To test if the decomposition is caused by the generated Ce^{3+}, a solution with 1.0 mM Ce^{4+} and 9 mM Ce^{3+} was used in a catalytic run. The added Ce^{3+} slowed the Ce^{4+} consumption rate, ruling out the possibility that Ce^{3+} caused decomposition of the MOF (Figure 5.8d). The slower Ce^{4+} consumption of the Ce^{3+}-added solution is due to slower Ce^{4+} diffusion at a higher total Ce concentration, which will be further discussed in Section 5.5.

UV-Vis data showed that **12** is more prone to decomposition than **11**. At an initial [Ce^{4+}] of 3 mM, **12** quickly decomposed as indicated by the Ce^{4+} consumption rate. The decomposition of **12** is further supported by the observation that at an initial [Ce^{4+}] of 0.5 - 3 mM, the Ce^{4+} consumption rate was much higher for the second catalytic run than the first one.

MOF decomposition was also confirmed by PXRD studies. PXRD patterns of the MOFs were taken at different time points with different initial [Ce^{4+}]'s. The broadening or even disappearance of the PXRD peaks at high [Ce^{4+}]'s is indicative of framework decomposition. Moreover, there is strong correlation between UV-Vis kinetics and PXRD patterns on the onset of MOF decomposition. At higher [Ce^{4+}]'s, the UV-Vis data showed accelerated consumption of Ce^{4+} when the PXRD pattern indicated that MOFs started to decompose. It is likely that the Ir moieties are released into solution to form much more active non-molecular WOCs when the MOF structures collapse, leading to much enhanced Ce^{4+} consumption rates.

To investigate if the MOF decomposition is due to the instability of the SBUs, we synthesized an analogous UiO MOF using the 5-benzoic-2-(4-benzoic-phenyl)-pyridine acid (**ppy-dc**) bridging ligand and $Zr_6O_4(OH)_4(CO_2)_{12}$ SBUs. This Ir-free MOF exhibits

the same UiO topology but adopts an interpenetrated structure as revealed by the systematic absence of the [200] peak in its PXRD pattern. As shown by the PXRD patterns of the MOF after acid and Ce^{4+} treatment, the MOF is stable in pH=1 water solution and is much more stable than **11** and **12** at high [Ce^{4+}]. This control experiment indicates that the UiO framework and SBUs are stable under WOR conditions. The decomposition observed for **11** and **12** at high [Ce^{4+}]'s is thus attributed to degradation of $\mathbf{L_9}$ and $\mathbf{L_{10}}$ moieties under these harsh conditions.

5.10 A diffusion-reaction model for MOF-catalyzed water oxidation

Little is known about kinetics of MOF-catalyzed reactions, due to the difficulty in following MOF-catalyzed reactions and complicated data analysis involving both reaction kinetics and reactant/product diffusion rates. In this Ce^{4+}-driven WOR, however, the reaction can be readily followed by UV-Vis spectroscopy to accurately determine the consumption rate of Ce^{4+}. Kinetic analyses of MOF-catalyzed Ce^{4+}-driven WORs are further simplified due to two factors: 1) water is the reactant whose concentration remains constant throughout the WOR; 2) the product, oxygen molecules, can diffuse quickly and does not require consideration.

Water oxidation experiments were performed at several different initial [Ce^{4+}]'s. The [Ce^{4+}]'s determined from UV-Vis measurements were plotted against reaction time *t*. **11** and **12** exhibited different kinetic behaviors. For **11**, the [Ce^{4+}] – *t* plot is linear at the initial stage, indicating a quasi-zeroth order reaction with respect to [Ce^{4+}]. The deviation from a linear relationship at later times (particularly for higher [Ce^{4+}]'s) is likely due to

the decomposition of MOF catalysts. This quasi-zeroth order reaction rate depends on initial [Ce^{4+}] (Figure 5.9a). For **12**, the ln[Ce^{4+}] – *t* plot is linear at the initial stage, indicating a quasi-first order reaction with respect to [Ce^{4+}] (Figure 5.9b). We will show below that these seemingly different kinetic behaviors can be explained using the same diffusion-reaction model with different Ce^{4+} diffusivities and WOR rates for **11** and **12**.

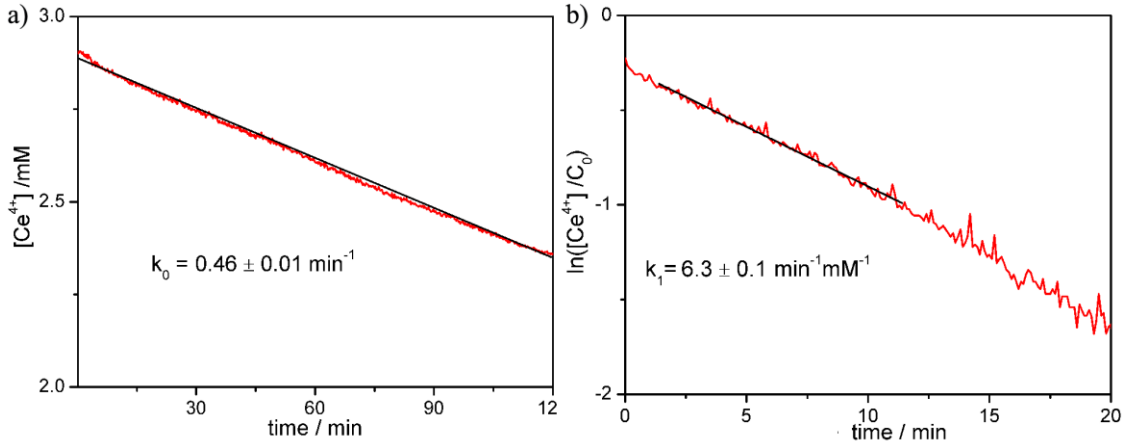

Figure 5.9 (a) [Ce^{4+}] – t plot of **11**-catalyzed water oxidation. The initial [Ce^{4+}] = 2.88 mM. The linear curve indicates a quasi-zeroth order reaction with respect to [Ce^{4+}], leading to a rate constant of k_0 = 0.46 ± 0.01 min^{-1}. (b) ln([Ce^{4+}]/C_0) – t plot of **12**-catalyzed water oxidation. The initial [Ce^{4+}] = 0.32 mM. The linear fitting indicates a quasi-first order reaction with respect to [Ce^{4+}], leading to a rate constant of k_1 = 6.3 ± 0.1 min^{-1} mM^{-1}. All the WOR experiments were performed in pH =1 HNO_3 solution with 10 μM Ir. (Reprinted with permission from ref [1]. Copyright American Chemical Society 2012)

With *c*(*r*,*t*) denoting the [Ce^{4+}] inside a MOF (where *r* is the distance from the center of a spherical MOF particle and *t* is the reaction time), we can write Eq. 5.1 to express *c(r,t)* by considering diffusion of Ce^{4+} inside a MOF particle following Fick's law (the first term) and the WOR catalyzed by the isolated Ir sites with a first-order dependence

on the local [Ce^{4+}] (the second term). The corresponding boundary conditions to describe this diffusion-reaction process inside the MOF particle are shown in Eq 5.2 and Eq 5.3.

$$\frac{\partial c(r,t)}{\partial t} = D\frac{1}{r^2}\frac{\partial}{\partial r}\left(r^2\frac{\partial c(r,t)}{\partial r}\right) - kc(r,t) \qquad \text{(Eq 5.1)}$$

$$t = 0 \quad 0 < r < a,\ c = 0; r = a, c = c_0 \qquad \text{(Eq 5.2)}$$

$$r = a, \quad V\frac{\partial c(r,t)}{\partial t} = -N \cdot 4\pi a^2 D\frac{\partial c(r,t)}{\partial r} \qquad \text{(Eq 5.3)}$$

where the radius of the MOF particle is *a* (the particle is approximated as spherical).

The total solution volume – V = 2 mL

The MOF concentration (the concentration of ligand **L** in the solution) -- C_{MOF} = 10 μM

The Avogadro's constant – $N_A = 6.02\times10^{23}$ mol^{-1}

The volume of unit cell per ligand **L** from the crystal structure – v = 2.4 nm^3

The number of MOF particles in the solution – $N = V\cdot C_{MOF}\cdot N_A\cdot v/(4/3\pi a^3)$

The diffusivity of Ce^{4+} inside MOF – D

The initial [Ce^{4+}] in solution—C_0

The rate constant of reaction inside MOF – k (first order with respect to [Ce^{4+}])

Although Ce^{4+} diffusivity should have a strong dependence on Ce^{4+} and Ce^{3+} concentrations, a constant diffusivity D is assumed in the model based on two approximations: (1) the diffusion of Ce^{4+} or Ce^{3+} in the MOF channel is fast compared to the experimental time scale so that the sum of [Ce^{4+}] + [Ce^{3+}] within the MOF, especially

in the outer-shell that can be reached by Ce^{4+} (see below), quickly reaches the same level of the bulk solution at the very beginning of the experimental measurement; (2) Ce^{4+} and Ce^{3+}, due to the similarity of their chemical structures, have a similar concentration effect on the diffusivity of Ce^{4+}, so that the Ce^{4+} diffusivity only depends on the sum of $[Ce^{4+}]$ + $[Ce^{3+}]$, which is constant throughout the course of reaction.

The first approximation can be validated by calculating a characteristic diffusional time of Ce^{4+}, $t_D = \frac{(\%d_{0.01}a)^2}{D}$ (where $\%d_{0.01}$ is the depth of the outer shell of a MOF particle that can be reached by Ce^{4+} with concentration > 1% of that in the solution.), and comparing it to the experimental time scale. As listed in Table 5.4 and Table 5.5, all of these characteristic diffusional times (0.03 – 0.18 minutes for **11** and 0.004 – 0.014 minutes for **12**) were significantly smaller than the experimental time scale (>1 minute), indicating that the $[Ce^{4+}]$ + $[Ce^{3+}]$ concentration quickly reached the level in the bulk solution at the very beginning of the experiments.

To validate the second approximation of a similar influence of $[Ce^{3+}]$ and $[Ce^{4+}]$ on the diffusivity of Ce^{4+}, we carried out WORs with **11** by adding a mixture of Ce^{3+} and Ce^{4+} to the catalyst. As shown in Figure 5.10a, with different initial Ce^{4+} concentrations (C_0) but the same total Ce concentration ($[Ce^{3+}]+[Ce^{4+}]$), the $[Ce^{4+}]/C_0$ curves nearly overlap with each other, indicating that Ce^{4+} exhibits similar diffusivity in **11** under these conditions. Moreover, the kinetic data with different initial Ce^{3+} and Ce^{4+} concentrations were fitted to the diffusion-reaction model to obtain Ce^{4+} diffusivities. The dependence of Ce^{4+} diffusivities on the sums of $[Ce^{3+}]$ + $[Ce^{4+}]$ only slightly deviates from the dependence of Ce^{4+} diffusivities on the $[Ce^{4+}]$ when pure Ce^{4+} was added to the catalyst at the beginning. (see section 5.11) These results indicate that there is a only slight

difference of the dependence of Ce^{4+} diffusivity on [Ce^{4+}] and [Ce^{3+}], thus validating our approximation of a similar influence of [Ce^{3+}] and [Ce^{4+}] on the diffusivity of Ce^{4+}. Ce^{4+} can be transported into the MOF interior via the Ce^{4+}/Ce^{3+} self-exchange in addition to the direct diffusion of Ce^{4+} through the channels. However, the negligible dependence of Ce^{4+} diffusivity on Ce^{3+}/Ce^{4+} ratios indicates that the self-exchange pathway is not significant in these reactions.

The reaction rate law of a single catalyst site in the MOF can be estimated from kinetic measurements of homogeneous catalysts. The reaction rate dependence of HOMO-**1** (see scheme 5.1) on [Ce^{4+}] was reported to be of the 0.7th order.[23] Our own measurements also confirmed that the rate dependence slightly deviates from the first order, which is presumably due to the decomposition of the WOC during the course of the reaction. To account for less decomposition of the WOC in the MOF and to simplify mathematical derivations, we approximated the rate dependence to be first order and determined a rate constant of 100 $min^{-1}\cdot mM^{-1}$ using HOMO-**1**. A similar approximation was applied to HOMO-**2** with a rate constant of 200 $min^{-1}\cdot mM^{-1}$. HOMO-**2** was chosen as the homogeneous model because the aromatic amine is protonated at pH =1 to increase the catalyst solubility in water.

Eq 5.1 was solved by Laplace transformation under the boundary conditions of Eq 5.2 and Eq 5.3 (See Section 5.11 detailed approximations and mathematical derivations).[41] The obtained infinite summation solution was simplified by approximating an elliptic theta function to a simpler piecewise function.

Assuming the [Ce^{4+}] in the bulk solution C_s (which can be detected by UV-Vis measurements) equals the [Ce^{4+}] on the MOF surface, Eq 5.4 was then obtained, which describes the quasi-first order kinetic behavior for the **12**-catalyzed reaction. The amount of Ce^{4+} inside the MOF at a given time was insignificant (< 0.0043%) compared to the amount in the solution and can be ignored in the C_s quantification.

$$\frac{dln(\frac{c_s}{c_0})}{dt} = -\beta\frac{\sqrt{kD}}{a}(1-\frac{1}{a}\sqrt{\frac{D}{k}}) \qquad \text{(eq 5.4)}$$

Here β is defined as $= \frac{N\cdot 4\pi a^3}{V}$. For **11**, however, a further linearization approximation can be made (see section 5.11), leading to a quasi-zeroth order reaction described by:

$$\frac{d\frac{c_s}{c_0}}{dt} = -\beta\frac{\sqrt{kD}}{a}(1-\frac{1}{a}\sqrt{\frac{D}{k}}) \qquad \text{(eq 5.5)}$$

This linearization approximation will only hold when $\beta\frac{\sqrt{kD}}{a}\left(1-\frac{1}{a}\sqrt{\frac{D}{k}}\right)t \ll 1$. The validity of this assumption for **11** but not for **12** can be verified by calculating a characteristic time $t_a = {1}\Big/{\beta\frac{\sqrt{kD}}{a}\left(1-\frac{1}{a}\sqrt{\frac{D}{k}}\right)}$. Only when $t_a \gg t$, the approximation holds. As shown in Table 5.4 and Table 5.5, $t_a \gg t$ holds for **11** (120 – 670 minutes) but does not hold for **12** (12 – 55 minutes). This difference in t_a explains different kinetic behaviors of the two MOFs.

By fitting the experimental data to these equations, the Ce^{4+} diffusivity values were obtained (Table 5.3). As expected, the Ce^{4+} diffusivities determined from these analyses are highly dependent on the Ce concentration: the lower the concentration, the higher the

diffusivity. Ce^{4+} diffusivities in **12** are significantly larger than those in **11**, consistent with the expectation that positively charged species should diffuse faster through neutral channels in **12** than through positively charged channels in **11**.

Table 5.3 Diffusivities of Ce^{4+} at different initial [Ce^{4+}]'s in **11** and **12**.

11		**12**	
c_0 (mM)	D ($/10^{-11}$ cm^2s^{-1})	c_0 (mM)	D ($/10^{-11}$ cm^2s^{-1})
0.29	1.52	0.11	67.9
0.98	0.221	0.30	38.8
2.03	0.099	0.40	41.0
2.88	0.053	0.51	4.6
4.61	0.050	0.61	4.1
5.69	0.046	1.09	3.4
6.97	0.046		

As the experimental time scale is significantly larger than the characteristic diffusional time $t_D = \frac{a^2}{D}$, the diffusion-reaction process inside these MOFs are at the steady-state. With the kinetic model, the Ce^{4+} distributions inside the MOFs at the steady-state can be calculated, using the following equation (see section 5.11 for details)

$$\frac{c}{c_s} = \frac{a}{r} \cdot \frac{\sinh(\sqrt{\frac{k}{D}}r)}{\sinh(\sqrt{\frac{k}{D}}a)} \qquad \text{(eq 5.6)}$$

The [Ce^{4+}] inside the MOF relative to that in the solution C/C_s at the steady state with a total Ce concentration of 1mM is plotted in Figure 5.10b. Because of the fast reaction rate and relatively slow diffusion rate, the Ce^{4+} can only diffuse into the particle of **11** at

~11% in depth (30% in volume for a spherical object) before being consumed for the WOR to form Ce^{3+} (with $[Ce^{4+}] < 1\%\ C_s$). As the diffusion of Ce^{4+} in **12** is much faster, Ce^{4+} can diffuse deeper inside the particle (27% in depth and 61% in volume) before being reduced to Ce^{3+}.

The uneven distribution of Ce^{4+} inside the MOF particle in this diffusion-reaction model perfectly explains the fact that the original Cp*Ir catalysts were still observed from digested samples of the recovered **11** in spite of extensive oxidative degradation of the Cp* rings. Based on this diffusion-reaction model, the outer shell of the MOF particles can be oxidatively modified, while the interior of the MOF particle is seldom reached by Ce^{4+} and remains intact. As a result, both the original unmodified complexes and oxidatively modified complexes were observed in the digested samples of the recovered **11**.

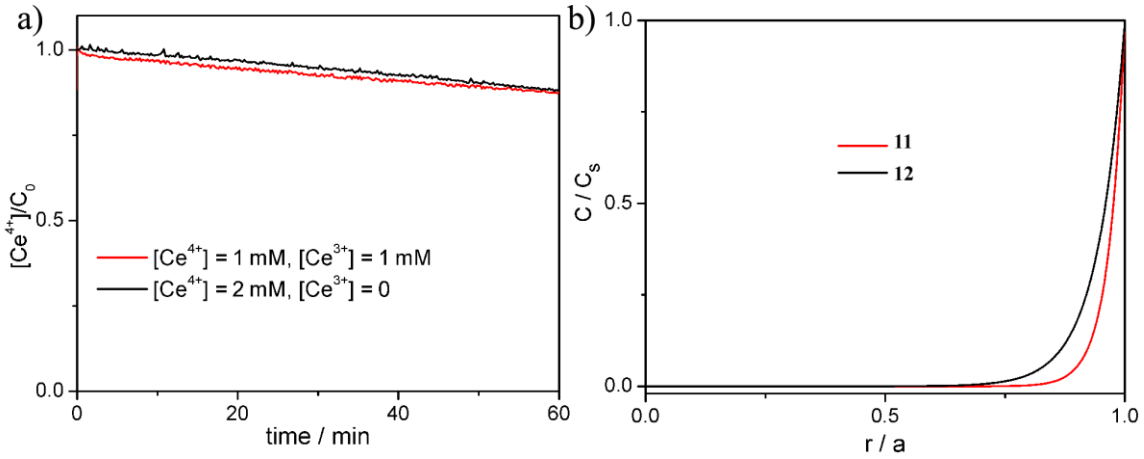

Figure 5.10 (a) Ce^{4+} consumption monitored by UV-Vis spectroscopy at 420 nm for **11** with an initial $[Ce^{4+}]$ of 1 mM and a $[Ce^{3+}]$ of 1 mM (red), vs. a $[Ce^{4+}]$ of 2 mM and a a $[Ce^{3+}]$ of 0 mM (black). The overlap of these two curves indicates similar influence of $[Ce^{4+}]$ and $[Ce^{3+}]$ on the diffusivity of Ce^{4+}. The experiments were performed in pH =1 HNO_3 solution with 10 μM Ir. (b) Ce^{4+} distributions inside the particles of **11** and **12**. The

initial [Ce^{4+}] is 1 mM. C_s is the [Ce^{4+}] in the solution. (Reprinted with permission from ref [1]. Copyright American Chemical Society 2012)

5.11 The detailed derivation of the Diffusion-Reaction Kinetic Model for MOF-Catalyzed Reactions

5.11.1 Derivation of the diffusion-reaction model to describe MOF kinetics.

The diffusion equation and boundary conditions can be written as

$$\frac{\partial c}{\partial t} = D\frac{1}{r^2}\frac{\partial}{\partial r}\left(r^2\frac{\partial c}{\partial r}\right) - kc \qquad \text{(eq 5.1)}$$

$$t = 0 \quad 0 < r < a,\ c = 0; r = a, c = c_0 \qquad \text{(eq 5.2)}$$

$$r = a, \quad V\frac{\partial c}{\partial t} = -N \cdot 4\pi a^2 D\frac{\partial c}{\partial r} \qquad \text{(eq 5.3)}$$

let $\beta = \frac{N\cdot 4\pi a^3}{V} = 3\frac{N\cdot 4/3\pi a^3}{V} = 3\frac{V_{MOF}}{V} = 3c_{MOF}N_A v = 4.3\times 10^{-5}$

then (eq 5.3) can be transformed to $r = a, \quad \frac{\partial c}{\partial t} = -\frac{\beta D}{a}\frac{\partial c}{\partial r}$ (eq 5.7)

Now solve this partial differential equation, we get

$$c = c_0\left(\sum_{n=1}^{\infty}\frac{\frac{asin\lambda_n r}{rsin\lambda_n a}e^{p_n t}}{1+\frac{\beta}{2}-\frac{p_n}{2D\lambda_n^2}+\frac{a^2p_n^2}{2\beta D^2\lambda_n^2}}\right) \qquad \text{(eq 5.8)}$$

where p_n 's and λ_n 's are the n[th] roots of the equations

$$\frac{a^2}{\beta D}p - 1 + \lambda a\cdot cot\lambda a = 0 \qquad \text{(eq 5.9)}$$

$$\lambda^2 = -\frac{p+k}{D} \qquad \text{(eq 5.10)}$$

Now change these entities into unitless quantities.

let $q_n = \frac{p_n}{k}$, $\gamma = \frac{D}{a^2 k}$, $\kappa_n = a\lambda_n$, $s = \frac{r}{a}$, $\tau = kt$

equation (eq 5.8) can be converted to

$$\frac{c}{c_0} = \sum_{n=1}^{\infty}\frac{\frac{sin\kappa_n s}{s\cdot sin\kappa_n}e^{q_n\tau}}{1+\frac{\beta}{2}+\frac{q_n}{2(q_n+1)}-\frac{q_n^2}{2\beta\gamma(q_n+1)}} \qquad \text{(eq 5.11)}$$

and equation (eq 5.9) and (eq 5.10) are converted to

$$\frac{q}{\beta\gamma} - 1 + \kappa\cdot cot\kappa = 0 \qquad \text{(eq 5.12)}$$

$q = -\gamma\kappa^2 - 1$ (eq 5.13)

as we know $\beta = 4.3\times10^{-6} \ll 1$. An estimation on γ is that $\gamma < 10^{-3}$

Under these conditions, the real number roots of equations (eq 5.12) and (eq 5.13) are

$\kappa_n \approx \pm n\pi$, $q_n \approx -\gamma(n\pi)^2 - 1$ (n = 1,2,…) (eq 5.14)

while the imaginary solution is $\kappa_i \approx i/\sqrt{\gamma}$, $q_i \approx \beta\gamma\left(1 - \sqrt{\frac{1}{\gamma}}coth\sqrt{\frac{1}{\gamma}}\right)$ (eq 5.15)

the concentration of Ce^{4+} in the solution is equal to that on the MOF surface $c_s(t) = c(r,t)|_{r=a}$

then $\frac{c_s}{c_0} = \frac{e^{q_i\tau}}{1+\frac{\beta}{2}+\frac{q_i}{2(q_i+1)}-\frac{q_i^2}{2\beta\gamma(q_i+1)}} + \sum_{n=1}^{\infty}\frac{e^{q_n\tau}}{1+\frac{\beta}{2}+\frac{q_n}{2(q_n+1)}-\frac{q_n^2}{2\beta\gamma(q_n+1)}}$ (eq 5.16)

Denote the first term as

$$F_i(\tau) = \frac{e^{q_i\tau}}{1+\frac{\beta}{2}+\frac{q_i}{2(q_i+1)}-\frac{q_i^2}{2\beta\gamma(q_i+1)}} \approx e^{q_i\tau}\left(1 - \frac{\beta}{2} - \frac{q_i}{2} + \frac{q_i^2}{2\beta\gamma}\right) = e^{q_i\tau}\left(1 - \frac{\beta}{2}\left[1 + \sqrt{\gamma}Coth\frac{1}{\sqrt{\gamma}} - \left(Coth\frac{1}{\sqrt{\gamma}}\right)^2\right]\right)$$ (eq 5.17)

Denote the second term as

$$F_n(\tau) = \sum_{n=1}^{\infty}\frac{e^{q_n\tau}}{1+\frac{\beta}{2}+\frac{q_n}{2(q_n+1)}-\frac{q_n^2}{2\beta\gamma(q_n+1)}} \approx 2\beta\gamma\sum_{n=1}^{\infty}\frac{-(q_n+1)e^{q_n\tau}}{q_n^2} = \beta\gamma\left(\sum_{n=1}^{\infty}\frac{2e^{-[\gamma(n\pi)^2+1]\tau}}{\gamma(n\pi)^2+1} - \sum_{n=1}^{\infty}\frac{2e^{-[\gamma(n\pi)^2+1]\tau}}{[\gamma(n\pi)^2+1]^2}\right)$$ (eq 5.18)

Now let $A(\tau) = \sum_{n=1}^{\infty}\frac{2e^{-[\gamma(n\pi)^2+1]\tau}}{\gamma(n\pi)^2+1}$ and $B(\tau) = -\sum_{n=1}^{\infty}\frac{2e^{-[\gamma(n\pi)^2+1]\tau}}{[\gamma(n\pi)^2+1]^2}$

then $F_n(\tau) = \beta\gamma[A(\tau) + B(\tau)]$ (eq 5.19)

$\frac{dB(\tau)}{d\tau} = A(\tau)$ (eq 5.20)

$$\frac{dA(\tau)}{d\tau} = -\sum_{n=1}^{\infty}2e^{-[\gamma(n\pi)^2+1]\tau} = e^{-\tau}\left[1 - EllipticTheta\left(3,0,e^{-\gamma\pi^2\tau}\right)\right] \approx \begin{cases} e^{-\tau}\left[1 - \frac{1}{\sqrt{\gamma\pi\tau}}\right] & ,when\ \tau < \frac{a_0}{\gamma\pi^2} \\ -e^{-\tau}\sqrt{\pi}e^{-\gamma\pi^2\tau} & ,when\ \tau \geq \frac{a_0}{\gamma\pi^2} \end{cases}$$ (eq 5.21)

$$a_0\ is\ the\ root\ to\ the\ equation\ \frac{1}{\sqrt{a_0}} = \frac{1}{\sqrt{\pi}} + e^{-a_0}\ , a_0 = 2.18129$$

$$A(0) = \sum_{n=1}^{\infty} \frac{2}{\gamma(n\pi)^2 + 1} = -1 + \sqrt{\frac{1}{\gamma}} coth \sqrt{\frac{1}{\gamma}}$$

$A(\tau) = A(0) + \int_0^{\tau} \frac{dA(\tau)}{d\tau} d\tau$ (eq 5.22)

$$when\ \tau < \frac{a_0}{\gamma\pi^2}$$

$A(\tau) = -e^{-\tau} - \frac{1}{\sqrt{\gamma}} Erf\left(\sqrt{\tau}\right) + \sqrt{\frac{1}{\gamma}} coth \sqrt{\frac{1}{\gamma}}$ (eq 5.23)

$$when\ \tau \geq \frac{a_0}{\gamma\pi^2}$$

$A(\tau) = -\frac{\sqrt{\frac{\pi}{a_0}} + \gamma\pi^2}{1+\gamma\pi^2} e^{-\frac{a_0}{\gamma\pi^2}} - \frac{1}{\sqrt{\gamma}} Erf\left(\frac{\sqrt{a_0}}{\sqrt{\gamma}\pi}\right) + \sqrt{\frac{1}{\gamma}} coth \sqrt{\frac{1}{\gamma}} + \frac{\sqrt{\pi}}{1+\gamma\pi^2} e^{-(1+\gamma\pi^2)\tau} \approx -\frac{1}{\sqrt{\gamma}} + \sqrt{\frac{1}{\gamma}} coth \sqrt{\frac{1}{\gamma}} + \frac{\sqrt{\pi}}{1+\gamma\pi^2} e^{-(1+\gamma\pi^2)\tau}$ (eq 5.24) Here the assumption of $\gamma < 0.1$ is used

$$B(0) = -\sum_{n=1}^{\infty} \frac{2}{[\gamma(n\pi)^2 + 1]^2} = 1 - \frac{1}{2\sqrt{\gamma}} Coth\left(\frac{1}{\sqrt{\gamma}}\right) - \frac{1}{2\gamma} [Csch\left(\frac{1}{\sqrt{\gamma}}\right)]^2$$

$B(\tau) = B(0) + \int_0^{\tau} A(\tau) d\tau$ (eq 5.25)

$$when\ \tau < \frac{a_0}{\gamma\pi^2}$$

$B(\tau) = e^{-\tau} - \frac{1}{\sqrt{\gamma}} \left[\frac{e^{-\tau}\sqrt{\tau}}{\sqrt{\pi}} + \left(\tau - \frac{1}{2}\right) Erf\left(\sqrt{\tau}\right)\right] + \sqrt{\frac{1}{\gamma}} coth \sqrt{\frac{1}{\gamma}} \tau - \frac{1}{2\sqrt{\gamma}} Coth\left(\frac{1}{\sqrt{\gamma}}\right) - \frac{1}{2\gamma} [Csch\left(\frac{1}{\sqrt{\gamma}}\right)]^2$ (eq 5.26)

$$when\ \tau \geq \frac{a_0}{\gamma\pi^2}$$

$B(\tau) = \frac{1}{2\sqrt{\gamma}} - \frac{1}{2\sqrt{\gamma}} Coth\left(\frac{1}{\sqrt{\gamma}}\right) - \frac{1}{2\gamma} [Csch\left(\frac{1}{\sqrt{\gamma}}\right)]^2 + \left[-\frac{1}{\sqrt{\gamma}} + \sqrt{\frac{1}{\gamma}} coth \sqrt{\frac{1}{\gamma}}\right] \tau - \frac{\sqrt{\pi}}{(1+\gamma\pi^2)^2} e^{-(1+\gamma\pi^2)\tau}$ (eq 5.27)

After these evaluations, we can get expression for $F_n(\tau)$

When $\tau < \frac{a_0}{\gamma\pi^2}$

$$F_n(\tau) = \beta\gamma\{-\frac{1}{\sqrt{\gamma}}\left[\frac{e^{-\tau}\sqrt{\tau}}{\sqrt{\pi}} + \left(\tau + \frac{1}{2}\right) Erf\left(\sqrt{\tau}\right)\right] + \sqrt{\frac{1}{\gamma}} Coth\sqrt{\frac{1}{\gamma}}\tau + \frac{1}{2\sqrt{\gamma}} Coth\left(\frac{1}{\sqrt{\gamma}}\right) - \frac{1}{2\gamma}\left[Csch\left(\frac{1}{\sqrt{\gamma}}\right)\right]^2\}$$ (eq 5.28)

$$\frac{c_s}{c_0} = F_i(\tau) + F_n(\tau) = e^{\beta\left(\gamma - \sqrt{\gamma} Coth\sqrt{\frac{1}{\gamma}}\right)\tau}\left(1 - \frac{\beta}{2}[1 + \sqrt{\gamma} Coth\frac{1}{\sqrt{\gamma}} - \left(Coth\frac{1}{\sqrt{\gamma}}\right)^2]\right) + \beta\gamma\left(-\frac{1}{\sqrt{\gamma}}\left[\frac{e^{-\tau}\sqrt{\tau}}{\sqrt{\pi}} + \left(\tau + \frac{1}{2}\right) Erf\left(\sqrt{\tau}\right)\right] + \sqrt{\frac{1}{\gamma}} Coth\sqrt{\frac{1}{\gamma}}\tau + \frac{1}{2\sqrt{\gamma}} Coth\left(\frac{1}{\sqrt{\gamma}}\right) - \frac{1}{2\gamma}\left[Csch\left(\frac{1}{\sqrt{\gamma}}\right)\right]^2\right)$$

$$\approx 1 - \beta\gamma\tau\left(\frac{1}{\sqrt{\gamma}} Erf\left(\sqrt{\tau}\right) - 1\right) - \beta\sqrt{\gamma}\left[\frac{e^{-\tau}\sqrt{\tau}}{\sqrt{\pi}} + \frac{1}{2} Erf\left(\sqrt{\tau}\right)\right]$$ (eq 5.29)

At the experimental time scale, we know $\tau \gg 1$

so $\frac{c_s}{c_0} \approx 1 - \beta\gamma\tau\left(\frac{1}{\sqrt{\gamma}} - 1\right) - \frac{\beta}{2}\sqrt{\gamma} \approx 1 - \beta\gamma\tau\left(\frac{1}{\sqrt{\gamma}} - 1\right)$ (eq 5.30)

When $\tau \geq \frac{a_0}{\gamma\pi^2}$

$$F_n(\tau) = \beta\gamma\{-\frac{1}{2\sqrt{\gamma}} + \frac{1}{2\sqrt{\gamma}} Coth\left(\frac{1}{\sqrt{\gamma}}\right) - \frac{1}{2\gamma}\left[Csch\left(\frac{1}{\sqrt{\gamma}}\right)\right]^2 + \left[-\frac{1}{\sqrt{\gamma}} + \sqrt{\frac{1}{\gamma}} coth\sqrt{\frac{1}{\gamma}}\right]\tau + \frac{\gamma\pi^2\sqrt{\pi}}{(1+\gamma\pi^2)^2} e^{-(1+\gamma\pi^2)\tau}\}c$$ (eq 5.31)

$$\frac{c_s}{c_0} = F_i(\tau) + F_n(\tau) = e^{\beta\left(\gamma - \sqrt{\gamma} Coth\sqrt{\frac{1}{\gamma}}\right)\tau}\left(1 - \frac{\beta}{2}[1 + \sqrt{\gamma} Coth\frac{1}{\sqrt{\gamma}} - \left(Coth\frac{1}{\sqrt{\gamma}}\right)^2]\right) + \beta\gamma\left\{-\frac{1}{2\sqrt{\gamma}} + \frac{1}{2\sqrt{\gamma}} Coth\left(\frac{1}{\sqrt{\gamma}}\right) - \frac{1}{2\gamma}\left[Coth\left(\frac{1}{\sqrt{\gamma}}\right)\right]^2 + \frac{1}{2\gamma} + \left[-\frac{1}{\sqrt{\gamma}} + \sqrt{\frac{1}{\gamma}} coth\sqrt{\frac{1}{\gamma}}\right]\tau + \frac{\gamma\pi^2\sqrt{\pi}}{(1+\gamma\pi^2)^2} e^{-(1+\gamma\pi^2)\tau}\right\} \approx e^{\beta\left(\gamma - \sqrt{\gamma} Coth\sqrt{\frac{1}{\gamma}}\right)\tau} + \beta\gamma\left[-\frac{1}{\sqrt{\gamma}} + \sqrt{\frac{1}{\gamma}} coth\sqrt{\frac{1}{\gamma}}\right]\tau - \frac{\beta}{2}(\sqrt{\gamma}) = e^{-\beta\gamma\tau\left(\frac{1}{\sqrt{\gamma}} - 1\right)} + e^{-\beta\gamma\tau\left(\frac{1}{\sqrt{\gamma}} - 1\right)}\left(e^{\beta\left(\sqrt{\gamma} - \sqrt{\gamma} Coth\sqrt{\frac{1}{\gamma}}\right)\tau} - 1\right) + \beta\gamma\left[-\frac{1}{\sqrt{\gamma}} + \sqrt{\frac{1}{\gamma}} coth\sqrt{\frac{1}{\gamma}}\right]\tau - \frac{\beta}{2}(\sqrt{\gamma} + 1) \approx e^{-\beta\gamma\tau\left(\frac{1}{\sqrt{\gamma}} - 1\right)} + \left(1 - e^{-\beta\gamma\tau\left(\frac{1}{\sqrt{\gamma}} - 1\right)}\right)\beta\gamma\left[-\frac{1}{\sqrt{\gamma}} + \sqrt{\frac{1}{\gamma}} coth\sqrt{\frac{1}{\gamma}}\right]\tau - \frac{\beta}{2}(\sqrt{\gamma}) \approx e^{-\beta\gamma\tau\left(\frac{1}{\sqrt{\gamma}} - 1\right)}$$ (eq 5.32)

Here again we used the assumption that $\gamma < 0.1$

if $|\beta\gamma\tau\left(\frac{1}{\sqrt{\gamma}} - 1\right)| \ll 1$

$$\frac{c_s}{c_0} \approx 1 - \beta\gamma\tau\left(\frac{1}{\sqrt{\gamma}} - 1\right)$$ (eq 5.33)

It is easy to prove that under experimental condition $\tau \geq \frac{a_0}{\gamma\pi^2}$

The condition of $|\beta\gamma\tau(\frac{1}{\sqrt{\gamma}}-1)| \ll 1$ applies for **11**, and does not apply for **12**, leading to quasi-zeroth order reaction for **11** with respect to [Ce^{4+}] and quasi-first order reaction for **12** with respect to [Ce^{4+}]

Now change the parameters back to the parameters with units

$\frac{d\frac{c_S}{c_0}}{dt} = -\beta\frac{\sqrt{kD}}{a}(1-\frac{1}{a}\sqrt{\frac{D}{k}})$ (eq 5.5) for **11**

$\frac{dln(\frac{c_S}{c_0})}{dt} = -\beta\frac{\sqrt{kD}}{a}(1-\frac{1}{a}\sqrt{\frac{D}{k}})$ (eq 5.4) for **12**

5.11.2 Ce^{4+} diffusivities inside 11 and 12 and justification of the approximations

In order to derive information on the diffusivity, we must make assumptions on the reaction rate.

If we assume that the activity of the catalyst inside the MOF is exactly the same as that of the homogeneous compound, as the concentration of ligand inside MOF is $1/(N_A\nu)$ = 0.69 M, we obtained the rate constant inside MOF as k = 0.100 $min^{-1}\mu M^{-1}\times 0.69M = 6.9\times10^4$ min^{-1} for **11** and k = 0.210 $min^{-1}\mu M^{-1}\times 0.69M = 1.4\times10^5$ min^{-1} for **12**. The average radius of the MOF particles can be obtained from the SEM/TEM images to be a = 400 nm. $\beta = 4.3\times10^{-5}$ is what we have already calculated above.

For **11**, $-\frac{d\frac{c_S}{c_0}}{kdt} = \frac{C_{MOF}k_0}{c_0k} = \frac{k_0}{Qk}$ is what we obtained experimentally (Q is the number of equivalents of Ce^{4+} added with respect to the MOF concentration).

Solving equation 5.5 for *D*, we can obtain the values for diffusivities.

With the numbers obtained we can check if the condition $\left|\beta\gamma\tau\left(\frac{1}{\sqrt{\gamma}}-1\right)\right| \ll 1$ holds. To do this, we can calculate the characteristic time $t_a = 1/[\beta\gamma k\left(\frac{1}{\sqrt{\gamma}}-1\right)]$. Only when t $\ll t_a$, the approximation can be valid. As listed in Table 5.4. $t \ll t_a$ can be well fulfilled at the intial stage of the reaction.

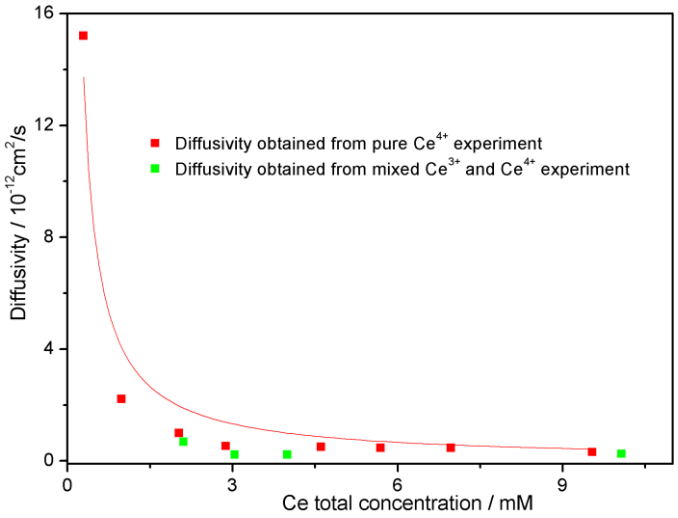

Figure 5.11 Comparison of the diffusivities of Ce^{4+} in **11** obtained from experiments with different initial concentrations of Ce^{4+} and Ce^{3+}. The red squares are for reactions with initial Ce^{4+} only whereas the green squares are for initial mixtures of both Ce^{3+} and Ce^{4+} (**[Ce^{4+}]** = 1 mM, **[Ce^{3+}]** = 0, 1, 2, 3, 9 mM). The red line is an exponential fitting of diffusivities with different total Ce concentrations. (Reprinted with permission from ref [1]. Copyright American Chemical Society 2012)

Table 5.4. Diffusivities of Ce^{4+} at different initial Ce^{4+} concentrations for **11**.

c_0 /mM	Q	k_0 /min^{-1}	$-\frac{a\frac{c_S}{c_0}}{\beta d\tau}$ /10^{-3}	$\gamma = \frac{D}{a^2 k}$ /10^{-5}	D /10^{-11} cm^{2}s^{-1}	t_a/min	t_D/min	%$d_{0.01}$	%$V_{0.01}$

0.29	29	0.247	2.87	0.83	1.52	120	0.03	26%	59%
0.98	98	0.324	1.11	0.12	0.221	300	0.07	16%	40%
2.03	203	0.443	0.73	0.054	0.099	460	0.11	13%	34%
2.88	288	0.459	0.54	0.029	0.053	630	0.15	11%	30%
4.61	461	0.707	0.52	0.027	0.050	650	0.16	11%	30%
5.69	569	0.843	0.50	0.025	0.046	670	0.18	11%	30%
6.97	697	1.05	0.51	0.025	0.046	670	0.18	11%	30%

Table 5.5. Diffusivities of Ce^{4+} at different initial Ce^{4+} concentrations for **12**.

c_0 /mM	k_1 /min^{-1}μM^{-1}	$-\frac{dln\frac{c_S}{c_0}}{\beta d\tau}$ /10^{-3}	$\gamma = \frac{D}{a^2k}$ /10^{-5}	D /10^{-11} cm^{2}s^{-1}	t_a/min	t_D/min	%$d_{0.01}$	%$V_{0.01}$
0.11	0.0080	5.74	18.2	67.9	12	0.004	66%	96%
0.30	0.0061	2.23	10.4	38.8	16	0.005	54%	90%
0.40	0.0063	1.47	11.0	41.0	16	0.005	56%	91%
0.51	0.0021	1.07	1.22	4.6	47	0.012	29%	65%
0.61	0.0020	1.03	1.11	4.1	50	0.013	29%	63%
1.09	0.0018	1.00	0.90	3.4	55	0.014	27%	61%

For **12**, $-\frac{dln\frac{c_S}{c_0}}{kdt} = \frac{c_{MOF}k_1}{k} = \frac{c_{MOF}k_1}{k}$ is what we obtained experimentally. Solving equation 5.4 for *D*, we can obtain the values for diffusivities.

If we calculate the characteristic time $t_a = 1/[\beta\gamma k\left(\frac{1}{\sqrt{\gamma}} - 1\right)]$ for **12**, we see that these $t_a's$ are comparable to the experimental timescale which is the reason why it cannot be approximated to quasi-zeroth order reaction with respect to [Ce^{4+}].

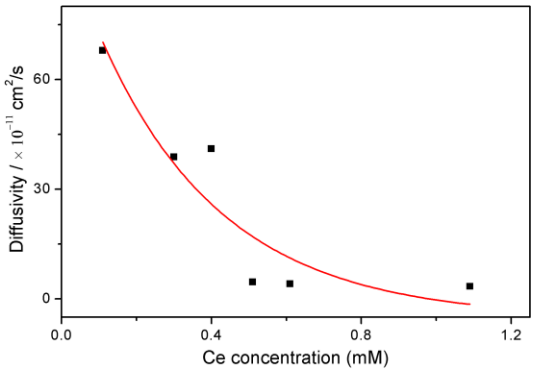

Figure 5.12 Dependence of diffusivity of Ce^{4+} in **12** on Ce concentration. (Reprinted with permission from ref [1]. Copyright American Chemical Society 2012)

5.11.3 Ce^{4+} distributions inside the MOFs at steady state conditions

The timescale of diffusion can be evaluated by the characteristic diffusion time $t_D = \frac{(\%d_{0.01}a)^2}{D}$, where a is the radius of MOF particles, and $\%d_{0.01}$ is the depth Ce^{4+} can penetrate with >1% concentration with respect to that in the solution. As shown in Table 5.4 and 5.5. Within experimental time, $t \gg t_D$ can be reached, that is when steady-state condition can be applied to the system.

$$\frac{\partial c}{\partial t} = 0 = D\frac{1}{r^2}\frac{\partial}{\partial r}\left(r^2\frac{\partial c}{\partial r}\right) - kc \quad \text{(eq 5.34)}$$

the boundary condition is $c|_{r=a}=c_s$ (eq 5.35)

It is straightforward to solve this equation to obtain:

$$\frac{c}{c_s} = \frac{a}{r}\cdot\frac{e^{\sqrt{\frac{k}{D}}r} - e^{-\sqrt{\frac{k}{D}}r}}{e^{\sqrt{\frac{k}{D}}a} - e^{-\sqrt{\frac{k}{D}}a}} = \frac{a}{r}\cdot\frac{\sinh(\sqrt{\frac{k}{D}}r)}{\sinh(\sqrt{\frac{k}{D}}a)} = \frac{1}{s}\cdot\frac{\sinh(\sqrt{\frac{1}{\gamma}}s)}{\sinh(\sqrt{\frac{1}{\gamma}})} \quad \text{(eq 5.6)}$$

The concentration changes dramatically near the surface of the particles. We can depict the concentration changes of $\frac{c}{c_s}$ vs $\frac{r}{a}$, choosing D = 1.1×10^{-12} cm^2/s.

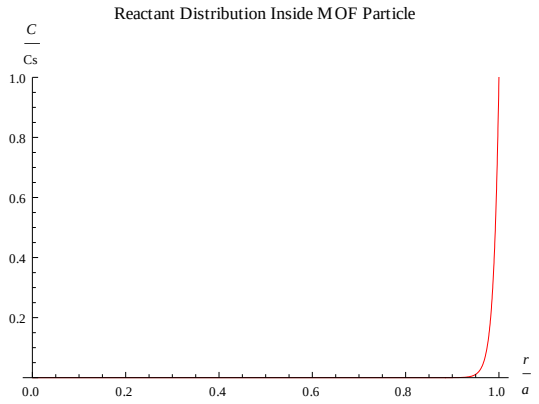

Figure 5.13 Ce^{4+} distribution inside the **11** particle with a total Ce concentration of 3 mM. (Reprinted with permission from ref [1]. Copyright American Chemical Society 2012)

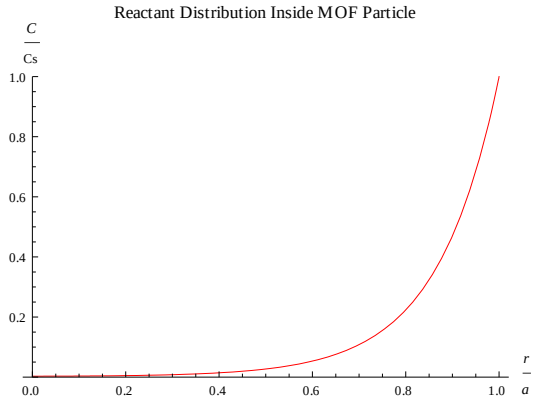

Figure 5.14 Ce^{4+} distribution inside the **12** particle with a total Ce concentration of 0.3 mM. (Reprinted with permission from ref [1]. Copyright American Chemical Society 2012)

If we want to calculate the position inside MOF at which the Ce^{4+} concentration drops to 1% of that in the solution, we can let $\frac{c}{c_s} = 0.01$ and solve equation 5.6. The number we

obtained is the r/a ratio at this point. The depth percentage of MOF outer shell reached by Ce^{4+} with >1% concentration can be expressed as

$$\%d_{0.01} = [1 - (r/a)_{0.01}] \times 100\% \qquad \text{(eq 5.36)}$$

The volume percentage of MOF outer shell reached by Ce^{4+} with >1% concentration is then

$$\%V_{0.01} = [1 - (1 - \%d_{0.01})^3] \times 100\% \qquad \text{(eq 5.37)}$$

These calculated values are listed in Table 5.3 and 5.4

It is obvious that although the diffusivity of Ce^{4+} inside the MOF is large enough for fast diffusion of Ce^{4+} into the MOF, at reaction-diffusion equilibrium, when the reaction rate is high enough, the supply of diffusional flux of reactants will be consumed by the first few layers of catalysts close to the particle surface, leading to a sharp decrease of Ce^{4+} concentration inside the MOF. The overall reaction rate is limited by diffusion of Ce^{4+} into the MOF. This competition between reaction and diffusion to dictate the reactant distribution inside MOF particle can be represented by the unitless quantity $= \frac{D}{a^2 k}$, where *D* is the diffusivity, *k* is the reaction rate constant and *a* is the radius of the MOF particle. With $\gamma \gg 1$, the diffusion is fast with respect to the reaction rate, the reactant will occupy the whole volume of the MOF particle and the reaction kinetics will resemble that of the homogeneous catalysts. When $\gamma \ll 1$ applies, the diffusion is the limiting factor of the reaction, and the reactant will scarcely reach the core of the MOF particles.

As during the reaction, Ce^{4+} is continuously reduced to Ce^{3+}, and the diffusion-reaction reached equilibrium during the first few minutes, it is reasonable to consider the sum

$[Ce^{3+}]$ + $[Ce^{4+}]$ to be constant inside the MOF, equaling to the initial concentration of Ce^{4+} in the solution. We can assume the Ce^{3+} and Ce^{4+} concentration has similar influence on the diffusivity of Ce^{4+}, then the diffusivity of Ce^{4+} only depends on the total concentration of $[Ce^{3+}]$ + $[Ce^{4+}]$.

As already shown in the manuscript, this hypothesis can be evaluated by doing experiments with an initial concentration of both Ce^{4+} and Ce^{3+}. The recorded kinetic data was fitted to the diffusion-reaction model and the diffusivities were calculated. Quantitatively, the dependence of diffusivity on the total concentration of $[Ce^{3+}]$ + $[Ce^{4+}]$ slightly deviates from the relationship we obtained in the previous experiments with pure $[Ce^{4+}]$ in the beginning. This deviation may be due to slight difference of the influence from $[Ce^{3+}]$ and $[Ce^{4+}]$.

Table 5.6 Diffusivities of Ce^{4+} in the presence of different Ce^{3+} concentrations in **11**.

Initial Ce^{4+} concentration c_0 (mM)	Initial Ce^{3+} concentration c_0 (mM)	Total concentration $[Ce^{3+}]$+$[Ce^{4+}]$	Number of equivalents Q	The rate of consumption of Ce^{4+} catalyzed by MOF k_0 (min^{-1})	Diffusivity D ($\times 10^{-12}$ cm^2s^{-1})
0.98	0	0.98	98	0.324	2.2
1.11	1	2.11	111	0.201	0.68
1.04	2	3.04	104	0.107	0.22
1.00	3	4.00	100	0.100	0.22
1.07	9	10.07	107	0.119	0.25

5.12 Conclusions

We have constructed two porous and stable Zr-carboxylate MOFs (**11** and **12**) with elongated bpy- or ppy-containing dicarboxylate ligands (**bpy-dc** and **ppy-dc**) attached to the Cp*Ir moieties and studied their water oxidation activities. As a result of site isolation in the crystalline frameworks, these MOFs provided an interesting platform to study water oxidation pathways owing to the elimination of multi-molecular degradation pathways. Oxidative modification of the Cp* rings of the immobilized Ir complexes was observed with Ce^{4+} as an oxidant. Careful studies of the recovered **11** from WORs revealed the identity of (**bpy-dc**)Ir$(H_2O)_2$XCl (X is likely a formate or acetate group) as an active catalyst for water oxidation, which was supported by XPS, UV-Vis, luminescence, and infrared spectroscopies as well as detailed kinetic studies of Ce^{4+}-driven WORs. Although it is difficult to confirm the role of the original catalyst $\mathbf{L_9}$ itself as a WOC from our experiments, the modified (**bpy-dc**)Ir$(H_2O)_2$XCl species resulted from the oxidative degradation of Cp* groups must be an active WOC to account for water oxidation activity of the reused MOFs. A reaction-diffusion model was developed to describe the kinetics of the MOF-catalyzed WORs, revealing an intricate balance between reaction and diffusion rates that account for the partial oxidative degradation of $\mathbf{L_9}$ to form (**bpy-dc**)Ir$(H_2O)_2$XCl. This work thus not only highlights the importance of studying water oxidation pathways in organized assemblies that more closely resemble the WOCs in functional devices but also presents a general strategy of using MOFs to study catalytic mechanisms of molecular species by taking advantage of site isolation in MOF structures and the ease of isolating solid materials from reaction mixtures for further spectroscopic and other characterization.

REFERENCES

(1) Wang, C.; Wang, J.-L.; Lin, W. *J. Am. Chem. Soc.* **2012**, *134*, 19895.

(2) Barber, J. *Chem. Soc. Rev.* **2009**, *38*, 185.

(3) Gust, D.; Moore, T. A.; Moore, A. L. *Acc. Chem. Res.* **2009**, *42*, 1890.

(4) Jiao, F.; Frei, H. *Angew. Chem. Int. Ed. Engl.* **2009**, *48*, 1841.

(5) Nakagawa, T.; Bjorge, N. S.; Murray, R. W. *J. Am. Chem. Soc.* **2009**, *131*, 15578.

(6) Ohno, T.; Bai, L.; Hisatomi, T.; Maeda, K.; Domen, K. *J. Am. Chem. Soc.* **2012**, *134*, 8254.

(7) Reece, S. Y.; Hamel, J. A.; Sung, K.; Jarvi, T. D.; Esswein, A. J.; Pijpers, J. J. H.; Nocera, D. G. *Science* **2011**, *334*, 645.

(8) Youngblood, W. J.; Lee, S. H. A.; Kobayashi, Y.; Hernandez-Pagan, E. A.; Hoertz, P. G.; Moore, T. A.; Moore, A. L.; Gust, D.; Mallouk, T. E. *J. Am. Chem. Soc.* **2009**, *131*, 926.

(9) Zhang, F.; Yamakata, A.; Maeda, K.; Moriya, Y.; Takata, T.; Kubota, J.; Teshima, K.; Oishi, S.; Domen, K. *J. Am. Chem. Soc.* **2012**, *134*, 8348.

(10) Zhao, Y.; Swierk, J. R.; Megiatto, J. D.; Sherman, B.; Youngblood, W. J.; Qin, D.; Lentz, D. M.; Moore, A. L.; Moore, T. A.; Gust, D.; Mallouk, T. E. *Proc. Nat. Aca. Sci.* **2012**, *109*, 15612.

(11) Moyer, B. A.; Meyer, T. J. *Inorg. Chem.* **1981**, *20*, 436.

(12) Concepcion, J. J.; Jurss, J. W.; Templeton, J. L.; Meyer, T. J. *J. Am. Chem. Soc.* **2008**, *130*, 16462.

(13) Concepcion, J. J.; Tsai, M.-K.; Muckerman, J. T.; Meyer, T. J. *J. Am. Chem. Soc.* **2010**, *132*, 1545.

(14) Barnett, S. M.; Goldberg, K. I.; Mayer, J. M. *Nat. Chem.* **2012**, *4*, 498.

(15) Dismukes, G. C.; Brimblecombe, R.; Felton, G. A. N.; Pryadun, R. S.; Sheats, J. E.; Spiccia, L.; Swiegers, G. F. *Acc. Chem. Res.* **2009**, *42*, 1935.

(16) Duan, L.; Bozoglian, F.; Mandal, S.; Stewart, B.; Privalov, T.; Llobet, A.; Sun, L. *Nat. Chem.* **2012**, *4*, 418.

(17) Fillol, J. L.; Codolà, Z.; Garcia-Bosch, I.; Gómez, L.; Pla, J. J.; Costas, M. *Nat. Chem.* **2011**, *3*, 807.

(18) Wasylenko, D. J.; Ganesamoorthy, C.; Borau-Garcia, J.; Berlinguette, C. P. *Chem. Comm.* **2011**, *47*, 4249.

(19) Kärkäs, M. D.; Åkermark, T.; Johnston, E. V.; Karim, S. R.; Laine, T. M.; Lee, B.-L.; Åkermark, T.; Privalov, T.; Åkermark, B. *Angew. Chem. Int. Ed. Engl.* **2012**, *51*,11589.

(20) Ellis, W. C.; McDaniel, N. D.; Bernhard, S.; Collins, T. J. *J. Am. Chem. Soc.* **2010**, *132*, 10990.

(21) McCool, N. S.; Robinson, D. M.; Sheats, J. E.; Dismukes, G. C. *J. Am. Chem. Soc.* **2011**, *133*, 11446.

(22) McDaniel, N. D.; Coughlin, F. J.; Tinker, L. L.; Bernhard, S. *J. Am. Chem. Soc.* **2007**, *130*, 210.

(23) Blakemore, J. D.; Schley, N. D.; Balcells, D.; Hull, J. F.; Olack, G. W.; Incarvito, C. D.; Eisenstein, O.; Brudvig, G. W.; Crabtree, R. H. *J. Am. Chem. Soc.* **2010**, *132*, 16017.

(24) Hull, J. F.; Balcells, D.; Blakemore, J. D.; Incarvito, C. D.; Eisenstein, O.; Brudvig, G. W.; Crabtree, R. H. *J. Am. Chem. Soc.* **2009**, *131*, 8730.

(25) Blakemore, J. D.; Schley, N. D.; Olack, G. W.; Incarvito, C. D.; Brudvig, G. W.; Crabtree, R. H. *Chem. Sci.* **2011**, *2*, 94.

(26) Grotjahn, D. B.; Brown, D. B.; Martin, J. K.; Marelius, D. C.; Abadjian, M. C.; Tran, H. N.; Kalyuzhny, G.; Vecchio, K. S.; Specht, Z. G.; Cortes-Llamas, S. A.; Miranda-Soto, V.; van Niekerk, C.; Moore, C. E.; Rheingold, A. L. *J. Am. Chem. Soc.* **2011**, *133*, 19024.

(27) Savini, A.; Belanzoni, P.; Bellachioma, G.; Zuccaccia, C.; Zuccaccia, D.; Macchioni, A. *Green Chem.* **2011**, *13*, 3360.

(28) Hara, M.; Lean, J. T.; Mallouk, T. E. *Chem. Mater.* **2001**, *13*, 4668.

(29) Hara, M.; Mallouk, T. E. *Chem. Comm.* **2000**, 1903.

(30) Hintermair, U.; Hashmi, S. M.; Elimelech, M.; Crabtree, R. H. *J. Am. Chem. Soc.* **2012**, *134*, 9785.

(31) Schley, N. D.; Blakemore, J. D.; Subbaiyan, N. K.; Incarvito, C. D.; D'Souza, F.; Crabtree, R. H.; Brudvig, G. W. *J. Am. Chem. Soc.* **2011**, *133*, 10473.

(32) Parent, A. R.; Blakemore, J. D.; Brudvig, G. W.; Crabtree, R. H. *Chem. Comm.* **2011**, *47*, 11745.

(33) Parent, A. R.; Brewster, T. P.; De Wolf, W.; Crabtree, R. H.; Brudvig, G. W. *Inorg. Chem.* **2012**, *51*, 6147.

(34) Zuccaccia, C.; Bellachioma, G.; Bolano, S.; Rocchigiani, L.; Savini, A.; Macchioni, A. *Euro. J. Inorg. Chem.* **2012**, 1462.

(35) Hong, D. C.; Murakami, M.; Yamada, Y.; Fukuzumi, S. *Energy & Environ. Sci.* **2012**, *5*, 5708.

(36) deKrafft, K. E.; Wang, C.; Xie, Z. G.; Su, X.; Hinds, B. J.; Lin, W. B. *ACS Appl. Mater. & Interface* **2012**, *4*, 608.

(37) Ma, L.; Jin, A.; Xie, Z.; Lin, W. *Angew. Chem. Int. Ed. Engl.* **2009**, *48*, 9905.

(38) Curtis, N. J.; Sargeson, A. M. *J. Am. Chem. Soc.* **1984**, *106*, 625.

(39) Deeming, A. J.; Proud, G. P. *J. Organo. Chem.* **1986**, *301*, 385.

(40) Schmeier, T. J.; Dobereiner, G. E.; Crabtree, R. H.; Hazari, N. *J. Am. Chem. Soc.* **2011**, *133*, 9274.

(41) Crank, J. *The Mathematics of Diffusion*; 2nd ed.; Oxford University Press, 1975.

Chapter 6

Light-Harvesting Crosslinked Polymers for Efficient Photocatalysis

6.1 Introduction

The advancement of artificial photosynthesis heralds a promising and revolutionary approach toward green chemical transformations.[1-31] In order to achieve artificial photosynthesis, it is important to design molecular systems that can not only act as antenna for photon capture but are also able to transfer the energies to the reaction centers to drive desired chemical transformations.[4-6] Natural photosynthesis takes advantage of a wired network of chromophores and functional centers to facilitate energy and electron transfer within the system, leading to efficient conversion of sunlight energy to chemical potential stored in reactive chemical bonds.[7,8] Chemists have created a variety of macromolecular and supramolecular systems, including arrays of porphyrins and other chromophores,[9,10] linear polymers,[11-13] dendrimers,[14] metal-organic frameworks,[15,16] bridged semiconducting nanoparticles,[17,18] organogels and hybrid hydrogels,[19,20] vesicles,[21] and biomolecule-based assemblies,[22,23] in order to mimic the energy and electron transfer processes in natural photosynthesis. Efficient collection of photons in the artificial systems can lead to the formation of charge-separated redox pairs or light harvesting species such as singlet oxygen.[24-27] However, few of the reported antenna systems can effectively use the harvested energy to drive productive chemical reactions.[28]

Organic transformations driven by visible light are gaining increasing interest from synthetic chemists, because of generally mild conditions for substrate activation, the ability to afford desired products without generating unwanted byproducts, and the potential to mediate

thermodynamically uphill reactions by harvesting energy from the sunlight.[29-33] Photocatalysts are often required in visible light driven organic reactions since the majority of organic substrates in these reactions do not readily absorb photons in the visible region. $[Ru(bpy)_3]^{2+}$ (bpy = 2,2'-bipyridine) is undoubtedly one of the most extensively studied photocatalysts since the pioneering work of Meyer and Whitten in the 1970s.[34] By taking advantage of the long lifetime of the ^{3}MLCT state of this Ru-based phosphor and its propensity to undergo redox quenching, a variety of new photocatalytic organic reactions, ranging from [2+2] cycloaddition to radical chemistry, have been developed recently.[29-33,35-43] Stephenson et al and MacMillan et al also reported the use of an Ir complex, $Ir(ppy)_2(dtbbpy)PF_6$ (ppy = 2-phenylpyridine; dtbbpy =4,4'-di-*tert*-butyl-2,2'-bipyridine), as a photoredox catalyst in tin-free dehalogenation, Aza-Henry reactions, and trifluoromethylation of aldehydes.[33,35,41,44] Like other precious metal catalyzed reactions, it is highly desirable to develop recyclable and reusable heterogeneous photocatalytic systems based on the Ir and Ru phosphors. The ability to recover and reuse such heterogeneous photocatalysts can not only eliminate the contamination of organic products by trace amounts of heavy metals but also reduce processing and waste disposal costs in large scale reactions.

Crosslinked polymers (CPs), including crystalline covalent-organic frameworks, can be built from well-designed organic precursors and represent a new class of robust, possibly nanoporous materials.[45-50] Like their metal-organic framework (MOF) counterparts, CPs have shown great promise in gas storage and separation and light harvesting.[51] Just like recently developed catalytic MOFs, CPs can serve as an ideal platform for incorporating molecular catalytic modules into highly stable, recyclable, and reusable heterogeneous catalyst systems by taking advantage of their unique solid state structure and the ability to tune their compositions and properties at the molecular level.[52] CPs are advantageous over MOFs as photocatalysts since

many MOFs are constructed from metal connecting points with unfilled d orbitals which can readily quench the photoexcited states of the photocatalytic building units, although CPs do not possess as well-defined structure as MOFs do. In this chapter, I will describe successful incorporation of the Ru and Ir phosphors into robust CPs by three different reactions: 1) cobalt carbonyl-mediated trimerization of the end alkyne groups on the monomers;[50] 2) Pd-catalyzed Sonogashira coupling between end alkyne and aromatic bromide; 3) Cu-catalyzed Eglinton coupling of end alkynes. The resulting CPs are either porous or non-porous, but they all serve as highly active photocatalysts in catalyzing a range of different organic transformations. These CP photocatalysts can also be readily recycled and reused.

6.2 Porous Crosslinked Polymers synthesized by cobalt carbonyl catalyzed trimerization of alkynes.[42]

6.2.1 Synthesis and characteriazation of crosslinked polymers

As shown in Scheme 6.1, phosphorescent Ir monomer $[(ppy)_2Ir(debpy)]Cl$ (debpy =5,5'-diethynyl-2,2'-bipyridine) and Ru monomer $[(bpy)_2Ru(debpy)]Cl_2$ were synthesized by allowing debpy to react with $[Ir(ppy)_2Cl_2]_2$ and $Ru(bpy)_2Cl_2$ at 90 ^oC overnight, respectively. Co-polymerization of the monomer $[(ppy)_2Ir(debpy)]Cl$ or $[(bpy)_2Ru(debpy)]Cl_2$ with tetra(4-ethynylphenyl)methane was achieved through $Co_2(CO)_8$-mediated trimerization of the end alkyne groups of the monomers in dioxane or dichloroethane at 115 ^oC for 10 min (Scheme 6.1). The resulting brown solids were stirred in concentrated hydrochloric acid at r.t. for 2 h to remove all of the Co species, and then washed with various solvents to afford **CP-1** and **CP-2** in 97 % yields. The **CP-1** and **CP-2** were characterized by thermogravimetric analysis (TGA), inductively coupled plasma-mass spectrometry (ICP-MS), infrared spectroscopy (IR), nitrogen

adsorption, scanning electron microscopy (SEM), transmission electron microscopy (TEM), and powder X-ray diffraction (PXRD).

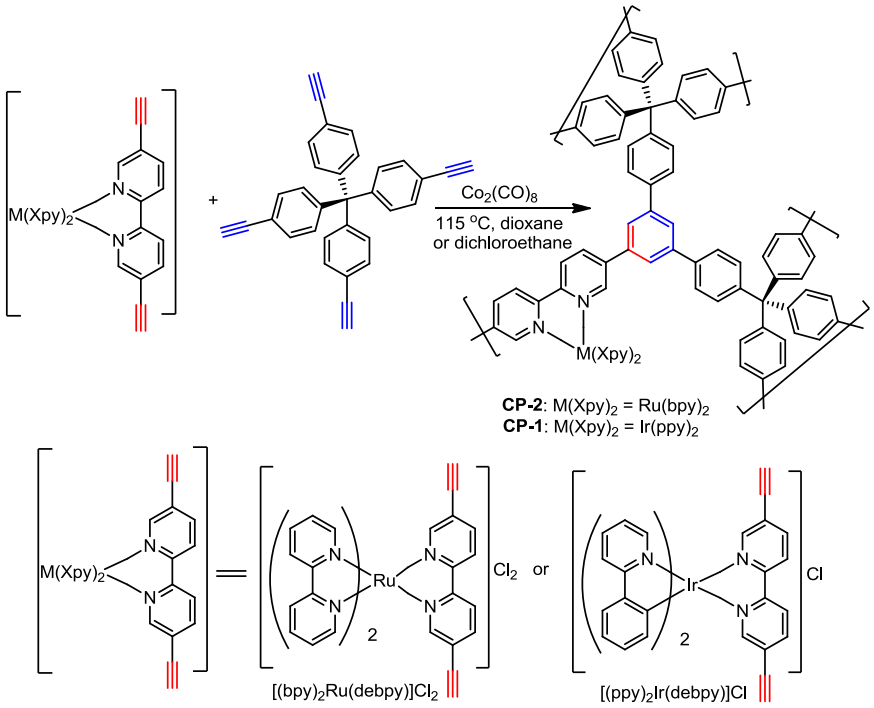

Scheme 6.1 Synthesis of **CP-1** and **CP-2**. (Reprinted with permission from ref [42]. Copyright American Chemical Society 2011)

Morphology of the CPs was examined by SEM and TEM (Figure 6.1a, 6.1b). Particles on the order of several micrometers in size displayed rather rough surfaces, and appear to be aggregates of much smaller particles with dimensions of around 10 nm. The PXRD patterns indicated that the **CP-1** and **CP-2** are amorphous in nature.

The **CP-1** and **CP-2** are insoluble in water, concentrated acids, and all of the organic solvents tested. The PCPs are stable in air up to 350 ^{o}C as revealed by TGA (Figure 6.1c). The Ir and Ru catalyst loadings for **CP-1** and **CP-2** were determined by ICP-MS to be 4.5 wt % and 2.2 wt %, respectively. The absence of the carbon-hydrogen stretching peak of the C≡C-H group around 3300 cm^{-1} in the IR spectra of the **CP-1** and **CP-2** suggested that most of the alkyne groups in

the starting materials have been consumed to form benzene rings in the PCPs, consistent with a high degree of polymerization (Figure 6.1d).

Porosity of the CPs was revealed by nitrogen sorption measurements at 77 K. The CPs exhibit large reversible adsorptions at low pressure ($P/P_0<0.1$) and hysteresis loops at higher pressure, suggesting the coexistence of micro- and meso-pores in the framework (Figure 6.1e). The BET surface areas were determined to be 1547 m^2/g and 1348 m^2/g for **CP-1** and **CP-2** in the P/P_0=0.03-0.2 range, respectively. Both of the COFs have wide pore size distributions with the pore widths centering around 7.5, 11.0, 13.5 and 16.5 Å as calculated by the nonlocal density functional theory method (NLDFT).

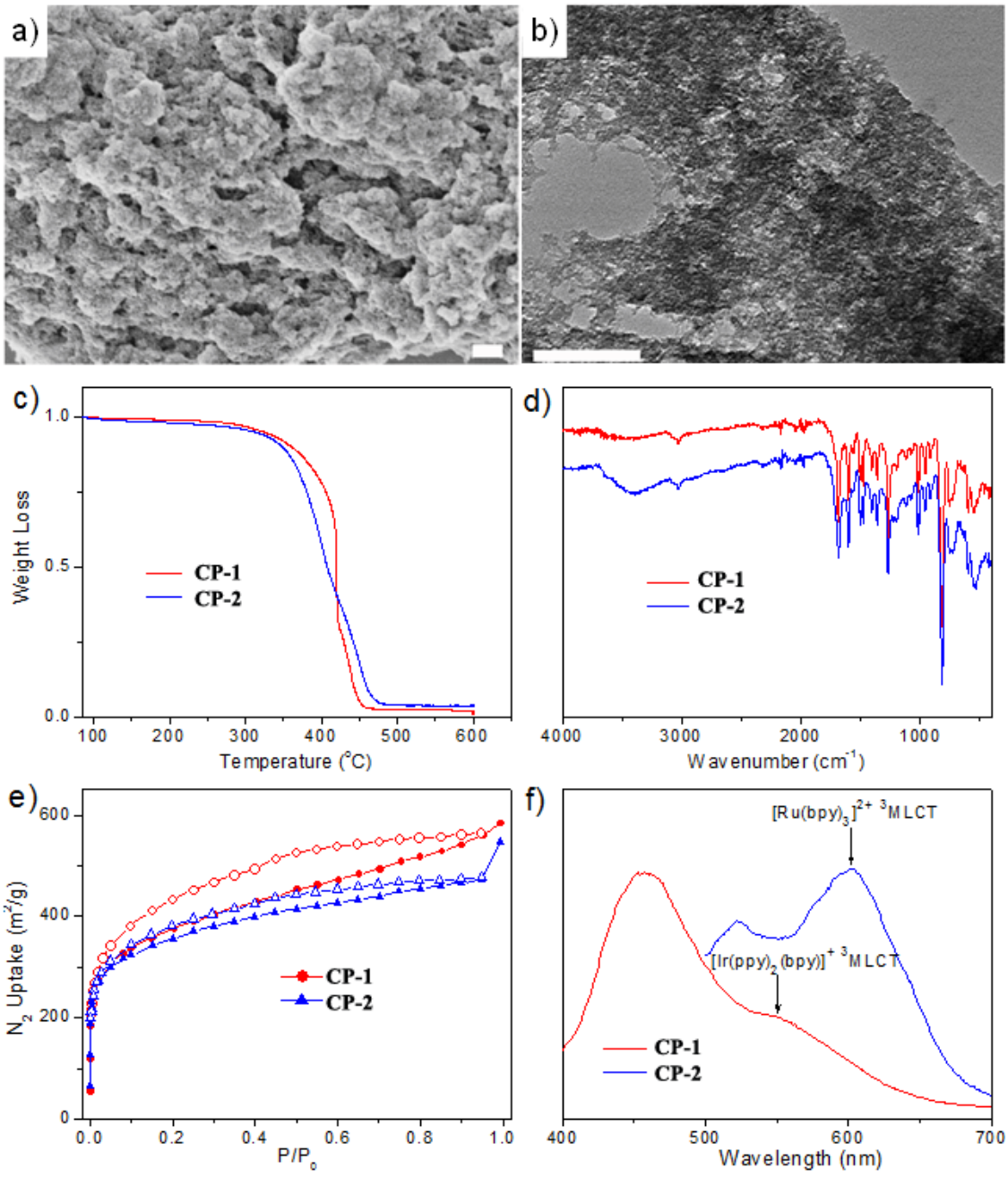

Figure 6.1. Characterization of **CP-1** and **CP-2**: (a) SEM and (b) TEM images of the Ir-COF. The scale bars represent 200 nm. (c) TGA (d) FT-IR (e) nitrogen adsorption isotherms at 77K (f) emission spectra. The **CP-1** emission spectrum (red line) was taken when excited at 380 nm. The broad emission at around 458.5 nm comes from fluorescence of the framework. The **CP-2** emission spectrum (blue line) was taken when excited at 450 nm. The broad emission at around

522.5 nm comes from fluorescence of the framework. (Reprinted with permission from ref [42]. Copyright American Chemical Society 2011)

6.2.2 Photocatalysis with the crosslinked polymers

With the Ir/Ru based phosphors covalently integrated into the skeletons, we hypothesized that the synthesized CPs can act as solid state photosensitizers by utilizing the ^{3}MLCT states of the Ir/Ru complexes. Phosphorescence measurements were performed on a stirred suspension of the CPs in CH_3NO_2, showing peaks originating from ^{3}MLCT → GS transitions, around 550 nm for the **CP-1**, and 602 nm for the **CP-2** (Figure 6.1f). We intended to explore the utility of the **CP-1** and **CP-2** in catalyzing visible light driven organic reactions such as the Aza-Henry reaction between nitromethane or nitroethane and aromatic tertiary amines. Before the catalysis test of the materials, a preliminary quenching experiment was carried out to confirm that the ^{3}MLCT state of the phosphors in the CPs can be reductively quenched by the amine substrate, which is the very first step of the photocatalytic cycle of homogeneous aza-Henry reactions as proposed by Stephenson and co-workers.[35] A Stern-Volmer plot for the **CP-2** was obtained by plotting the intensity ratio I_0/I at 602 nm vs the amine concentration, leading to a Stern-Volmer constant of 23 M^{-1} which is comparable to that of the monomeric $[(bpy)_2Ru(debpy)]Cl_2$ complex (20 M^{-1}). This result indicates effective quenching of the ^{3}MLCT phosphorescence of the **CP-2** by the amine. In the case of **CP-1**, the quenching effect was also observed but could not be quantified spectroscopically owing to the interference of the framework fluorescence (Figure 6.1f). The quenching result suggested that good photocatalytic performance of the CPs should be expected.

Table 6.1 Photocatalytic aza-Henry reactionsby **CP-1** and **CP-2** [a]

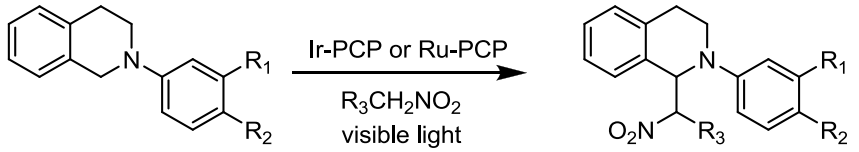

1a: R_1 = H, R_2= H
2a: R_1 = H, R_2=Br
3a: R_1 = H, R_2= OCH_3
4a: R_1 = OCH_3, R_2= H

1b: R_1 = H, R_2= H, R_3= H
2b: R_1 = H, R_2=Br, R_3= H
3b: R_1 = H, R_2= OCH_3, R_3= H
4b: R_1 = OCH_3, R_2= H, R_3= H
5b: R_1 = H, R_2= H, R_3= CH_3
6b: R_1 = H, R_2=Br, R_3= CH_3
7b: R_1 = H, R_2= OCH_3, R_3= CH_3
8b: R_1 = OCH_3, R_2= H, R_3= CH_3

entry	amine substrate	product	conv. (%) with different catalysts[b]			
			Ir-M	**CP-1**	Ru-M	**CP-2**
1[c]	**1a**	**1b**	99	94	85	90
2[c]	**2a**	**2b**	99	97	84	87
3[c]	**3a**	**3b**	81	91	90	>99
4[c]	**4a**	**4b**	79	98	65	85
5[d]	**1a**	**5b**	94	94	81	84
6[d]	**2a**	**6b**	73	75	57	78
7[d]	**3a**	**7b**	86	97	62	95
8[d]	**4a**	**8b**	66	86	76	91

[a]All the reactions were run at room temperature for 8 h with 1 mol% Ir-based catalyst or 0.2 mol% Ru-based catalyst; [b]Conversions were determined by integrating the ^{1}H NMR spectra. Ir-M and Ru-M are Ir monomer $[(ppy)_2Ir(debpy)]Cl$ and Ru monomer $[(bpy)_2Ru(debpy)]Cl_2$, respectively; [c]with nitromethane as solvent; [d]with nitroethane as solvent.

Catalytic activities of the **CP-1** and **CP-2** toward photocatalytic aza-Henry reaction were evaluated with tetrahydroisoquinoline (**1a**) as the amine substrate and CH_3NO_2 as solvent. The reaction was carried out in the presence of air with a common fluorescent lamp (26 W) as the light source. The reaction was stopped after 8 hours by filtering off the CP catalysts. Conversions of the reactions were determined by integrating the peaks of ^{1}H NMR spectra of the crude reaction mixtures. As shown in Table 6.1 (entry 1), both the **CP-1** and **CP-2** are highly effective photocatalysts for the aza-Henry reaction between **1a** and nitromethane with >90% conversions. These conversions are comparable to those of the homogeneous counterparts. We have also

explored the scope of substrates for this photocatalytic reaction (Table 6.1). The **CP-1** and **CP-2** catalyzed aza-Henry reactions between nitromethane and a variety of tertiary aromatic amines with different functional groups (Table 6.1, Entries 1-4). The CPs also catalyzed Aza-Henry reactions between nitroethane and tertiary aromatic amines (Table 6.1, Entries 5-8). Interestingly, most of the CP-catalyzed aza-Henry reactions have higher conversions than those catalyzed by their homogeneous counterparts.

A number of control experiments were carried out to demonstrate the heterogeneous and photocatalytic nature of the reactions. The reaction of **1a** in the dark yielded negligible amounts of aza-Henry products (<5%), demonstrating the necessity of light in this reaction. On the other hand, the background reaction in the absence of the catalysts but in the presence of light showed only around 10% conversions after 8 hours, verifying that the CPs played a catalytic role in the reactions. These observations are consistent with those for the homogeneous system reported by Stephenson and co-workers.[35] In addition, a cross-over experiment was carried out to prove the heterogeneity of the CP catalyst. Substrate **1a** was used in the **CP-1** catalyzed aza-Henry reaction, and 94% conversion was achieved after 8 hours. The CP catalyst was then removed by filtering through Celite, and another substrate **3a** was added to the supernatant solution. After stirring the solution under light for 8 hours, only 12% conversion was observed for the second substrate (**3a**). This low conversion, comparable to that of the background reaction with visible light but without a photocatalyst, proved that the supernatant of the **CP-1** catalyst reaction mixture is inactive in photocatalysis. This result supports the heterogeneous nature of the CP photocatalysts.

We also demonstrated the applicability of the PCP photocatalysts in other photo-driven reactions. As shown in Scheme 6.2, **CP-2** efficiently catalyzed the α-arylation of

bromomalonate via direct intermolecular C-H functionalization as well as oxyamination of 3-phenylpropanal, with comparable isolated product yields to those of the homogeneous control catalyst. These results illustrate the generality of the CP materials in catalyzing photo-driven organic transformations.

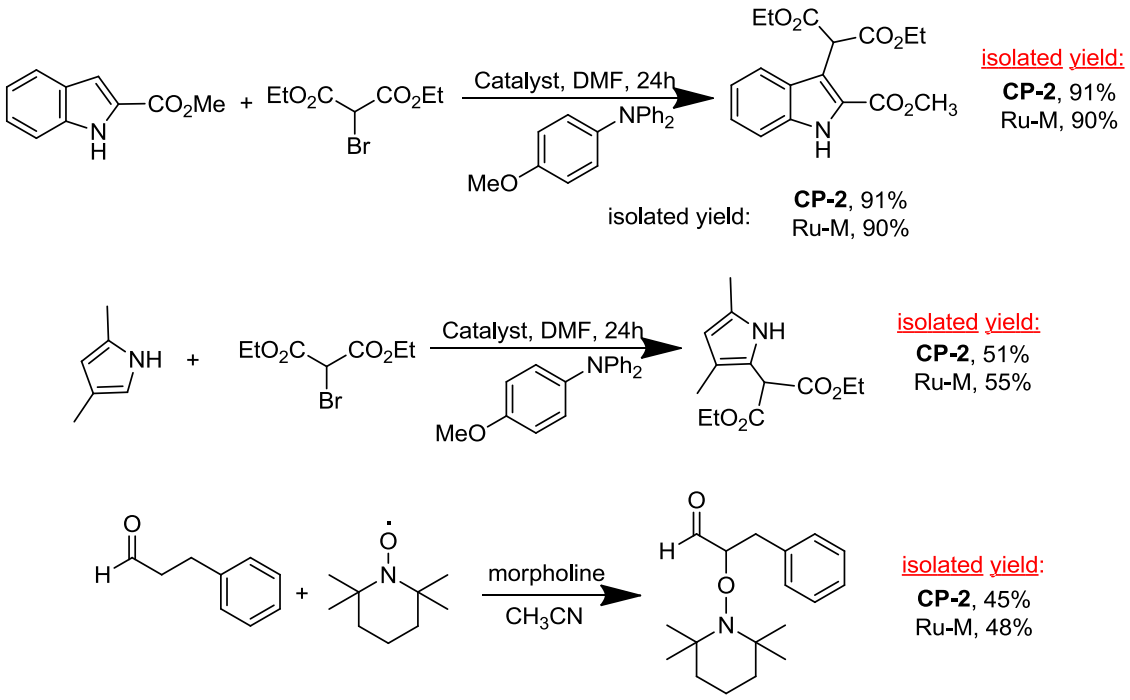

Scheme 6.2 **CP-2** catalyzed α-arylation of bromomalonate and oxyamination of 3-phenylpropanal. (Reprinted with permission from ref [42]. Copyright American Chemical Society 2011)

We also examined recyclability and reusability of the CP catalysts. **CP-1** and **CP-2** were readily recovered from the reaction mixtures via simple filtration. The recovered catalyst showed no deterioration of conversion % after recycling 4 times. Furthermore, UV-Vis analysis of the supernatant showed no sign of Ir/Ru-complex leaching into the solution, proving the stability of the CPs under the reaction conditions. This is further supported by the absence of Ir or Ru in the supernatants of the CP-catalyzed reaction mixtures by ICP-MS.

6.3 Non-Porous Crosslinked Polymers synthesized by Pd-catalyzed coupling reaction.[53]

6.3.1 Synthesis and Characterization of Crosslinked Polymer

The polymerization between the tetrahedral tetra(*p*-ethynylphenyl)methane and the linear dibromo compound, $[Ru(bpy)_2(dbbpy)]^{2+}$ or $Ir[(bpy)_2(dbbpy)]^{+}$, was realized through a Pd/CuI catalyzed Sonogashira cross-coupling reaction (Scheme 6.3). Based on the inductively coupled plasma mass spectrometry (ICP-MS) results, the resultant $[Ru(bpy)_3]^{2+}$ and $Ir[(bpy)_2(bpy)]^{+}$-based polymers (**CP-3** and **CP-4**) possess exceptionally high Ru and Ir catalysts loadings of 76.3 wt% and 71.6 wt%, respectively, very close to that of the stoichiometric polymer formulae (78.3 wt% for **CP-3** and 79.1% for **CP-4**). These phosphor loadings are exceptionally high when compared to the **CP-1** and **CP-2** in the previous section (2.2 wt% and 4.5 wt%, respectively).

Similar Sonagashira coupling reactions were recently used by Cooper et al. to synthesize conjugated microporous polymers with metallo-complexes in the backbones.[47] In their work, linear 1,4-dibromobenzene was added to the feed to achieve micro-porosity. It was found that increasing the amounts of the metallo-complexes drastically decreases the surface areas of the CPs, due to channel blocking by the bulky metallo-complexes. Since the **CP-3** and **CP-4** in our work contain stoichiometric amounts of the Ru and Ir complexes, they are nonporous with negligibly small BET surface areas of 2.9 m^2/g and 2.7 m^2/g, respectively (Figure 6.2a). In comparison, the control polymer (**CP-6**) made by cross-coupling between dbbpy and tetra(*p*-ethynylphenyl)methane gave a BET surface area of 333.6 m^2/g (Figure 6.2a).

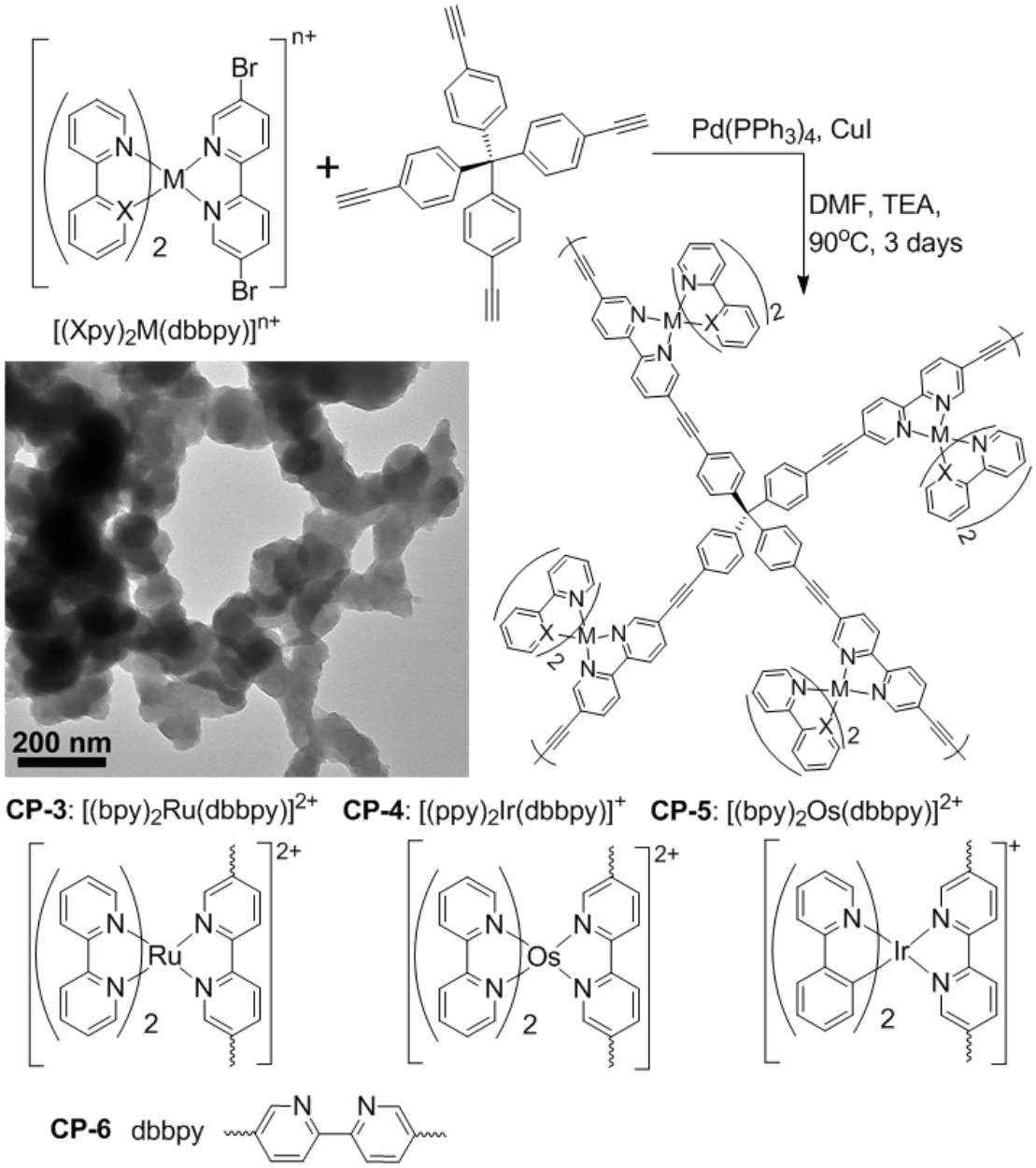

Scheme 6.3 Synthesis of **CP-3**, **CP-4, CP-5**, and **CP-6**. A TEM image of **CP-3** is also shown. (Reprinted with permission from ref [53]. Copyright American Chemical Society 2012)

Transmission electron microscopy (TEM) images (Scheme 6.3) showed that the **CP-3** and **CP-4** are composed of inter-connected nanoparticles of 100-200 nm in dimensions. The particles are stable up to 300 ^{o}C in air, as revealed by thermogravimetric analysis (TGA) (Figure 6.3d).

The crosslinked polymers are insoluble in water and all of the organic solvents tested. The high degree of polymerization is indicated by the IR spectra. The absence of the carbon-hydrogen stretching peak of the C≡C-H group around 3300 cm^{-1} suggested that most of the alkyne groups in the starting materials have been consumed in the coupling reaction (Figure 6.3c).

6.3.2 Light Harvesting by Crosslinked Polymers: Photon Capture and Excited State Dynamics

With such nonporous crosslinked polymer nanoparticles that contain stochiometric amounts of Ru and Ir dye molecules, we hypothesized that the nanoparticles can serve as light-harvesting antenna to collect energy and drive chemical reactions on the polymer surfaces. The phosphor molecules in the interior of the nonporous CP materials can readily absorb visible light to form ^{3}MLCT excited states which can efficiently migrate to the particle surface. Based on the molar extinction coefficient of **CP-3** at 485 nm (Figure 6.3a), 90% of the light can reach the interior chromophoric centers for a nanoparticle with a size of 100 nm. The surface Ru and Ir phosphor molecules, which can either be excited directly by light or accept excited state energy from the phosphors in the interior of the polymer particle, will undergo photoredox reactions and initiate a cascade of chemical transformations in a catalytic cycle. Such a core-to-surface excited state transport process followed by a redox catalytic reaction on the surface renders all of the phosphors in the nonporous solid photoactive, akin to the light-harvesting processes in natural photosynthesis. A high choromophore concentration in the framework is essential for such effective light-harvesting, since the probability of Dexter-type energy migration between adjacent chromophores decays exponentially with the increased distance between them.

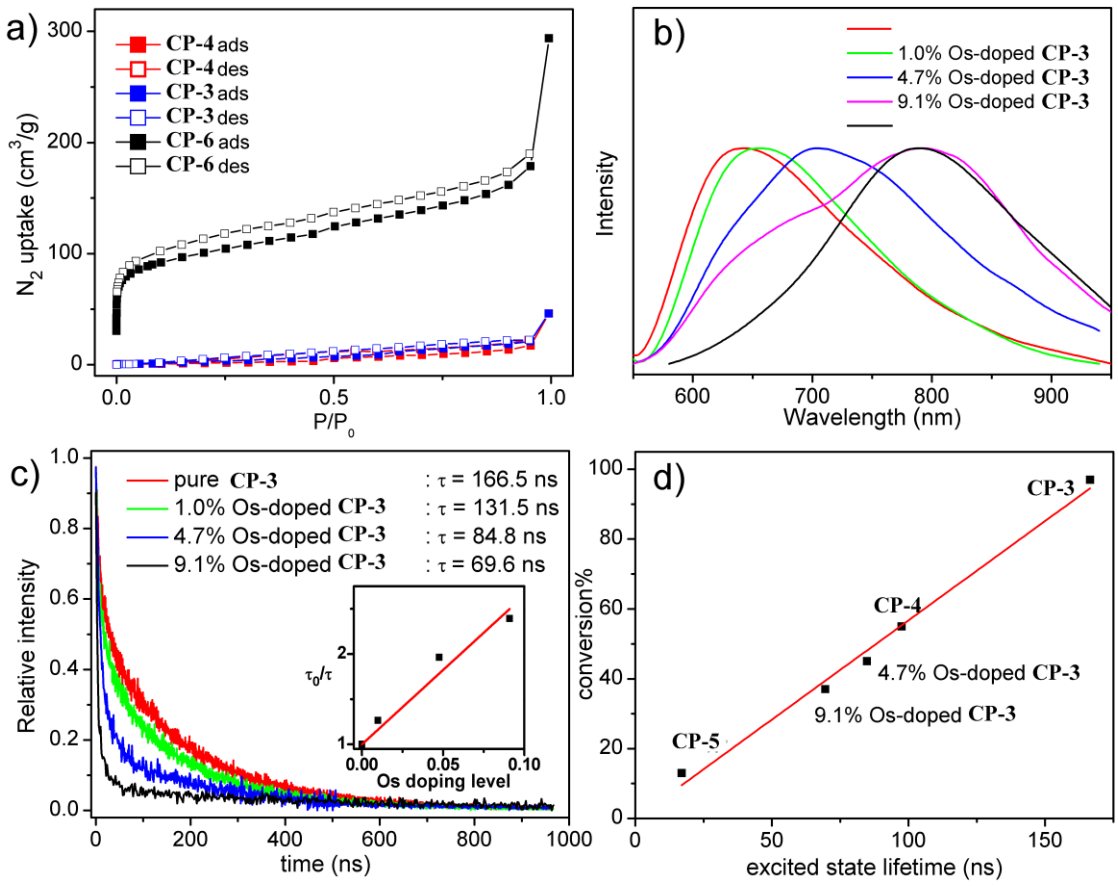

Figure 6.2 (a) Nitrogen sorption isotherms of **CP-3** (blue), **CP-4** (red) and **CP-6**(black) at 77K; (b) Smoothed steady-state emission spectra of **CP-3** (red), 1.0 mol% Os-doped **CP-3** (green), 4.7 mol% Os-doped **CP-3** (blue), 9.1 mol% Os-doped **CP-3** (purple) and pure **CP-5** (black); all of the spectra were taken while excited at 485 nm; (c) Decay transients measured at 630 nm (with 445 nm excitation) for **CP-3** (red), 1.0 mol% Os-doped **CP-3** (green), 4.7 mol% Os-doped **CP-3** (blue) and 9.1 mol% Os-doped **CP-3** (black); insert: plot of τ_0/τ vs. Os doping levels. The emission decays in (c) were fit to bi-exponential expression $A = A_1e^{-t/\tau 1} + A_2e^{-t/\tau 2}$. The reported lifetime τ is the weighted lifetime $\tau = (A_1\tau_1^2 + A_2\tau_2^2)/(A_1\tau_1 + A_2\tau_2)$. (d) Conversion % for the reactions between **1a** and nitromethane catalyzed by different CP catalysts vs. the phosphorescent lifetimes of these catalysts. Reactions were run at r. t. for 8 hours, with 0.2 mol% catalyst loadings, ~5 cm in front of a 26 W fluorescent lamp. (Reprinted with permission from ref [53]. Copyright American Chemical Society 2012)

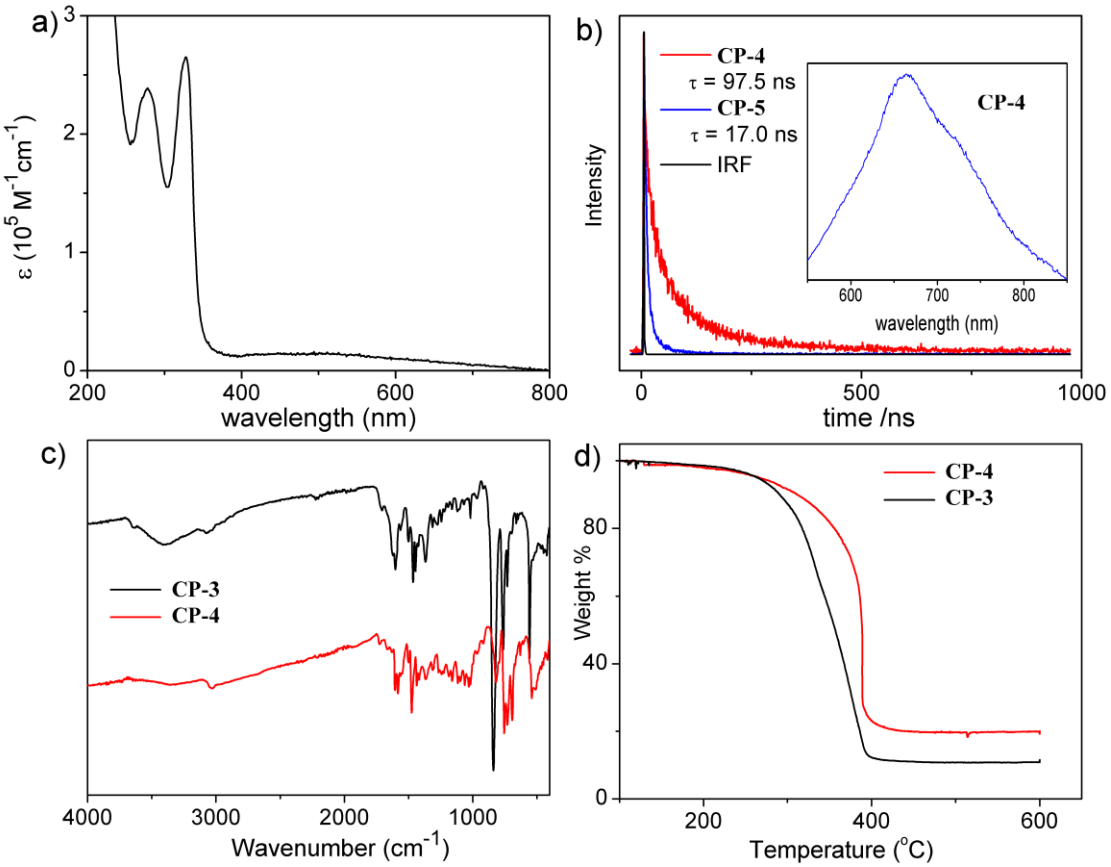

Figure 6.3 (a) UV-Vis absorption spectrum of **CP-3** particles suspended in MeCN (b) Decay transient measured at 650 nm for **CP-4** with excitation at 350 nm (red) and decay transient measured at 830 nm for **CP-5** with excitation at 444.2 nm (blue). IRF is Instrument Response Function for excitation at 444.2 nm (black). The emission decay was fit to bi-exponential expression $A = A_1e^{-t/\tau 1} + A_2e^{-t/\tau 2}$. The reported lifetimes are the weighted lifetimes $\tau = (A_1\tau_1^2 + A_2\tau_2^2)/(A_1\tau_1 + A_2\tau_2)$. Inset: steady state emission spectrum of **CP-4** (excited at 440 nm). (c) FT-IR spectra of **CP-3** (black) and **CP-4** (red). (d) TGA curves of **CP-3** (black) and **CP-4** (red). (Reprinted with permission from ref [53]. Copyright American Chemical Society 2012)

To test the hypothesis of efficient excited state migration through the CP framework, we doped different amounts of $[Os(bpy)_3]^{2+}$ entities into **CP-3** by copolymerization, and detected energy transfer from $[Ru(bpy)_3]^{2+*}$ to $[Os(bpy)_3]^{2+}$ by luminescence measurements. If efficient energy transfer from $[Ru(bpy)_3]^{2+*}$ to $[Os(bpy)_3]^{2+}$ can occur at relatively low $[Os(bpy)_3]^{2+}$ loadings, the $[Ru(bpy)_3]^{2+*}$ excited states must have hopped from site to site before reaching the

$[Os(bpy)_3]^{2+}$ traps. Steady-state luminescence measurements indicated a dramatic increase of the $[Os(bpy)_3]^{2+}$ based emission at ~800 nm as the Os doping level increased from 0 to 9.1 mol% (Figure 6.2b). Deconvolution of the emission spectrum of the 9.1 mol% Os-doped **CP-3** gave a value of 2.46 for the ratio of $[Os(bpy)_3]^{2+}$ to $[Ru(bpy)_3]^{2+}$ emission. Considering the different quantum yields and extinction coefficients of $[Os(bpy)_3]^{2+}$ and $[Ru(bpy)_3]^{2+}$ moieties in the framework [QY(Os)/QY(Ru) = 0.116 and $\varepsilon(Os)_{485nm}/\varepsilon(Ru)_{485nm}$ = 0.538 were experimentally determined with the polymer built from 100% Os (**CP-5**) and 100% Ru (**CP-3**)], we concluded that 95% of the excited state energy on $[Ru(bpy)_3]^{2+}$ had migrated to the 9.1 mol% $[Os(bpy)_3]^{2+}$ in the CP. The analysis is presented as following.

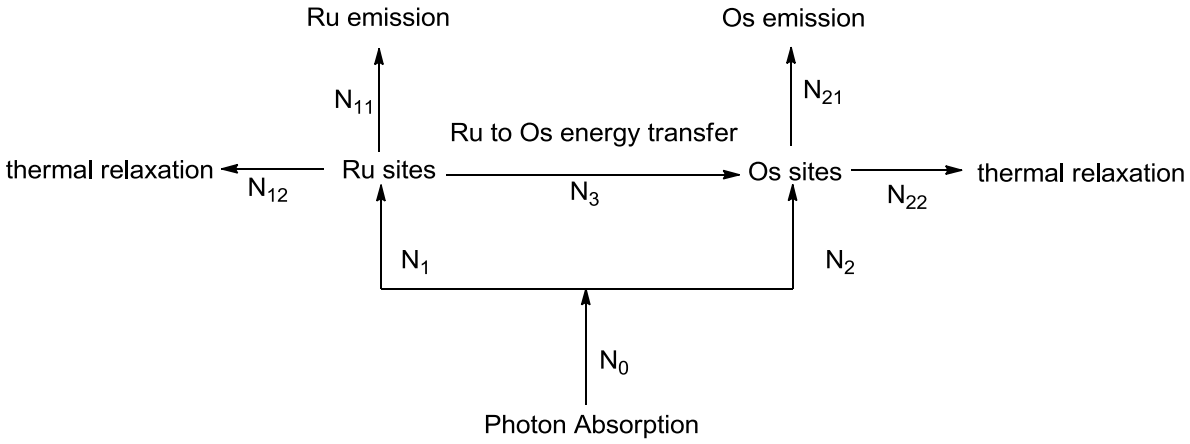

Scheme 6.4 Energy transfer scheme in 9.1% Os-doped **CP-3** sample.

As shown in Scheme 6.4, N_0 photons are absorbed by the CP during a given time. The ratio of the extinction coefficients between the Ru and Os cores ($\varepsilon(Os)/\varepsilon(Ru)$) in the structure is 0.537 as determined from pure **CP-3** and **CP-5** samples. The ratio of the concentration of Os [c(Os)] and Ru [c(Ru)] in the structure is 1/10.

Therefore the ratio of the amount of photons absorbed by Os sites (N_2) and Ru sites (N_1) is

$$N_2 / N_1 = [\varepsilon(Os)/\varepsilon(Ru)]\times[c(Os)/c(Ru)]=0.537\times0.1=0.0537 \quad \text{(Eq 6.1)}$$

And we know that

$$N_2 + N_1 = N_0 \quad \text{(Eq 6.2)}$$

From Eq S1 and Eq S2, we can obtain

$$N_1 = 0.949\ N_0 \quad \text{(Eq 6.3)}$$

$$N_2 = 0.051\ N_0 \quad \text{(Eq 6.4)}$$

The $[Ru(bpy)_3]^{2+*}$ excited state can get back to the $[Ru(bpy)_3]^{2+}$ ground state either by thermal relaxation (N_{12}) or emissive transition (N_{11}), or it can be quenched by $[Os(bpy)_3]^{2+}$ through $[Ru(bpy)_3]^{2+*}$ to $[Os(bpy)_3]^{2+}$ energy transfer (N_3). The Os excited state can get back to the Os ground state by either thermal relaxation (N_{22}) or emissive transition (N_{21}).

The amount of Os emission vs. Ru emission can be obtained from the deconvolution of steady-state emission spectra of the sample (Figure 6.4). From the experimental data, we can obtain 2.46 as the ratio of Os-component to Ru-component, so

$$N_{21} / N_{11} = 2.46 \quad \text{(Eq 6.5)}$$

We can also measure the ratio of quantum yields (QYs, in the absence of any quencher) of $[Os(bpy)_3]^{2+}$ vs $[Ru(bpy)_3]^{2+}$ inside the CP. Using the pure **CP-3** and **CP-5** polymers, The QY(Os)/QY(Ru) value is determined experimentally to be 0.116.

That is

$$QY(Os) / QY(Ru) = [N_{21}/(N_2+N_3)] / [N_{11}/(N_1-N_3)] = 0.116 \quad \text{(Eq 6.6)}$$

Using Eq 6.1 to Eq 6.6, we can obtain

$$N_3 = 0.904\ N_0$$

So the efficiency of energy transfer from Ru to Os in this polymer network is

$$(N_3/N_1) \times 100\% = 95.2\%$$

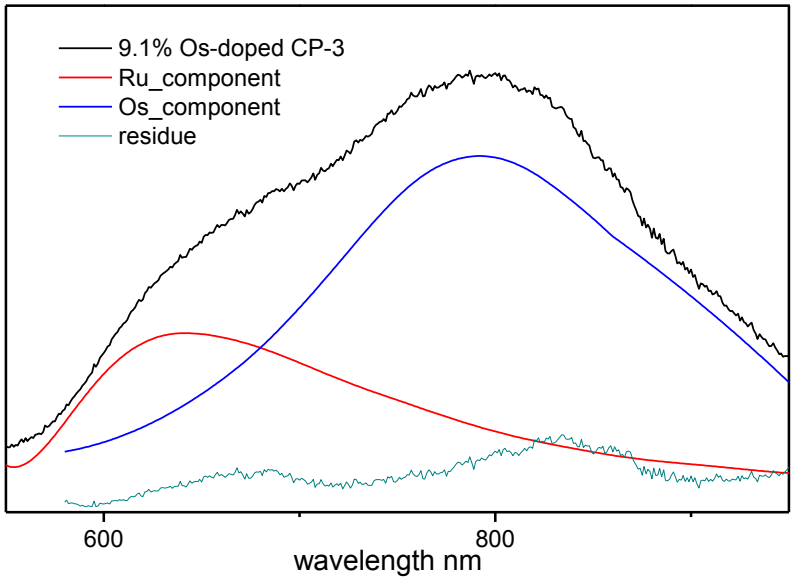

Figure 6.4. Deconvolution of emission spectra from 9.1% Os-doped **CP-3** sample (black) to the Ru-component (red) and the Os-component (blue), and the residue after the deconvolution (green). The ratio of the areas of the Os-component and Ru-component is 2.46. (Reprinted with permission from ref [53]. Copyright American Chemical Society 2012)

This analysis indicates efficient excited state migration, which was also evident in the steady-state emission spectra of 1.0 mol% and 4.7 mol% Os-doped **CP-3**s. Quantitative analyses were less reliable for these systems due to incompatibly disparate Os and Ru emission intensities. The efficient energy transfer from $[Ru(bpy)_3]^{2+*}$ to $[Os(bpy)_3]^{2+}$ was confirmed by time-resolved emission measurements of Os-doped **CP-3**s taken at 630 nm [λ_{max} for the $[Ru(bpy)_3]^{2+}$ emission]. The averaged lifetime of the 630 nm emission steadily decreased as the Os doping level increased (Figure 6.2c), consistent with an increasing level of energy transfer from $[Ru(bpy)_3]^{2+*}$ to $[Os(bpy)_3]^{2+}$.

6.3.3 Photocatalysis with CP-3

We then examined the photocatalytic activity of the **CP-3** particles, using the aza-Henry reaction as a test reaction. The reaction between tetrahydroisoquinoline derivatives **1a**-**3a** (Table

6.2) and nitromethane or nitroethane were carried out in air with a common fluorescent lamp (26 W) as the light source. As shown by the ^{1}H-NMR-determined reaction conversions in Table 6.2, the **CP-3** is a highly effective photocatalyst for all the six reactions with 88% to >99% conversions at 0.2 mol% **CP-3** loadings. These conversions are higher than those of the homogeneous counterparts (Table 6.2). The efficient photocatalytic aza-Henry reactions are supported by high isolated yields of 77% and 74% for **1b** and **2b**, respectively. Control experiments were carefully carried out to demonstrate the photocatalytic and heterogeneous nature of the reactions (Table 6.3). Reactions in the absence of either light or the catalysts showed zero or simply background conversions. The reaction supernatant after removing the CP was also proved to be inactive by a substrate crossover experiment. Substrate **3a** was used in the **CP-3** catalyzed aza-Henry reaction, and a complete conversion was achieved in 8 h. The **CP-3** catalyst was then removed by filtering through Celite, and the second substrate **1a** was added to the filtrate. After stirring the solution under light for 8 h, only 11% conversion was observed for **1a**. This low conversion, comparable to that of the background reaction, proved that the supernatant of the reaction mixture is inactive in photocatalysis. In addition, ICP-MS studies showed very little Ru leaching (<0.3%) to the solution during the reaction. The **CP-3** was also easily recovered from the reaction mixture by centrifugation, and reused four times without loss of activity (Table 6.3).

Table 6.2. Photocatalytic aza-Henry reactions with **CP-3**[a]

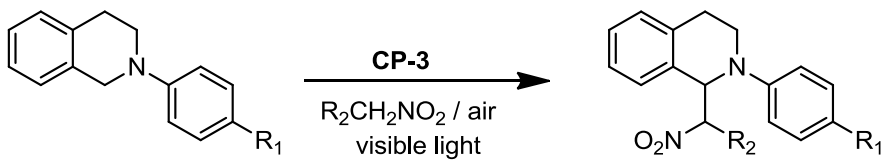

1a: R_1= H
2a: R_1=Br
3a: R_1= OCH_3

1b: R_1= H, R_2= H
2b: R_1=Br, R_2= H
3b: R_1= OCH_3, R_2= H
5b: R_1= H, R_2= CH_3
6b: R_1=Br, R_2= CH_3
7b: R_1= OCH_3, R_2= CH_3

entry	*amine substrate*	*product*	*conv. (%) with different catalysts*[b]	
			CP-3	Ru-M
1[c]	**1a**	**1b**	97	85
2[c]	**2a**	**2b**	>99	84
3[c]	**3a**	**3b**	>99	90
4[d]	**1a**	**5b**	94	81
5[d]	**2a**	**6b**	88	57
6[d]	**3a**	**7b**	>99	62

[a]All the reactions were run at r.t. for 8 h with 0.2 mol% catalyst; [b]Conversions were determined by integrating the ^{1}H NMR peaks. Ru-M is $[(bpy)_2Ru(debpy)]Cl_2$ (debpy=5,5'-diethynyl-2,2'-bipyridine), which models the Ru phosphor in the CP; [c]with nitromethane as solvent; [d]with nitroethane as solvent.

Table 6.3 Control experiments and catalyst reuse for photocatalytic aza-Henry reactions[a]

entry	*Condition*	*Substrate*	*Conversion (%)*[b]
1	No light, **CP-3**	**1a**	< 5
2	No catalyst	**1a**	10
3	No catalyst	**2a**	11
4	No catalyst	**3a**	19
5	**CP-6**	**1a**	36
6	**CP-6**	**2a**	29
7	**CP-3** (1st re-use)	**1a**	97
8	**CP-3** (2nd re-use)	**1a**	94
9	**CP-3** (3rd re-use)	**1a**	96
10	**CP-3** (4th re-use)	**1a**	92

[a] Reactions were run at r. t. for 8 hours, with 0.2 mol% catalyst loadings, ~5 cm in front of a 26 W fluorescent lamp. [b] Conversions were determined by ^{1}H NMR.

We also demonstrated the applicability of nonporous **CP-3** in other light-driven reactions. At 1 mol% loading, **CP-3** efficiently catalyzed aerobic oxidative coupling of a series of primary amines[37,40] with 84% to 99% conversions in 1 h (Table 6.4, entries 1-3), again comparable to that of the homogeneous catalyst. The isolated yield for **1d** was 88%. The recyclability and reusability of the **CP-3** catalyst was also evaluated for this reaction. The recovered catalyst after simple filtration was reused three times, showing no deterioration in conversion% (Table 6.4). Similarly, a visible light driven dehalogenation of benzyl bromoacetate[32] catalyzed by 1 mol% **CP-3** catalyst also gave complete substrate transformation in 8 h, with an isolated yield of 84% (Table 6.5).

Table 6.4. Photocatalytic aerobic oxidative coupling of amines by **CP-3** [a]

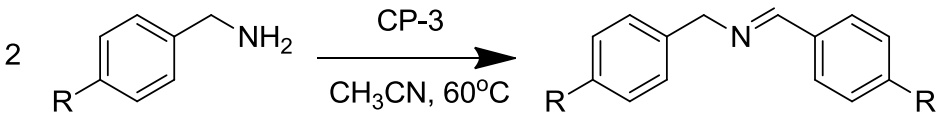

1c: R = H
2c: R = CH_3
3c: R = OCH_3

1d: R = H
2d: R = CH_3
3d: R = OCH_3

Entry	*Catalyst*	*substrate*	*conversion%* [b]
1	**CP-3**	**1c**	99
2	**CP-3** (1st reuse)	**1c**	99
3	**CP-3** (2nd reuse)	**1c**	99
4	**CP-3**	**2c**	95
5	**CP-3**	**3c**	84
6	$Ru(bpy)_3Cl_2$	**1c**	97
7	**CP-6**	**1c**	8
8[c]	No catalyst	**1c**	<5
9[d]	**CP-3**	**1c**	<5
10[d]	$Ru(bpy)_3Cl_2$	**1c**	<5

[a]All the reactions were run at 60 °C for 1 h with 1 mol% **CP-3** at a distance of ~10 cm from a 450 W Xe lamp; [b]Conversions were determined by integrating the ^{1}H NMR peaks; [c]without photocatalyst; [d]without light.

Table 6.5 Photocatalytic dehalogenation of benzyl bromoacetate by **CP-3** [a]

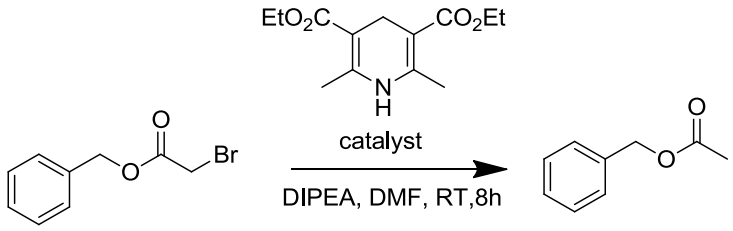

Entry	*Catalyst*	*Conversion %* [b]
1	**CP-3**	>99
2	$Ru(bpy)_3Cl_2$	>99
3	No catalyst	8
4	**CP-6**	27

[a] Reactions were run at r. t. for 8 h with 1 mol% Ru-based catalyst; [b] Conversions were determined by ^{1}H NMR.

The nonporous nature of **CP-3** indicates that only a very small fraction of $[Ru(bpy)_3]^{2+}$ phosphors are at or near the surface and accessible to the organic substrates. The reason why **CP-3** still exhibits extremely high photocatalytic activity can only be explained by the fact that Ru

phosphors embedded in the core of **CP-3** can serve as antenna to harvest light energy and the excited states generated at the interior of the material can easily migrate through the framework and reach the surface active sites (Scheme 6.5).

Catalysis results using Os-doped **CP-3** and **CP-5** support the light-harvesting nature of these photocatalytic reactions. Aza-Henry reaction between **1a** and CH_3NO_2 was employed to probe the photocatalytic activity of Os-doped **CP-3**s. The 4.7 mol% Os-doped **CP-3** gave only 45% conversion of the substrate after reactions of 8 hours, compared to 97% conversion catalyzed by the **CP-3** under identical conditions. The 9.1 mol% Os-doped **CP-3** catalyst further decreased the conversion to 37%. Interestingly, although the homogeneous $Os(bpy)_3(PF_6)_2$ catalyst gave a complete conversion of **1a** under the same reaction conditions, the **CP-5** gave 13% conversion, which is only slightly above that of the background reaction (10%). The drastically different behavior of **CP-5** compared to its **CP-3** counterpart indicates that the $[Os(bpy)_2(dbbpy)]^{2+*}$ excited state cannot effectively migrate in the **CP-5** framework. This is consistent with the much shorter lifetime of **CP-5** (τ=17 ns, Figure 6.3b), which translates to less time and shorter distance the $[Os(bpy)_3]^{2+*}$ excited state can travel. In the Os-doped **CP-3** catalyzed reactions, the $[Ru(bpy)_3]^{2+*}$ excited states generated in the interior of the solid may transfer energy to the $[Os(bpy)_3]^{2+}$ traps before migrating to the solid surface to drive redox reactions. In both cases, the low activities of the **CP-5** and the Os-doped **CP-3**s can be explained by the inability of the excited states to reach the polymer surface, supporting the role of core-to-surface excited state migration in the **CP** photocatalysis.

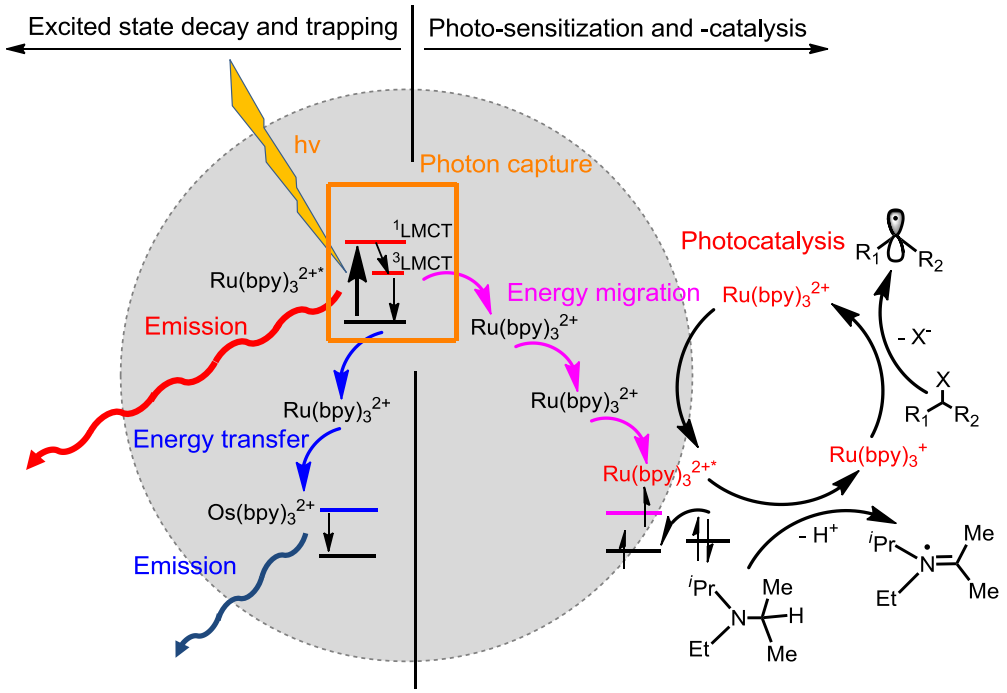

Scheme 6.5 Schematic representation of core-to-surface excited state transport in **CP-3** catalyzed photoreactions. (Reprinted with permission from ref [53]. Copyright American Chemical Society 2012)

We also tested the photocatalytic activity of **CP-4** using the aza-Henry reaction. As a result of the core-to-surface excited state migration, the **CP-4** also serves as an active photocatalyst with 55%, 54%, and 99% conversions in 8 hours for reactions between nitromethane and **1a**, **2a**, and **3a**, respectively. (Table 6.6). Except for substrate **3a**, the conversions of the reactions catalyzed by **CP-4** are significantly lower than that of the **CP-3** catalyzed reactions, which is consistent with the shorter lifetime of the **CP-4** (τ=97.5 ns, Figure 6.3b) than the **CP-3** counterpart (τ=166.5 ns). An empirical linear relationship was obtained by plotting the conversions of reactions between **1a** and nitromethane catalyzed by different CP catalysts against the phosphorescent lifetimes of those catalysts (the catalysts include **CP-3**, **CP-4**, 4.7% Os-doped **CP-3**, 9.1% Os-doped **CP-3**, **CP-5**, see Figure 6.2d). Such correlation between photochemical activity and

excited state lifetime in CPs, which is absent in homogeneous molecular catalytic systems,[35] provides additional evidence for the core-to-surface excited state transport mechanism of these highly active CP photocatalysts.

Table 6.6 Photocatalytic aza-Henry reactions[a] using **CP-4** and homogeneous Ir complex (Ir-M) as photocatalysts

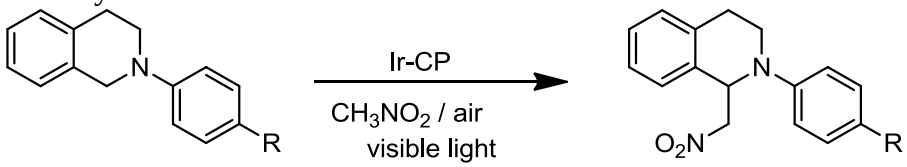

1a: R = H
2a: R = Br
3a: R = OCH_3

1b: R = H
2b: R =Br
3b: R = OCH_3

entry	*Condition*	*substrate*	*Conversion (%)*[b]
1	**CP-4**	**1a**	55
2	**CP-4**	**2a**	54
3	**CP-4**	**3a**	>99
4	**Ir-M**	**1a**	99
5	**Ir-M**	**2a**	99
6	**Ir-M**	**3a**	81

[a] Reactions were run at r. t. for 8 hours, with 0.2 mol% catalyst loadings, ~5 cm in front of a 26 W fluorescent lamp. [b] Conversions were determined by ^{1}H NMR. Ir-M is $[(ppy)_2Ir(debpy)]Cl$ which models the Ir phosphor in the CP.

In an additional control experiment, we observed that photocatalytic reactions with **CP-6** (without the metallo-phosphor) gave slightly higher conversions than corresponding background reactions. For example, in the aza-Henry reactions with nitromethane, **CP-6** gave conversions of 36% and 29% for **1a** and **2a**, in comparison to the background conversions of 10% and 11% (Table 6.3). In the aerobic oxidative coupling of **1c**, **CP-6** gave a conversion of 8% in comparison to <5% for the background reaction (Table 6.4). **CP-6** gave a conversion of 27% in the dehalogenation reaction, as compared to the 8% conversion for the background reaction. We thus believe that the antenna effect of the framework, through either sensitizing ^{3}MLCT

excitation of the $[Ru(bpy)_3]^{2+}$ phosphor or directly activating the substrates, also contributes to the excellent photocatalytic activities of **CP-3**.

6.4 Crosslinked Polymers synthesized by Cu-catalyzed coupling reaction.[54]

6.4.1 synthesis and characterization of crosslinked polymers

4,4'-bis[tri(isopropyl)silylethynyl]-2,2'-bipyridine was prepared by a Pd-catalyzed Sonogashira reaction between 4,4'-dibromo-2,2'-bipy[55] and [tri(isopropyl)silyl]acetylene in 93% yield. 4,4'-bis[tri(isopropyl)silylethynyl]-2,2'-bipy was treated with $[Ru(DMSO)_4Cl_2]$ in DMF at 140 ^oC for 8 h to give bis{[4,4'-bis(triisopropyl)silylethynyl]-2,2'-bipy}ruthenium dichloride in 83% isolated yield,[56] which was converted to Ru{[4,4'-bis(triisopropyl)silylethynyl]-2,2'-bipy}$_2$(2,2'-bipy)Cl_2 (TIPS-**Ru-1**) in 73% yield by treating with 2,2'-bipy. Removal of the tri(isopropyl)silyl (TIPS) groups with tetrabutylammonium fluoride (TBAF) gave Ru[4,4'-bis(ethynyl)-2,2'-bipy]$_2$(2,2'-bipy)$(NO_3)_2$ (**Ru-1**) in 60% isolated yield. The regioisomers with ethynyl groups in the 5,5'-positions of the bipy ligands, Ru{[5,5'-bis(triisopropyl)silylethynyl]-2,2'-bipy}$_2$(2,2'-bipy)Cl_2 (TIPS-**Ru-2**) and Ru[5,5'-bis(ethynyl)-2,2'-bipy]$_2$(2,2'-bipy)$(NO_3)_2$ (**Ru-2**) were similarly synthesized starting from 5,5'-dibromo-2,2'-bipy[57] in 58% and 23% overall yield, respectively (Scheme 6.6). All of the compounds were purified by silica gel chromatography and characterized by ^1H and ^{13}C NMR spectroscopy and electrospray ionization-mass spectrometry. The ^1H NMR spectra of **Ru-1** and **Ru-2** both showed a pair of closely spaced singlets at approximately δ 4.35 ppm and 4.07 ppm for the terminal alkynyl protons, respectively. These chemical shifts have moved downfield as a result of coordination to the Ru centers when compared with the chemical shift of ~δ 3.2 ppm for the alkynyl protons of free bipy derivatives.[58] The monomers **Ru-1** and **Ru-2** are readily soluble in polar solvents such as MeOH, CH_3CN, and H_2O.

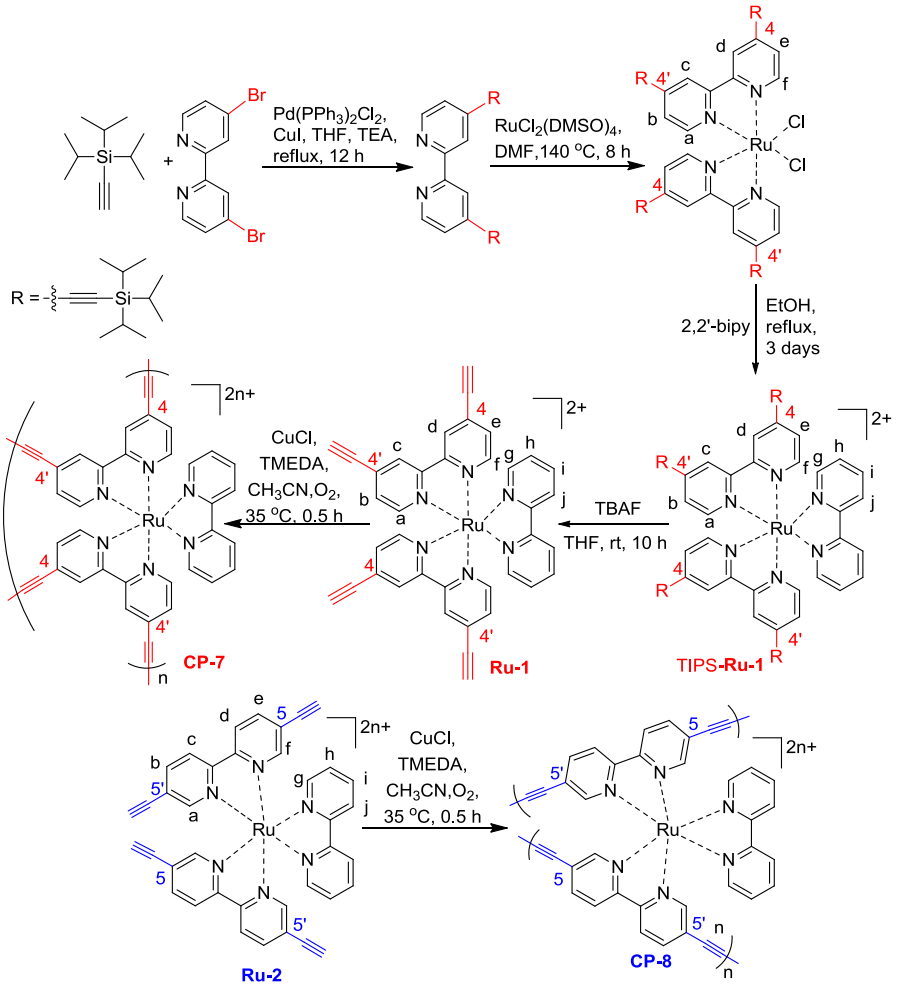

Scheme 6.6. Synthesis of $Ru(bipy)_3^{2+}$-based crosslinked polymers **CP-7** and **CP-8.** (Reprinted with permission from ref [54]. Copyright American Chemical Society 2012)

Oxidative Eglinton coupling reactions of the two regioisomeric tetra(ethynyl) derivatives of $Ru(bpy)_3^{2+}$ were carried out with the CuCl/*N,N,N',N'*-tetramethylethylenediamine catalyst under an oxygen atmosphere in acetonitrile at 35 °C for 0.5 h.[59] The resulting solids were washed with pyridine, methanol, water, and dried in vacuo to afford **CP-7** and **CP-8** in 95% and 91% yield, respectively. Both **CP-7** and **CP-8** are black-red amorphous powders that are insoluble in common organic solvents such as DMF, H_2O, CH_3CN, and resistant toward acids and bases. **CP-7** and **CP-8** were characterized by inductively coupled plasma mass spectroscopy (ICP-MS),

Fourier transform-infrared spectroscopy (FT-IR), thermogravimetric analysis (TGA), nitrogen adsorption, and transmission electron microscopy (TEM).

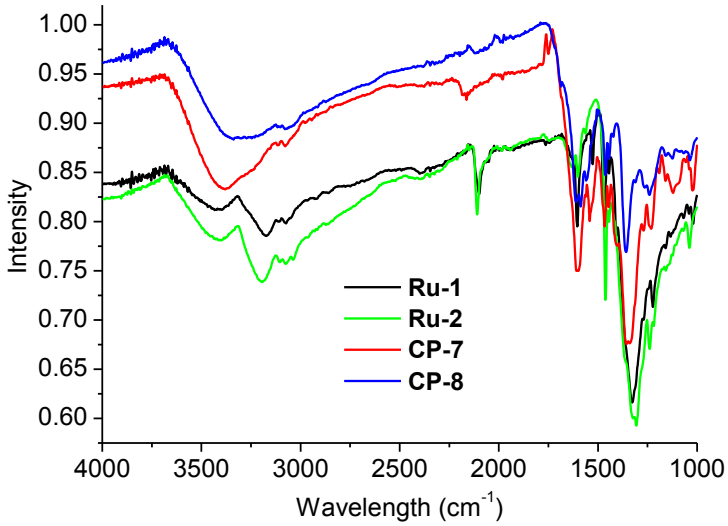

Figure 6.5 FT-IR spectra of **Ru-1**, **Ru-2**, **CP-7** and **CP-8.** (Reprinted with permission from ref [54]. Copyright American Chemical Society 2012)

Based on the ICP-MS results, **CP-7** and **CP-8** possess exceptionally high $[Ru(bpy)_3]^{2+}$ loadings of 91.0±5.0 wt% and 89.6±5.0 wt%, respectively, close to that of the stoichiometric polymer formulae (87.0 wt%). Compared to previously reported $[Ru(bpy)_3]^{2+}$-containing porous CPs (2.2-4.5 wt%),[42] the phosphor loadings in **CP-7** and **CP-8** have drastically increased as a result of support-less single component homocoupling reactions. The high concentrations of $[Ru(bpy)_3]^{2+}$ dyes in the structures can not only enhance visible light absorption but also facilitate excited state migration in the CP networks through Dexter triplet to triplet energy transfer. The degree of polymerization is indicated by the IR spectra. IR spectra of monomers **Ru-1** and **Ru-2** showed a diagnostic absorption of carbon-hydrogen stretching peak of the C≡C-H group at about 3180 cm^{-1} and 3200 cm^{-1}, respectively (Figure 6.5). These peaks are mostly absent in the IR spectra of the CPs, indicating that most of the terminal alkyne groups in the

monomers have been consumed in the oxidative Eglinton coupling reactions. The particles are stable up to 200 ^{o}C in air, as revealed by TGA, which is consistent with previously reported CPs polymers based on butadiyne linkages.[60]

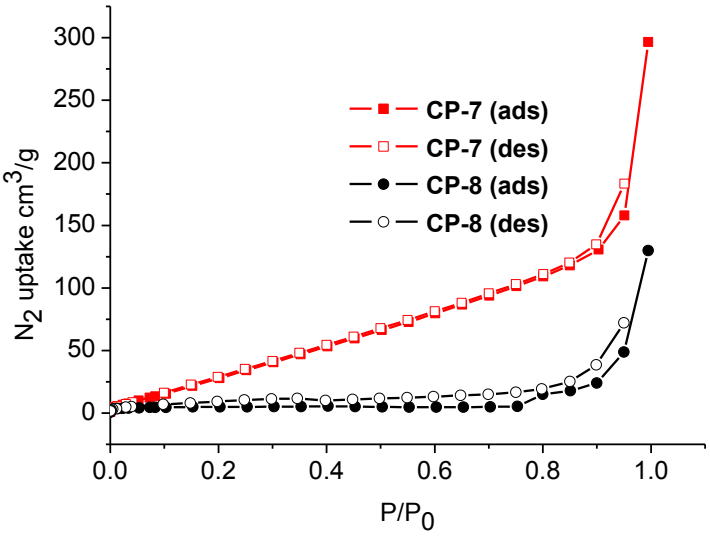

Figure 6.6 Nitrogen sorption isotherms of **CP-7** and **CP-8** in at 77 K. (Reprinted with permission from ref [54]. Copyright American Chemical Society 2012)

The porosity of the CPs was investigated by nitrogen sorption measurements at 77 K. **CP-7** exhibits a BET surface area of 198 m^2/g whereas **CP-8** shows a negligible BET surface area of 15 m^2/g (Figure 6.6). These surface areas are significantly lower than the CPs based on tetrakis(4-ethynyl-phenyl)methane.[60,61] We attributed the low porosity of **CP-7** and **CP-8** to the bulky groups of the $[Ru(bpy)_3]^{2+}$ complexes in the polymer networks, which is known to reduce the porosity of CPs.[47] The TEM sample was prepared by first dispersing the CPs in methanol, and then placing them on carbon-coated Cu/Ni grids. TEM images of both **CP-7** and **CP-8** showed that they are aggregates of spherical nanoparticles of ~100 nm in diameter (Figure 6.7).

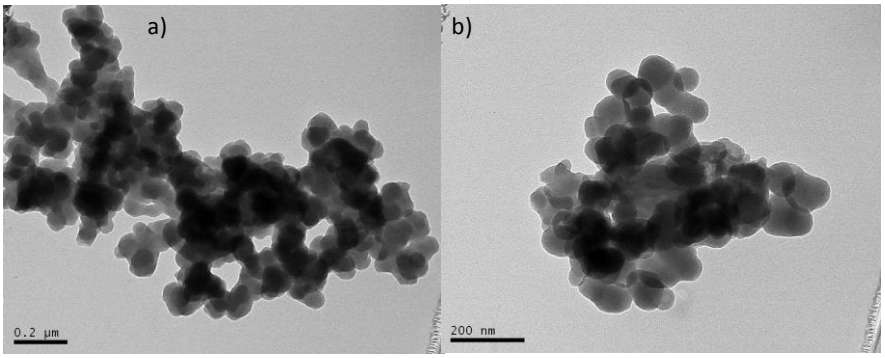

Figure 6.7 TEM images of **CP-7** (a) and **CP-8** (b) on a carbon-coated Cu/Ni grid. (Reprinted with permission from ref [54]. Copyright American Chemical Society 2012)

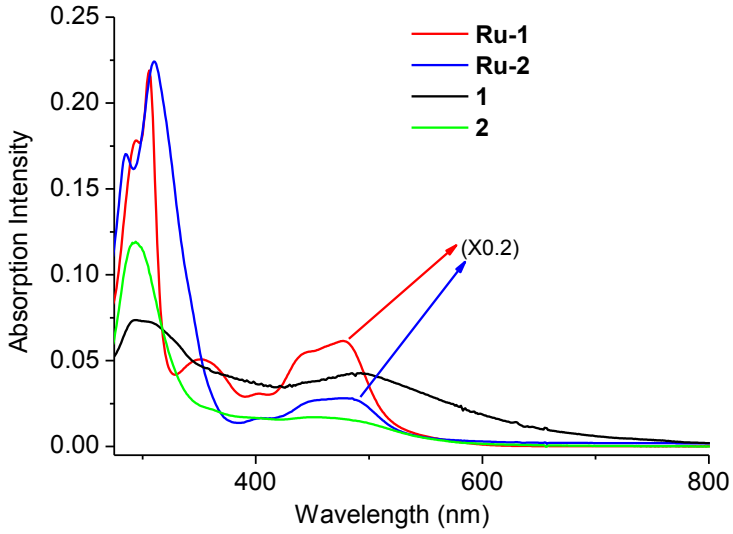

Figure 6.8 Steady-state absorption spectra of stirred suspensions of **CP-7** and **CP-8** in CH_3CN (0.74 mg/50 mL) and dilute solutions of **Ru-1** and **Ru-2** in CH_3CN (2×10^{-5} M). Absorption spectra of **Ru-1** and **Ru-2** are on a reduced scale (× 0.2). (Reprinted with permission from ref [54]. Copyright American Chemical Society 2012)

CPs built from $[Ru(bpy)_3]^{2+}$ complexes act as insoluble but dispersible photosensitizers by taking advantage of redox-active ^{3}MLCT excited states of the chromophores. Steady-state UV-vis absorption and emission spectra and time-resolved phosphorescence spectra were recorded with a stirred suspension of **CP-7** or **CP-8** in CH_3CN and dilute solutions of **Ru-1** and **Ru-2**

monomers in CH_3CN (2×10^{-5} M). They all showed a broad absorption between 300-800 nm with two or three additional discernible absorption bands (Figure 6.8). For **CP-7**, the absorption peak at ~294 nm is assigned to the $\pi\rightarrow\pi^*$ bipy ligands in the $[Ru(bpy)_3]^{2+}$ whereas the peak at ~493 nm is attributed to the metal-to-ligand charge transfer (^{1}MLCT) transition. Compared with **Ru-1** amd **Ru-2**, the ^{1}MLCT peaks in CPs **1** and **2** became broadened and showed a slight red-shift, which is beneficial to absorbing the solar radiation. In the steady-state phosphorescence spectra, the emission maximum λ_{max} centered at 705 nm for **CP-8** and at 696 nm for **CP-8** (Figure 6.9). Interestingly, the phosphorescence maximum λ_{max} of **CP-7** exhibited obviously red shift in comparison with monomer **Ru-1** owing to the increased effective conjugation length of ligands in **CP-7** and aggregation of **CP-7** in the particle. The phosphorescence lifetimes of the CPs were measured using an Edingburgh FLS 920 in the time-correlated photon counting mode. When excited at ~ 440 nm, the decays of monomers **Ru-1** and **Ru-2** and **CP-7** were well fitted with a mono-exponential model, leading to emission lifetimes of 962 ns, 574 ns, and 423 ns, respectively (Figure 6.10). The emission decay of **CP-8** was fitted with a double-exponential model to give an averaged lifetime of 112 ns, indicating a much shorter-lived ^{3}MLCT phosphorescence. The broad absorption bands together with relatively long excited state lifetimes of the CPs make them good candidates as heterogeneous photocatalysts.

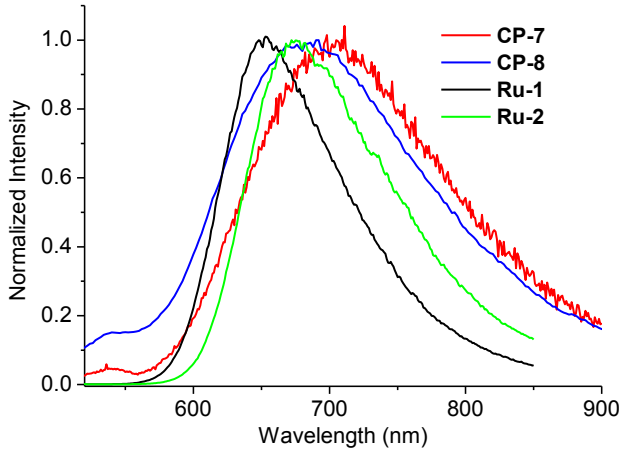

Figure 6.9 Steady-state phosphorescence spectra of stirred suspensions of **CP-7** and **CP-8** in CH_3CN (0.74 mg/50 mL) and dilute solutions of **Ru-1** and **Ru-2** in CH_3CN (2×10^{-5} M). (Reprinted with permission from ref [54]. Copyright American Chemical Society 2012)

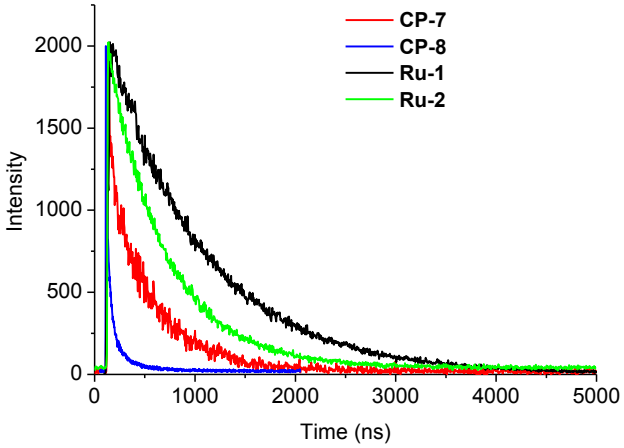

Figure 6.10 Time-resolved phosphorescence decays of **CP-7** and **CP-8** and monomers **Ru-1** and **Ru-2** (excitation: 440 nm; emission: 660 nm). (Reprinted with permission from ref [54]. Copyright American Chemical Society 2012)

6.4.2 Photocatalysis with CP-7 and CP-8

We examined the photocatalytic activities of the CP particles, using the aza-Henry reaction,[35,62] aerobic oxidative coupling of amine,[37] and dehalogenation of benzyl bromoacetate[32] as representative reactions. **CP-7** and **CP-8** exhibited high photocatalytic activities in these

reactions. Aza-Henry reactions between tetrahydroisoquinoline derivatives **1a-3a** and nitromethane were carried out in air for 8 h with 0.2 mol% of CPs as the catalysts and a common fluorescent lamp (26 W) as the light source, in a similar fashion as those reported previously.[45] As shown in Table 6.7, the conversions of the reactions were calculated based on the ^{1}H-NMR peak integrations of the crude products. After filtering off the CP catalysts, the solvents were removed and the crude products were analyzed by ^{1}H-NMR. The integrations of peaks of the featured protons in the products (about δ 5.5 ppm) and those of the corresponding starting materials (about δ 4.4 ppm) were used in the calculation. **CP-7** gave a slightly higher conversion (94% for **1a** with the phenyl substituent, 96% for **3a** with the *para*-methoxylphenyl substituent, and 99% for **2a** with the *para*-bromophenyl substituent) than **CP-8** (92% for **3**, 96% for **5**, and 94% for **2a**). Notably, these conversions are slightly higher than those catalyzed by other Ru- or Ir-based crosslinked polymers in the precious section.[42] Moreover, aza-Henry products were isolated in very high yields after purification by chromatography (Table 6.7).We found that the isolated yields for these CP-catalyzed reactions are comparable to those of the homogeneous systems even though we reduced the reaction time (avg. 16 h to 8 h) and catalyst loading (1 mol% to 0.2 mol%) in these heterogeneous photocatalytic reactions. We have also carried out several control experiments to further investigate the details of these heterogeneous photocatalytic reactions. For example, the conversions and isolated yields afforded by **CP-7** and **CP-8** are higher than those of the monomer homogeneous catalysts (TIPS-**Ru-1** and TIPS-**Ru-2**). **Ru-1** and **Ru-2** are unstable and will polymerize under the photocatalytic reaction conditions and could not be used as control homogeneous catalysts. Moreover, low conversions (< 20%) were detected in the absence of either light or the catalyst, indicating the photocatalytic nature of these reactions. We have also recycled and reused the CP catalysts. **CP-7** was easily recovered

from the reaction mixture by filtration, and could be re-used for at least three times. ICP-MS studies showed very little Ru leaching (<0.5%) to the supernatant after these photocatalytic reactions. The recovered solid CP catalysts showed only slight decrease in conversions and isolated yields of aza-Henry products.

Table 6.7 Photocatalytic aza-Henry reactions using **CP-7** and **CP-8** as catalysts.[a]

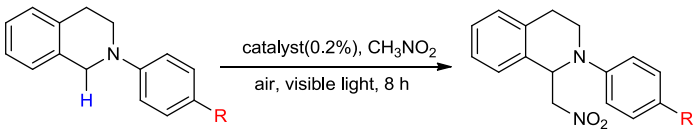

1a R = H **1b** R = H

2a R = Br **2b** R = Br

3a R = CH_3O **3b** R = CH_3O

Compds	Catalyst	Conversion%[b]	Isolated yield%[c]
1a	**CP-7**	94	85
1a	TIPS-**Ru-1**	91	76
2a	**CP-7**	99	89
2a	**CP-7 (2nd-use)**	91	85
2a	**CP-7 (3rd-use)**	90	80
2a	**CP-7 (4th-use)**	87	76
3a	**CP-7**	96	90
1a	**CP-8**	92	81
1a	TIPS-**Ru-2**	90	77
2a	**CP-8**	94	83
3a	**CP-8**	96	82

[a]All of the reactions were carried out at room temperature with 0.2 mol% ratio catalyst for 8 h with a 26 W fluorescent lamp; [b]converisions were determined by integrating the ^{1}H NMR peaks; [c]isolated yields were calculated based on pure products after column chromatography.

We further examined the scope of reactions catalyzed by the CPs. As shown in Table 6.8, aerobic oxidative coupling of a series of primary amines were also efficiently catalyzed at 1 mol% CP catalyst loadings with a 450 W Xe lamp. The conversions of various substrates catalyzed by the CPs were calculated based on the integration of the ^{1}H-NMR peaks of the featured protons in the products and those of the corresponding starting materials. Nearly complete conversions (99%) of all the three substrates were observed with **CP-7** as photocatalyst,

which compare favorably with the monomer control catalyst. In contrast, the conversions for **CP-8** were highly dependent on the substrates (99% for benzylamine, 76% for *p*-methylbenzylamine, 67% for *p*-methoxylbenzylamine). Moreover, low conversions (< 5%) were obtained in the absence of either light or the catalysts, confirming the photocatalytic role of the CPs. We have also determined the yields of oxidative coupling products by gas chromatography (GC) with *n*-undecane as the internal standard. The GC yields were slightly lower than the ^{1}H-NMR conversions, but they both showed the same trends. We believe that some of the starting materials were consumed to form other byproducts that were not detected by GC. We also demonstrated that the photocatalyst **CP-7** could be readily recovered and reused twice for all these three substrates with only slight decrease of the conversions and yields.

Table 6.8 Photocatalytic aerobic oxidative coupling reactions using **CP-7** and **CP-8** as catalysts.

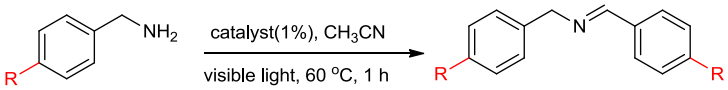

1c R = H
2c R = CH_3
3c R = OCH_3

1d R = H
2d R = CH_3
3d R = OCH_3

Compds	Catalyst	Conversion %[b]	GC yield%
1c	**CP-7**	99	93
2c	**CP-7**	99	88
2c	**CP-7 (2nd-use)**	99	85
2c	**CP-7 (3rd-use)**	97	84
3c	**CP-7**	99	87
1c	**CP-8**	99	88
2c	**CP-8**	76	52
3c	**CP-8**	67	51
1c	TIPS-**Ru-2**	99	89
2c	TIPS-**Ru-2**	97	87
3c	TIPS-**Ru-2**	90	79

[a]All of the reactions were done at 60 °C for 1 h with 1mol% catalyst under a 450 W Xe lamp; [b]Converisions were determined by integrating the ^{1}H NMR peaks.

The photocatalyzed reductive dehalogenation reaction was also examined using the CP photocatalysts (Scheme 6.7). Benzyl bromoacetate was chosen as the substrate and a 26 W

fluorescent lamp was used as the light source. Benzyl bromoacetate was completely converted to benzyl acetate with 1 mol% loadings of photocatalyst **CP-7** or **CP-8** based on ^{1}H NMR spectra. These results have been corroborated with high isolated yields of the benzyl acetate (92% for **CP-7** and 86% for **CP-8**). A control reaction in the absence of the CPs gave <10% conversion. The CP photocatalyst could also be recovered and reused without significant decrease in conversions and yields.

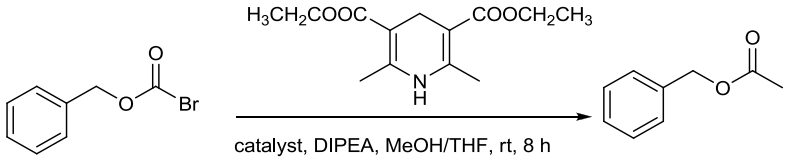

Scheme 6.7 Photocatalytic dehalogenation of benzyl bromoacetate using **CP-7** and **CP-8** as catalysts. (Reprinted with permission from ref [54]. Copyright American Chemical Society 2012)

The almost nonporous nature of Ru-based CPs indicates that only a small fraction of $[Ru(bpy)_3]^{2+}$ chromophores is at or near the surface and is accessible to the organic substrates. The reason why such nonporous heterogeneous crosslinked polymers still exhibit extremely high photocatalytic activity can again be explained by efficient excited state migration among the chromophore framework just like in Section 6.3. The interior $[Ru(bpy)_3]^{2+}$chromophores of the crosslinked polymers can be excited by light, and the generated excited states can migrate among the chromophore networks through Dexter triplet to triplet energy transfer, finally reaching the reactive sites of the polymer surface to drive redox reactions.[63] We suggested that Ru chromophores in the interior of the polymers can effectively serve as light harvesting antenna to collect photon energy and transfer them to the reactive sites, which is dominant and much faster compared to the reversed process of excited state migration from the surface to the interior of the polymers. The Ru chromophores on the surface can either be directly excited by light or accept

excited state energy from the interior of the polymer particle to form the ^{3}MLCT states and then undergo redox reactions to initiate the photocatalytic cycle.[16] Such a light-harvesting phenomenon was recently unambiguously demonstrated by Lin et al. in $[Ru(bpy)_3]^{2+}$-derived MOFs.[15]

6.5 Conclusions

Ir and Ru phosphors have been successfully integrated into porous crosslinked polymers and extremely high chromophore loadings via cobalt catalyzed alkyne trimerization, Sonogashira cross-coupling reactions and Eglinton alkyne homocoupling. The resultant framework materials are stable in various solvents, including concentrated hydrochloric acid, and are thermally and oxidatively stable in air up to 350 ^{o}C. These phosphorescent Ir- and Ru-based CPs were shown to be highly active, recyclable and reusable heterogeneous photocatalysts in Aza-Henry reactions aerobic amine coupling, and a variety of different organic transformations.

Interestingly, the very high catalytic activities were not only observed with porous CPs but also with nonporous CPs as well. The activities of the nonporous CPs result from their light-harvesting ability, which allows collection of photons by exciting the ^{3}MLCT states of the phosphors via framework sensitization and migration of the excited states to the particle surface to drive the redox catalysis. This light-harvesting mechanism was supported by steady-state and time-resolved emission data as well as the reduced catalytic activities of and Os-doped Ru-**CP**s. The work illustrates the potential for designing highly efficient photocatalysts based on light-harvesting crosslinked polymers.

REFERENCES

(1) Barber, J. *Chem. Soc. Rev.* **2009**, *38*, 185.

(2) Ciamician, G. *Science* **1912**, *36*, 385.

(3) Gust, D.; Moore, T. A.; Moore, A. L. *Acc. Chem. Res.* **2009**, *42*, 1890.

(4) Dau, H.; Zaharieva, I. *Acc. Chem. Res.* **2009**, *42*, 1861.

(5) Guldi, D. M. *Chem. Soc. Rev.* **2002**, *31*, 22.

(6) Wasielewski, M. R. *Acc. Chem. Res.* **2009**, *42*, 1910.

(7) Engel, G. S.; Calhoun, T. R.; Read, E. L.; Ahn, T. K.; Mancal, T.; Cheng, Y. C.; Blankenship, R. E.; Fleming, G. R. *Nature* **2007**, *446*, 782.

(8) Magnuson, A.; Anderlund, M.; Johansson, O.; Lindblad, P.; Lomoth, R.; Polivka, T.; Ott, S.; Stensjö, K.; Styring, S.; Sundström, V.; Hammarström, L. *Acc. Chem. Res.* **2009**, *42*, 1899.

(9) Kobuke, Y. *Euro. J. Inorg. Chem.* **2006**, *2006*, 2333.

(10) Wagner, R. W.; Lindsey, J. S. *J. Am. Chem. Soc.* **1994**, *116*, 9759.

(11) Fleming, C. N.; Maxwell, K. A.; DeSimone, J. M.; Meyer, T. J.; Papanikolas, J. M. *J. Am. Chem. Soc.* **2001**, *123*, 10336.

(12) Fox, M. A. *Acc. Chem. Res.* **1992**, *25*, 569.

(13) Jones, W. E.; Baxter, S. M.; Strouse, G. F.; Meyer, T. J. *J. Am. Chem. Soc.* **1993**, *115*, 7363.

(14) Xu, Z.; Moore, J. S. *Acta Polymerica* **1994**, *45*, 83.

(15) Kent, C. A.; Liu, D. M.; Ma, L. Q.; Papanikolas, J. M.; Meyer, T. J.; Lin, W. B. *J. Am. Chem. Soc.* **2011**, *133*, 12940.

(16) Kent, C. A.; Mehl, B. P.; Ma, L. Q.; Papanikolas, J. M.; Meyer, T. J.; Lin, W. B. *J. Am. Chem. Soc.* **2010**, *132*, 12767.

(17) Nabiev, I.; Rakovich, A.; Sukhanova, A.; Lukashev, E.; Zagidullin, V.; Pachenko, V.; Rakovich, Y. P.; Donegan, J. F.; Rubin, A. B.; Govorov, A. O. *Angew. Chem. Int. Ed. Engl.* **2010**, *49*, 7217.

(18) Spitler, M. T.; Parkinson, B. A. *Acc. Chem. Res.* **2009**, *42*, 2017.

(19) Nakashima, T.; Kimizuka, N. *Adv. Mater.* **2002**, *14*, 1113.

(20) Sugiyasu, K.; Fujita, N.; Shinkai, S. *Angew. Chem. Int. Ed. Engl.* **2004**, *43*, 1229.

(21) Nagata, N.; Kuramochi, Y.; Kobuke, Y. *J. Am. Chem. Soc.* **2009**, *131*, 10.

(22) Borjesson, K.; Tumpane, J.; Ljungdahl, T.; Wilhelmsson, L. M.; Norden, B.; Brown, T.; Martensson, J.; Albinsson, B. *J. Am. Chem. Soc.* **2009**, *131*, 2831.

(23) Channon, K. J.; Devlin, G. L.; MacPhee, C. E. *J. Am. Chem. Soc.* **2009**, *131*, 12520.

(24) D'Souza, F.; Smith, P. M.; Zandler, M. E.; McCarty, A. L.; Itou, M.; Araki, Y.; Ito, O. *J. Am. Chem. Soc.* **2004**, *126*, 7898.

(25) Kodis, G.; Terazono, Y.; Liddell, P. A.; Andreasson, J.; Garg, V.; Hambourger, M.; Moore, T. A.; Moore, A. L.; Gust, D. *J. Am. Chem. Soc.* **2006**, *128*, 1818.

(26) Xing, C. F.; Xu, Q. L.; Tang, H. W.; Liu, L. B.; Wang, S. *J. Am. Chem. Soc.* **2009**, *131*, 13117.

(27) Yuhas, B. D.; Smeigh, A. L.; Samuel, A. P. S.; Shim, Y.; Bag, S.; Douvalis, A. P.; Wasielewski, M. R.; Kanatzidis, M. G. *J. Am. Chem. Soc.* **2011**, *133*, 7252.

(28) Takeda, H.; Ohashi, M.; Tani, T.; Ishitani, O.; Inagaki, S. *Inorg. Chem.* **2010**, *49*, 4554.

(29) Andrews, R. S.; Becker, J. J.; Gagne, M. R. *Angew. Chem. Int. Ed. Engl.* **2010**, *49*, 7274.

(30) Chen, W.; Rein, F. N.; Rocha, R. C. *Angew. Chem. Int. Ed. Engl.* **2009**, *48*, 9672.

(31) Ischay, M. A.; Anzovino, M. E.; Du, J.; Yoon, T. P. *J. Am. Chem. Soc.* **2008**, *130*, 12886.

(32) Narayanam, J. M.; Tucker, J. W.; Stephenson, C. R. *J. Am. Chem. Soc.* **2009**, *131*, 8756.

(33) Nicewicz, D. A.; MacMillan, D. W. *Science* **2008**, *322*, 77.

(34) Bock, C. R.; Meyer, T. J.; Whitten, D. G. *J. Am. Chem. Soc.* **1974**, *96*, 4710.

(35) Condie, A. G.; Gonzalez-Gomez, J. C.; Stephenson, C. R. *J. Am. Chem. Soc.* **2010**, *132*, 1464.

(36) Dai, C.; Narayanam, J. M.; Stephenson, C. R. *Nat. Chem.* **2011**, *3*, 140.

(37) Lang, X.; Ji, H.; Chen, C.; Ma, W.; Zhao, J. *Angew. Chem. Int. Ed. Engl.* **2011**.

(38) Narayanam, J. M.; Stephenson, C. R. *Chem. Soc. Rev.* **2011**, *40*, 102.

(39) Neumann, M.; Fuldner, S.; Konig, B.; Zeitler, K. *Angew. Chem. Int. Ed. Engl.* **2011**, *50*, 951.

(40) Su, F.; Mathew, S. C.; Mohlmann, L.; Antonietti, M.; Wang, X.; Blechert, S. *Angew. Chem. Int. Ed. Engl.* **2011**, *50*, 657.

(41) Tucker, J. W.; Nguyen, J. D.; Narayanam, J. M.; Krabbe, S. W.; Stephenson, C. R. *Chem. Commun.* **2010**, *46*, 4985.

(42) Xie, Z.; Wang, C.; deKrafft, K. E.; Lin, W. *J. Am. Chem. Soc.* **2011**, *133*, 2056.

(43) Yoon, T. P.; Ischay, M. A.; Du, J. *Nat. Chem.* **2010**, *2*, 527.

(44) Pham, P. V.; Nagib, D. A.; MacMillan, D. W. C. *Angew. Chem. Int. Ed. Engl.* **2011**, *50*, 6119.

(45) Cooper, A. I. *Angew. Chem. Int. Ed. Engl.* **2011**, *50*, 996.

(46) Ding, X.; Guo, J.; Feng, X.; Honsho, Y.; Seki, S.; Maitarad, P.; Saeki, A.; Nagase, S.; Jiang, D. *Angew. Chem. Int. Ed. Engl.* **2011**, *50*, 1289.

(47) Jiang, J. X.; Wang, C.; Laybourn, A.; Hasell, T.; Clowes, R.; Khimyak, Y. Z.; Xiao, J. L.; Higgins, S. J.; Adams, D. J.; Cooper, A. I. *Angew. Chem. Int. Ed. Engl.* **2011**, *50*, 1072.

(48) Thomas, A. *Angew. Chem. Int. Ed. Engl.* **2010**, *49*, 8328.

(49) Trewin, A.; Cooper, A. I. *Angew. Chem. Int. Ed. Engl.* **2010**, *49*, 1533.

(50) Yuan, S. W.; Kirklin, S.; Dorney, B.; Liu, D. J.; Yu, L. P. *Macromolecules* **2009**, *42*, 1554.

(51) Chen, L.; Honsho, Y.; Seki, S.; Jiang, D. L. *J. Am. Chem. Soc.* **2010**, *132*, 6742.

(52) Ma, L.; Wanderley, M. M.; Lin, W. *ACS Catalysis* **2011**, *1*, 691.

(53) Wang, C.; Xie, Z.; deKrafft, K. E.; Lin, W. *ACS Appl. Mater. & Interfaces* **2012**, *4*, 2288.

(54) Wang, J.-L.; Wang, C.; deKrafft, K. E.; Lin, W. *ACS Catalysis* **2012**, *2*, 417.

(55) James, P. V.; Yoosaf, K.; Kumar, J.; Thomas, K. G.; Listorti, A.; Accorsi, G.; Armaroli, N. *Photochem. & Photobio. Sci.* **2009**, *8*, 1432.

(56) Haberecht, M. C.; Schnorr, J. M.; Andreitchenko, E. V.; Clark, C. G.; Wagner, M.; Müllen, K. *Angew. Chem. Int. Ed. Engl.* **2008**, *47*, 1662.

(57) Bruce, J. I.; Chambron, J.-C.; Kolle, P.; Sauvage, J.-P. *J. Chem. Soc., Perkin Trans.* **2002**, *1,* 1226.

(58) Wang, J.-L.; Li, X.; Lu, X.; Hsieh, I. F.; Cao, Y.; Moorefield, C. N.; Wesdemiotis, C.; Cheng, S. Z. D.; Newkome, G. R. *J. Am. Chem. Soc.* **2011**, *133*, 11450.

(59) Iyoda, M.; Yamakawa, J.; Rahman, M. J. *Angew. Chem. Int. Ed. Engl.* **2011**, *50*, 10522.

(60) Holst, J. R.; Stöckel, E.; Adams, D. J.; Cooper, A. I. *Macromolecules* **2010**, *43*, 8531.

(61) Lu, W.; Yuan, D.; Zhao, D.; Schilling, C. I.; Plietzsch, O.; Muller, T.; Bräse, S.; Guenther, J.; Blümel, J.; Krishna, R.; Li, Z.; Zhou, H.-C. *Chem. Mater.* **2010**, *22*, 5964.

(62) Li, Z.; Li, C.-J. *J. Am. Chem. Soc.* **2005**, *127*, 3672.

(63) Durham, B.; Caspar, J. V.; Nagle, J. K.; Meyer, T. J. *J. Am. Chem. Soc.* **1982**, *104*, 4803.